An imaging-genetic study of the asymmetries in the temporal lobe structures : association of these human-specific markers of development with genetics

Yann Le Guen

NNT : 2018SACLS268

Thèse de doctorat

Etude en imagerie-génétique des asymétries des structures du lobe temporal : association de leurs caractéristiques propres à l'homme avec des données génétiques

Thèse de doctorat de l'Université Paris-Saclay
préparée à l'Université Paris Sud,
Neurospin (CEA)

École doctorale n°575 : electrical, optical, bio : physics and engineering (EOBE)

Spécialité de doctorat : **Imagerie et physique médicale**

Thèse présentée et soutenue à Gif-sur-Yvette, le 24 septembre 2018, par

Yann Le Guen

Composition du Jury :

Florence d'Alché-Buc Professeur, Télécom Paristech, Paris, France	Présidente du jury
Peter Kochunov Professeur, Université du Maryland, Washington, USA	Rapporteur
Roberto Toro Directeur de recherche, Institut Pasteur, Paris, France	Rapporteur
Pascal Belin Professeur, INT, Marseille, France	Examinateur
Vincent Frouin Directeur de recherche, Neurospin, CEA, Saclay, France	Directeur de thèse
Ghislaine Dehaene-Lambertz Professeur, Neurospin, INSERM U992, Saclay, France	Co-Directrice de thèse

université PARIS-SACLAY
ÉCOLE DOCTORALE
Physique et ingénierie : électrons, photons, sciences du vivant (EOBE)

Titre : Etude en imagerie-génétique des asymétries des structures du lobe temporal : association de leurs caractéristiques propres à l'homme avec des données génétiques

Mots clés : imagerie génétique, asymétries cérébrales, lobe temporal, IRM, traits spécifiques humains

Résumé : La structure asymétrique du lobe temporal a déjà été démontrée. Ces asymétries structurelles sont souvent supposées comme support à la latéralisation du langage chez l'homme. Une asymétrie remarquable est celle du sillon temporal supérieur (STS) observée dès la naissance chez l'homme, mais pas chez le chimpanzé. Dans cette thèse, nous nous intéressons aux origines génétiques sous-jacentes à cette asymétrie. Dans ce but, nous utilisons des méthodes d'extraction automatiques de structures asymétriques comme les racines sulcales ou les gyri transverses (plis de passage, PPs). Premièrement, nous reproduisons l'asymétrie de profondeur du STS dans deux grandes cohortes (HCP et UK Biobank) et nous démontrons que le STS gauche est plus souvent interrompu par un PP que son homologue à droite. Secondement, l'héritabilité de la profondeur des racines sulcales dans le STS et de la présence de PP est supérieure dans l'hémisphère gauche. Ceci suggère des signaux génétiques asymétriques qui contribuent à la formation des asymétries de structures du lobe temporal.
Par ailleurs, nous avons montré que les activations fonctionnelles dans le gyrus angulaire ont une variance génétique partagée significative avec la performance cognitive.
Enfin, nous avons identifié une zone cis-régulatrice du gène KCNK2, comme significativement associée avec la largeur et l'épaisseur corticale des sillons, qui sont des caractéristiques du vieillissement du cerveau.

Title: An imaging-genetic study of the asymmetries in the temporal lobe structures: association of these human-specific markers of development with genetics

Keywords: imaging genetics, brain asymmetries, temporal lobe, MRI, human specific traits

Abstract: The asymmetrical structure of the temporal lobe has already been demonstrated. These structural asymmetries are often assumed to contribute to the human language lateralization. One noticeable asymmetry is the one of the superior temporal sulcus (STS) depth observed from birth in humans, but not in chimpanzee. In this thesis, we were interested in the genetic roots underlying this asymmetry. To this aim, we used automated extraction method of asymmetrical structures such as the sulcal roots or transverse gyri (so called plis de passage, PPs). First, we reproduced the STS rightward depth asymmetry in two large cohorts (HCP and UK Biobank) and we demonstrated that the left STS is more often interrupted by a PP than its counterpart. Second, the heritability estimates of depth and convexity of sulcal roots in the STS and the presence of PP are higher in the left hemisphere. This suggests asymmetric genetic cues contributing to the formation of these asymmetrical structures in the temporal lobe.
In addition, we have shown that the functional activations in the angular gyrus have a significant shared genetic variance with the human cognitive performance.
Finally, we have identified a cis-regulating region of the KCNK2, as being significantly associated with the width and cortical thickness of the brain sulci, which are features of brain ageing.

Université Paris-Saclay
Espace Technologique / Immeuble Discovery
Route de l'Orme aux Merisiers RD 128 / 91190 Saint-Aubin, France

Introduction and context of the study

In this part, I present the main elements around which my thesis was built namely the imaging genetics field, the brain cortical folding and asymmetries, and the functional significance of these structures.

First, I define the main notions necessary to understand the imaging genetics field. Then, I give a brief overview of the main methods that have been used in the literature to quantify the genetic influence or identify causal variants on brain phenotypes. Second, I present the different theories that are currently supported to describe the origin of the regular cortical folding in humans. Third, I emphasize that the brain has a general inter-hemisphere symmetric organization, with notable exceptions, that could constitute key human specific brain features. Finally, I review the literatures that pinpoint a strong link between the brain structure and its functions.

1. Brain cortical folding

Most higher mammals have a folded cortex (Ronan and Fletcher, 2014), and these species are named gyrencephalic as opposed to the ones with a smooth cortex which are named lissencephalic. The complex gyrification of the human brain develops during the last trimester of pregnancy in parallel with the final migration of neurons in the cortical plate. At term, all neurons are organized in the cortex in six layers that can be observed in stained slices (Kostović and Judaš, 2010). In humans, the six neuronal layers laminar structure is folded and its thickness is thinner in sulci and thicker in gyri. However, the underlying process from which the cortical folds originate remains largely debated (Mota and Herculano-Houzel, 2015). Additionally, humans have very consistent primary sulci organization across individuals and abnormal folding is often associated with various brain pathologies. Two schools of thought exist to try to explain the folding origin and its consistency: the mechanical forces (Kroenke and Bayly, 2018) versus the cellular mechanisms (Borrell, 2018). These two are not necessarily antagonist but can rather be seen as complementary.

1.1. Modelling the mechanical forces

The first theory advocates that biomechanical constraints lead to the cortical convolutions. At first sight, this could result from the growing tissue limited by the cranium volume, but this theory was discarded by experimental observation (Barron, 1950). Several models have been proposed:

0) The axonal tension theory (Van Essen, 1997), see **Figure 2a**, which advocates that axons pull the cortex to form gyri and thus the complementary sulci. We should note that this theory was rejected in part by recent studies (Ronan et al., 2014; Xu et al., 2010).

1) The surface expansion that produces folds via pressure within the surface mitigated by foldings with two possible explanatory models:

1. The relative difference in surface expansion between the supra-granular and the infra-granular layers of the cortex that causes folding (Richman et al., 1975), see **Figure 2b**. This model describes the cortex as closed surface in which axons fibers pull radially.
2. The differential tangential expansion leading to in-plane pressure evacuated by out-plane foldings (Ronan et al., 2014), see **Figure 2c**. This model put the emphasis on the differential growth rate between the expanding outer and inner zones (Kroenke and Bayly, 2018).

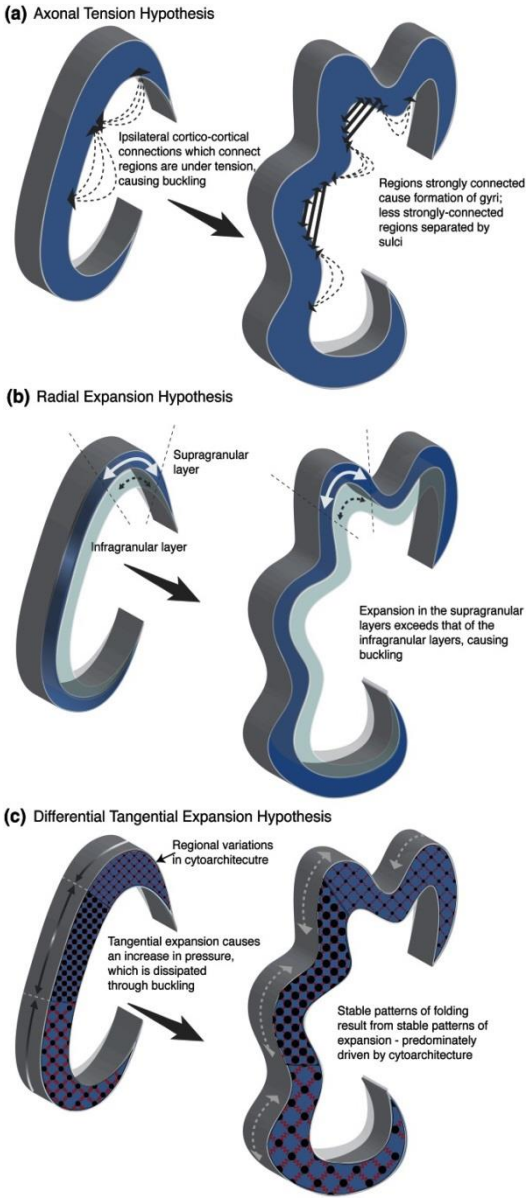

Figure 2. From Ronan & Fletcher 2014**. "**Three distinct mechanisms proposed for gyrification. **a** The axonal tension hypothesis proposes that axons under tension pull regions of the cortex which are strongly connected together, causing folds. However, there are a number of problems with this hypothesis (1) axonal connectivity is not commensurate with the hypothesized pattern of connectivity; (2) axonal innervation post-dates the formation of folds; (3) axons are not under requisite tension to cause folding; (4) removal of axons during developing causes an increase in the number of folds. **b** The radial gradient hypothesis proposes that the increase in expansion of the supragranular layers relative to the infra-granular layers causes buckling. However, several experimental observations militate against this (1) the incidence of basal radial glia (bRG) (which contribute to supragranular layer expansion) is similar in gyrencephalic and lissencephalic species; (2) gyrification may be induced without a change in the proliferation of bRG; (3) reduction in the proliferation of bRG does not change the degree of gyrification; (4) disruption in the formation of supragranular layer neurons does not affect gyrification. **c** The differential tangential expansion hypothesis proposes that tangential expansion of the cortex causes an increase in tangential pressure which is mitigated through buckling. Empirical evidence suggests that the pattern of differential expansion (predominantly influenced by the pattern of cytoarchitecture), causes pattern-specific folding. As such, the stability of folds represents the stability of expansion forces in that region."

Additionally, under the surface expansion hypothesis, several morphogenic models (Foubet et al., 2018; Toro and Burnod, 2005) and experimental observations (Tallinen et al., 2016, 2014) suggest that if the pattern of differential expansion is consistent across individuals then the folds should also be consistent. In particular, the initial prefolding geometry of these models and the regional growth pattern have been reproduced by simulation. Concrete mechanical model have been built giving rise to realistic cortical folds (Tallinen et al., 2016).

1.2. Modelling the cellular mechanisms

However, some argue that they do not account well for the regularity of human sulcal pattern which seems to be developmentally pre-determined laying the foundation for the second school of thought (Borrell, 2018). Experimental studies have shown that progenitor cell, cellular process and genetic programs play a decisive role in cortical folding.

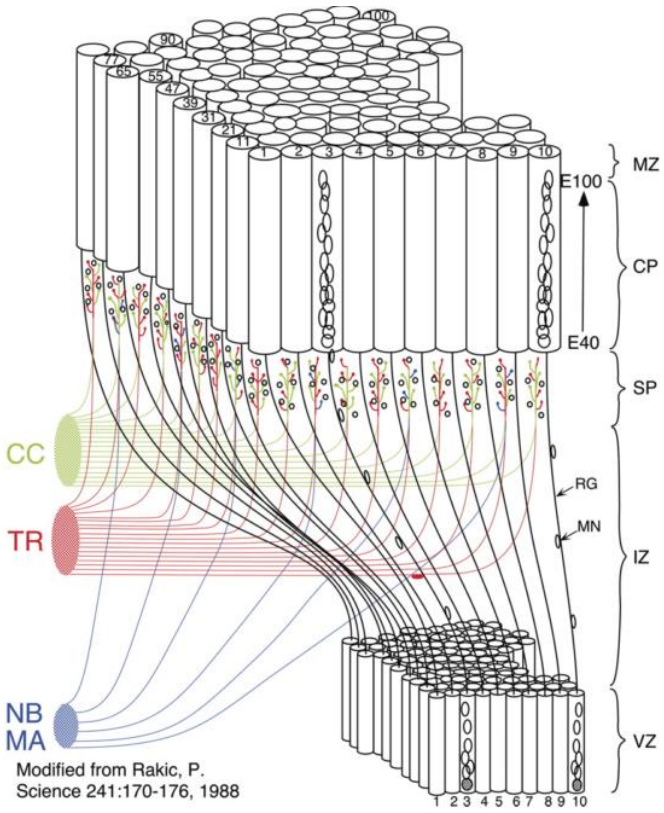

Figure 3. "The model based on (Rakic, 2007, 1988) emphasizes the radial mode of migration which underlies prominent columnar organization in primates. The cohorts of neurons generated in the ventricular zone (VZ) traverse the intermediate (IZ) and subplate zones (SP) containing "waiting" afferents from several sources (CC: cortico-cortical connections, TR: thalamic radiation, NB: the nucleus basalis:, MA: the monoamine nuclei of the brain stem) and finally pass through the earlier generated deep layers before settling in at the interface between cortical plate (CP) and marginal zone (MZ). The positional information of the neurons in the VZ and corresponding protomap within the SP and CP is preserved during cortical expansion by transient radial glial scaffolding."

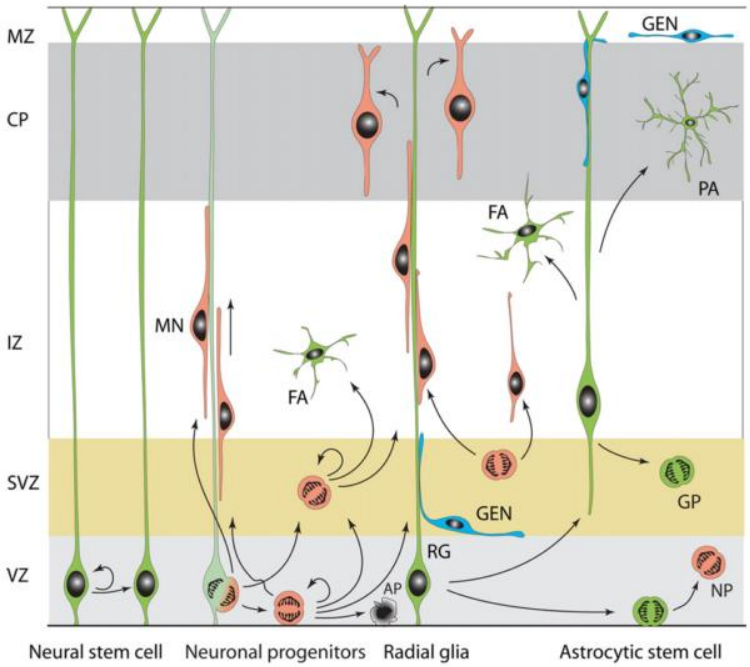

Figure 4. From Rakic 2007**. "**Schematic diagram of the composition, cellular events and the relationship in the developing cerebral wall, based on data obtained from species ranging from the mouse to human and non-primates. Initially homogeneous population of neural stem cells (green), which divide symmetrically transform into radial glial cells (RG) which divide asymmetrically and over time produce migrating neurons (MN, red) and dedicated neuronal progenitors with short processes (red mitotic divisions) that populate the ventricular (VZ) and subventricular (SVZ) zones and produce all projection neurons as well as the majority of interneurons in human and a small fraction in rodents. In addition, a population of tangentially migrating neurons arrives to the dorsal telencephalon from the ganglionic eminence mostly via SVZ and marginal (MZ) zones to supply the majority of interneurons in rodents and about one third in human. Eventually RG undergo apoptosis (AP) or directly or indirectly generate ependymal cells, fibrillary astrocytes (FA), protoplasmic astrocytes (PA), glial progenitors (GP) or astrocytic stem cells that retain a neurogenic potential (NP)."

1.2.1. The corticogenesis

To understand the formation of the cortex and its parcellation into diverse cytoarchitectonic fields, we briefly described the corticogenesis based on the radial unit hypothesis proposed by (Rakic, 1988). From this hypothesis, the embryonic cerebral ventricle hosts a layer of proliferative units which acts as a protomap for the formation of cytoarchitectonic areas. According to this model, the neurons

produced in the ventricular zone migrate along the fibers of the glial cells towards the cortical plate. Once they reached the cortical plate, they overpassed the neurons that arrived earlier and produce the cortical column organization. In the adult cortex, neurons that belong to the same functional column have similar neural response (Rakic, 2007). This model is described on a schematic **Figure 3.** The life cycle of the neural cell is depicted **Figure 4**. Briefly, development starts with symmetric divisions of cells along the ventricular wall. This results in an increase of the number of progenitor cells (neuroepithelial cells and radial glia) and gives rise to the neurons of the cortex (Rakic, 1995).

1.2.2. Cellular mechanisms leading to folding

The formation of the cortical columns is closely linked to the gyrification of the cortex (Reillo et al., 2011). Indeed, it has been shown that increasing the relative abundance of basal radial glial cells (bRGCs) result in the formation of cortical folds in the mouse cortex (normally lissencephalic) (Borrell and Reillo, 2012). The regulation of bRGCs abundance in mouse embryo cortex has been achieved through various genetic manipulations such as: loss of function of the nuclear protein Trnp1 (Stahl et al., 2013), activation of Sonic hedgehog (Shh) signaling (Wang et al., 2016), and overexpression of the hominoid specific genes ARHGAP11B (Florio et al., 2015) and TBC1D3 (Florio et al., 2017; Ju et al., 2016). The effect of bRGCs abundance on the cortical folding is summarized on **Figure 5**. Additionally, manipulation of neurogenesis, in the ventricular zone (VZ), without a concomitant increase of bRGCs, has enabled to induce gyrification in the mouse cortex (Rash et al., 2013). These observations suggest that gyrification is primarily caused by tangential expansion of the cortex to which these cells contribute (Ronan and Fletcher, 2014). Two points are necessary to be underlined here. First, as mentioned in the mechanical theory due to the tangential expansion, the pressure within the surface increases and foldings mechanically mitigates this increase. Second, it appears that multiple factors contribute to the tangential cortical expansion including: the prolonged neurogenesis (Rash et al., 2013); an increase in number and type of progenitors cells (Borrell and Reillo, 2012); and the conical migration trajectory of neurons to the developing cortex (Torii et al., 2009). These evolutionary adaptations were shown to increase gyrification but where not unique to gyrencephalic species (Borrell and Reillo, 2012). This last remark emphasizes that gyrification is probably caused by multiple developmental processes and is not reducible to a single evolutionary adaptation (Ronan and Fletcher, 2014) and may explain the independent occurrence of gyrencephaly across the mammalian order (Lui et al., 2011). Thus, multiple genes and pathways likely work all together to form the cortical folding.

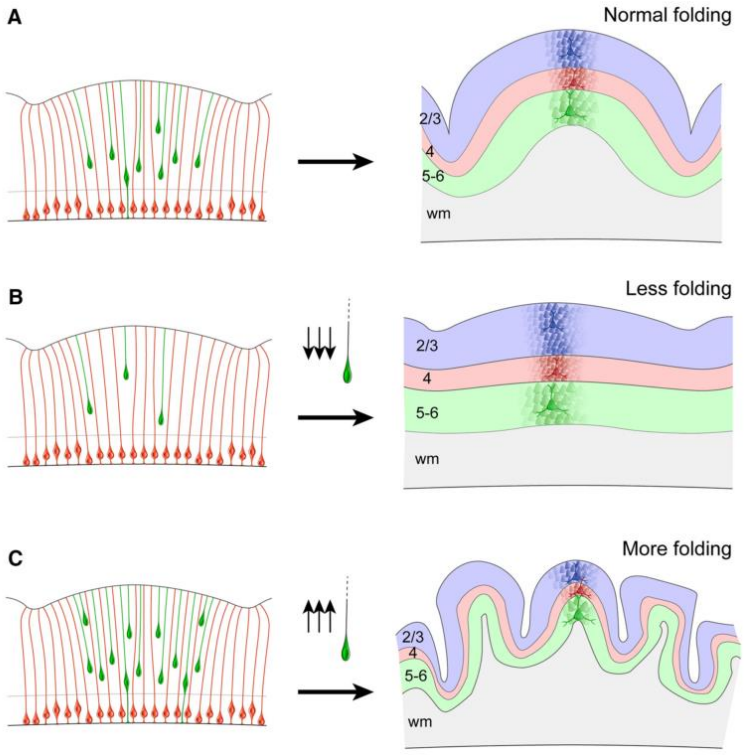

Figure 5. From Borrell 2018. "Schematic drawings illustrating the effect of bRGC abundance on cortical folding. **A.** Under physiological conditions, during development (left), there is a certain ration between the abundance of bRGCs (green) and apical Radial Glia Cells (aRGCs) (red) that leads to the relative tangential expansion of the neuronal layers, and this leads to cortical folding (Reillo et al., 2011). **B**. Reduced numbers of basal progenitors during development, particularly in OSVZ and especially bRGCs, lead to lower tangential expansion and thickening of neuronal layers, resulting in less folding (Poluch and Juliano, 2015; Reillo et al., 2011). **C**. Increased numbers of bRGCs during development produce an excessive tangential expansion of neuronal layers, and this leads to increased folding (Florio et al., 2017; Masuda et al., 2015; Nonaka-Kinoshita et al., 2013; Stahl et al., 2013)."

1.2.3. The genetic program

A concrete outcome of this complex genetic program is the consistency of sulcal patterns across primate species. These evidence derived from MRI studies of the cortex have shown a consistent organization of the sulcal roots across individuals (Lohmann et al., 2008; Régis et al., 2005). These sulcal roots are the putative first folding locations and they provide a general framework which defines the primary sulci. Their location being highly similar across brains this advocates for a deterministic program imprinted in humans. Additionally, secondary folds location are less well conserved and higher order folds might appear stochastic and thus less predetermined (Borrell, 2018). To clarify, in the literature the terms primary/secondary/tertiary folds are not always consistently used. One definition is based on the ontogenic classification of the sulci and describes the similarity in primary gyrification between human and non-human primates. In this case, primary cortical folds appear in utero and are preserved among primates, secondary cortical folds are present at birth but may not be preserved across primates, while tertiary cortical folds appear during childhood and adolescence. However, in this thesis, I rather used the definition based on postmortem fetuses by Chi et al., (1977), primary folds are observed from 20 weeks of gestational age (w GA), secondary folds from 32w GA and tertiary folds around term age (40w GA). This classification is also highlighted by spectral analysis of the cortical folds (Dubois et al., 2016).

Study of folding patterns comparing monozygotic twins (MZ) to unrelated individuals indicates that foldings are more similar in MZ (Lohmann et al., 1999) suggesting the genetic origin of

this program. A number of genes implicated in human malformation of the cortex have already been associated to gyrification including: LIS1 and DCX regulating radial migration and linked to lyssencephaly (Borrell and Reillo, 2012; Taylor et al., 2000); ASPM influencing the surface area and linked to microcephaly (Bond et al., 2002); EMX2 regulating the proliferation of stem cells in the central nervous system and linked to schizencephaly (Galli et al., 2002). Proteins have also been identified such as Gpr56 associated to factors controlling neuronal migration (Li et al., 2008), frontal lobe polymicrogyria (Piao et al., 2004), and selective disruption of the cortex surrounding the Sylvian fissure bilaterally, including the Broca's area implicated in human language processing (Bae et al., 2014) (see schematic **Figure 6**). Less specific regulation mechanisms are also known to be involved in modulating gene expression such as chromatin opening, DNA substitutions, histone methylation or non-coding RNAs. We note that the recent progress in DNA editing with the new technique CRISPR-Cas9 will enable more efficient gene knocknout. In particular, a recent study in the ferret underlined that Cdk5 is required in the upper-layer neurons to developed cortical foldings (Shinmyo et al., 2017), **Figure 7**.

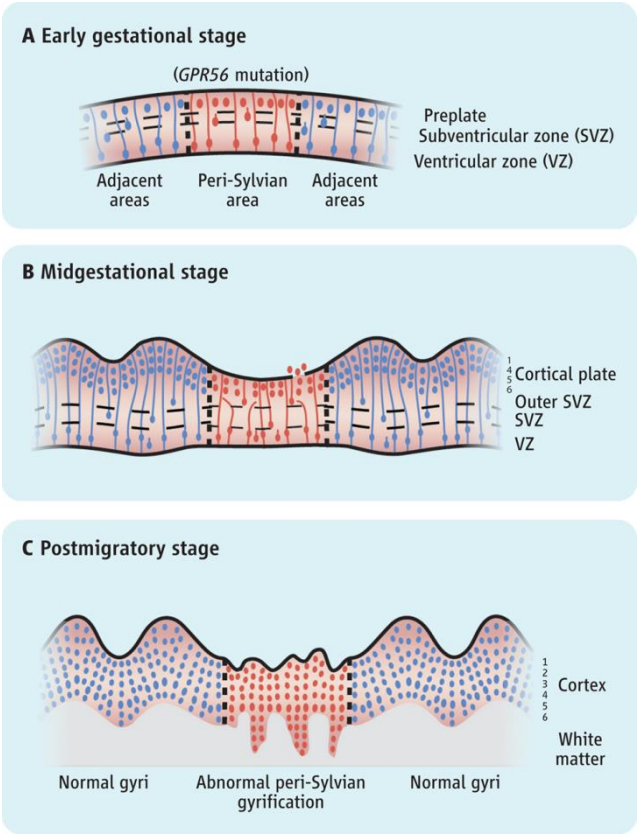

Figure 6. From Rash & Rakic 2014. "**Localized gyral abnormalities. A.** Early embryonic stage in an individual with the *GPR56* mutation showing the prospective areas surrounding the Sylvian fissure (red) and adjacent cortex (blue) within the indicated zones. **B.** Middle stage of corticogenesis indicating the prospective normal and affected peri-Sylvian cortical areas. **C**. Postmigratory stage, showing abnormal gyrification and cytoarchitecture in the peri-Sylvian region flanked by normal cortical areas."

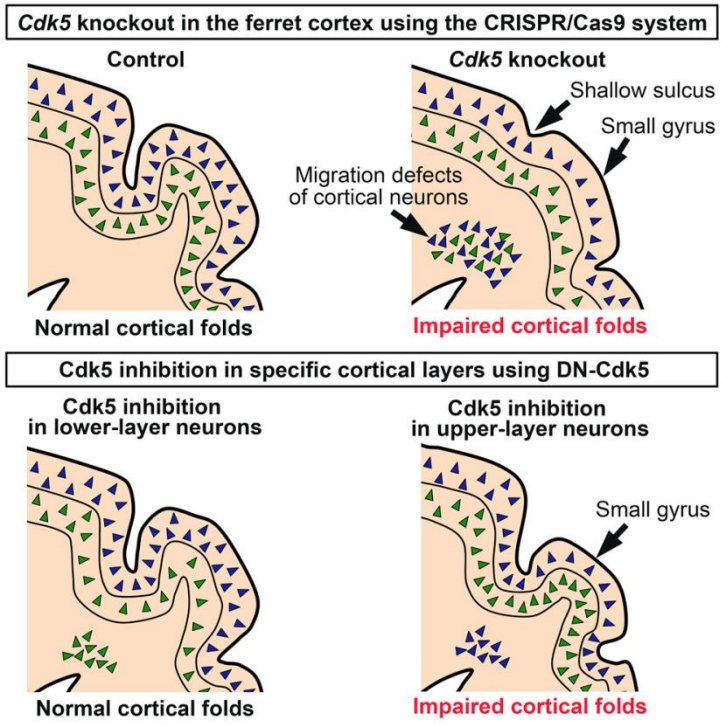

Figure 7. From Shinmyo et al. 2017. Folding of the Cerebral Cortex Requires Cdk5 in Upper-Layer Neurons in Gyrencephalic Mammals

1.2.4. Summary

To summarize, a recent review by Borrell emphasizes that there are two type of "cell" factors that determine the specific folding patterns: spatial factors and temporal factors (Borrell, 2018). The protomap proposed by Rakic (Rakic, 1988) and observations of progenitor proliferation in the developing ferret cortex (Reillo et al., 2011) advocate for such spatial constraint with regional variation in the density of cell proliferation. Notably, genes, whose expression is modulated regionally, are particularly implicated in human malformation of the cortex (de Juan Romero et al., 2015), supporting that these genes are essential to shape the cortex. In addition to the spatial gradients the timing of the progenitor cells appears key to produce the folding. For example, transiently blocking progenitor cell in the ferret during a specific timeframe of development prevent cortical folding (Poluch and Juliano, 2015). Specific gene expression signals mark the beginning and end of this critical period. An hypothesis is that altering the timeline of gene expression might affect the critical period, thus varying the quantity of progenitor cells, finally changing the size of cortical folds (Borrell, 2018).

1.3. Conclusion

Overall, the cellular mechanisms produced by genetically regulated processes undoubtedly participate in the formation of the primary cortical folds. These first foldings are highly conserved across individuals and co-localize with the cytoarchitectonic boundaries (Fischl et al., 2008; Welker, 1990). Yet MZ twins, who are identical genetically, do not have identical folds (Lohmann et al., 1999) thus other factors than genetic undoubtedly play a role in shaping the brain.

2. Brain asymmetries

2.1. Asymmetries in the human adults' brain

In spite of an overall symmetric organization the human brain presents notable asymmetries. Since the 19th century and the reports of Broca and Wernicke the left hemisphere language lateralization is the most studied brain asymmetry (Toga and Thompson, 2003). It is followed by the right handedness lateralization, which is manifested in leftward activation in the motor cortex, in the vicinity of the so-called hand knob structure of the central sulcus. These two left lateralized processes are likely correlated because the majority of right handers are left lateralized (Pujol et al., 1999; Springer et al., 1999). However, they do not always go hand in hand together because language lateralization is not clearly observed for left handers (Coren, 1992), who have greater atypical hemisphere dominance (Pujol et al., 1999).

The first discovered structural marker of this asymmetry is the planum temporale whose surface is larger in the left hemisphere (Geschwind and Levitsky, 1968). This asymmetry may originate from the brain petalias, which designate cerebral asymmetries formed by greater profusion of

the surface of one hemisphere beyond the other hemisphere. The most observed are the right frontal lobe petalia and the left occipital lobe petalia. An MRI study noted that the intensity of petalia correlated with right handedness (Kertesz et al., 1986). The phenomenon causing the petalias and leading to brain asymmetry of positions between hemispheres is a torsion of the brain, named the Yakovlian torque. The action of this torque rotates the structures around the right Sylvian fissure forward (towards the frontal lobe) relative to their counterparts on the left hemisphere (see **Figure 8**) (Toga and Thompson, 2003). This torque causes the right superior temporal sulcus to appear shorter than the left in its posterior part. This last region is particularly important because it is implicated in phonological encoding and speech perception (Pallier et al., 2011). It is adjacent to the Wernicke's area in the posterior temporal-parietal, which contributes to language comprehension. In addition, the brain torque was found to be correlated with the planum temporale asymmetry (Barrick et al., 2005).

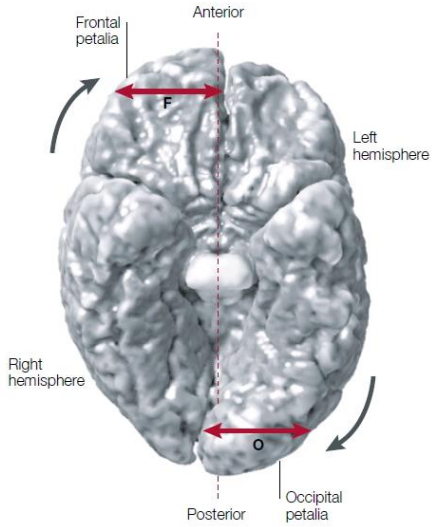

Figure 8. From Toga & Thompson (2003) . "This three-dimensional rendering of the inferior surface of a human brain is derived from an in vivo magnetic resonance imaging (MRI) scan that has been exaggerated to illustrate prominent asymmetries found in the gross anatomy of the two brain hemispheres. Noticeable protrusions of the hemispheres, anteriorly and posteriorly, are observed, as well as differences in the widths of the frontal (F) and occipital (O) lobes. These protrusions produce imprints on the inner skull surface, known as petalia. A twisting effect is also observed, known as Yakovlevian torque, in which structures surrounding the right Sylvian fissure are 'torqued forward' relative to their counterparts on the left. The left occipital lobe is also splayed across the midline and skews the inter hemispheric fissure in a rightward direction."

The second main region implicated in language is the Broca's area in the left inferior frontal, involved in language production and syntactic processing. In this region, Amunts and colleagues observed that the Broadmann Area (BA) 44 had a larger volume and higher cell density in the left hemisphere (Amunts et al., 1999).

Another interesting landmark that supports the language lateralization is the paracingulate sulcus, which occurs more frequently in the left hemisphere (Paus et al., 1996) and when its presents the language task related activation do not spread along the cingulate sulcus and are thus more focused (Crosson et al., 1999).

Beyond the structural asymmetry, the whiter matter fiber tract asymmetries have also been investigated. Two major tracts that relate to functional asymmetry were found to have higher fractional anisotropy in the left hemisphere namely the cortico-spinal tract and the arcuate fasciculus, supporting handedness and language respectively (Büchel et al., 2004).

2.2. Asymmetries in the human infant's brain

To study these brain asymmetries with a minimal environmental influence, the infants' brain is a good proxy. Additionally, because infants have a smaller and less educated brain, they might be considered as a bridge between gyrencephalic animal and human adult research to disambiguate the genuine human brain specificities compare to the ones emerging from brain size, education or culture (Dehaene-Lambertz and Spelke, 2015).

Hemispheric asymmetries analyses in infants revealed that their cortical structure is similar to adults. As the adults, they notably include a larger left planum temporale observed in term-born infants (Hill et al., 2010) and deeper right superior temporal sulcus observed in preterm newborns (Dubois et al., 2008) and reproduced in infants (Glasel et al., 2011; Hill et al., 2010). Mirroring this structural asymmetry, a tensor imaging (DTI) study in preterm newborns demonstrated that the arcuate fasciculus is larger and more posterior in the left temporal region (Dubois et al., 2010). However, the hemispheric differences increase during childhood, which suggests that white matter maturation and myelination occurring regionally during this period may contribute to this asymmetry (Thompson et al., 2000). Structural asymmetries in fetuses and infants are also reported in term of maturational calendar. Postmortem studies on brains between 10 to 44 weeks' gestational age have revealed that the right hemisphere sulci generally appear earlier than the left (Chi et al., 1977). This observation includes the right perisylvian structures, which are visible about one week earlier than the left ones (Geschwind and Miller, 2001). Most of left sulci later catch up their delay but not the left superior temporal sulcus. The right hemisphere earlier gyral complexity was recently confirmed in vivo in preterm newborns (Dubois et al., 2008). MRI studies in infants quantifying the maturation of structures reported that a faster maturation of gray matter in the right hemisphere relative to the left (Leroy et al., 2011), as well as a faster maturation of the left arcuate fasciculus over the right (Dubois et al., 2015)

Because, the structural asymmetries in the temporal lobe are observed in both newborns (or infants) and adults. This suggests that they are not caused by the postnatal environment, even though they might be reinforced later on under environmental exposure.

2.3. Comparison with non-human primates and the human-specific STS asymmetry

Several of the asymmetries in the temporal lobe and inferior frontal region have also been reported in non-human primates although to a lesser extent than in humans. In particular, the Sylvian fissure (SF) was found to be longer on the left hemisphere in chimpanzees, as in humans but not in rhesus monkeys (Yeni-Komshian and Benson, 1976). In agreement with this study, Hopkins and colleagues have reported that Old World monkeys showed a rightward asymmetries of the length of the lateral SF and lateral STS, but not the New World monkeys (Hopkins et al., 2000). These

observations may be due to a genetic drift within the primate lineage. Cantalupo & Hopkins studied Broca's area in great apes and found that the left hemisphere area 44 was larger, as the homologous region in humans (Cantalupo and Hopkins, 2001). Consistently with this result, a voxel-based morphometry study underlined leftward gray matter asymmetries in inferior frontal gyrus and posterior superior temporal lobe in chimpanzee (Hopkins et al., 2008).

Even though at the macroscopic level there seems to be no difference in term of asymmetries in this region when looking at the microscopic level differences might be revealed. Indeed, when comparing Nissl-stained slides of normal human, chimpanzee and rhesus monkey brains in a region of the planum temporale, Buxhoeveden et al. (2001) found that only human brain tissue presented robust asymmetry of cortical column morphology. They noted that in the left planum temporale the cortical columns were wider and had more neuropil space in humans, but not in chimpanzee and rhesus monkeys.

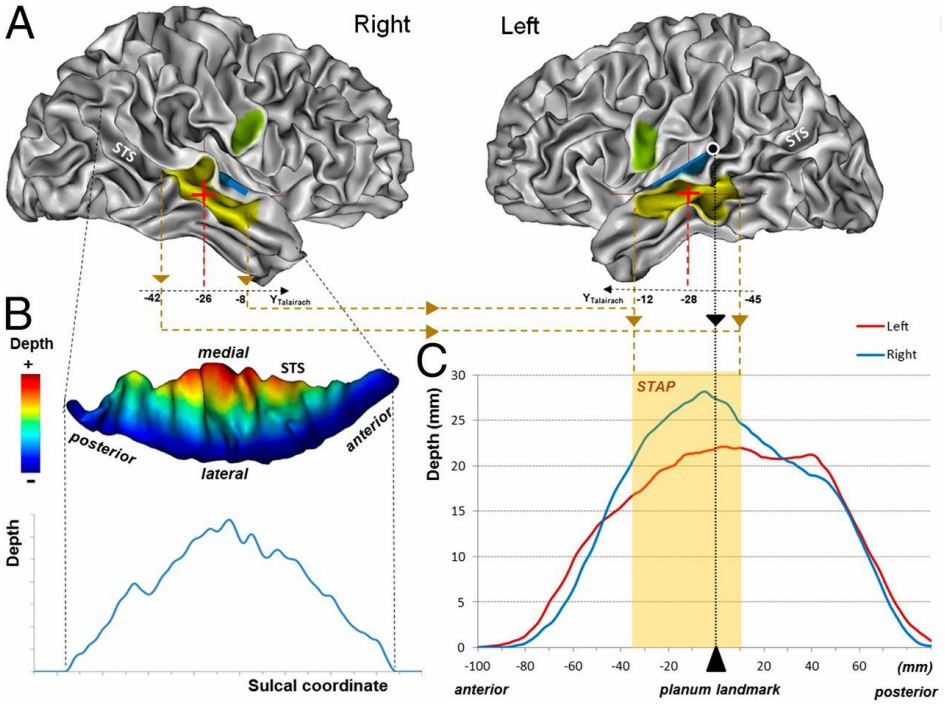

Figure 9. From Leroy et al. (2015). "(*A*) Location of the STAP (yellow) relative to Heschl's gyrus (blue) and the ventral tip of the central sulcus (green) on both left and right inner cortical surfaces of an individual adult brain. The STAP center is shown by a cross. The black dot with a white contour line shows the planum temporale landmark. (*B*, *Upper*) Sulcal depth shown by color coding of the sulcal mesh (seen from above). (*Lower*) Sulcal depth profile in the right hemisphere of an individual subject. (*C*) Adult sulcal depth profile; STAP anterior and posterior ends as well as the planum landmark are drawn in dotted lines. The light orange overlay illustrates the STAP (deeper on the right), defined as the common asymmetrical segment in the three typical groups (infant, right-handed children, and adults)."

To explain the specific formation of language in humans, researches have tried to identify human brain specific features. Such robust landmark would enable to investigate the genetic underlying the human specific cognitive ability. As already introduced, the language asymmetry is the most studied and evidences suggest the roots of this human-specific function lies in the perisylvian region. Leroy et al. (2015) demonstrated that a segment of the STS, ventral to Heschl's gyrus, they

called the superior temporal asymmetrical pit (STAP) (**Figure 9**), presents a significant rightward depth asymmetry in infants, children and adults but not in chimpanzee (177 humans and 73 chimpanzees) (**Figure 10**).

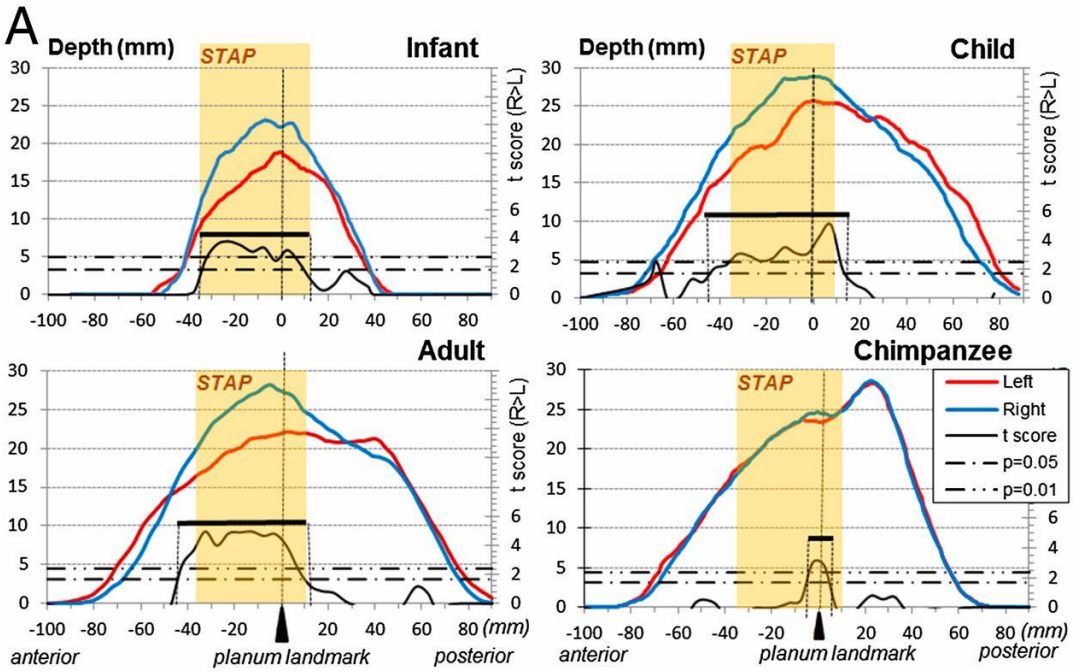

Figure 10. From Leroy et al. (2015). "(*A*) Left (red line) and right (blue line) STS depth profiles from the temporal pole to its parietal caudal end. Depth profiles are shown for infants, right-handed children, adults, and chimpanzees. The asymmetrical part of the STS is computed for each group by permutation tests over 5-mm-long intervals along the sulcus. Two statistical thresholds (P_{corr} = 0.05; P_{corr} = 0.01) are shown by horizontal dashed-and-dotted lines. The extent of the asymmetrical segment is given by the range of the Student *t* variable (black line) above the lower threshold and is identified by a black bar. The extent of the common region across the three typical human groups (STAP) is shown in light orange overlay."

2.4. Relationship between functional and structural asymmetries

To better characterize the role of the asymmetric structures in the human brain, we consider studies that have looked into their association with co-localized functional territories that in turn may be asymmetrical or not. MRI multimodal studies are ideal tools to decipher the link between functional and structural asymmetries, because they can measure in the same set of subjects these asymmetries and infer their relationship, providing adequate alignment across modalities. For example, combining fMRI and tractography allowed to emphasized that subjects with more lateralized fMRI activations during language related tasks have a more lateralized mean fractional anisotropy in the superior longitudinal fascilus tract (Powell et al., 2006). This tract connects the Broca's and Wernicke's areas bilaterally, but the fronto-temporal connectivity is reinforced on the left (Powell et al., 2006). In the same region, Pinel and Dehaene (2010) found a collateralization of the posterior STS activation during sentence processing and of intraparietal sulcus during arithmetic. This emphasized the role the posterior STS as a central hub, which deciphers the semantic information available from auditory input. Considering structural MRI and fMRI data, Sun and colleagues have shown that the domain of reading activation along the STS is larger when the posterior branches are less developed

(Sun et al., 2016). Another important brain landmark structure correlates with fMRI activations, the central sulcus "hand knob" structure position was shown to match the hand motor activation (Sun et al., 2016). The authors also underlined that the amplitude of left hand activation in the right hemisphere was associated to hand knob location in the central sulcus. Additionally, they reported a less known landmark the central sulcus "lower knob", which when visible corresponds to the lips and larynx motor activation.

The human auditory cortex has a particular composition including larger columns (Buxhoeveden and Casanova, 2002) and dense-short range connectivity (Turken and Dronkers, 2011). These particular properties appear to support the processing of auditory temporal features. But, there seems to be a bias towards the left hemisphere to process rapid stimuli. Thus, this hemisphere is favored for speech signals, which contain fast temporal transition (Boemio et al., 2005; Zatorre and Belin, 2001). This sensitivity of the left posterior temporal region to fast temporal transition is already observed in pre-terms infants (28-32 weeks' gestational age) (Mahmoudzadeh et al., 2013). At this age the cortical organization in layers is not completed, which might suggest innate factors, including genetics, that are involved in this hemispheric specialization (Dehaene-Lambertz and Spelke, 2015).

3. Imaging Genetics

3.1. Definitions

3.1.1. Measured data - Essentials

Imaging genetics refers to the use of imaging techniques to obtain image-derived phenotypes on which the genetic influence is assessed.

Several magnetic resonance images (MRI) modalities are used to investigate the genetic influence on the human brain. Depending on the sequence used three types of phenotypes may be distinguished in this thesis.

1) **Structural MRI** uses sequences sensitive to tissue density and interaction with the magnetic field and can be used to distinguish between the different types of tissues grey matter, white matter and cerebrospinal fluid.
2) **Functional MRI** (fMRI) uses sequences sensitive to the BOLD (blood-oxygen-level dependent) effect and enables indirect measurement of brain activation during a pre-defined task (tfMRI) or at rest (rfMRI).
3) **Diffusion MRI** (dMRI) uses sequences sensitive to the diffusion of water molecules in the brain. It allows obtaining tensor images from which tractography methods yield models of white matter fiber tracks.

In our analyses, the genetic information is either constituted of the filial relationship between individuals (a pedigree) or of single nucleotide polymorphisms (SNPs):

I- **A pedigree** defines the lineage or genealogy of an individual and all the direct ancestors, which gives an a priori genetic relationship between individuals.

II- **A SNP** is a variation in a single nucleotide that occurs at a specific position in the genome.

3.1.2. SNPs bi-allelic coding

The DNA (deoxyribonucleic acid) is composed of four types of nucleobase: Adenine (A), Cytosine (C), Guanine (G), and Thymine (T). Most SNPs are bi-allelic (for example allele A and allele T) with possible genotypes coded AA, AT and TT. It may also be coded according to the count of mutated (minor) allele (T in this example) and genotype becomes 0, 1, 2. Different genetic models are considered when studying phenotype association with a SNP. The most widely used model assumes that having twice the minor allele should lead to a twofold variation in phenotype compare to the case with only one minor allele (**Figure 1.**). This model, namely additive genetic model will be used for quantitative phenotype association with SNP to identify causal variant in this work. Although, this model is used in most imaging genetics studies it brings important assumptions. It is now confirmed that most of the additive effects account for a small proportion of the phenotype.

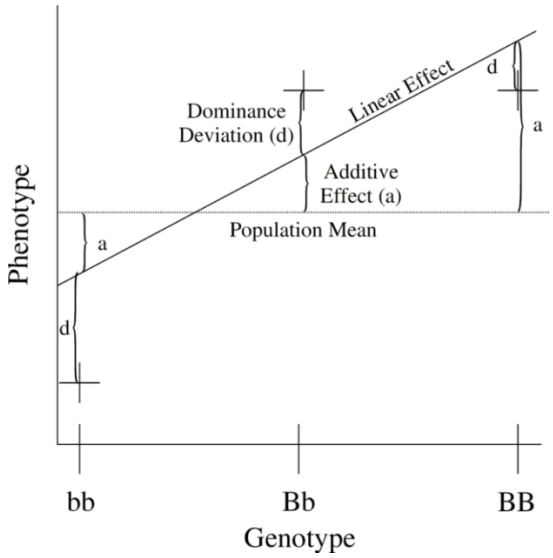

Figure 1. Illustration of additive and dominant genetic effects (source Wikipedia)

Other association tests with SNP consider the dominant model, which tests if individuals with at least one minor allele have a significantly different phenotype than the ones having none (**Figure 1**). Finally, other genetic effects like for example epistasis – involving the interaction between different genes and the mutated SNP – are known to largely influence the development of a given phenotype and they are modeled in various statistical approaches.

3.1.3. The heritability

The heritability is the proportion of a variance in a given phenotype that is due to the genetic factors as opposed to environmental or stochastic (random) factors. It is specific to a particular

population and a particular moment in time. A common example is the heritability of intelligence that increases from 20% in childhood to 80% in adulthood (Plomin and Deary, 2015), and has increased over the past decades due to the standardization of education and easier access to early schooling. Thus, the heritability is informative only if it is provided with the full information on the population from which it has been estimated.

Two definitions are commonly used:

1 The narrow sense heritability (h^2), defined as the proportion of phenotypic variance due to the additive genetic effects;

2 The broad sense heritability (H^2), defined as the proportion of phenotypic variance due to all genetic factors including additive, dominant, and epistatic (multi-gene interaction) genetic effects.

In this work, "heritability" will refer to the narrow sense heritability. However, there are two different experimental settings to estimate h^2 and they require introducing specific nomenclatures. First, it can be estimated from a pedigree of individuals, using the a priori genetic relationship between individuals or pedigree. In this case, the shared environment is well controlled in twin studies (including homozygotic/dizygotic pairs) but in more general pedigree studies it is often not well controlled. Therefore, this common environment is not well accounted for and might lead to overestimation of heritability, denoted as h^2_{ped}. Second, it can be estimated using unrelated individuals by building a relationship matrix of these individuals based on their genetic differences (variation in SNPs), denoted as h^2_{SNP}. In this case, individuals are assumed to share no common environment or to a small extent. However, it is important to underline that h^2_{SNP} will still be dependent of the society environment of the cohort as well as the era.

3.2. Cohorts investigated

During my thesis, I used data from three cohorts with neuroimaging and genetics available in my lab.

When I started my thesis in October 2015, only the IMAGEN cohort was readily available in our team with 1,600-1,700 unrelated young adults (14 years old) that were scanned in 8 centers (Berlin, Dresden, Dublin, Hamburg, London, Mannheim, Nottingham, Paris). At this point, it is worth underlining that the statistical power provided by this sample to identify causal variants at the genomic threshold (p-value < $5 \cdot 10^{-8}$) was not sufficient for common variants with small effect sizes. It was neither sufficient to accurately estimate h^2_{SNP}. We only had 50% statistical power to significantly detect heritability values above 0.45, according to GCTA Power Calculator (Yang et al., 2011). In addition to the data heterogeneity, due to multi-site scans, the lack of statistical power incited us to look for other cohorts to investigate our phenotypes.

Early 2016, we accessed to the Human Connectome Project (HCP) cohort, which first included approximately 900 individuals with self-reported relatedness pedigree and later in 2017 included 1200 individuals with genetically confirmed relatedness pedigree. The HCP data include structural MRI, tfMRI, rfMRI, dMRI of very high quality and subjects were scanned on a dedicated scanner. However, at the time of writing we are still in the process of gaining access to the SNPs genetic information, which was only released at the beginning of 2018.

In parallel, in 2016, we applied to access the UK Biobank dataset, for which we were granted access to the first 10,000 subjects with structural MRI and genetics in August 2017.

3.2.1. The Human Connectome Project cohort

For the first three chapters, we used the data from the Human Connectome Project (HCP) S1200 release: details are available in the HCP reference manual.

a. Subjects

For analyses in chapters 1 and 2, we included 820 subjects (383/437 M/F), labelled as Caucasian with 69 individuals from the Hispanic ethnicity. The pedigree is composed of 191 twin pairs (127 monozygotic (MZ) with 123 siblings, and 64 dizygotic (DZ) with 64 siblings and 1 half sibling), 190 siblings, 1 half sibling and 59 unpaired individuals, aged between 22 and 36 years old ($\mu \pm \sigma = 29.0 \pm 3.6$ years).

In chapter 3, we only subjects, who completed the fMRI language task, and restrained our analysis to Caucasian including 785 individuals (372/413 M/F) with 69 individuals from the Hispanic ethnicity. This subgroup of the HCP contains 178 twin pairs (117 monozygotic twins (MZ) with 103 siblings and 61 dizygotic twins (DZ) with 61 siblings and 1 half sibling), 203 siblings, 1 half sibling and 60 unpaired individuals.

Unpaired individuals did not contribute to the genetic parameter estimation but allowed for a more accurate estimation of mean and variance effects. Subjects were chosen by the HCP consortium to represent healthy adults beyond the age of major neurodevelopmental changes and before the onset of neurodegenerative changes (Van Essen et al., 2012). They underwent a battery of tests to determine if they met the inclusion/exclusion criteria of the HCP, described in Van Essen et al. (2012). All subjects provided written informed consent on forms approved by the Institutional Review Board of Washington University.

b. MR Image acquisition and processing

Structural MRI data in Chapters 1, 2 and 3

MR images were acquired by using a Siemens "Connectome Skyra" 3T scanner housed at Washington University in St Louis using a 32-channel head coil. For T1-weighted images, 256 slices per slab were acquired with the three-dimensional magnetization-prepared rapid gradient echo (3D-

MPRAGE) sequence: TR = 2400 ms, TE = 2.14 ms, TI = 1000 ms, flip angle = 8°, FOV = 224*224 mm, and resolution 0.7 mm isotropic. For T2-weighted images, 256 slices per slab were acquired with a 3D-T2SPACE sequence: TR = 3200 ms, TE = 565 ms, variable flip angle, FOV = 224*224 mm, and resolution 0.7 mm isotropic. More details on the acquisition and reconstruction can be found in the HCP S900 Reference Manual.

Structural images were first processed by HCP using the HCP structural preprocessing pipeline, whose details can be found in the HCP S900 Reference Manual. We used the preprocessed T1w and T2w volume from each individual subject's MR data as input of the HCP Freesurfer pipeline, which is based on Freesurfer 5.3.0 (Fischl, 2012) with a number of improvements specifically optimized for the HCP data. We additionally performed surface-based interhemispheric registration as proposed in (Greve et al., 2013). First, we created the *xhemi* of each subject using the *xhemireg* command of Freesurfer, to transform the right hemisphere into a left one, and then compute the registration to the left side of the symmetric Freesurfer template (*fsaverage_sym*) using the *surfreg* command. The Freesurfer outputs needed for the sulcal pits extraction and analysis methods are the white meshes and the registration spheres files, which we converted to the gifti format using Freesurfer command *mris_convert*.

We are aware of the benefits of the quality control performed by HCP for structural scans. The outputs of the HCP structural pipelines, including Freesurfer surface generation, have been examined by HCP for surface reconstruction quality in the native volume space with the native mesh. However, some Freesurfer outputs needed for interhemispheric registration were not distributed by HCP (list of these files Method S2), so we decided to re-run the HCP Freesurfer pipeline. We used as inputs the distributed outputs from the PreFreesurfer pipeline and used the HCP Freesurfer pipeline code available on HCP GitHub (github.com/Washington-University/Pipelines/tree/master/FreeSurfer, commit 04/2016). Our study relying mostly on the subjects' white mesh estimated by the pipelines, we assessed the similarity between the white matter segmentations available from the HCP repository and the ones we computed locally. We compared the correspondence between the white matter segmentation in the *wmparc* file for all subjects and found 97% of common voxels in average. We visually inspected the differences on few subjects, randomly selected. Using *fsl_view*, we assessed whether the white matter mask encompassed properly the folds of the white matter mesh. In some cases, the HCP repository data more finely delineate the white matter, whereas in other cases our locally computed data correspond to a better segmentation. Thus, we concluded that the differences in white matter segmentation were negligible between the HCP repository and locally computed data.

Task functional MRI data in Chapter 3

fMRI data acquisition parameters were as follows: TR=720 ms, TE=33.1 ms, flip angle=52 deg, BW=2290 Hz/Px, in-plane FOV=208×180 mm, 72 slices, and 2.0 mm isotropic voxels, with a multi-band acceleration factor of 8. Two runs of each task were acquired, one with right-to-left and the

other with left-to-right phase encoding 2; each run interleaved 4 blocks of a story task with 4 blocks of a math task. The lengths of the blocks varied (average of approximately 30 seconds), but the task was designed so that the math task blocks matched the length of the story task blocks, with some additional math trials at the end of the task to complete the 3:57 (min:sec) run.

The details of the HCP data analysis pipelines are described elsewhere (Barch et al., 2013; Glasser et al., 2013). Briefly, they are primarily built using tools from FSL (Jenkinson et al., 2012) and Freesurfer (Fischl, 2012)**.** The HCP fMRIVolume pipeline generates "minimally preprocessed" 4D time series that include gradient unwarping, motion correction, fieldmap-based EPI distortion correction, brain-boundary- based registration of EPI to structural T1-weighted scans, non-linear (FNIRT) registration into MNI152 space, and grand-mean intensity normalization (Glasser et al., 2013). For the S500 release, two smoothing approaches were chosen by the HCP: volume-based smoothing or smoothing constrained to the cortical surface and subcortical gray-matter parcels. For the former, standard FSL tools can be applied for analysis, while for the latter, the HCP adapted these tools to this the 'grayordinate' approach (Barch et al., 2013; Glasser et al., 2013). The grayordinate approach refers to fMRI analyses performed on the cortical surfacen, as opposed to a volume-based approach. This is more accurate spatially because activation occurs in gray, not white, matter. Unconstrained volume-based smoothing causes blurring effects by mixing signals from cortex regions adjacent in volume but not on the surface. For these reasons, our study analyses were carried out on the surface of the cortex.

The HCP fMRISurface pipeline brings the time series from the volume into the CIFTI grayordinate standard space. This is accomplished by mapping the voxels within the cortical gray matter ribbon onto the native cortical surface, transforming them according to the surface registration onto the 32k Conte69 mesh, and mapping the set of subcortical gray matter voxels from each subcortical parcel in each individual to a standard set of voxels in each atlas parcel. The result is a standard set of grayordinates in every subject (i.e., the same number in each subject, with spatial correspondence) with 2mm average surface vertex and subcortical volume voxel spacing. These data are smoothed with surface and parcel constrained smoothing of 2mm FWHM (full width half maximum) to regularize the mapping process (Glasser et al., 2013).

3.2.2. **The UK Biobank project (January 2018 release)**

Chapter 4 and 5 analyses were conducted under UK Biobank data application number 25251. The UK Biobank is a health research resource that aims to improve the prevention, diagnosis and treatment of a wide range of illnesses. Between the years 2006 and 2010, about 500,000 people aged between 45 and 73 years old, were recruited in the general population across Great Britain. In chapter 4, we used the data released on January 2018, consisting of 20,060 subjects with a T1-weighted MRI. We included 15,040 in our discovery sample and 5,020 in our replication sample. The subjects were

separated according to their availability in NIFTI format. In January 2018, replication sample was available only in DICOM format.

The UK Biobank genetic data underwent a stringent QC protocol, which was performed at the Wellcome Trust Centre for Human Genetics (Bycroft et al., 2017). We restrained our analysis to people identified by UK Biobank as belonging to the main white British ancestry subset (using the variable *in.white.British.ancestry.subset* in the file *ukb_sqc_v2.txt*). Additionally, we excluded from our analysis subjects with high missingness, high heterozygosity, first degree related individuals or sex mismatches. In total ~12,150 subjects in the discovery cohort and ~3,430 subjects in the replication cohort passed the image processing steps and the genetic criteria filtering. Both sets include approximately 48% of males and 52% of females.

3.3. Imaging genetics methods

3.3.1. **Heritability studies**

In the early time of imaging genetics, the first goal was to identify brain features that are under genetic control and to quantify the heritability of these traits (Polderman et al., 2015). This trend followed the existing practice on other more conveniently measurable phenotypes, such as height. These models date back more than 50 years ago. They traditionally used cohorts composed of monozygotic and dizygotic twins and estimated the heritability using the Falconer formula:

$H^2 = 2\times(r_{MZ} - r_{DZ})$, where r_{MZ}, r_{DZ} refer to the correlations considering identical twins and fraternal twins, respectively.

This approach, which was refined over time, brought fruitful results in imaging genetics including that the brain volume is most likely highly heritable ($h^2 \approx 0.8$), whereas gyral-sulcal structures are less heritable ($h^2 \approx 0.2$-0.4) (Bartley et al., 1997).

Later on, the heritability estimation was performed using extended-pedigrees, meaning cohorts that include groups of individuals that are related. In each group, the *a priori* genetic relationship is known and it is thus possible to decompose the variance of a phenotype into genetic and non-genetic components. This enabled to estimate the heritability of various phenotypes including grey and white matter volume or thickness (Winkler et al., 2010), fractional anisotropy (Kochunov et al., 2015) or even functional activations (Blokland et al., 2011; Koten et al., 2009).

Another way to estimate the heritability is to use a cohort of unrelated individuals and to estimate their relationship matrix based on their genetic differences in term of SNPs. This method is based on the genome wide complex trait analysis (GCTA) (Yang et al., 2011) and was for example used in imaging genetics to estimate the heritability of subcortical structures (Toro et al., 2015).

Higher performance computation software even enable to estimate the heritability in pedigree voxel-wise (Ganjgahi et al., 2015), as well as in independent individuals (Ge et al., 2015).

a. Heritability computation in the Human Connectome Project

The variance components method, as implemented in the Sequential Oligogenic Linkage Analysis Routines (SOLAR, http://solar-eclipse-genetics.org/) (Almasy and Blangero, 1998), was used for the heritability estimations of the presence PP in the considered segment. The between subjects covariance matrix Ω for a pedigree of individuals is given by:

$\Omega = 2\cdot\Phi\cdot\sigma_g^2 + I\cdot\ \sigma_e^2$, where σ_g^2 is the genetic variance due to the additive genetic factors, Φ is the kinship matrix representing the pair-wise kinship coefficients among all individuals, σ_e^2 is the variance due to individual-specific environmental effects, and I is the identity matrix, assuming all environmental effects are uncorrelated among family members.

$\Omega = 2\cdot\Phi\cdot\sigma_g^2 + H\cdot\ \sigma_c^2 + I\cdot\ \sigma_e^2$, where H is the structuring matrix for σ_c^2, the variance due to common environment effects. H contains zeros and ones depending upon whether a pair of individual shares the same household. The household information is not directly available in HCP data. Thus, we assumed that two individuals share the same household if they reported to HCP the same two parents (not necessarily the genetic ones for the few half siblings).

Narrow sense heritability is defined as the fraction of the phenotype variance σ_p^2 attributable to additive genetic factors: $h = \sigma_g^2/\ \sigma_p^2$.

Significance of the heritability is tested by comparing the likelihood of the model in which σ_g^2 is constrained to zero with that of a model in which σ_g^2 is estimated. Before testing for the significance of heritability, phenotype values for each individual within the HCP cohort were adjusted for the following covariates: sex, age, age², age·sex interaction, age²·sex interaction, ethnicity (Hispanic or not). Note that we restrained our analysis to individuals whose race has been labelled as "White" and thus excluded the ones labelled "Asian", "Black" or others to avoid population stratification. Inverse Gaussian transformation was also applied to ensure normality of the measurements. SOLAR computes the heritability value (h^2), the significance value (p) and the standard error (SE) for each phenotype.

In chapter 1, in each areal of the symmetric template, we selected, separately for each hemisphere, all subjects having a sulcal pit and considered the DPF value associated to the deepest pit of each subject as our phenotype. SOLAR was used for the heritability estimation of the DPF of the pit in each areal. In this chapter we tested the household model. Given the limitations of using household as a proxy for common environmental influence in a pedigree comprising a large number of siblings like the HCP cohort (Docherty et al., 2015; Koran et al., 2014), we compared the Akaike information criterion (AIC) of the two models to discriminate the more suitable, with AIC = 2×[number of estimated parameters] – 2×ln(likelihood). We estimated the maximized log-likelihood of each model over all areals with SOLAR and computed the AICs of AE and ACE models to select the one lowering the information criterion for studying the heritability of the pits. We found that on average over the

128 areals (64 on each side) the AIC of ACE model is 754.0 and 752.5 for the AE model, with only 11 areals (8.5%) preferably selecting the ACE model. Unlike population studies containing twins only with controlled household information, the HCP extended twin population with a large number of siblings does not seem to be suitable for adding the household information in the model. Thus, we selected the AE model for our heritability analysis and acknowledge the possible inflation of our heritability estimates due to uncontrolled shared environment as one of the limitations of our study.

In chapter 2, the presence or absence of PPs in various sulci was considered as a phenotype in a heritability study. Total intracranial volume, and handedness (measured by Edimburg test (Schachter et al., 1987)) were additionally added as covariates.

In chapter 3, SOLAR was used for the heritability estimations of the phenotypes under analysis, such as the median activation in each areal (Glasser et al., 2016). Education level was additionally added as a covariate. We used the number of years of education as a proxy for the education level to account for environmental differences in family socioeconomic status. This is a conservative approach because the number of years of education was shown to be associated not only with the family socioeconomic status (7%) but also with the general cognitive ability (3.5%) (Selzam et al., 2017). Thus, it likely has shared environmental ground with the former and shared genetic origin with the latter. HCP data do not contain the information that would disentangle this issue. Following this last remark, one should note that the heritability estimates and shared genetic variances, described in chapter 3, were underestimated.

b. Heritability computation in the UK Biobank

In our discovery sample, we used GCTA (Yang et al., 2011) that yields an estimate of the heritability (h^2_{SNPs}) in population studies with genotyped unrelated participants. We considered the genotyped SNPs variants common to the UKBiobank and UKBileve arrays (details at http://www.ukbiobank.ac.uk). In order to compute the kinship matrix of the population, specific SNPs were selected with PLINK v1.9 (Purcell et al., 2007) using the following thresholds: missing genotype = 5% (70.783 variants excluded), Hardy-Weinberg equilibrium test (hwe) = 10^{-6} (11.318), and minor allele frequency (maf) = 1,0% (102.559). We kept the SNPs in moderate linkage disequilibrium with variation inflation factor 10 within a window of 50 SNPs (92.081 variants excluded). Then, we computed the genetic relationship matrix with GCTA using the 507.515 SNPs left. The amount of phenotypic variance captured by this matrix is estimated using a mixed-effects linear model. As covariates in our genetic analyses, we systematically included the gender, the genotyping array type, the age at the MRI session and the 10 genetic principal components provided by UK Biobank to account for population stratification. Correction for multiple comparisons were achieved using Bonferroni correction accounting for all our phenotypes and we retained as significant $p < 0.00125 = 0.05/40$ (2 hemispheres × 2 cortical features × 10 sulci). Using the GCTA Power Calculator (Visscher

et al., 2014), the discovery cohort sample size provides above 99% statistical power to detect heritability values above 15%, with $p < 0.00215$.

3.3.2. Univariate association analysis

The heritability studies do not inform on the underlying genetic variants or mechanisms that contribute to the phenotypic variance. To identify causal variants, the most common approach consists in performing a univariate association test between the trait under scrutiny and each SNP.

If one restricts the analysis to parts of the genome, often adjacent to pre-selected genes, this type of analysis is named **candidate gene association study**. This type of analysis is based on genes previously identified in **genetic linkage studies**; a family based approach which is used to map a trait to a genomic location by exhibiting co-segregation of the disease with genetic markers. For example, FOXP2 was identified in a large family affected with language disorder (Vargha-Khadem et al., 1995) and was later used in gene candidates imaging study (Pinel et al., 2012) and elsewhere. In the early age of imaging genetics, results from studies with insufficient statistical power or insufficient control on population structure lead to the identification of misleading causal genes. Eventually, this ruled out the gene candidates approaches.

If one considers the SNPs on all the chromosomes, this type of analysis is called **genome wide association study (GWAS)**. The imaging genetics community now largely favors GWAS because they do not require making any assumptions, but still need to be replicated following current good practices. Indeed, past results from gene candidate approaches are often not replicable due to the fact that hypotheses on candidate genes might have been made to satisfy a statistically significant threshold.

Given the cost of neuroimaging and genetic, building cohorts large enough to have sufficient statistical power to detect variants with small effect size was particularly challenging. During the last few years, efforts have been made by consortia such as ENIGMA (Thompson et al., 2014) or CHARGE (Psaty et al., 2009) that have pooled together data from numerous imaging genetics cohorts in order to reach an adequate sample size to significantly identify causal variants. Meta-analyses are used to study these data and were notably successful to identify common genetic variants influencing brain, hippocampus (Stein et al., 2012) and subcortical volumes (Hibar et al., 2015). Another trend has been to developed methods able to capture multivariate effects from neuroimaging and genetics data (Liu and Calhoun, 2014). However, mixed results were obtained (Le Floch et al., 2012; Vounou et al., 2010) and univariate analyses, to date, have remained the gold standard. Current developments in association methods consist in including prior information on the DNA structure or its tissue specific availability to the biological machinery (Lu et al., 2017).

3.4. Discussion on the imaging-genetics practices

Originally, the assumption was made that brain-based phenotypes would require smaller samples than phenotypes assessed through cognitive or behavioral tests (Glahn et al., 2007). This assumption was made because the brain-based phenotypes were supposed to reflect more closely the biological mechanisms at stake. However, it turned out that the brain-based phenotypes are not simpler than other behavioral traits (Glahn et al., 2014). Essentially, there are no reason that the genetic architecture of neural function should be modular (Mitchell, 2018), i.e. there are no single gene or group of genes that would support one cognitive function. It has been observed that each brain-based phenotype results from the action of a multitude of genetic variants, in ways as complex as cognitive traits.

The emergence of GWAS in all genetic communities was largely supported by the development of SNPs chips enabling cost effective and efficient genotyping of common variants (variants with minor allele frequency > 0.01). This was essentially made possible thanks to the HapMap consortium (2003) initiative to map common variants across the genome. However, in the imaging-genetic community the issue of measuring the phenotypes still remains a critical issue, due to the cost and duration MRI scan. This issue prevented samples to scale up, with the exception of the remarkable UK Biobank effort which is ongoing. Additionally, the standardization of procedure to acquire brain images is still challenging due to the different equipment and protocols used in each lab. For example, the IMAGEN study was composed of 8 MRI acquisition centers, which lead to approximately 57% subjects scanned on a Siemens MRI scanner, 18% on a General Electric and 25% on a Philips. These discrepancies need to be accounted for by covariates in the analyses and question whether or not the brain features measured are comparable due to the different scanner properties.

A tremendous effort of ENIGMA has been to gather outputs from GWAS analyses from various centers into a meta-analysis, trying to account for the discrepancies during acquisition between collection centers. Their first results suggest that most of the candidate genes for brain-based phenotype that were long praised in the literature did not replicate (Bogdan et al., 2017; Jahanshad et al., 2017). This remark emphasizes the need to increase sample sizes, set more restrictive default p-value threshold, restrict researcher degrees of freedom and most importantly independently replicate each finding (Mitchell, 2018). Meta-analysis by ENIGMA on large sample have underlined that among the common variants (SNPs) that reach the genomic significance level, the one with the largest effect size barely account for 1% of the variance explained by the genes (Hibar et al., 2017, 2015). In contrast, heritability estimates of these phenotypes obtained via relationship matrix inferred from the common variants (GCTA method) suggest that the heritability accounted by the variants tagged by SNPs is about 30-50%. This result emphasizes that common genetic variants which influence the brain-based phenotype each only account for a very small proportion of this heritability. This is best exemplified with a more common phenotype used due to its easiness of measurement, such as the

height. In that case GWAS results have underlined that genetic control of the height is the result of the cumulative effect of more than ten thousand variants, with very tiny effect sizes – that nonetheless reach genomic significance level for the current "maximum" sample size (Visscher et al., 2017). Even if the height phenotype is simple to measure, but complex regarding the multiple development issues and potential gene interactions involved, we may assume similar genetic architecture for brain-based phenotypes. They are probably regulated by thousands of variants each with a very small effect size. This remark opens an important question which is: "until which minimum effect size the action of a gene is still relevant to the general population?". Today, technologies based on common variants still produce the majority of causal variant discoveries.

Rare variants at the opposite are more likely to have larger effects. Indeed, rare mutations in various genes have been found to explain an important share of cases of neurodevelopmental disorders, such as autism or schizophrenia (Mitchell, 2015). Specific methods have been developed for rare variant association testing, such as SKAT (Wu et al., 2011), however there are more relevant to whole genome data rather than SNPs genotyping data. Whole genome sequencing is more expensive and thus has not been generalized yet. Furthermore, it might be necessary as for the common variants to distinguish subgroups with different diagnosis, or other classification criterion that could help homogenize the subgroup under scrutiny and reinforce the direction of effect of a genetic variant.

Overall, we criticized the gene candidate approach due to the publication bias observed to this day, only positive results are reported, and because these findings have failed to replicate in larger samples. These critics should not undermine candidate gene associations that are based on hypotheses honestly built prior to any exploratory analyses and strict control of type I errors. Finally, in both GWAS and candidate gene approaches an independent replication sample not used during the discovery analysis should be preserved to confirmed the genetic association.

4. Thesis rationale and plan

Our research with imaging-genetics of the human-specific brain asymmetry was motivated by the recent discovery of the STAP region by Leroy et al. (2015), with the aim to identify causal genetic variants. To identify such genetic variants, we needed first to select and robustly extract a phenotype, which characterizes this asymmetry. We did not consider gene-candidate because of the consensus in imaging genetics to cautiously avoid such practices that artificially decrease the significant statistical threshold (D. Hibar, Imaging-genetics workshop, OHBM 2016). Instead, we preferred heritability and GWA studies even if they require having enough statistical power. Given that most variants involved have small effect on the phenotypic variance, we needed a sufficiently large cohort. Thus, the phenotype extraction method should be automated to be feasible on a large number of subjects.

To the best of our knowledge in previous studies, the planum temporale, Heschl's gyrus or even the STAP were all manually or semi-automatically delimited. The first contribution of this thesis is therefore to find automatically extracted anatomical proxies for these asymmetrical landmarks.

The sulcal pits constitute a first proxy; they are the putative first folding locations of the brain. Four reasons justify their choice: (i) the deepest locations of the brain sulci appear less sensitive to noise, (ii) because they are formed early in brain development they might be less susceptible to environmental influence, (iii) one of our partner group had recently developed an algorithm allowing their automated extraction in hundred subjects (Auzias et al., 2015), (iv) sulcal pits density was found to be asymmetric in the STS (Im et al., 2010).

A second interesting proxy, is the *pli de passage*, which is a transverse gyrus – or tertiary fold - separating a sulcus into two parts. In particular, this structure has been observed by neuroanatomists to be more frequent in the left STS than in its counterpart (Ochiai et al., 2004) and is contributing to the STAP human-specific asymmetry (Leroy et al., 2015). However, existing automated pipeline never addressed the extraction of these tertiary folds and we proposed a method de novo to extract them automatically.

Once these brain structures are extracted we investigated whether or not they are under genetic control. As a second contribution of this thesis, we have quantified their heritability (i.e. genetic contribution to their phenotypic variance). Until the release of UK Biobank subjects or HCP genotyping data, the limited number of subjects in the IMAGEN cohort did not allow us to perform genome wide genetic association. For this reason, we initially restricted our genetic analyses to the heritability.

An additional phenotype is the task fMRI activations, which has been scarcely studied, the language task of HCP offered us the unique opportunity to investigate the heritability of the group asymmetric activations of auditory and semantic brain areas. In addition, the availability of behavioral data enabled us to look into the shared genetic variance between these brain activations and human cognitive ability as a third contribution of this thesis.

Finally, once the UK Biobank data were made available to our group, as a fourth contribution, we looked into the genetic influence on the brain sulci and genetic variants influencing the sulcal width and gray matter thickness. We discovered and replicated several causal variants of these features, which we also confirmed as markers of brain aging.

Chapter 1. Genetic Influence on the Sulcal Pits: on the Origin of the First Cortical Folds

1. Introduction to the chapter

In this chapter, we propose to quantify the genetic influence on the primary folding locations of the brain, so-called sulcal pits. The molecular and mechanical factors that lead the cortex to fold are very complex and the brain folds result from the addition of multiple factors as described in the context parts. The regularity of folding patterns across human supposes a genetic plan that dictates the genetic gradients necessary to control the progenitor cells' proliferation and to form this consistent pattern of folding. The sulcal pits are of particular interest because they are formed early in development and might keep a strong genetic component in their variance across individuals. First, we extracted the sulcal pits in a large cohort and assessed the asymmetry of their distribution and depth, using a symmetrical template. Second, we estimated the heritability of their depth potential function value, which takes into account the depth and convexity of the cortex surrounding the sulcal pit.

2. Abstract

The influence of genes on cortical structures has been assessed through various phenotypes. The sulcal pits, which are the putative first cortical folds, have for long been assumed to be under tight genetic control, but this was never quantified. We estimated the pit depth heritability in various brain regions using the high quality and large sample size of the Human Connectome Project pedigree cohort. Analysis of additive genetic variance indicated that their heritability ranges between 0.2 to 0.5 and displays a regional genetic control with an overall symmetric pattern between hemispheres. However, a noticeable asymmetry of heritability estimates is observed in the superior temporal sulcus and could thus be related to language lateralization. The heritability range estimated in this study reinforces the idea that the variance of cortical shape, across individuals, is determined primarily by nongenetic factors. This is consistent with the important increase of cortical folding from birth to adult life and thus predominantly constrained by environmental factors. Nevertheless, the genetic cues, implicated with various local levels of heritability in the formation of sulcal pits, play a fundamental role in the normal gyral pattern development. Quantifying their influence and identifying the underlying genetic variants would provide insight into neurodevelopmental disorders.

3. Introduction

The human cerebral cortex is highly convoluted and the process of gyrification starts in utero. To better understand the role of various factors in this phenomenon, detailed models of the cortical folding have been proposed, which include geometric, mechanic and genetic constraints (Tallinen et al., 2016; Toro and Burnod, 2005; Van Essen, 1997). A tension-based model proposed that the shape and location of sulci result from the global minimization of the visco-elastic tensions due to the axonal

connectivity between cortical areas (Van Essen, 1997). Another morphogenetic model underlines the need to include asymmetric gradients of the growth rate to explain the human characteristic brain asymmetries (Toro and Burnod, 2005). However, these models and findings have not estimated the proportion of genetic influence on the cortical folds shape. In addition, the formation of the first sulci is supposed to be related to the specialization of the cortex and following the protomap model described by Rakic (Rakic, 1988). The central sulcus materializes such boundary between the primary sensory and motor areas.

To represent the first folding locations, the notion of *sulcal roots* was introduced by Régis et al (Régis et al., 2005). They correspond to indivisible units whose shapes and locations are supposed to be stable across individuals, as opposed to sulci that form later. In order to extract these putative first cortical folds, algorithms have been proposed over the past few years to extract the deepest points lying at the bottom of sulcal basins (Auzias et al., 2015; Im et al., 2010; Meng et al., 2014). These points located at the maximum depth in a basin, denoted as *sulcal pits*, show less intersubject variability than more superficial ones (Lohmann et al. 2008). In addition, these anatomical landmarks were shown to be reliably identified over different scan sessions, scanners and surface extraction tools (Im et al., 2013). Previous studies have shown that the pattern of the sulcal pits is more consistent in monozygotic twins than unrelated individuals (Im et al., 2011; Lohmann et al., 1999). These results lead to the hypothesis of the pits being under genetic control and having close relationship to functional organization (Lohmann et al., 2008). Furthermore, a longitudinal study has demonstrated that the spatial distribution of the pits already exists at term birth and becomes more pronounced during the first two years of life along with the rapid brain volume increase (Meng et al., 2014). This result suggests a genetic plan which is implemented before birth, as proposed by Rakic (Rakic, 1988). The hemispherical asymmetry of the sulcal pits organization has also been widely studied (Auzias et al., 2015; Im et al., 2010; Leroy et al., 2015; Meng et al., 2014). Consistent results across these studies underline the superior temporal sulcus (STs) as being the most asymmetrical area in term of sulcal pits likely related to language lateralization, in the left hemisphere around the Heschl's gyrus and planum temporale.

To the best of our knowledge, the heritability of the sulcal pits depth has not been estimated yet. In a recent study (McKay et al., 2013), the depth profile of the central sulcus has been extracted in a pedigree study and the highest heritability estimates were found at the two peaks, in sulcal depth position profile. These two peaks, close to the hand and mouth cortical regions, actually correspond to the definition of the sulcal pits and reinforced the idea of a tighter genetic control at these points than other parts along the sulcus. Still little is known about the heritability of sulcal pits in the rest of the cortex and the underlying associated genetic variants. Moreover, the potential genetic influence on the asymmetrical distribution of some of the pits remains unknown.

Several studies have already emphasized the feasibility of using sulcal pits as biomarkers to distinguish healthy subjects from diseased ones. Examples of such applications range from quantitatively describing the abnormal sulcal pattern in polymicrogyria (Im et al., 2012) to characterizing the atypical sulcal pattern in children with developmental dyslexia (Im et al., 2016) by using sulcal graph matching. Understanding the genetic underpinnings would provide insight into morphological phenotypes of neurodevelopmental disorders.

4. Materials and methods

4.1. Pits extraction

The BrainVISA process "Sulcal Pits Extraction" (brainvisa.info, version 4.5.0) was used to obtain the sulcal pits from the white meshes of both hemispheres for each individual (Auzias et al., 2015). The procedure first estimates the sulcal depth by computing the depth potential function (DPF) on each white mesh as introduced in (Boucher et al., 2009). The DPF is a scalar field corresponding to the signed traveled distance that quantifies how much a curve is bent inward or outward (i.e. average convexity). It represents the overall shape of a fold as the function whose Laplacian is as close as possible to the mean curvature (κ_{mean}) of the surface. $(\alpha I + \Delta)D_\alpha = 2\kappa_{mean}$, where D_α is the DPF field, α controls the decay rate of the curvature influence as we move further from a given point, and I and Δ represent the identity and Laplacian matrices, respectively. When α tends to infinity, the DPF tends to the mean curvature, when α tends to 0 the DPF tends to the average convexity, and for intermediate values of α, the DPF integrates both types of geometrical information. In this work, we used the default value of α: 0.03. Thus, the DPF provides a regularized estimation of the depth of the folds based that takes into account information from both convexity and curvature, see (Auzias et al., 2015; Boucher et al., 2009) for implementation details. Several advantages, compared to other methods for depth estimation, make it a relevant phenotype to estimate the genetic influence on the sulcal pits. Three main other techniques to estimate the depth may have been used: computing the Euclidean distance to the closest point on the external hull (Im et al., 2010), estimating the geodesic distance to the ridges on the crown of gyri that are in contact with the brain hull (Rettmann et al., 2002), using an adaptive distance transform based on graph-searching algorithm to find the shortest path from each vertex to the brain hull (Kao et al., 2007; Yun et al., 2013). The caveats of these methods are extensively detailed elsewhere (Auzias et al., 2015; Boucher et al., 2009), the main one being the problematic definition of the brain surface hull. The definition of a reference level required by these methods is avoided by the DPF. On this depth map a watershed algorithm is applied to distinguish the different sulcal basins and localize their respective deepest point. During the flooding procedure, the basin merging decision rule was based on the following features: the ridge height (R) which is the height difference between the shallowest pit and the ridge point, the basin area (A) and the geodesic distance between the two pits (D). During the flooding, the two basins were merged if R or D were below corresponding predefined thresholds (ThR, ThD). After the flooding, the small shallow basins

for which A was below a given threshold (ThA) were merged with their respective neighbors with which the shared border was the longest. The motivation for this approach as well as the definition of the predefined parameters [ThR=1.5, ThD=20, ThA=50] are described in Auzias et al. (2015).

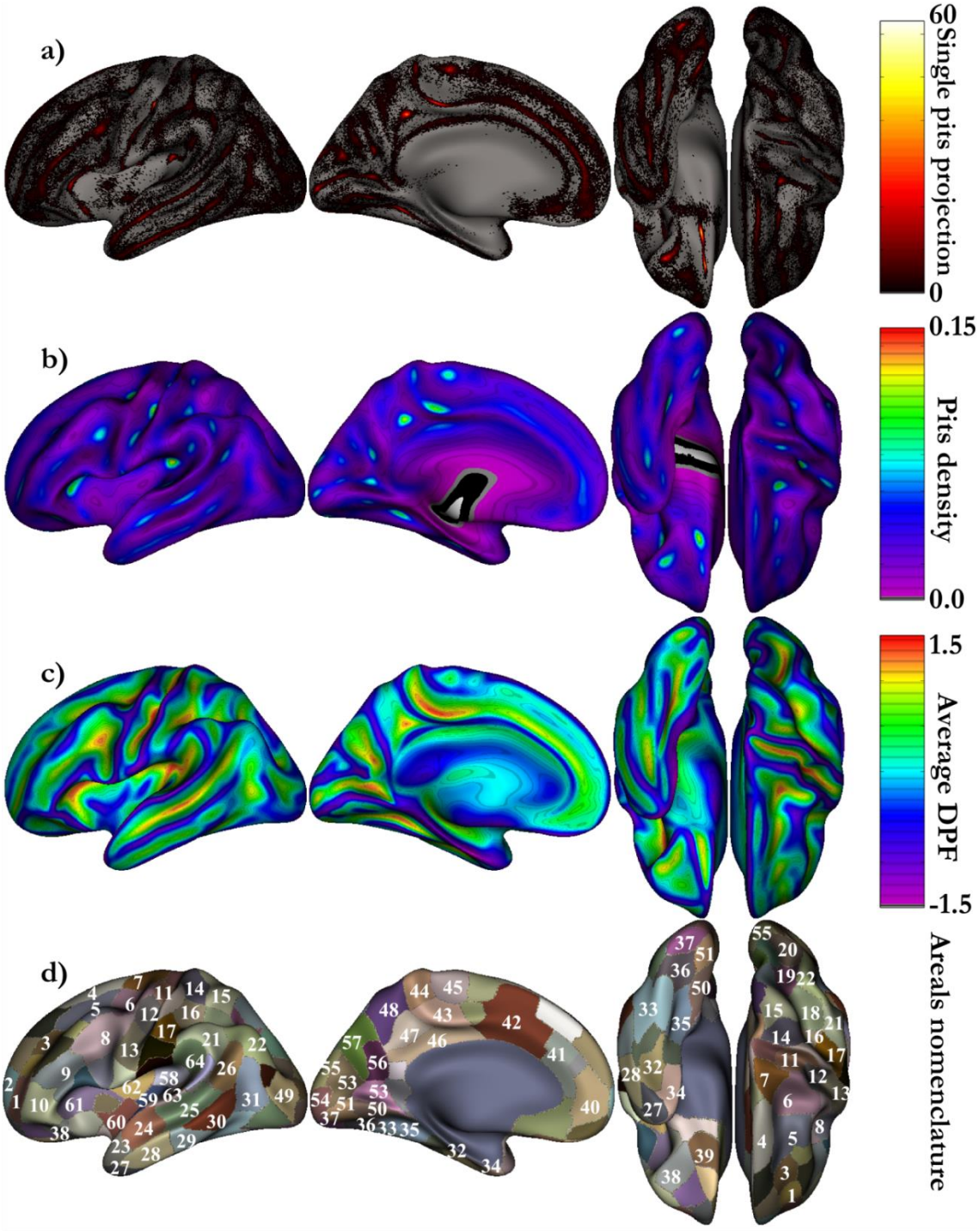

Figure 1. Group averages on symmetric template. (a) All the pits from every individual projected onto the left *fsaverage_sym* template (presented with external, internal, bottom and top views of the left hemisphere). **(b)** Density map corresponding to the sum of the smoothed pits map across subjects and across hemispheres. **(c)** Average DPF map corresponding to the same sum as for the density map. **(d)** Group-level sulcal basins obtained after performing the watershed on the density map. Nomenclature of our areals mainly based on existing literature (Im et al., 2010; Meng et al., 2014). 1 mid frontal a, 2 sup frontal a, 3 mid frontal b, 4 sup frontal b, 5 mid frontal c, 6 junct sup frontal and precentral, 7 precentral, 8 junct precentral and inf frontal, 9 inf frontal b, 10 inf frontal a, 11 central a, 12 central b, 13 central c, 14 postcentral a, 15 postcentral a bis, 16 postcentral b, 17

postcentral c, 18 intraparietal a, 19 intraparietal b, 20 intraparietal c, 21 supra marginal gyrus, 22 junct intraparietal and sup temporal, 23 sup temporal a, 24 sup temporal b, 25 sup temporal c, 26 sup temporal d, 27 temporale pole, 28 inf temporal a, 29 inf temporal b, 30 inf temporal c, 31 inf temporal d, 32 occipito temporal a, 33 occipito temporal b, 34 collateral a, 35 collateral b, 36 collateral c, 37 collateral d, 38 orbital, 39 olfactory, 40 cingulate a, 41 cingulate b, 42 cingulate c, 43 cingulate d, 44 cingulate e, 45 supplementary motor area, 46 below subparietal and cingulate, 47 subparietal, 48 subparietal b, 49 lateral occipital a, 50 junct collateral and calcarine a, 51 junct collateral and calcarine b, 52 calcarine a, 53 calcarine b, 54 calcarine c, 55 lateral occipital b, 56 parieto occipital a, 57 parieto occipital b, 58 circular insular a, 59 circular insular b, 60 circular insular c, 61 circular insular d, 62 circular insular e, 63 planum temporale area, 64 planum parietale

4.1. Parcellation scheme and areal nomenclature

After the extraction of the pits at the individual level, we computed the symmetric group-level cluster regions as proposed by Auzias et al. (2015). Briefly, the correspondences between cortical meshes from the left and right hemispheres were obtained through spherical interhemispheric registration based on the Freesurfer symmetric template *fsaverage_sym* (Greve et al., 2013). Individual sulcal pit maps were iteratively smoothed corresponding to a Gaussian smoothing keeping a maximum peak height of 1 with 5 mm full width half maximum (FWHM). The smoothed maps from both hemispheres were projected onto the left side of *fsaverage_sym*, and summed across subjects to obtain the group density map (**Figure 1.b**). This density map indicates the probability of presence of pits in each location, taking into account information from both hemispheres. A second application of the watershed algorithm was then performed on the pits density map to obtain group-level clusters of pits -denoted in the following as areals. This procedure leads to a parcellation of the template surface into a set of regions where the probability of a having a pit is high. The watershed parameters [gThR = 2, gThD = 15, gThA=100] were used in order to obtain areals that fit well the geometry of the cortical surface as in (Auzias et al., 2015).

The resulting areals were then labelled manually and thus defined the intersubject and inter-hemispheric correspondence of pits. Note that using a symmetric template was crucial for quantifying the asymmetries: information from both hemispheres was taken into account when computing sulcal pit clusters so that cortical areals of the same size and shape were compared across hemispheres. **Figure 1** summarizes the definition of the group map, which includes the projection of all the sulcal pits on the template (**Figure 1.a**), the density map (**Figure 1.b**), the average DPF map (**Figure 1.c**). **Figure 1.d** introduces the nomenclature we used for our areals based on previous names in the literature (Im et al., 2010; Meng et al., 2014). Note that the group clusters of pits used in this chapter are from HCP S900 subjects described in our published study (Le Guen et al., 2018a). The main results of the chapter are not changed but have been updated here using HCP S1200 labelled as "White" to avoid population stratification.

4.2. Definitions of the pits frequency and asymmetry index (AI)

First, the pits frequency is defined as the number of individuals having at least one pit in this areal divided by the total number of subjects.

We compute the asymmetry index, also known as laterality index (Greve et al., 2013) for any metric, the following way: AI = $\frac{(L-R)}{(L+R)}$. For instance, L can be the density of pits in the left hemisphere and R for the right hemisphere, both taken in the same group-level cluster of the symmetric template. AI varies from -1 (completely right lateralized) to 1 (completely left lateralized). It's worth noting that this quantification of the asymmetry can also be used for any metric other than the pits frequency. We computed the AI for the heritability values in each areal as well as for the DPF of the pits.

4.3. Confidence interval for heritability estimates and asymmetry significance

We can compute the confidence interval for heritability estimates under the asymptotic normality assumption of the maximum likelihood estimator where the sample size is ~ 850 with the following formula:

Asymptotic confidence interval at 100·(1-α) % is $[h^2 - Z(\alpha/2) \times \sigma,\ h^2 + Z(\alpha/2) \times \sigma]$ (Neale and Miller, 1997). For 95%, Z(α/2) ≈ 2, for 67%, Z(α/2) ≈ 1.

Using the confidence interval for the heritability estimates in the left and right hemispheres, we deduced that the two estimates are significantly different at 100(1-α) %, assuming the two heritability estimates are independent, if:

$$diff = |{h^2}_{right} - {h^2}_{left}| > \ Z(\alpha/2) \times (\sigma_{h^2 right} + \sigma_{h^2 left}).$$

4.4. Thresholding procedure

The pits extraction procedure extracts indiscernibly deep and shallower sulcal pits. This distinction can be made in areals corresponding to sulci, in which a clear deep sulcal point can be selected, but also sometimes a bump in the sulcus shape leads to the identification of a shallower pit. The former pits belong to the deep sulcal pits distribution (see **Figure 2.a** for example in three areals) more commonly referred to in the literature and formed early in utero brain development (Im et al., 2010; Meng et al., 2014; Régis et al., 2005). The latter pits are part of the shallower pits distribution (**Figure 2.a**), that we assumed are formed later in the brain development. The deep sulcal pits are of particular interest because they are supposed to be the phenotypic manifestation of the sulcal roots under tight genetic control (Lohmann et al., 2008). We describe in details in the supplementary materials a method to filter out the shallower pits, by setting an adaptive threshold per areal (**Method S1**). Briefly, when we considered the DPF distributions of all pits in an areal we observed either one or two underlying Gaussian distributions (**Figure 2.a**, **Figure S2.a**). Our method consists in fitting a mixture of two Gaussians to the whole distribution in the considered areal, in order to set a threshold to separate them while minimizing both the numbers of false positives and false negatives for the deep pits selection. In **Figure 2.a**, we clearly distinguish two underlying DPF distributions for the areals

considered, some other areals having only one clear Gaussian peak. It also represents how the threshold (the dark line) is set with regard to the pits DPF distribution in each considered areal. Two variants of the sulcal root phenotype were studied for each areal: the depth of the deepest pit without applying a threshold and the depth of the deepest pit after applying the adaptive threshold. Notice that in the main text, only the results without thresholding are presented and other results are available in the supplementary materials. We explain this choice in the discussion.

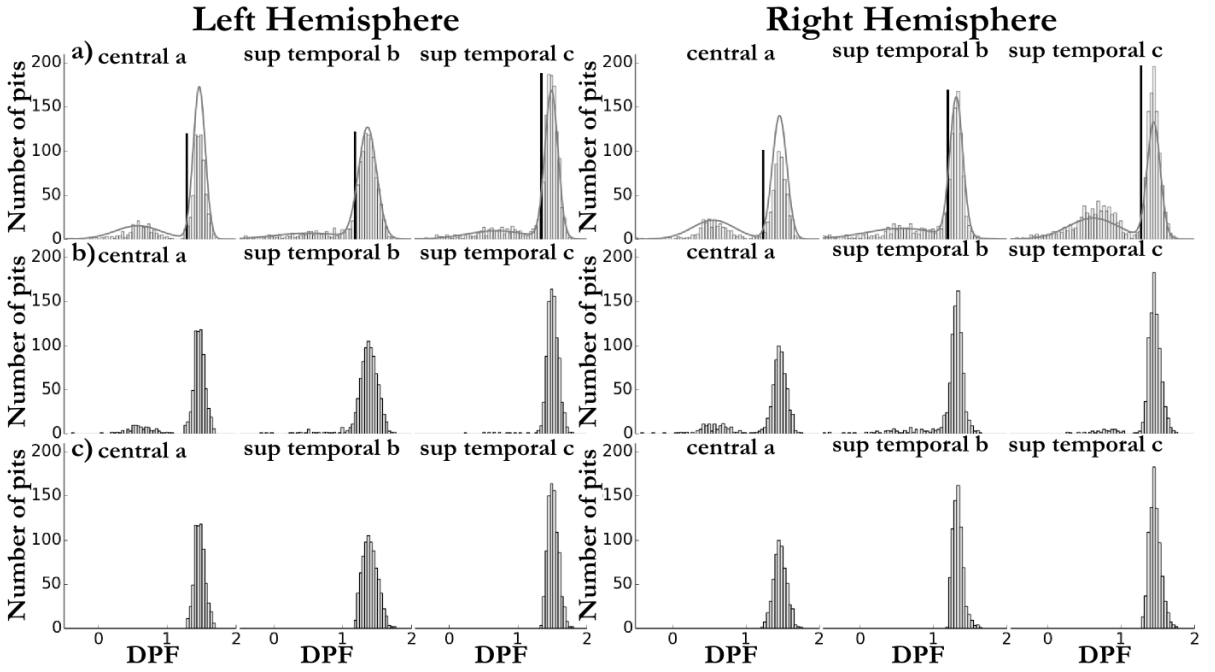

Figure 2. (a) Example of the thresholding procedure on all pits DPF per areal in each hemisphere. **(b)** Phenotypes when selecting the deepest pit for each individual without any thresholding. **(c)** Phenotypes when selecting the deepest pit for each individual after the adaptive thresholding.

5. Results

5.1. Pits frequency

As opposed to previous literature (Im et al., 2010; Meng et al., 2014), we also included in our heritability analysis cluster regions that do not specifically lie at the bottom of the sulci, among them are shallow regions such as the planum temporale area, planum parietal or the supra marginal gyrus. To include an areal in our analysis, the general constraint we imposed is that the pits frequency must be above 75% in the selected areals on both hemispheres. Nevertheless, a few areas that were present in the previous literature but do not meet this criterion were also included: calcarine (Cal) c, cingulate (Cing) (b, e), collateral (Col) a, superior temporal (ST) a, temporale pole (TP). All of them had a pits frequency above 70% on both sides, except the ST *a* areal (pits frequency *~55%)*, that we kept to be consistent with previous nomenclature of the STs. As described in Auzias et al. (2015), the method we used has a higher reliability of extraction resulting in increased pits frequencies compared to Im et al. (2010). We obtained pits frequencies above 90% on both sides in the following areals: "below subparietal (SP) and Cing", Cal (a, b), central b, Cing (a, c, d), circular insular (Circ) (a, c, d, e), Col (b, c), inferior frontal (IF) (a, b), inferior temporal (IT) (a, c, d), intraparietal (Int) (a, b, c), lateral

occipital (LO) (a, b), middle frontal (MF) (a, c), occipito temporal (a, b), olfactory, orbital, parieto occipital (PO) a, SP (a, b), superior frontal (SF) b, ST (b, c, d), supra marginal gyrus, junction (jct) Int and ST, jct precentral (PreC) and IF, jct SF and PreC; above 80%: central c, Circ b, Col d, IT b, jct Cal and Col, MF b, PO b, planum temporale area, postcentral PostC (a, a bis, c), SF a, supplementary motor area; and above 75%: central a, planum parietale, PostC b, PreC. The frequency in each areal is shown on **Figure 3.a** for all areals with a pits frequency above 50%, notice that results for both the right and left hemispheres are displayed on the symmetric template left side. This representation is complementary to the density map **Figure 1.b**, which depicts how the pits are concentrated.

5.2. Pits DPF

Figure 2.a and **Figure S2.a** introduce the sulcal pits DPF distribution in six areals (central (a, b, c) and ST (b, c, d)) corresponding to two important primary sulci. We distinguish in central a and ST c, two underlying Gaussian distributions, which correspond respectively to pits that have been extracted in a wall cavity of the sulci and pits that lie at the bottom of the sulci. The first Gaussian distribution is of minor interest in our study because it is not reliably extracted across individuals (see **Figure 1.a**). Our phenotype distributions in these areals correspond to **Figure 2.b** and **Figure S2.b**, for which we have selected the deepest pit of each individual in the areal considered. **Figure 3.b** presents the median DPF value of the pit in all parcels to emphasize the regional pit depth differences and summarizes with a discrete representation the average DPF map (**Figure 3.c**) from the pits point of view. The pits being the putative first cortical folds, the differences observed between various regions might reflect the strength and time course of the folding process regional particularities. We computed the asymmetry index for both the frequency of pits and the median DPF for all cluster regions, the results are respectively displayed on **Figure 3.e.f**. We notice that the two asymmetry maps are roughly similar, emphasizing the link between the DPF and the frequency of pits. In other words, to be reliably extracted across individuals a pit must be buried deep enough.

5.3. Quantitative genetic analysis of the pits DPF

We performed a quantitative genetic analysis of the DPF pit value in each areal named in the nomenclature **Figure 1.d**. The numbers of subject included in each areal varies according to the detection of sulcal pit or not for each subject in the areal. We found that more than half of all areals considered on both sides had a heritability estimate significant ($p < 0.05$) without correction for multiple comparisons. These heritability estimates and their associated p-values are displayed respectively on **Figure 3.c,d**. and **Tables 1 and 2**, for the left and right hemispheres respectively, summarize the significant results after strict Bonferroni correction ($p < 0.05/128 \approx 0.0004$) accounting for the multiple tests due to the number of areals considered. These areals, significant after correction, are the ones with a color above yellow on **Figure 3.d**. The full tables with heritability estimates significant ($p < 0.05$, uncorrected) are given as supplementary material (**Table S1, Table S2**). In the

collateral sulcus, we note significant heritability estimates, after correction, for the *collateral a* in both hemispheres. Other interesting heritability results are found in the central sulcus, where areal *central a* is found heritable after correction in both hemispheres. While the areals *cingulate a, d* are significantly heritable in the right hemisphere. The areals b, c of the STs corresponding to the auditory and semantic networks are noticeably more heritable on the left hemisphere. The *olfactory* sulcus has relatively symmetric significant heritability estimates (about 0.41), which indicates a genetic influence on the shape of the cortex in this sensory area.

Table 1. Results of the additive analysis for the DPF of the pits in the *left hemisphere*: heritability estimate and associated p-values for each covariate.

Trait	**h^2±SE (p)**	**Age**	**Age^2**	**Sex**	**Ag*Sx**	**Ag^2*Sx**	**Ethni**	**h^2cov(%)**	**Sbj**
		p-val							
below subparietal and cingulate	0.38±0.07 ($2.0\cdot10^{-7}$)	0.13	0.47	0.09	0.94	0.48	0.83	0.7	757
calcarine c	0.38±0.1 ($1.3\cdot10^{-4}$)	0.03	0.74	0.64	0.03	0.82	0.72	1.4	527
central a	0.32±0.07 ($4.2\cdot10^{-6}$)	0.93	0.5	$3.9\cdot10^{-3}$	0.69	0.18	0.22	1.2	674
circular insular a	0.25±0.07 ($7.7\cdot10^{-5}$)	0.34	0.19	$9.7\cdot10^{-4}$	0.35	0.39	$2.1\cdot10^{-4}$	3.6	776
circular insular d	0.36±0.07 ($4.8\cdot10^{-8}$)	0.64	0.81	0.19	0.5	0.37	0.12	0.0	807
collateral a	0.46±0.09 ($1.2\cdot10^{-6}$)	0.42	0.37	0.05	0.75	0.41	0.17	0.2	545
collateral b	0.31±0.07 ($1.5\cdot10^{-6}$)	0.66	0.98	0.36	0.9	0.38	0.53	0.0	788
junct collateral and calcarine a	0.27±0.07 ($1.3\cdot10^{-4}$)	0.29	0.29	0.38	0.51	0.23	0.19	0.0	675
lateral occipital b	0.32±0.07 ($5.8\cdot10^{-6}$)	0.22	0.27	0.46	0.54	0.18	0.33	0.0	714
olfactory	0.42±0.07 ($2.9\cdot10^{-9}$)	0.43	0.77	0.07	0.14	0.84	0.14	0.9	742
parieto occipital a	0.35±0.07 ($1.0\cdot10^{-7}$)	0.48	0.46	0.18	0.67	0.87	0.39	0.0	728
subparietal	0.22±0.07 ($2.9\cdot10^{-4}$)	0.51	0.66	0.33	0.55	0.23	0.14	0.0	780
sup temporal b	0.26±0.07 ($3.6\cdot10^{-5}$)	0.4	0.17	0.94	0.21	0.62	0.08	0.4	763
sup temporal c	0.38±0.06 ($3.6\cdot10^{-10}$)	0.7	0.77	1.0	0.57	0.34	0.64	0.0	803

Table 2. Results of the additive analysis for the DPF of the pits in the *right hemisphere*: heritability estimate and associated p-values for each covariate.

Trait	**h^2±SE (p)**	**Age**	**Age^2**	**Sex**	**Ag*Sx**	**Ag^2*Sx**	**Ethni**	**h^2cov(%)**	**Sbj**
		p-val							
below subparietal and cingulate	0.37±0.06 ($1.3\cdot10^{-8}$)	0.57	0.25	0.14	0.35	0.6	$9.7\cdot10^{-3}$	1.2	756
central a	0.42±0.08 ($5.0\cdot10^{-7}$)	0.51	0.85	0.71	0.65	0.59	0.39	0.0	644
cingulate a	0.23±0.07 ($2.4\cdot10^{-4}$)	0.64	0.58	0.02	0.63	0.55	0.86	0.6	789
cingulate d	0.38±0.06 ($6.4\cdot10^{-11}$)	0.02	0.84	$5.7\cdot10^{-4}$	0.17	0.84	0.55	3.3	795
circular insular a	0.34±0.06 ($6.9\cdot10^{-9}$)	0.98	0.46	$1.5\cdot10^{-3}$	0.88	0.35	$2.1\cdot10^{-3}$	5.2	809
circular insular d	0.29±0.07 ($7.3\cdot10^{-6}$)	0.35	0.34	$1.8\cdot10^{-4}$	0.13	0.78	0.62	2.9	800
collateral a	0.32±0.08 ($5.1\cdot10^{-5}$)	0.13	0.27	$4.8\cdot10^{-3}$	0.04	0.07	0.93	1.6	542
collateral c	0.25±0.07 ($2.7\cdot10^{-4}$)	0.76	0.78	$3.1\cdot10^{-4}$	0.39	0.08	0.17	2.2	721
collateral d	0.37±0.08 ($2.6\cdot10^{-6}$)	0.14	0.29	0.71	0.1	0.71	0.09	0.6	646
junct collateral and calcarine a	0.3±0.07 ($1.2\cdot10^{-5}$)	0.09	0.64	0.01	0.07	0.75	0.61	2.2	689
junct precentral and inf frontal	0.22±0.06 ($3.0\cdot10^{-4}$)	0.43	0.41	0.64	0.49	0.77	0.74	0.0	801
olfactory	0.41±0.08 ($2.0\cdot10^{-7}$)	0.12	0.49	$7.0\cdot10^{-6}$	0.19	0.26	0.05	4.0	726

postcentral a	0.25±0.07 ($1.8 \cdot 10^{-4}$)	0.79	0.67	0.5	0.31	0.7	0.97	0.0	710

Only significant results after strict Bonferroni correction $p < 0.05/128$ are presented here.
Abbreviations: h^2, heritability; SE, standard error; p, associated p-value; h^2_{cov}, variance explained by the covariates; Sbj, number of subjects. Ethni: covariate accounts for Hispanic ethnicity. Ag*Sx accounts for age and sex interactions, Ag²*Sx account for age² and sex interactions. Trait abbreviations are defined in the text.

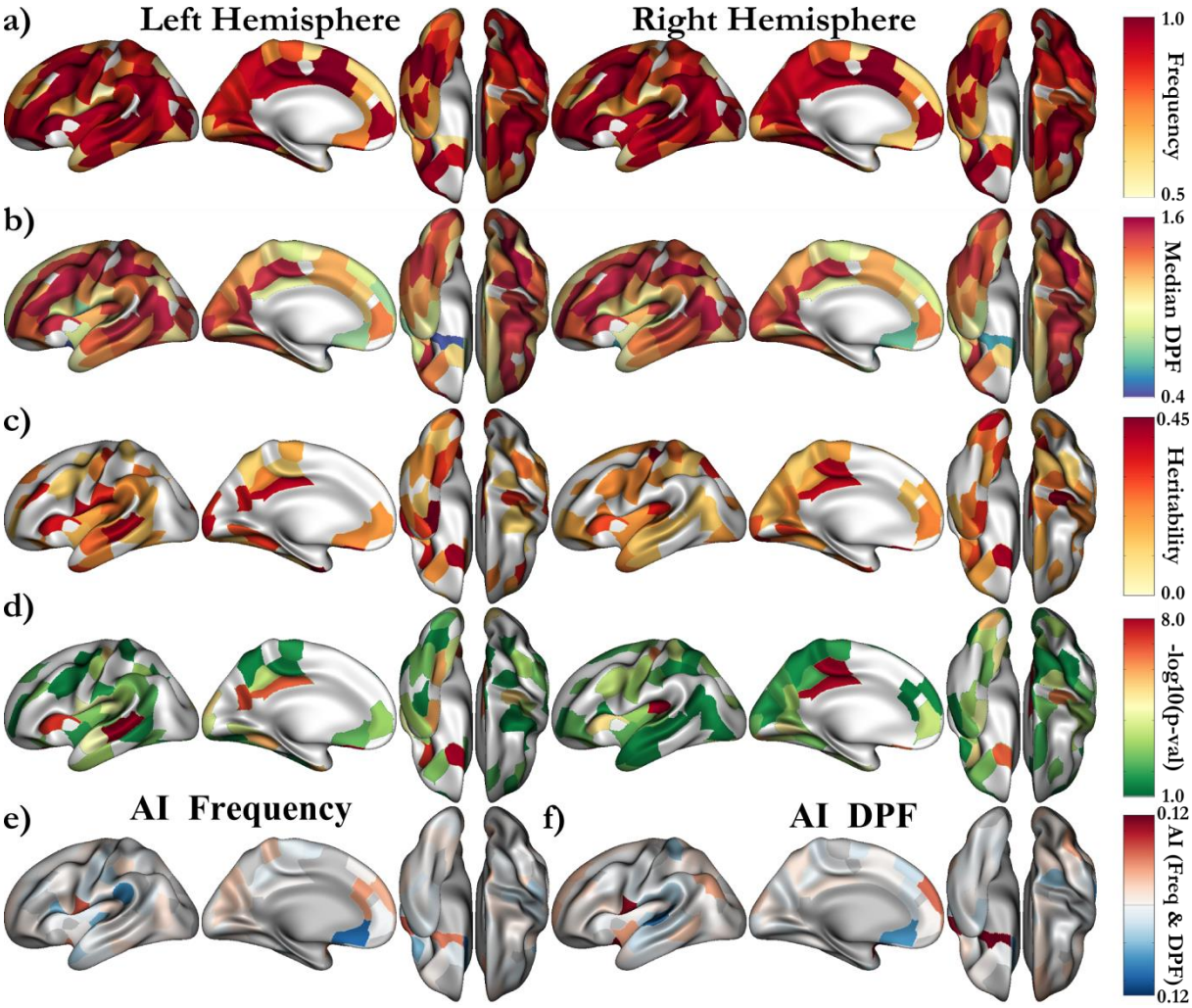

Figure 3. (a) Deep pits frequency and **(b)** median DPF of the pits selected as phenotypes in each areal. **(c)** Heritability and **(d)** associated –log10(p-values) for all the areals being significant without correction ($p < 0.05$). The areals which are significant after strict Bonferroni are shown with a color above yellow. Both left and right hemisphere results **(a, b, c, d)** are presented on the symmetrized (left) template. **(e)** Asymmetry Index frequency. **(f)** Asymmetry Index median DPF.

In addition, we quantified the correlation between hemispheres of the frequency and the heritability, as well as the relationship between these two and the DPF value. For the frequency-related quantifications, we considered areals with a pits frequency above 50%. For heritability-related quantifications, we kept only areals with a heritability estimate significant ($p < 0.05$, uncorrected) on both sides. As expected, given the relative symmetry of the brain, the pits frequency on both sides are highly correlated (Pearson correlation: $r^2 = 0.91$, $p = 10^{-38}$, **Figure 4.a**), as well as the DPF between hemispheres ($r^2 = 0.92$, $p = 10^{-41}$, **Figure 4.c**). The heritability estimates across hemispheres are significantly positively correlated ($r^2 = 0.34$, $p = 0.05$, **Figure 4.b**), suggesting some symmetric genetic influences over the pits DPF. As observed by Auzias et al. 2015, we note that the DPF and the

pits frequency are positively correlated (r^2 = 0.63, p = 10^{-10}, **Figure 4.d**), showing a higher reproducibility of the deeper sulcal pits. This might be due do a better registration of the deeper folds. But, it could also reflect a more consistent genetic plan for deeper sulcal pits. However, this second hypothesis seems to be contradicted by the negative correlation trend between the pits DPF and heritability estimates (r^2 = -0.22, p = 0.15, **Figure 4.e**). The role of mechanical constraints will be discussed to account for a less important genetic control over pits with higher depth. Besides, the standard errors of the heritability estimates are still relatively large 0.06 to 0.10 to be compared to the values of these estimates 0.22 to 0.42. In addition, the heritability and the pits frequency were found to be correlated (r^2 = -0.3, p = 0.05, **Figure 4.f**).

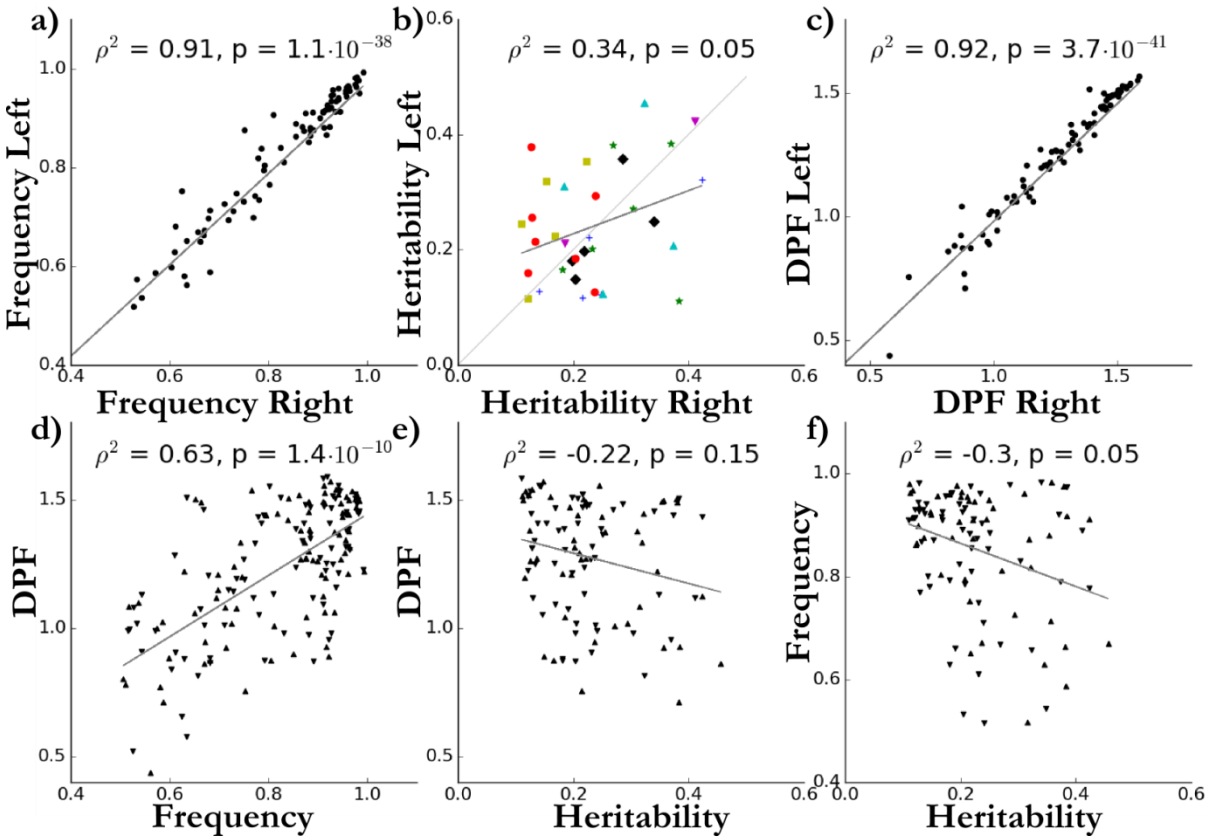

Figure 4. (a) Correlation between left and right pits frequency for all areals with frequency above 50%. **(b)** Correlation and comparison of heritability estimates with associated p-values < 0.05 between hemispheres. Significant areals are grouped according to their location with the following legend: *light grey line*: y = x, *green star*: Cingulate-Calcarine, *dark blue cross*: Central-Frontal, *black diamond*: Sylvian fissure, *light blue up triangle*: Collateral, *red disk*: Temporal, *yellow square*: Occipital-Parietal, *purple down triangle*: Olfactory-Orbital. **(c)** Correlation between hemisphere of pits median DPF per areal. **(d)** Positive correlation between DPF and pits frequency (up: left hemisphere, down: right hemisphere). **(e)** Negative correlation between pits median DPF and heritability estimates (up: left hemisphere, down: right hemisphere). **(f)** Correlation not significant between frequency and heritability estimates (up: left hemisphere, down: right hemisphere). For all plots, the regression line is in grey.

In spite of a general symmetric genetic control, we found two areals having a significant difference of genetic control between hemispheres, using the criterion previously introduced for a confidence interval of ± 2σ (95%) (i.e. $diff = |{h^2}_{right} - {h^2}_{left}| > 2 \times (\sigma_{h^2 right} + \sigma_{h^2 left})$). These are the *superior temporal c* (diff = -0.25) and the *cingulate d* (0.27). Reducing the confidence interval to 67% ($Z(\alpha/2) \approx 1$), we also found asymmetric heritability in the *collateral b, c, d* (-0.13,

0.13, 0.10), the *lateral occipital b* (-0.17), the *parieto occipital* (-0.13) and the *superior temporal b* (-0.13). **Figure S4.** presents a graphical interpretation of these differences presenting the heritability estimates with their confidence intervals in both hemispheres for each areal with an associated p-value < 0.05 for h^2 on both sides.

6. Discussion

To the best of our knowledge, this quantitative genetic study of the pits depth is the first to estimate the additive genetic effects on the pits, which were for long assumed (Im et al., 2010; Lohmann et al., 2008). First, we confirmed the high reliability of pits extraction in a large population using the procedure described in (Auzias et al., 2015). In addition, we demonstrated the highly symmetric distribution for most pits in term of frequency and DPF, with low values of asymmetry index and high correlation between hemispheres. We also emphasized the link between pits DPF and frequency, underlining the fact that deep pits are more consistently extracted across individuals. Second, we reported the heritability estimates for all the pits cluster regions in both hemispheres using the large sample size of the HCP pedigree study enabling to have enough statistical power to estimate the heritability of phenotypes with low genetic influence. We found that pits DPF of areals in the central, cingulate, collateral, occito-temporal, parieto-occipital and superior temporal sulci, among others, are significantly heritable after strict Bonferroni correction in one or both hemispheres. Finally, we highlighted a few remarkable asymmetrical areals among an overall symmetrical pattern of genetic influence across the brain.

6.1. Sulcal pits distribution

During the early period of brain development, sulcal roots correspond to the locations where the cortical folding begins (Régis et al., 2005). The sulcal pits associated to these roots are the ones lying at the bottom of the sulci and were previously extracted by imposing a threshold considered as a minimum required depth (Im et al., 2010; Meng et al., 2014). The concept was recently extended (Auzias et al., 2015) to include shallower pits, because algorithmically other vertex points might have fulfilled the requirements of the sulcal pits and might contain information on later periods of brain development or on less deep regions. Including shallower pits offers the opportunity to study folds in shallow region, such as the planum temporale area, planum parietal or the supra marginal gyrus. The main caveat is that, in areals having already one deep sulcal pits, shallower pits can also be extracted, for example in a sulcus wall cavity. If we consider the two types of phenotype distributions: one (**Figure 2.b**, **Figure S2.b**) is composed of all deepest pit DPF of individuals having at least one pit and the other one (**Figure 2.c**, **Figure S2.c**) being the same distribution after only considering the pits with a DPF above the threshold. We notice that both are almost identical, for the six areals under scrutiny in both hemispheres, except that in the second case the left tail of the Gaussian is cut, thus deliberately ignoring part of the population with lower DPF. However, the central a areal phenotype also contains

pits from the shallow distribution (**Figure 2.b**), when we take the deepest pits without thresholding before. Indeed, this specific issue is reflected in the higher heritability estimate and significance for this areal when its distribution has been thresholded (**Figure S3.c**). Overall, the heritability estimates in other areals (**Figure S3**) are identical, except that the standard error increases because the thresholding is conservative and excludes some subject with deep sulcal pits. Despite a better "homogeneity" of the phenotype we decided not to insert this thresholding step in order to include the largest sample possible representative from the general population, which also contains individual belonging to the left tail of the Gaussian distribution. This choice differs from the ones made by (Im et al., 2010; Meng et al., 2014) but avoid the caveat of arbitrarily choosing a threshold (Auzias et al., 2015).

6.2. Genetic influence on the sulcal pits

From the current literature, two complementary theories emerge that support the genetic influence on the sulcal pits and call for a quantitative genetic study. The first model, based on observations in rhesus macaque, assumed that the morphology of earlier developing brain structures is more genetically controlled (Cheverud et al., 1990). The older the structure ontogenic's age, the more genetically predetermined it is (Cheverud et al., 1990). A second hypothesis supported by Lohmann and colleagues, who studied the sulcal variability in human twin-pairs and noticed that deeper sulci are more similar than superficial ones, proposed that the deeper cortical structures are more genetically influenced (Lohmann et al., 1999). Since this hypothesis is based on the fact that deep cortical sulci formed earlier in development, this second proposition is actually a consequence of the first model. Both related hypotheses were never formally tested but explained findings in normal cortical variability (Cykowski et al., 2008) as well as in disease-specific difference observed such as in schizophrenia (Narr et al., 2004). However, the studies that formulated these hypotheses had major weaknesses. Notably, the former (Cheverud et al., 1990) was performed in the sulcal indentation in the skulls and the latter (Lohmann et al., 1999) was done in a very small sample. Therefore, any conclusions from these studies should be treated by preliminary and taken with appropriate caution. Kochunov and colleagues tested both of these hypotheses by studying the genetic contribution to regional morphological variability in the cerebral cortex of baboons (Kochunov et al., 2010). They could not replicate the findings of Lohmann and colleagues and rejected this theory. The negative correlation trend we found (**Figure 4.e**) between the median DPF and the heritability of DPF, means that deeper pits are not necessarily more heritable than more superficial ones and seems to contradict the hypothesis that deeper cortical structures are more genetically influence.

Nevertheless, our study in a human pedigree cohort supports a genetic influence on the sulcal pits, which displays regional variabilities with heritability estimates ranging from 0.2 to 0.5. These results consolidate the hypothesis of a genetic control on these structural landmarks (Lohmann et al., 2008). Our study confirms that the term landmark is appropriate because of the higher pits frequency

for pits lying deeper in the cortex (**Figure 4.d**), thus suggesting a general framework to compare individual sulcal variability. Furthermore, the sulcal pits are key points of the cortical folds, which are often thought to be related to cytoarchitectonic areas (Fischl et al., 2008) and therefore assessing the genetic component of their shape seems particularly relevant. Indeed, the DPF partly includes shape information, because it not only reflects the depth but also the convexity of the pit neighboring white matter. Besides, we note that this range of heritability estimates (below 0.5) suggests pits DPF and thus the cortical structure shape phenotypic variance is primarily influenced by nongenetic factors, even though the genetic control over the formation of the gyral pattern is significant. The shape of sulci continues to evolve throughout the adult life as opposed to the total brain volume or the intracranial volume, which are fixed after adolescence and whose heritability estimates are closed to 0.8 (Stein et al., 2012). This conclusion was noticeably reached twenty years ago by Barltey, Jones and Weinberger with only 10 pairs of MZ and 9 pairs of DZ, who found high heritability for the cerebral size (>0.9) and relatively low heritability for the gyral pattern (<0.2) (Bartley et al., 1997). They underlined the significant role of the genes in shaping the cortical shape by observing that MZ twins were more alike than DZ twins and noticing the interhemispheric symmetry of the gyral pattern within subjects (Bartley et al., 1997).

Focusing on the central sulcus, we found significant ($p < 0.05$) heritability estimates, ranging between 0.22 to 0.42, for the sulcal pits in the three areals composing *central sulcus a, b, c* in both hemispheres. Moreover, a study on the heritability of the depth position profile found three heritability peaks in both left and right hemispheres depth profiles (McKay et al., 2013). Due to the high variability of depth profiles between individuals, the authors could not conclude if the heritability peaks collocated with the maximum depth positions. However, following the average depth trace the sulcal depth peaks seem to correspond to the heritability peaks. Combined with our results, this would support the importance of the sulcal pits as cleaving points in the genetic plan. Interestingly, the locations of the heritability peak were adjacent to specialized functional areas, with the activations in fMRI tasks activating the hand and mouth regions (McKay et al., 2013). This emphasizes the potential role of the sulcal pits as landmarks separating functional areas, such as the somatotopic arrangement along the central sulcus. Moreover, the average depth in the finger tapping area was pleiotropic with the average reaction time of the corresponding fMRI task. This finding, associated to our heritability estimates, comforts the hypothesis that sulcal pits have close relationship to functional areas (Lohmann et al., 2008) and might suggest a common set of genes influencing the brain function and structure.

We found our highest heritability estimate for the DPF of the sulcal pit in the areal *collateral a* ($h^2_{left} = 0.46$, $h^2_{right} = 0.32$), followed closely by the one in the *olfactory sulcus* ($h^2_{left} = 0.42$, $h^2_{right} = 0.41$). The collateral sulcus showed significant heritability estimates on both sides in three areals. These were superior in the anterior areal collateral a in comparison to posterior ones b, d. The anterior

areal a corresponds to Rhinal sulcus (Sarnat and Netsky, 1981) which is considered, from a phylogenetic point of view, as the second hemispheric sulcus following hippocampal sulcus and demarcates the border between the paleocortex and neocortex (Ribas, 2010). In humans, the Rhinal sulcus delineates the parahippocampal uncus from the rest of the neocortical temporal lobe. Thus, the Rhinal sulcus was already present in early mammals (Nishikuni and Ribas, 2013; Ribas, 2010). Such phylogenetic seniority could explain the higher heritability of the anterior areal of the collateral sulcus.

In addition, we have shown a significant correlation between the heritability of the left and right hemispheres (**Figure 4.b**), which seems to be in line with initial symmetric morphogenic protein gradients, such as Sonic hedgehog and members of the bone morphogenetic protein family, (Echevarría et al., 2003). This is also in agreement with the "symmetry rule" from McKay and colleagues postulating that a feature in one hemisphere is likely under the control of the same genes or set of genes in the opposite hemisphere (McKay et al., 2013). Genetic clustering based on cortical surface area resumes this rule by showing a genetic organization predominantly bilaterally symmetric across hemispheres (Chen et al., 2012). Similarly, our heritability map of the sulcal pits DPF (**Figure 3.e**) and the positive correlation found (**Figure 4.b**), both confirm this postulate.

6.3. Asymmetric genetic control in particular regions

Despite an overall symmetric genetic control, two areals in the STs have highly asymmetric heritability estimates, respectively for areals b and c: h^2(STb) = 0.26 ($p = 10^{-5}$) and h^2 (STc) = 0.38 ($p = 10^{-10}$) in the left hemisphere whereas in the right hemisphere h^2 (STb) = 0.13 (p = 0.04) and h^2 (STc) = 0.13 (p = 0.03) (**Tables 1, 2**). These results advocate for a higher genetic control in the left STs. Furthermore, these areals in the left hemisphere might correspond to functional zones involved in language comprehension in adults (Pallier et al., 2011). Specifically, areals ST b and c are located along the linguistic ventral pathway and would map sounds to meaning with phonetic processing in ST c and computations related to larger constituents in ST b (DeWitt and Rauschecker, 2012; Skeide and Friederici, 2016). Our results suggest genetic cues to increase the genetic control in the lay down of the cortex organization in regions involved in such language functions. These genetic cues, such as differential gene expression, could contribute to the functional gradient of linguistic processes which has been reported along the STs early in life (Dehaene-Lambertz et al., 2006).

Karlebach and Francks have recently demonstrated in a molecular biology study the lateralization of individual genes expression and gene ontology groups in the human language cortex (Karlebach and Francks, 2015). These genes are likely to tailor the genetic control over brain particular functions including synaptic transmission and glutamate receptor activity, and pave the way to the nervous system development (Karlebach and Francks, 2015). These asymmetrical gene contributions may account for our asymmetric quantitative genetic results, which exhibited a higher heritability in the left hemisphere where the fine-tuning is the most required.

We can also relate this asymmetry of additive genetic effects to various structural asymmetries already demonstrated in the vicinity of the STs. The most notable ones consist of: the planum temporale and Heschl's gyrus larger on the left side (Dorsaint-Pierre et al., 2006) ; The asymmetry of the STs depth profile, which is more pronounced in humans than chimpanzee (Leroy et al., 2015) and visible in infant brain (Glasel et al., 2011); Specifically, plis de passage across areals STs b and c, which are complementary shapes to sulcal pits and are more consistent in the left hemisphere from early in life along the lifespan (Leroy et al., 2015; Ochiai et al., 2004); Finally the arcuate fasciculus, which is larger in the left temporal region and whose asymmetry is observed from birth (Dubois et al., 2010). The language lateralization is the main working hypothesis to explain these asymmetries and our findings support stronger genetic control over the underlying structure in the left side of the brain. In another study, the left temporal area was also hypothesized to be the hemisphere mostly influenced by in utero environment (Geschwind et al., 2002), which mitigate our finding even if it seems coherent with the initial delay in maturation observed in the left hemisphere compared to the right. The hypothesis of Geschwind and colleagues hypothesis was based on results in a cohort of aged twins (61 MZ pair and 67 DZ pair, average age 71 years old), in which they found the temporal lobe volume more heritable in the right hemisphere (Geschwind et al., 2002). However, due to the population size and age, these results, which considered the whole temporal lobe, are to be taken with caution. In addition, the delay formation of the left STs could also be explained by a protracted genetic control to allow the fine tuning of the particular electrophysiological and neurotransmission properties of this key cognitive area. Indeed, Geschwind's work also supports a genetic contribution to the development of cerebral asymmetry (Geschwind and Miller, 2001) and quantitative genetic studies with sufficient statistical power like ours are still needed to validate the importance of the genetic control on each side.

One limitation of our study is that we did not model the shared environment since: first, HCP does not provide direct household information, and second due to the limitations of household as a proxy for common environmental influences in extended pedigree designs. Thus, some of our heritability estimates might be inflated due to shared environmental influences. However, the sulcal pits are the putative first cortical folds supposed to be formed early during the cortex development, hence we believe household environmental influence should have a limited effect on their depth.

This study underlines the role of the sulcal pits as good candidates for future genome wide association analysis, using for example the large UK Biobank cohort to have adequate statistical power to detect small effect size variants. Further aim is to build novel polygenic scores in which genotypes at many loci are influencing the sulcal pits. These polygenic scores could be used to investigate the genetic influence of these loci on other phenotypes and neurological disorders.

7. Supplementary methods

7.1. Method S1. Shallow pits filtering

The extraction procedure we used extracts indiscernibly deep and shallower sulcal pits. The local-DPF distributions are obtained from all the pits DPF values which once projected onto the template are in the areal under scrutiny. Thus, we observe that in most of our group-level areals, we have two underlying local-DPF distributions. One corresponds to the deep sulcal pits more commonly referred to in the literature and formed early in utero brain development (Im et al., 2010; Meng et al., 2014; Régis et al., 2005). The second one consists of shallower pits, we assumed that they are formed later in the brain development. The formers are of particular interest because they are supposed to be the phenotypic manifestation of the sulcal roots under tight genetic control (Lohmann et al., 2008). The problem might arise when we did not extract any deep sulcal pit for an individual in a given areal but a shallow one. This type of pit should not be mixed with the one formed earlier in development because they are undoubtedly resulting from different genetic mechanisms, resulting from delayed mixed effects of genetic and environments. Therefore, we fix a lower-bound threshold on the DPF for a pit to be taken into account in our analysis. In order to set a threshold in a way less arbitrarily as possible, we fit the DPF distribution in each parcel a mixture of two Gaussians using Scikit-learn Python package. Then, we set the threshold between the two Gaussians in order to minimize both the numbers of false positives and false negatives for the deep pits selection. **Figure 2** shows examples in the central and superior temporal sulci of the DPF distribution for sulcal pits extracted in the respective group-level areals in the HCP cohort. The areal names correspond to the ones of Im et al. (2010) and are explicitly defined in our case (**Figure 1.d**). In the plots corresponding to areals like “central a” and “superior temporal c” we clearly distinguished the two Gaussians distributions, with the highest values corresponding to deep sulcal pits under consideration here. After filtering, if a subject still has more than one pit in an areal then only the deepest of his pits is retained as well as its local-DPF for that areal. This value of local-DPF constitutes the phenotype under scrutiny for our heritability estimation for the results on **Figure S3**. **Figure S1.** illustrates the result of the filtering, by projecting the remaining pits on each hemisphere and is to be compared with Figure1.a where all the pits extracted were projected on the template. For example, the reader can notice that the pits which were not at the bottom of central and temporal sulci have overall been removed.

7.2. Method S2. List of HCP not distributed files to perform interhemispheric registration

To perform the surface based interhemispheric registration the Freesurfer *xhemireg* command requires several input files that were not directly included by HCP among them are orig.mgz, brain.mgz, norm.mgz, nu.mgz, lh.volume, rh.volume, lh.area.pial, rh.area.pial, lh.area.mid,

rh.area.mid, lh.orig, rh.orig, lh.curv.pial, rh.curv.pial, lh.smoothwm, rh.smoothwm, rh.cortex.label, lh.cortex.label.

8. Supplementary Figures

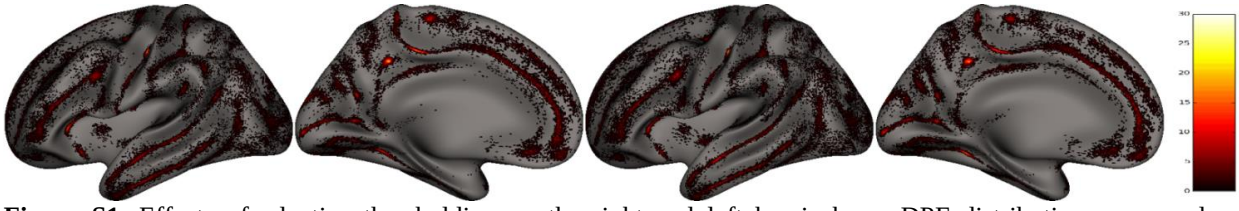

Figure S1. Effects of adaptive thresholding on the right and left hemispheres DPF distributions per areal. Compare with **Figure 1.a** we observe less pits on the gyri.

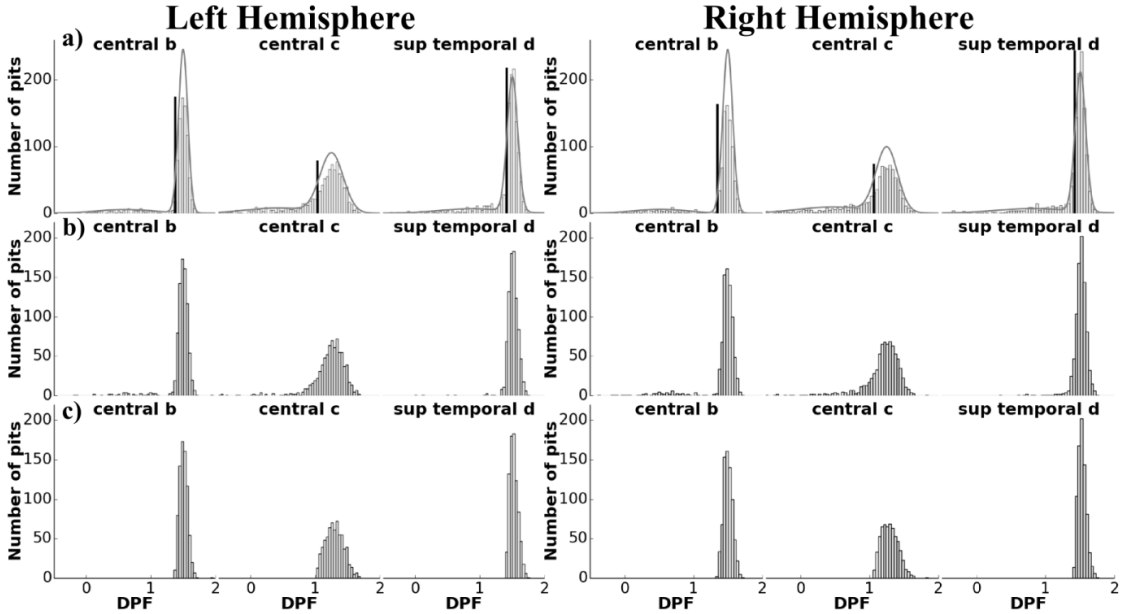

Figure S2. (a) Thresholding procedure on all pits DPF per areal in each hemisphere. **(b)** Phenotypes when selecting the deepest pit for each individual. **(c)** Phenotypes when thresholding and then selecting the deepest pit.

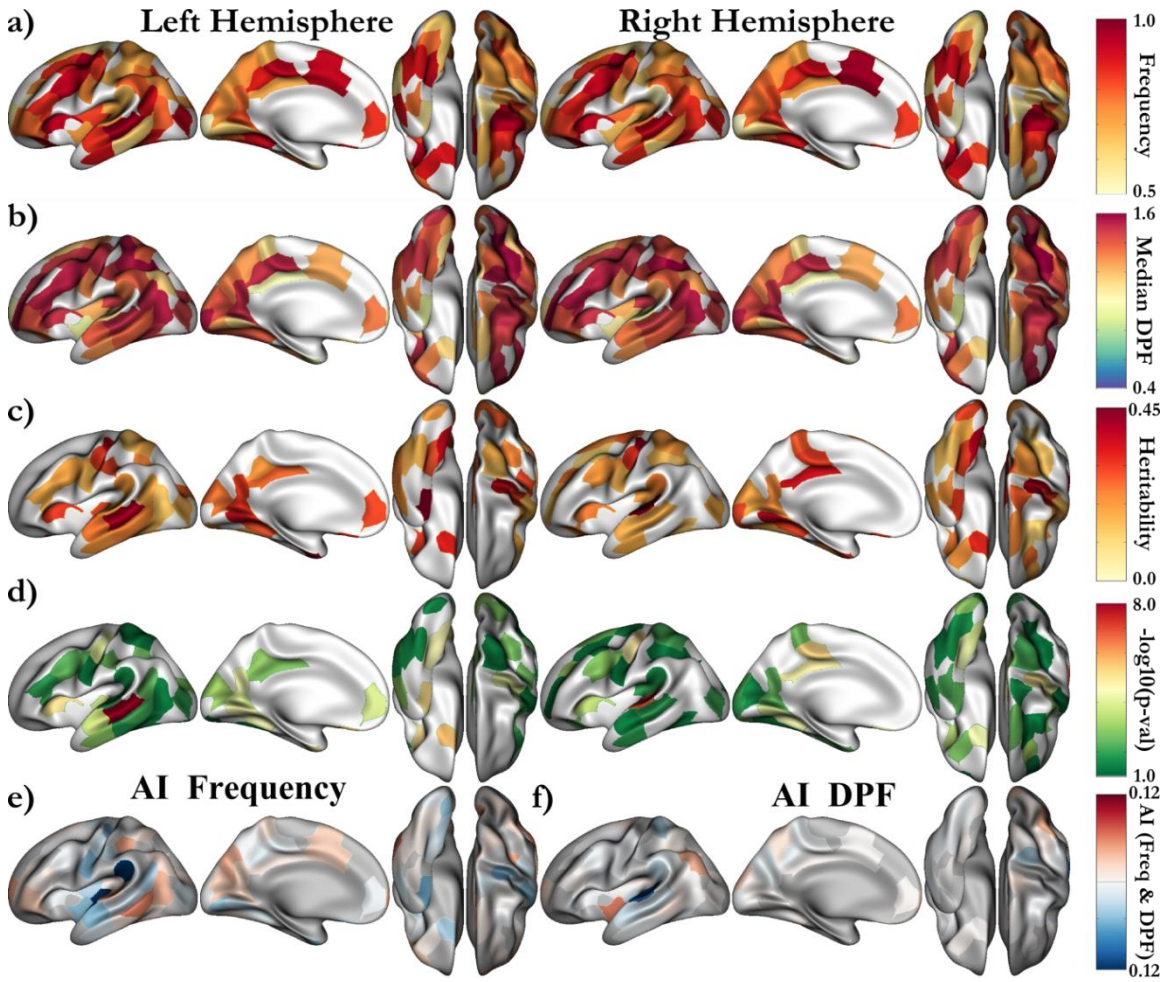

Figure S3. Results similar as the ones **Figure 3**, except that the distribution of pits has been thresholded in each areal. Therefore, it corresponds to the case of phenotype **Figure 2.c** rather than **Figure 2.b**. **(a)** Deep pits frequency and **(b)** median DPF of the pits selected as phenotypes in each areal. **(c)** Heritability and **(d)** associated –log10(p-values) for all the areals being significant without correction ($p < 0.05$). The areals which are significant after strict Bonferroni are shown with a color above yellow. **(e)** Asymmetry Index frequency. **(f)** Asymmetry Index median DPF.

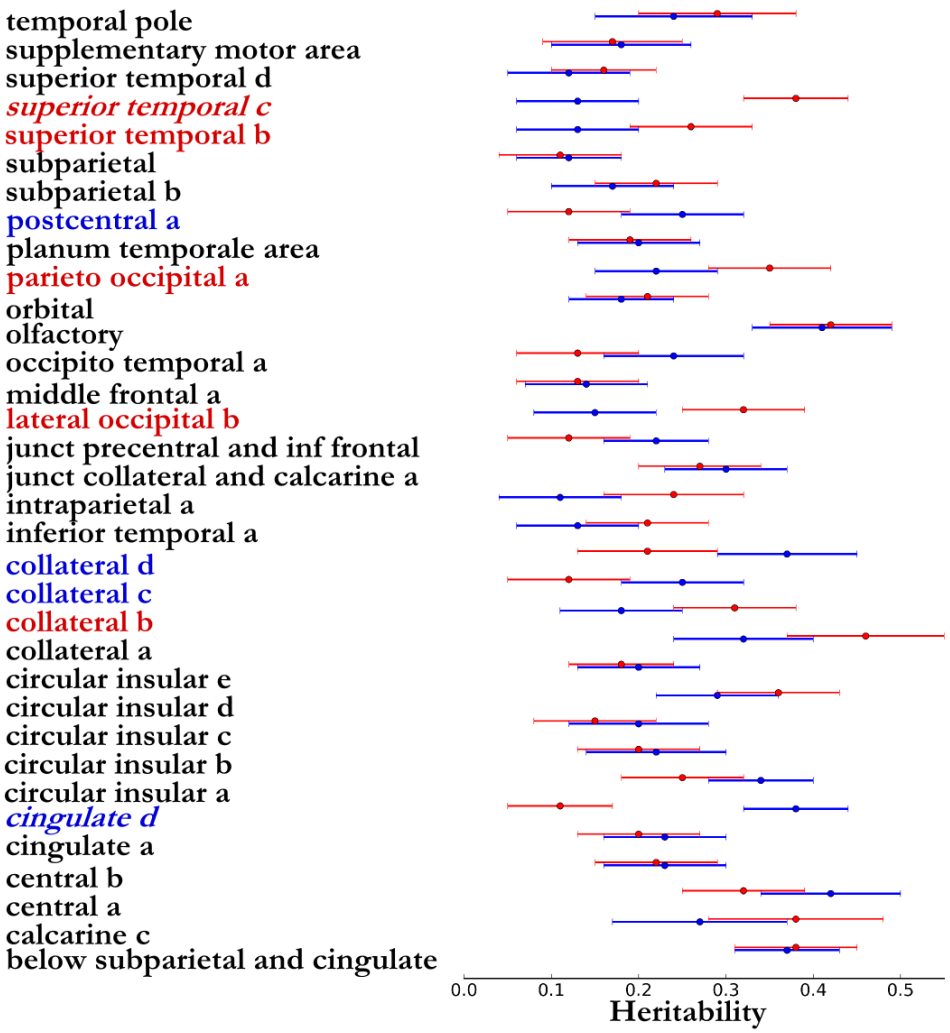

Figure S4. Heritability estimates and 1σ confidence intervals (67%) for all areals having an associated p-value < 0.05 on both sides. The red corresponds to the left hemisphere heritability estimates and the blue to the right hemisphere. The heritability estimates significantly asymmetric at approximately 1σ are in color (red for left asymmetry, blue for right asymmetry) and significant at 2σ are in italic.

9. Supplementary Tables

Table S1. Results of the additive analysis for the DPF of the pits in the *left hemisphere*, including the heritability estimates (h^2column) and associated p-values for each of the five covariates. Only results significant at $p < 0.05$ are displayed. Traits nomenclature is defined Figure 1.d.

Trait	h^2±SE (p)	Age	Age^2	Sex	Ag*Sx	Ag^2*Sx	Ethni	h^2_{cov}(%)	Sbj
		p-val							
below subparietal and cingulate	0.38±0.07 ($2.0\cdot10^{-7}$)	0.13	0.47	0.09	0.94	0.48	0.83	0.7	757
calcarine c	0.38±0.1 ($1.3\cdot10^{-4}$)	0.03	0.74	0.64	0.03	0.82	0.72	1.4	527
central a	0.32±0.07 ($4.2\cdot10^{-6}$)	0.93	0.5	$3.9\cdot10^{-3}$	0.69	0.18	0.22	1.2	674
central b	0.22±0.07 ($5.5\cdot10^{-4}$)	0.54	0.89	0.21	0.46	0.14	0.16	0.0	746
cingulate a	0.2±0.07 ($9.8\cdot10^{-4}$)	0.26	0.28	0.32	0.51	0.99	0.03	0.8	790
cingulate d	0.11±0.06 (0.03)	0.33	0.19	$1.0\cdot10^{-6}$	0.81	0.86	0.65	5.9	803
circular insular a	0.25±0.07 ($7.7\cdot10^{-5}$)	0.34	0.19	$9.7\cdot10^{-4}$	0.35	0.39	$2.1\cdot10^{-4}$	3.6	776
circular insular b	0.2±0.07 ($2.4\cdot10^{-3}$)	0.27	0.16	0.04	0.75	0.22	0.88	1.9	746
circular insular c	0.15±0.07 (0.01)	0.02	0.39	0.4	0.12	0.67	0.69	0.6	759
circular insular d	0.36±0.07 ($4.8\cdot10^{-8}$)	0.64	0.81	0.19	0.5	0.37	0.12	0.0	807
circular insular e	0.18±0.06 ($1.8\cdot10^{-3}$)	0.91	0.74	0.06	0.22	0.99	0.13	0.7	788
collateral a	0.46±0.09 ($1.2\cdot10^{-6}$)	0.42	0.37	0.05	0.75	0.41	0.17	0.2	545
collateral b	0.31±0.07 ($1.5\cdot10^{-6}$)	0.66	0.98	0.36	0.9	0.38	0.53	0.0	788
collateral c	0.12±0.07 (0.04)	0.16	0.58	0.92	0.08	0.44	0.58	0.2	697
collateral d	0.21±0.08 ($4.8\cdot10^{-3}$)	0.77	0.85	0.55	0.48	0.15	0.36	0.0	656
inf temporal a	0.21±0.07 ($5.5\cdot10^{-4}$)	0.01	0.88	0.24	0.22	0.73	0.21	1.4	775
inf temporal c	0.14±0.07 (0.02)	0.7	0.76	0.39	0.63	0.27	0.44	0.0	712
intraparietal a	0.24±0.08 ($7.0\cdot10^{-4}$)	0.65	0.71	0.08	0.64	0.97	0.66	0.8	744
intraparietal b	0.15±0.07 (0.01)	0.18	0.68	0.08	0.72	0.06	0.38	2.7	753
junct collateral and calcarine a	0.27±0.07 ($1.3\cdot10^{-4}$)	0.29	0.29	0.38	0.51	0.23	0.19	0.0	675
junct precentral and inf frontal	0.12±0.07 (0.04)	0.11	0.37	0.63	0.65	0.64	0.87	0.0	797
junct sup frontal and precentral	0.11±0.07 (0.05)	0.25	0.77	0.03	0.16	1.0	0.14	1.2	790
lateral occipital b	0.32±0.07 ($5.8\cdot10^{-6}$)	0.22	0.27	0.46	0.54	0.18	0.33	0.0	714
mid frontal a	0.13±0.07 (0.02)	0.34	0.32	0.81	0.81	0.23	0.04	0.4	768
occipito temporal a	0.13±0.07 (0.03)	0.68	0.97	0.76	0.43	0.4	0.07	0.5	741
occipito temporal b	0.19±0.07 ($2.3\cdot10^{-3}$)	0.68	0.2	0.29	0.66	0.44	0.64	0.0	803
olfactory	0.42±0.07 ($2.9\cdot10^{-9}$)	0.43	0.77	0.07	0.14	0.84	0.14	0.9	742
orbital	0.21±0.07 ($1.5\cdot10^{-3}$)	0.97	0.7	0.71	0.44	0.56	0.04	0.7	779
parieto occipital a	0.35±0.07 ($1.0\cdot10^{-7}$)	0.48	0.46	0.18	0.67	0.87	0.39	0.0	728
planum parietale	0.22±0.07 ($8.4\cdot10^{-4}$)	0.14	0.43	0.96	0.45	0.29	0.6	0.0	717
planum temporale area	0.19±0.07 ($2.5\cdot10^{-3}$)	0.12	0.58	$1.9\cdot10^{-3}$	0.36	0.81	0.87	2.3	718
postcentral a	0.12±0.07 (0.03)	0.7	0.19	0.56	0.73	0.24	0.3	0.0	702
subparietal	0.22±0.07 ($2.9\cdot10^{-4}$)	0.51	0.66	0.33	0.55	0.23	0.14	0.0	780
subparietal b	0.11±0.07 (0.04)	0.3	0.8	0.44	0.55	0.73	0.53	0.0	751
sup temporal b	0.26±0.07 ($3.6\cdot10^{-5}$)	0.4	0.17	0.94	0.21	0.62	0.08	0.4	763
sup temporal c	0.38±0.06 ($3.6\cdot10^{-10}$)	0.7	0.77	1.0	0.57	0.34	0.64	0.0	803
sup temporal d	0.16±0.06 ($5.4\cdot10^{-3}$)	0.17	0.59	0.02	0.06	0.73	$5.7\cdot10^{-3}$	2.1	782

supplementary motor area	0.17±0.08 (0.02)	0.71	0.49	0.16	0.37	0.88	0.94	0.0	653
supra marginal gyrus	0.2±0.07 ($2.4\cdot10^{-3}$)	0.32	0.53	0.16	0.09	0.88	0.51	0.4	782
temporale pole	0.29±0.09 ($5.6\cdot10^{-4}$)	0.21	0.95	0.31	0.29	0.22	0.77	0.0	594

Table S2. Results of the additive analysis for the DPF of the pits in the *right hemisphere*, including the heritability estimates (h^2 column) and associated p-values for each of the five covariates. Only results significant at $p < 0.05$ are displayed. Traits nomenclature is defined Figure 1.d.

Trait	**h^2±SE (p)**	**Age**	**Age^2**	**Sex**	**Ag*Sx**	**Ag^2*Sx**	**Ethni**	**h^2_{cov}(%)**	**Sbj**
		p-val							
below subparietal and cingulate	0.37±0.06 ($1.3\cdot10^{-8}$)	0.57	0.25	0.14	0.35	0.6	$9.7\cdot10^{-3}$	1.2	756
calcarine a	0.21±0.07 ($1.4\cdot10^{-3}$)	0.25	0.82	0.38	0.16	0.83	0.35	0.0	761
calcarine b	0.14±0.07 (0.02)	0.53	0.65	0.26	0.2	0.87	0.04	0.6	752
calcarine c	0.27±0.1 ($3.1\cdot10^{-3}$)	0.98	0.43	0.5	0.89	0.66	0.83	0.0	521
central a	0.42±0.08 ($5.0\cdot10^{-7}$)	0.51	0.85	0.71	0.65	0.59	0.39	0.0	644
central b	0.23±0.07 ($5.1\cdot10^{-4}$)	0.3	0.25	$3.4\cdot10^{-4}$	0.51	0.39	0.15	2.8	713
central c	0.22±0.07 ($9.2\cdot10^{-4}$)	0.81	0.23	0.23	0.74	0.24	0.73	0.0	697
cingulate a	0.23±0.07 ($2.4\cdot10^{-4}$)	0.64	0.58	0.02	0.63	0.55	0.86	0.6	789
cingulate b	0.13±0.08 (0.05)	0.69	0.58	0.32	0.53	0.66	0.59	0.0	632
cingulate d	0.38±0.06 ($6.4\cdot10^{-11}$)	0.02	0.84	$5.7\cdot10^{-4}$	0.17	0.84	0.55	3.3	795
cingulate e	0.15±0.08 (0.04)	0.44	0.43	0.12	0.12	0.55	0.22	0.0	645
circular insular a	0.34±0.06 ($6.9\cdot10^{-9}$)	0.98	0.46	$1.5\cdot10^{-3}$	0.88	0.35	$2.1\cdot10^{-3}$	5.2	809
circular insular b	0.22±0.08 ($2.2\cdot10^{-3}$)	0.13	0.49	$6.7\cdot10^{-3}$	0.95	0.64	0.77	1.0	679
circular insular c	0.2±0.08 ($3.6\cdot10^{-3}$)	0.54	0.75	0.27	0.23	0.2	0.2	0.0	758
circular insular d	0.29±0.07 ($7.3\cdot10^{-6}$)	0.35	0.34	$1.8\cdot10^{-4}$	0.13	0.78	0.62	2.9	800
circular insular e	0.2±0.07 ($9.5\cdot10^{-4}$)	0.46	0.68	0.56	0.49	0.88	0.83	0.0	766
collateral a	0.32±0.08 ($5.1\cdot10^{-5}$)	0.13	0.27	$4.8\cdot10^{-3}$	0.04	0.07	0.93	1.6	542
collateral b	0.18±0.07 ($2.5\cdot10^{-3}$)	0.26	0.15	0.57	0.15	0.63	0.02	1.0	786
collateral c	0.25±0.07 ($2.7\cdot10^{-4}$)	0.76	0.78	$3.1\cdot10^{-4}$	0.39	0.08	0.17	2.2	721
collateral d	0.37±0.08 ($2.6\cdot10^{-6}$)	0.14	0.29	0.71	0.1	0.71	0.09	0.6	646
inf frontal a	0.17±0.07 ($3.9\cdot10^{-3}$)	0.25	0.44	0.76	0.33	0.21	0.07	0.4	786
inf temporal a	0.13±0.07 (0.03)	0.1	0.1	0.27	0.36	0.18	0.78	0.3	760
inf temporal d	0.13±0.07 (0.03)	$4.5\cdot10^{-3}$	0.1	0.04	$9.9\cdot10^{-4}$	0.39	0.44	1.7	769
intraparietal a	0.11±0.07 (0.05)	0.22	0.25	0.02	0.26	0.69	0.12	1.2	746
intraparietal c	0.22±0.07 ($6.6\cdot10^{-4}$)	0.86	0.27	0.13	0.18	0.67	0.19	0.0	724
junct collateral and calcarine a	0.3±0.07 ($1.2\cdot10^{-5}$)	0.09	0.64	0.01	0.07	0.75	0.61	2.2	689
junct precentral and inf frontal	0.22±0.06 ($3.0\cdot10^{-4}$)	0.43	0.41	0.64	0.49	0.77	0.74	0.0	801
lateral occipital b	0.15±0.07 (0.01)	0.48	0.61	0.12	0.55	0.34	0.88	0.0	708
mid frontal a	0.14±0.07 (0.02)	0.79	0.79	0.53	0.5	0.76	0.71	0.0	771
mid frontal b	0.2±0.07 ($2.5\cdot10^{-3}$)	0.17	0.4	0.29	0.41	0.17	0.97	0.0	676
occipito temporal a	0.24±0.08 ($7.9\cdot10^{-4}$)	$9.4\cdot10^{-4}$	$7.7\cdot10^{-5}$	0.2	$7.4\cdot10^{-3}$	0.04	0.02	2.9	738
olfactory	0.41±0.08 ($2.0\cdot10^{-7}$)	0.12	0.49	$7.0\cdot10^{-6}$	0.19	0.26	0.05	4.0	726
orbital	0.18±0.06 ($1.8\cdot10^{-3}$)	0.75	0.43	0.71	0.48	0.98	0.1	0.5	790
parieto occipital a	0.22±0.07 ($6.4\cdot10^{-4}$)	0.85	0.54	0.14	0.9	0.13	0.76	0.0	744
parieto occipital b	0.17±0.07 ($6.9\cdot10^{-3}$)	0.15	0.48	0.28	0.55	0.88	0.41	0.0	745

planum temporale area	0.2±0.07 ($2.3\cdot10^{-3}$)	0.43	0.12	$2.8\cdot10^{-4}$	0.07	0.23	0.22	2.3	731
postcentral a	0.25±0.07 ($1.8\cdot10^{-4}$)	0.79	0.67	0.5	0.31	0.7	0.97	0.0	710
postcentral a bis	0.13±0.07 (0.02)	0.54	0.61	0.57	0.84	0.5	0.16	0.0	716
postcentral b	0.14±0.07 (0.02)	0.15	0.27	0.07	0.06	0.9	0.71	1.2	668
postcentral c	0.21±0.08 ($4.4\cdot10^{-3}$)	0.79	0.09	0.33	0.23	0.38	0.07	1.3	642
precentral	0.23±0.08 ($2.8\cdot10^{-3}$)	0.35	0.29	0.15	0.3	0.01	0.67	0.7	624
subparietal	0.17±0.07 ($6.5\cdot10^{-3}$)	0.18	0.23	0.7	0.11	0.79	0.1	0.4	754
subparietal b	0.12±0.06 (0.03)	0.69	0.34	0.43	0.39	0.42	0.88	0.0	751
sup frontal b	0.17±0.07 ($9.3\cdot10^{-3}$)	0.78	0.49	0.05	0.78	0.75	0.79	0.8	745
sup temporal a	0.2±0.12 (0.05)	0.08	0.31	0.21	0.2	0.81	0.16	0.7	434
sup temporal b	0.13±0.07 (0.04)	0.09	0.08	0.71	0.03	0.22	0.22	0.7	760
sup temporal c	0.13±0.07 (0.03)	$2.2\cdot10^{-3}$	0.72	0.59	0.03	0.86	0.24	1.6	806
sup temporal d	0.12±0.07 (0.03)	0.64	0.69	0.25	0.49	0.9	$5.4\cdot10^{-3}$	0.9	762
supplementary motor area	0.18±0.08 (0.01)	0.78	0.98	0.1	0.88	0.54	0.85	0.4	642
temporale pole	0.24±0.09 ($2.5\cdot10^{-3}$)	$4.2\cdot10^{-3}$	0.28	0.05	0.07	0.44	$3.3\cdot10^{-3}$	4.1	589

Chapter 2. The Morphology of the Left Superior Temporal Sulcus is Genetically Constrained

1. Introduction to the chapter

In the previous chapter, we automatically extracted the sulcal pits in a large cohort and estimated their DPF heritability. We found that the heritability of the sulcal pits in the superior temporal areals were particularly asymmetric with a higher genetic contribution to the phenotypic variance in the left hemisphere. This region approximately corresponds to the one identified by Leroy et al. (2015) as containing the STS depth human-specific asymmetry.

In this chapter, we investigated the concrete cause of this asymmetry and proposed to automatically extract an anatomical marker, which can be used in future genetic studies with ten or hundred thousand of individuals. This anatomical structure, a bump in the cortex named *pli de passage* (PP), is a transverse gyrus that separates the sulcus into two parts. It was reported to be more frequent in the left STS than in the right. In this study, we replicated this observation in a cohort of 820 subjects and we extrapolated our extraction to other sulci than the STS to compare with their PP asymmetry. Finally, we estimated the genetic influence on the formation of this structure.

2. Abstract

The asymmetry of the superior temporal sulcus (STS) has been identified as a species-specific feature of the human brain. The so-called superior temporal asymmetrical pit (STAP) area is observed from the last trimester of gestation onwards and is far less pronounced in the chimpanzee brain. This asymmetry is associated with more frequent sulcal interruptions, named *plis de passage* (PPs), leading to the irregular morphology of the left sulcus. In this chapter, we aimed to characterize the variability, asymmetry, and heritability of these interruptions in the STS in comparison with the other main sulci. We developed an automated method to extract PPs across the cortex based on a highly reproducible grid of sulcal pits across individuals, which we applied to a subset of Human Connectome Project (HCP) subjects (N = 820). We report that only a few PPs across the cortex are genetically constrained, namely in the collateral, postcentral and superior temporal sulci and the calcarine fissure. Moreover, some PPs occur more often in one hemisphere than the other, namely in the precentral, postcentral, intraparietal sulci, as well as in both inferior and superior temporal sulci. Most importantly, we found that only the interruptions within the STAP region are both asymmetric and genetically constrained. Because this morphological pattern is located in an area of the left hemisphere related to speech, our results suggest structural constraints on the architecture of the linguistic network.

3. Introduction

Since hemispheric asymmetry might contributes to some human specific functions (Toga and Thompson, 2003), a better description of interhemispheric differences in the brain might shed light on human specificity. Recently, it has been shown that the superior temporal sulcus (STS) is deeper in the right hemisphere in most humans irrespective of their age, sex, or handedness, whereas this asymmetry is hardly observed in chimpanzees (Leroy et al., 2015). The location of this asymmetry might make it a macroscopic marker of the brain changes allowing for language and social cognition in our species (DeWitt and Rauschecker, 2012; Frith and Frith, 2007; Pelphrey et al., 2004). Therefore, we aimed to further describe this asymmetry considering not only the depth of this sulcus but also its sulcal interruptions. These interruptions are more frequent in the left sulcus and thus contribute to the interhemispheric difference reported in this sulcus (Leroy et al., 2015; Ochiai et al., 2004).

A sulcal interruption or *pli de passage* (PP) occurs when a transverse gyrus connects the two gyri bordering the sulcus (Gratiolet, 1854). It may potentially interrupt every primary and secondary sulcal structure across the brain. Hardly described in brain atlases, they are reported only when the transverse gyrus is superficial and breaks the sulcus into parts (full interruption) (Ono et al., 1990). However, a PP is often invisible in external views of the cortex when it is buried in the depth of the sulcus. It causes a local elevation of the sulcus floor and hence a decrease in the sulcal depth. PPs are commonly considered as tertiary folds, highly variable, related to the chaotic morphology of sulci, and therefore likely not inherited. However, this assumption could be questioned if one considers the number of sulcal interruptions across brains (Ono et al., 1990), notably in the STS (Ochiai et al., 2004) as well as in the precentral and intraparietal sulci (Zlatkina and Petrides, 2014, 2010). Some authors have also attributed a functional significance to some of these PPs, such as a relation between reading performance and PPs in the occipito-temporal sulcus (Borst et al., 2016). Thus, in this chapter, we challenged the view of PPs being highly variable tertiary folds and asked whether PPs can be robust landmarks, in particular in the STS and possibly other sulci of the human brain.

Moreover, we also assessed the heritability of PPs in the STS. Gyrification is a heritable trait in primates (Rogers et al., 2010). Kochunov et al. (2010) pinpointed that cortical anatomy is heritable in an extended pedigree of baboons and emphasized that the heritability of sulcal phenotypes might be modulated by the arcuate U-fiber systems. However, Gómez-Robles et al. (2015) underlined that heritability of cerebral cortical anatomy is less important in humans than in chimpanzees. Yet, we have shown that the heritability of sulcal pit depth is mostly symmetric in humans except in the STS (Le Guen et al., 2018a).

PPs are complex shapes difficult to match between subjects, due to the high variability of folding patterns in the cortex. To overcome this difficulty, Régis et al. (2005) developed a model of cortical gyrification based on indivisible units named sulcal pits (or roots), which correspond to the

first folding locations. Over the past few years, robust algorithms have been developed to extract these putative primary cortical folding locations (Auzias et al., 2015; Im et al., 2010). These points located at the maximum depth of a sulcal basin show less inter-subject variability than more superficial features and have been proposed as anatomical landmarks (Lohmann et al., 2008). Recent studies on fetal and perinatal MRI data support the assumption that early folding regions are less variable across subjects than other cortical regions (Dubois et al., 2008; Habas et al., 2012). Once sulcal pits are identified within an individual, PPs can then be detected and localized relative to them. Indeed, a sulcal interruption can be seen as a rapid variation in shape of the cortical surface between a pair of neighboring pits.

Thus, we first identified sulcal pits across the brain based upon our earlier study (Le Guen et al., 2018a). Then, we detected PPs between any pair of pits located in the same sulcus, as local variations in the fundus of the sulcus. A function was defined combining both depth and curvature parameters. PPs were considered present if this function reached a given threshold. We applied this method to the Human Connectome Project (HCP) dataset. This enabled us to see whether PPs are reproducible across a large set of individuals and if some are more frequent in one hemisphere or the other. Furthermore, we assessed the genetic control on the presence of PPs with the extended pedigree of 820 Caucasian individuals available in HCP. This pedigree information allowed us to estimate the phenotypic variance explained by the genes' additive effects.

4. Methods

4.1. Sulcal pits extraction and group areal definition

We extracted the sulcal pits from the white matter meshes of both hemispheres in the native space for each individual (Auzias et al., 2015; Le Guen et al., 2017) (**Fig. 1 a.**). The procedure first estimated the depth of each vertex on the surface using the depth potential function (DPF) (Boucher et al., 2009). The DPF is a scalar field corresponding to the signed traveled distance that quantifies how much a curve is bent inward or outward (i.e. average convexity). It represents the overall shape of a fold as the function whose Laplacian is as close as possible to the mean curvature (κ_{mean}) of the surface. $(\alpha I + \Delta)D_\alpha = 2\kappa_{mean}$, where D_α is the DPF field, α controls the decay rate of the curvature influence as we move further from a given point, and I and Δ represent the identity and Laplacian matrices, respectively. When α tends to infinity, the DPF tends to the mean curvature, when α tends to 0 the DPF tends to the average convexity, and for intermediate values of α, the DPF integrates both types of geometrical information. In this work, we used the default value of α: 0.03. Finally, for intermediate values of α, the DPF integrates both types of geometrical information. Thus, the DPF provides a regularized estimation of the depth of the folds and takes into account information from both convexity and curvature (see Auzias et al., 2015; Boucher et al., 2009 for implementation details). For each hemisphere, the DPF is estimated at each vertex of the white matter mesh resulting in a depth map to which we applied a filtered watershed algorithm to obtain the sulcal basins defined

from the local DPF maxima. After the extraction of pits at the individual level, we computed the symmetric group-level cluster regions as proposed in Auzias et al. (2015). The smoothed maps from both hemispheres were projected onto the left side of *fsaverage_sym*, and summed across subjects to obtain the group density map (**Fig. 1 b.**). From this density map, group-level clusters of pits denoted hereafter as "areals" were obtained by applying a watershed algorithm as detailed in Auzias et al. (2015) (**Fig. 1 c.**). Group sulcal pit areals were back-projected onto each subject's hemisphere thereby providing sulcal pit labelling consistent across individuals. The depth profile was then computed in the native space as described in the next section.

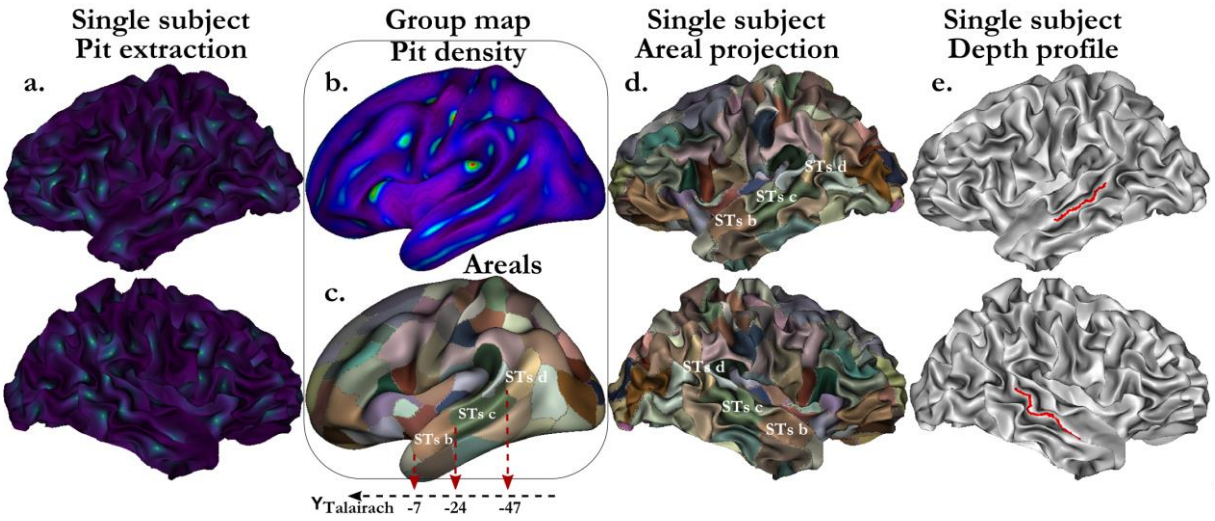

Fig. 1. Summary of the automated pipeline computing the STS depth profile, presented on HCP subject 100307 for "Single subject" steps and on *fsaverage_sym* for the "Group map". First, the sulcal pits of all subjects are extracted on the cortical surface. Individual smooth pit maps (**a.**) are projected and summed on the symmetric template to obtain the population pit density (**b.**). Areal boundaries (**c.**) are computed with a watershed on the density map. Then, these areals are projected onto each subject's white matter mesh (**d.**). The deepest pits in the areals identified as STs b and STs d, are used as start and end points of the geodesic path following the bottom of the STs. STAP depth profile (**e.**) is then truncated at the border between STs c and d.

4.2. Automated sulcal depth profile extraction

We propose a method to automatically extract the sulcal depth profile (SP). The sulcal fundus is the shortest path on the white matter mesh following the extremal values of the DPF between two extremity points. Such a definition of sulcal fundi has been proposed by Shattuck et al. (2009) and successfully used in Le Troter et al. (2012). They proposed to extract the shortest path between the two extremities on the surface, such as sulcal depth. We used their implementation in our current work. Additionally, we defined the geodesic depth on the white matter mesh as the geodesic distance to the ridges on the crown of gyri in contact with the brain hull (Rettmann et al., 2002). Then, we defined two sulcal depth profiles SP_{DPF} and SP_{GD} representing the DPF and geodesic depth of the vertices along the sulcal fundus geodesic path, respectively.

Our implementation of the sulcal fundus extraction relies on the identification of two extremities, which cannot be performed manually on large datasets such as HCP. In the absence of a

clear definition of the concept of sulcal line extremity, this identification is complex, and inter-individual correspondence is difficult to achieve. In order to provide consistent pairs of extremities able to be defined for each subject, we extended this framework by setting two sulcal pits in specifically chosen areals as the extremities of the sulcal fundus. It is worth emphasizing that we did not extract the SP_{DPF} (and the SP_{GD}) of the whole sulcus but only for a particular segment between these two sulcal pits. As suggested by previous literature (Im et al., 2010; Lohmann et al., 2008; Meng et al., 2014), we assumed anatomical correspondence between the sulcal pits across individuals, which was key to automatizing the SP extraction in a cohort as large as the HCP. In particular, the sulcal pit extraction algorithm proposed in Auzias et al. (2015) is designed to optimize this inter-subject correspondence. Prior to extracting the SP on the native meshes, all areals were projected from the group map onto the subject white matter meshes (left and right) through spherical inter-hemispheric registration (**Fig. 1 d.**). The group areals represent cluster regions with a high group density of pits. Each group areal name was based on previous literature (Im et al., 2010; Le Guen et al., 2018a; Meng et al., 2014)). **Fig. 2** displays the group areal nomenclature for the main sulci. The individual sulcal pits lying in these areals were then automatically identified, and the two deepest pits were used as extremities of the sulcal fundus. In the rare case (<10%) for which one subject had no deep pit in a group areal, the vertex with the maximum DPF was chosen (see **SFig. 1** for an example).

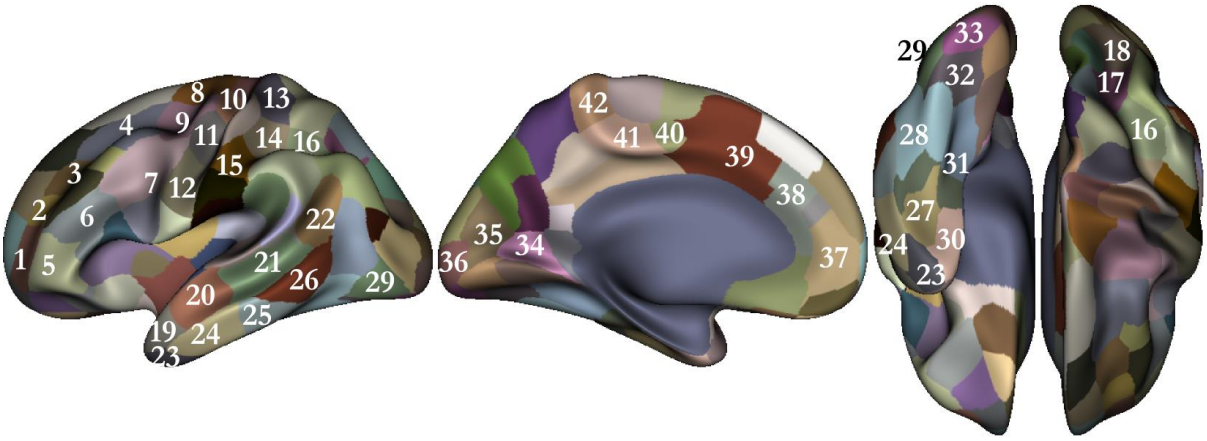

Fig .2. Areal nomenclature: 1 sup frontal a, 2 sup frontal b, 3 sup frontal c, 4 sup frontal d, 5 inf frontal a, 6 inf frontal b, 7 inf frontal c, 8 precentral a, 9 precentral b, 10 central a, 11 central b, 12 central c, 13 postcentral a, 14 postcentral b, 15 postcentral c, 16 intraparietal a, 17 intraparietal b, 18 intraparietal c, 19 sup temporal a, 20 sup temporal b, 21 sup temporal c, 22 sup temporal d, 23 inf temporal a, 24 inf temporal b, 25 inf temporal c, 26 inf temporal d, 27 occipito-temporal a, 28 occipito-temporal b, 29 occipito-temporal c, 30 collateral a, 31 collateral b, 32 collateral c, 33 collateral d, 34 calcarine a, 35 calcarine b, 36 calcarine c, 37 cingulate a, 38 cingulate b, 39 cingulate c, 40 cingulate d, 41 cingulate e, 42 cingulate f.

We illustrate here the sulcal depth profile extraction process for the STS and, more precisely, in the STAP (Superior Temporal Asymmetrical Pit) area described by Leroy et al. (2015). This sulcus is of particular interest it is consistently deeper in the right hemisphere compared to the left. On the areal group map (Fig. 1), areals corresponding to STS b, c, d were identified as regions 20, 21, 22 in **Fig. 2**. The STAP includes the areals STS c and partly STS b, according to the Talairach coordinates

provided in Leroy et al. (2015), y_{STAP} is between y ≈ -8;-12 to -42;-45. Thus, we extracted the SP_{DPF} and SP_{GD} between the deepest points in STS b and d, since pits b and d are the closest anterior and posterior landmarks, respectively. We truncated it at the border between areals STS c and d, since pit d in the right hemisphere was located posteriorly to the STS in approximately 15% of subjects. Localization errors were mainly due to a slightly shorter STS in this hemisphere compared to the left one. Furthermore, since the coronal coordinate of the border between areals STS c, d is -47 in Talaraich space, it well matched the posterior coordinate of the STAP region. This last remark enabled us to benchmark our method on the data in which the PPs were manually annotated PP from Leroy et al. (2015) by considering a segment as similar as possible to the one they reported.

4.3. Pli de passage detection applied in the superior temporal sulcus

Visual inspection of the data revealed that the left STS is often segmented in smaller sections by PPs. To extract the PPs, one method would consist in computing a watershed on the reverse depth map compared to the one used to identify the sulcal pits. However, the PPs might be difficult to disentangle from the noise of adjacent gyri. The second option would be to extract PPs from the sulcal depth profiles computed between the sulcal pits (used as the extremities of the sulcal fundus), as these are more stable across individuals. It should be noted that for the SP_{DPF} and SP_{GD} functions, peaks correspond to the maximum depth while low valleys represent PPs. Valleys were detected as local minima along sulcal depth profiles (**Fig 3.**) with a constraint on both the minimum gap between two valleys and minimum DPF height of the valley floor. In order to assess the best threshold of the minimum SP_{DPF} in the STAP, we measured the SP_{DPF} minima in all valleys computed across all subjects to establish its empirical distribution. This distribution was fit with a mixture of two Gaussians with low and high SP_{DPF} values corresponding to PPs and noise in the depth profiles, respectively (**SFig. 2**). Noise was removed using a standard 3σ threshold from the high Gaussian distribution (true PPs have $SP_{DPF} \leq 0.42$).

To improve detection, we also used SP_{GD} to assess how superficial a PP is. To set a threshold on the SP_{GD} and evaluate the pertinence of the SP_{DPF} one, we assessed our recognition method on manually labelled data outside the HCP from (Leroy et al., 2015). With SP_{DPF} and SP_{GD} thresholds set at 0.42 and 13 mm, respectively, we obtained a concordance of 80% between the reported presence/absence of PP in the STAP of 98 individuals (196 hemispheres).

To assess the robustness of these ad hoc parameters, we estimated the accuracy, sensitivity and specificity of our method using a grid of threshold parameters ($SP_{DPF} \times SP_{GD}$, with SP_{DPF} varying from -0.5 to 1.0, and SP_{GD} from 5.0 mm to 20.0 mm) on the previous 196 hemisphere dataset. The maximum accuracy (82%) was obtained with SP_{DPF} = 0.08 and SP_{GD} = 11.8 mm as thresholds. The accuracy slightly increased as compared to the previous set of parameters, and we noticed that the sensitivity decreased from 50% to 40.5%, while the specificity increased from 64.1% to 75% (**SFig.**

3). Overall, setting the SP_{DPF} threshold in the range 0 to 0.5 gave similar accuracy and a reasonable trade-off between sensitivity and specificity.

Furthermore, we looked into the causes of discordant cases and found that they were mostly due to two reasons. First, our delimitation of the STAP was sometimes longer or shorter than the reference. This is particularly difficult to reproduce in an automated process due to the manual identification of the planum landmark used in (Leroy et al., 2015). Secondly, some cases seemed to have been manually misidentified due to a slightly different procedure used at the time of identification with Brainvisa (Mangin et al., 2015; Perrot et al., 2011). After visual inspection of the PP detection in the HCP dataset, the first set of parameters (SP_{DPF} = 0.42 and SP_{GD} = 13) mm was chosen and proved to extract the PPs robustly.

To summarize, PPs were extracted in three steps: (i) extraction of the sulcal fundus between two extremal sulcal pits in a chosen sulcus; (ii) extraction of the sulcal depth profile along the sulcal fundus; (iii) detection of the PP when the sulcal depth profile reached a minimum DPF and geodesic depth value as previously defined.

4.4. Definition of sulcal depth profile extremities to extract the plis de passage

Plis de passage can be extracted between any pair of adjacent sulcal pits (i.e. located in adjacent group sulcal basins) using the corresponding two sulcal pits as extremities of the sulcal depth profile. Indeed, in the sulcal pit theory, two adjacent sulcal pits in a sulcus are separated by a more or less visible bump (PP) between the two. Our approach was dedicated to identifying the bumps that were prominent enough to create a significant interruption of the sulcus. Thus, the extraction of PPs previously described for the STAP was also able to be applied to several major sulci provided that pairs of sulcal pits were able to be used as sulcal fundus extremities. We analyzed the superior and inferior frontal, the precentral, the central, the postcentral, the intraparietal, the superior and inferior temporal, the occipito-temporal, the collateral, the calcarine and the cingulate sulci (**Fig. 2**). We restricted our analysis to these sulci as they are composed of at least two adjacent areals, even though some of their segmentations, such as for the occipito-temporal sulcus, could have been manually improved.

4.5. Quantifying the hemispheric asymmetry of plis de passage

Table 1. **Contingency table use for the Fisher exact test to quantify pli de passage asymmetries**. L0 R1: number of subjects with a PP solely on the right; L1 R0: number of subjects with a PP only on the left; L0 R0: number of subjects without PPs; L1 R1: number of subjects with a PP in both hemispheres. This test statistically assesses whether there is an asymmetric preference towards one hemisphere.

	Asymmetric configurations	**Symmetric configurations**
Nb of subjects with no PP on the left	L0 R1	L0 R0
Nb of subjects with PPs on the left	L1 R0	L1 R1

We defined the asymmetry of plis de passage as: Asym = L – R, where L and R are the percentage of plis de passage in the left and right hemispheres, respectively. We studied the asymmetry of PPs using the Fisher exact test, with **Table 1** as contingency table.

4.6. Comparison with an existing method: vertex-wise asymmetry using a symmetric template

We compared our result with a vertex-wise approach to detect the asymmetries of Freesurfer cortical thickness and sulcal depth (Chiarello et al., 2016; Fischl, 2012; Maingault et al., 2016; Toga and Thompson, 2003). We projected all individuals' hemispheres onto the left hemisphere of the symmetrical template and performed a t-test between the value at each vertex, considering the distribution to be independent across hemispheres. As opposed to sulcal depth, cortical thickness was not directly linked to our PP analysis; however, this enabled us to verify if the HCP cohort and our vertex-wise analysis method allowed us to identify the asymmetries already reported in the literature.

4.7. Relationship between intracranial volume and plis de passage in the STAP

Larger brains are known to be more folded (Germanaud et al., 2012; Toro et al., 2008). Thus, we studied to what extent the presence of a PP in the STAP is related to brain volume. We assessed the potential link between the recognition of a PP and brain volume, approximated by the Freesurfer estimated total intracranial volume (eTIV), using the Mann Whitney statistical test. In addition, we added the eTIV as a covariate in our heritability analysis to assess its significance.

5. Results

5.1. Asymmetry of plis de passage in the STAP

We extracted the sulcal pits, the depth profile, and *plis de passage* in the STS area in 820 subjects of the HCP cohort using the sulcal pits as anatomical landmarks. **Fig. 3** displays four typical depth profiles observed in the STAP. Our results show that most subjects (48.7%) had at least one PP solely in the left STS, while few (11.2%) had this configuration only in the right STS. When a PP was detected only in the right hemisphere, it mostly lied at the junction between the STS main horizontal branch and its caudal branch. Remaining subjects had a roughly symmetric STS organization with either no PPs on either side (33.8%) or one PP on each side (6.3%).

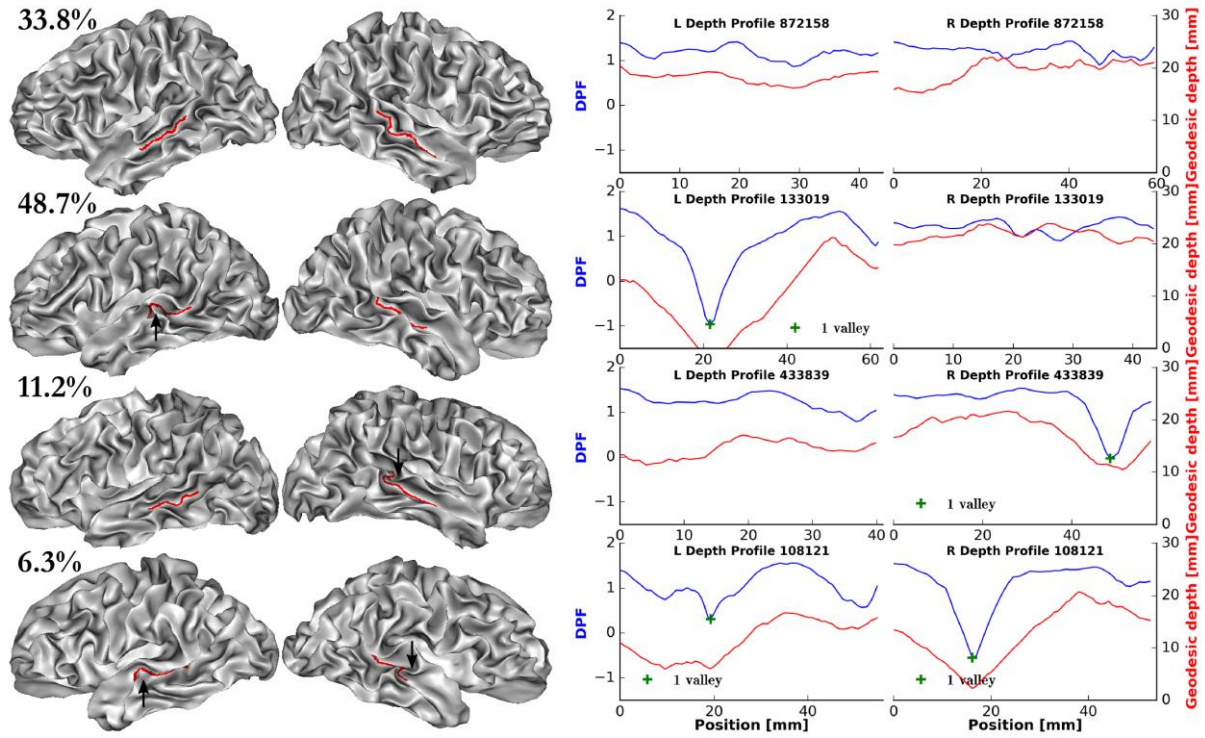

Fig. 4. Typical STAP patterns with either symmetric STAP with no PPs on either side (1st line: 33.8% of HCP Caucasians subjects) or one PP on each side (4th line: 6.3%), or asymmetric STAP with only one PP on the left (2nd line: 48.7%) or on the right (3rd line: 11.2%). The associated depth profiles in the STAP are shown on the right of the figure. Black arrows indicate the pli de passage position on the mesh. The subjects' white matter meshes have been slightly inflated and smoothed to allow a clearer view of the extracted geodesic path. **SFig. 11** shows the average depth profile in the STAP for each configuration.

5.2. Extrapolation of pli de passage detection to quantify asymmetries

We applied our previously described PP detection method between any two adjacent pits in other sulci (see section Definition of sulcal depth profile extremities to extract the plis de passage). Compared to the 42.3% asymmetry of the STAP, all segments had lower asymmetries of PP, and most of them were almost symmetric in terms of PP frequency (**Fig. 4, Table 2**). Six segments were nevertheless found significantly asymmetric according to the Fisher exact test. They included the STS segments (b, c, asym PP = +25.9%) and (c, d, +20.5%), whose combination partly corresponds to the asymmetry of the STAP. Other asymmetric sulci segments consisted of the inferior temporal (a, b, +11%), intraparietal (a, b, -15.4%), postcentral (a, b +26%), and precentral (a, b, -13%) sulci. Our results also emphasize the generally continuous aspect of the central sulcus with few prominent PPs identified (about 3-4% on each hemisphere for the central sulcus in two segments). It should be noted the well-known PP roughly corresponding to the hand area in the central sulcus is most often deeply buried in the sulcus and was thus not detected by our analysis.

Table 2. Pli de passage configuration percentages in all considered segments between any two adjacent of pits in the main sulci. Numbers within parentheses correspond to nomenclature Fig 2. An asym > 0 corresponds to L > R.

	Asym PP	p-val	L PP	R PP
calcarine a b (34, 35)	-1.3%	0.76	26.2%	27.6%
calcarine b c (35, 36)	-2.2%	0.42	48.3%	50.5%
central a b (10, 11)	0.1%	1.0	3.7%	3.5%
central b c (11, 12)	0.2%	1.0	3.9%	3.7%
cingulate a b (37, 38)	7.9%	0.02	63.7%	55.7%
cingulate b c (38, 39)	3.4%	0.38	48.0%	44.6%
cingulate c d (39, 40)	-5.7%	0.11	42.7%	48.4%
cingulate d e (40, 41)	-3.9%	0.23	6.0%	9.9%
cingulate e f (41, 42)	-2.8%	0.51	4.9%	7.7%
collateral a b (30, 31)	0.4%	0.88	66.7%	66.3%
collateral b c (31, 32)	-0.2%	1.0	31.0%	31.2%
collateral c d (32, 33)	-4.3%	0.08	68.8%	73.0%
inf frontal a b (5, 6)	0.6%	0.84	71.8%	71.2%
inf frontal b c (6, 7)	-3.2%	0.19	66.3%	69.5%
inf temporal a b (23, 24)	11.0%*	$9.0 \cdot 10^{-7}$	82.8%	71.8%
inf temporal b c (24, 25)	-2.1%	0.42	74.4%	76.5%
inf temporal c d (25, 26)	-0.5%	0.82	85.5%	86.0%
intraparietal a b (16, 17)	-15.4%*	$1.6 \cdot 10^{-13}$	67.9%	83.3%
intraparietal b c (17, 18)	-7.7%	0.01	10.5%	18.2%
occipito temporal a b (27, 28)	3.7%	0.01	93.2%	89.5%
occipito temporal b c (28, 29)	-6.1%	0.03	65.7%	71.8%
postcentral a b (13, 14)	26.0%*	$3.8 \cdot 10^{-15}$	59.3%	33.3%
postcentral b c (14, 15)	1.5%	0.74	24.9%	23.4%
precentral a b (8, 9)	-13.0%*	$8.3 \cdot 10^{-6}$	50.7%	63.8%
sup frontal a b (1, 2)	-4.3%	0.08	70.1%	74.4%
sup frontal b c (2, 3)	0.0%	1.0	65.6%	65.6%
sup frontal c d (3, 4)	-4.6%	0.07	66.6%	71.2%
sup temporal a b (19, 20)	6.1%	0.05	55.6%	49.5%
sup temporal b c (20, 21)	25.9%*	$1.2 \cdot 10^{-9}$	34.8%	8.9%
sup temporal c d (21, 22)	20.5%*	$7.2 \cdot 10^{-9}$	49.8%	29.3%
STAP	42.4%*	$3.3 \cdot 10^{-24}$	59.9%	17.6%

Asym PP: hemispheric asymmetry of plis de passage in this section; **L PP:** proportion of subjects with a pli de passage in the left hemisphere in the considered section; **R PP:** respectively in the right hemisphere;

* significant asymmetry for Fisher exact test with $p < 0.001 \approx 0.05/31$ (Bonferroni correction).

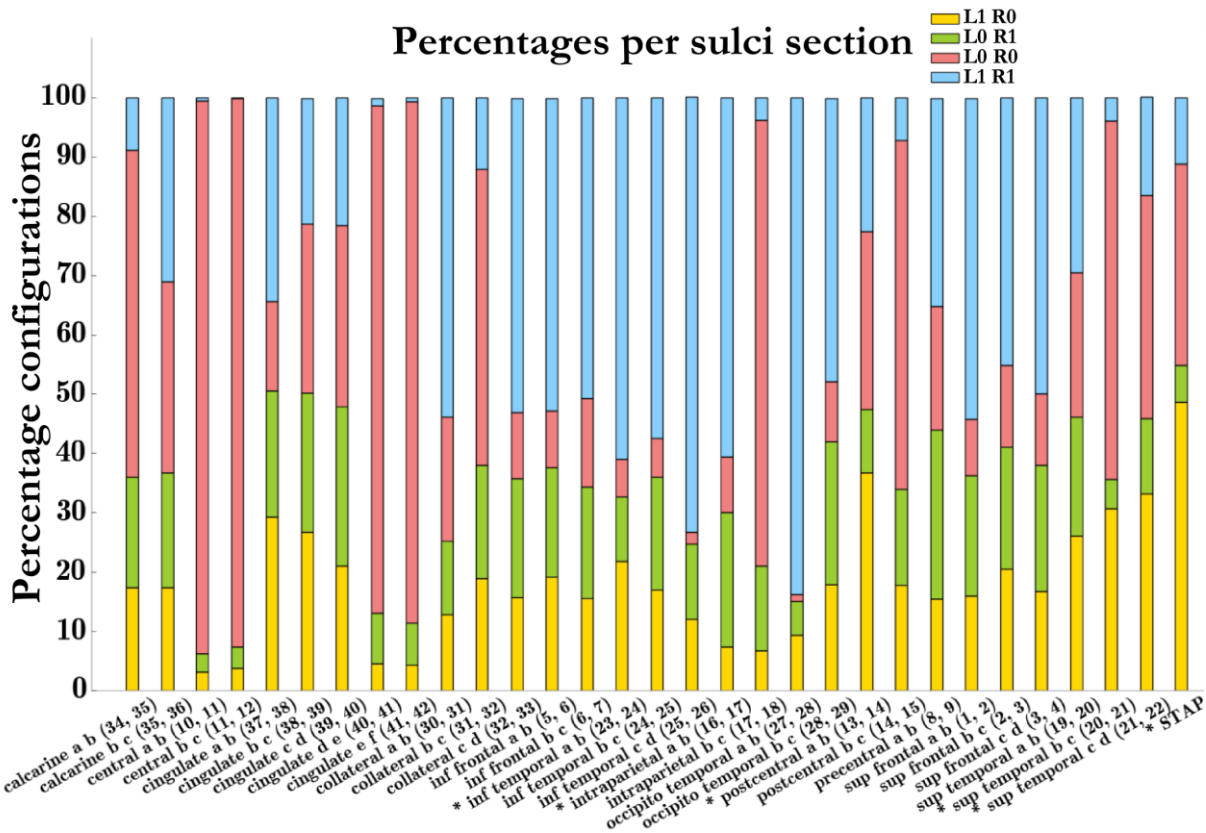

Fig. 2. Percentage of each configuration of pli de passage per sulci section. L1 R1 (blue): proportion of subjects with a pli de passage in both hemispheres for this section; L0 R0 (yellow): without plis de passage; L1 R0 (green): a pli de passage solely in the left hemisphere; L0 R1 (red): solely in the right hemisphere. STable 1 provides the exact percentages used to create this chart. Significantly asymmetric segment names are emphasized with * (see also STable 2.).

To allow the reader to have a clearer view of the local morphology of the three most asymmetric segments apart from the STS, we present typical subjects for each configuration. **Fig. 5** introduces the typical configurations in the postcentral a b (13, 14), intraparietal a b (16, 17) and precentral a b (8, 9) segments. Detailed depth profiles for each of these configurations are respectively shown on **SFig. 4-7**. This pipeline can also be applied to identify rare individuals who have a divided central sulcus (**Fig. 5**), estimated to be about 1% (Ono et al., 1990; Schweizer et al., 2014). Our pipeline identified about 3% of all hemispheres due to noise but can aid neuroanatomists who want to identify these particular subjects to considerably restrain their search.

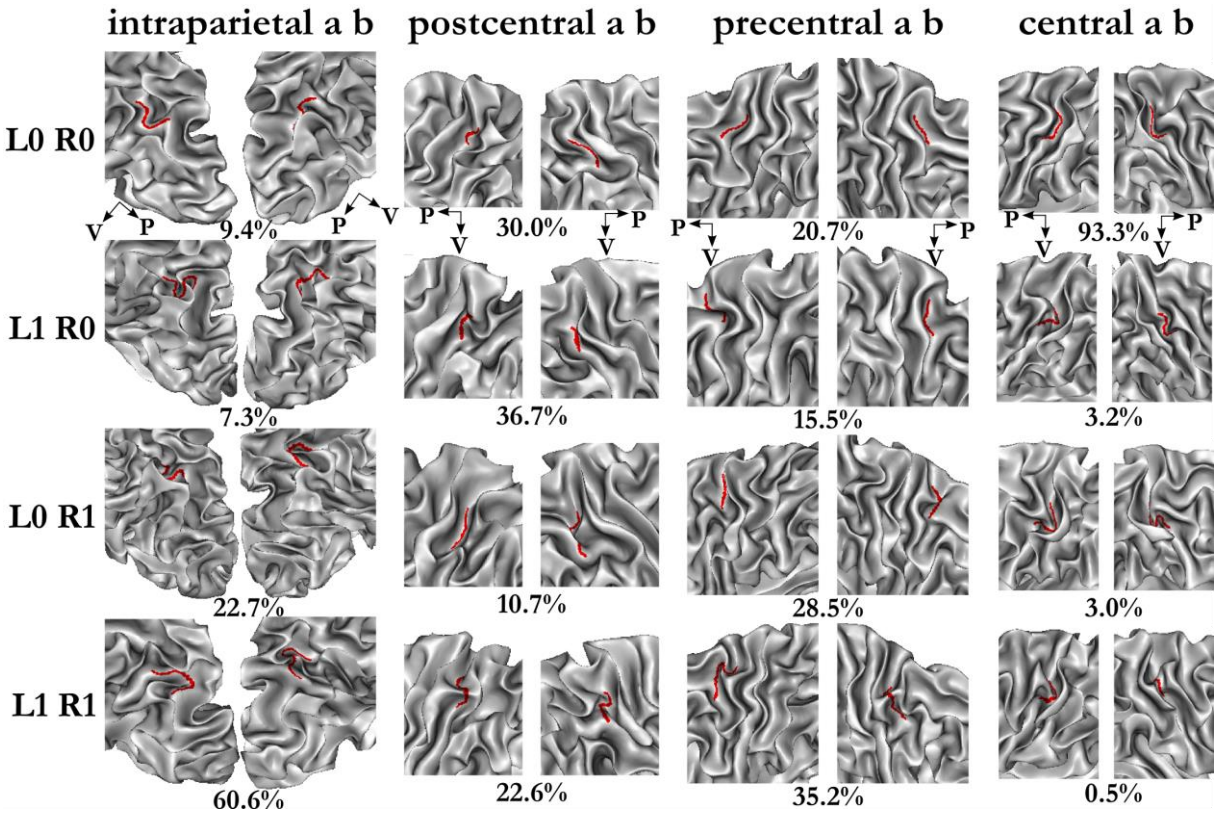

Fig 3. Typical patterns for each configuration in the intraparietal a b (16, 17), postcentral a b (13, 14), precentral a b (8, 9), central a b (10, 11). L0 R0: no PPs in either hemisphere, L1 R0: A PP in the left hemisphere, L0 R1: A PP in the right hemisphere, L1 R1: PPs in both hemispheres. P and V axes indicate the posterior and ventral directions, respectively.

5.3. Comparison with asymmetries found via vertex wise analysis of sulcal depth and cortical thickness

Traditional methods to assess structural asymmetry use a vertex-wise analysis projecting individual vertex values onto a group template corresponding to an average brain. These approaches are relevant to quantifying differences across hemispheres in terms of sulcal depth, cortical thickness, or cortical surface area and have been widely used in the past (Koelkebeck et al., 2014; Li et al., 2015; Maingault et al., 2016). They do not inform on the local shape along the sulci, such as the detection of a PP. However, there is a close relationship between sulcal depth and the presence of a PP, meaning that hemispheric asymmetry in the frequency of PP should translate to an asymmetry in sulcal depth. The asymmetry in sulcal depth **Fig. 6** shows that the right postcentral (a,b) is on average significantly deeper than the left (in red), while the left intraparietal (a,b) is deeper than the right. These results confirm the asymmetry we found in term of PPs in the postcentral (a,b) (+26%) and intraparietal (a,b) (-15.4%) segments. The asymmetries in the precentral (a,b) and inferior temporal (a,b) segments are not reflected by these data. In terms of cortical thickness (CT), the 2nd line of **Fig. 6** emphasizes traditionally reported areas, mainly including the rightward asymmetry CT in the STS and its surrounding gyri.

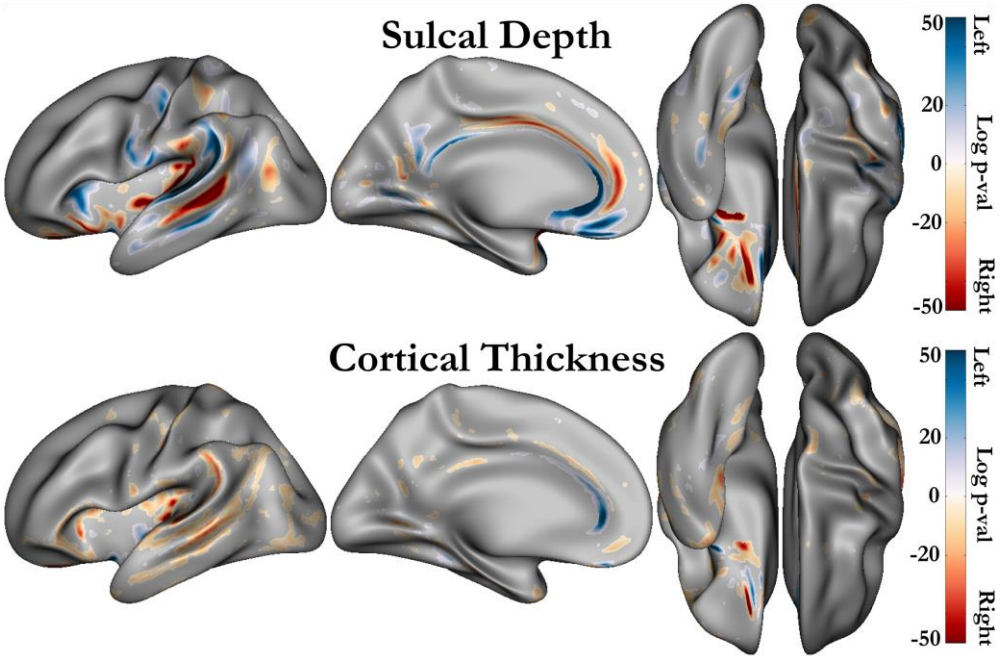

Fig. 7. Log p-values of the t-test assessing the asymmetry vertex-wise of sulcal depth and cortical thickness distributions. Only significant asymmetries after Bonferroni correction ($p < 0.05/163842 \approx 3 \cdot 10^{-7}$, where 163842 is the number of vertices on the mesh) are displayed. Blue regions correspond to leftward asymmetries, and red regions, to rightward asymmetries.

5.4. Relationship between the presence of PPs and intracranial brain volume

Larger brains are known to be more folded (Germanaud et al., 2012; Toro et al., 2008) and brain volume is known to be highly heritable (Bartley et al., 1997; Peper et al., 2007). It therefore appears important to assess to what extent the presence of a PP in the left STAP is related to brain volume. The logistic regression between the intracranial volume and PPs displayed a small trend with the probability of PPs slightly increasing with brain volume. In our sample, the mean intracranial volume was 1604 cm^3 ($\sigma = \pm$ 176 cm^3), and this probability increased by 0.046 per standard deviation. We applied the Mann-Whitney test to compare the mean intracranial volume distributions for individuals with and without PPs in the STAP. We obtained a significant, yet relatively low p-value of 0.001 for the dataset size. Overall, larger brains were slightly more likely to have a PP in the STAP, but we are unable to set any thresholds on brain volume to consistently confirm the presence or absence of PPs in the STAP. In addition, we performed these tests separately considering the hemispheric white and grey matter volumes and obtained similar results. Thus, we concluded that PPs in the STAP were not directly related to brain or hemispheric volume.

5.5. Heritability of the plis de passage

We found a significant heritability estimate for the presence of PPs in the left hemisphere STAP ($h^2 = 0.53$, $p = 10^{-7}$), whereas that for the right hemisphere did not reach significance ($h^2 = 0.26$, $p = 0.03$) (**Table 3.**). Taking into account all sulci segments in both hemispheres the Bonferroni

threshold was set to $p < 0.05/(31*2) \approx 8.1 \cdot 10^{-4}$. To compare the proportion of genetic additive effects found in the STAP, we additionally estimated the heritability for other sulci segments (**STables 3, 4**). Those significant after correction were the left collateral a b ($h^2 = 0.33$, $p = 10^{-4}$), the left superior temporal b c ($h^2 = 0.33$, $p = 10^{-4}$), the right calcarine b c ($h^2 = 0.48$, $p = 10^{-6}$), the right collateral c d ($h^2 = 0.38$, $p = 10^{-4}$) and the right postcentral b c ($h^2 = 0.37$, $p = 10^{-4}$). It should be noted that most of these estimates had larger standard errors (see **STables 3, 4**) due to ill balanced classes (i.e., either too large a proportion of subjects with or without PPs). One interesting point to emphasize is that the STS b-c was the only segment with significant asymmetry and heritability in the left hemisphere. Another interesting finding is that the handedness covariate was only significant for the right postcentral a b segment ($p = 5.5 \cdot 10^{-3}$), which indeed corresponds to the hand knob location.

Table 2. Heritability estimates for the presence of a *pli de passage* in the STAP in both hemispheres. The p-values associated to covariates related to Age, Sex, ethnic group (Hispanic), eTIV and Handedness are also displayed.

Trait	h^2±SE(p)	Age	Age²	Sex	Age*Sex	Age²*Sex	Hisp.	eTIV	Hand
		p-val							
PP in the Left STAP	0.53±0.09 ($1.0 \cdot 10^{-7}$)	0.49	0.19	0.06	0.73	0.76	0.4	0.21	0.3
PP in the Right STAP	0.27±0.15 (0.03)	1.0	0.69	0.85	0.92	0.93	0.8	0.36	0.33

5.6. Exploratory analysis for functional significance of the STAP asymmetry

We found several areals of the HCP multi-modal parcellation (Glasser et al., 2016) whose brain activations in HCP Language task had noticeable correlations ($p < 0.005$, uncorrected) with the depth asymmetry index in the STAP (see **SMethod 1, SFig. 9-10**). These areals corresponded to the Area STS dorsal (STSd) posterior, ParaBelt Complex, Area Temporo-Parieto-Occipital Junction 2 and VentroMedial Visual Area 3 (**STables 5-6**). Among these only the STSd posterior had a p-value ($p \approx 8 \cdot 10^{-5}$) that survived a strict Bonferroni correction from the 180 areals per hemisphere ($p < 0.05/(2*180) \approx 5.5 \cdot 10^{-4}$). This finding is interesting as a similar study on the STS asymmetry had not found any structural-functional correlations with a smaller sample (18 subjects) (Specht and Wigglesworth, 2018).

Regarding the correlation of the depth asymmetry index with the HCP cognitive scores, only that for Verbal Episodic Memory Reaction Time (for correct responses) was significant ($\rho = 0.078$, $p = 0.03$, uncorrected, **STable 7**). This result might emphasize the link between hemispheric specification and cognitive efficiency in support of Ringo's theory (Ringo et al., 1994).

6. Discussion

Thanks to a new method, we were able to study auxiliary cortical folds, called plis de passage (PPs), in a robust manner across a large cohort. We first observed that few of them are genetically constrained and, second, that some of them occur more often in one hemisphere than in the other. Finally, we found that only one PP is both asymmetric and genetically constrained across the cortex. This PP is located in the intermediate segment of the STS, the so-called STAP region.

The observation that a PP often divides the left STS within the STAP region is in agreement with the reported rightward asymmetry of the STS depth profile (Bodin et al., 2017; Glasel et al., 2011; Leroy et al., 2015), and contributes to this asymmetry to a large extent (Leroy et al., 2015; Ochiai et al., 2004). Furthermore, this interruption is part of an heritable morphological pattern along the left STS concerning the neighboring sulcal pits in areals b and c, which are also heritable (Le Guen et al., 2018a). Thus, the interruption in between the pits STS b-c-d forms a saddle-like shape under genetic constraints in the left STS. This rather complex conformation, which is the only one both asymmetrical and heritable across the cortex, suggests an evolutionary pressure in this region. Whereas the right STS lacks a PP between pits b and c.

Several asymmetries are present in the superior temporal region that may participate in this particular shape. First, the prominence of PPs in the left hemisphere may reflect an asymmetry in white-mater connectivity, which shapes the cortical surface (Hilgetag and Barbas, 2006). Numerous long-range tracts, namely the arcuate fasciculus, the middle longitudinal fasciculus, the inferior occipito-frontal fasciculus, and transcallosal fibers, (Turken and Dronkers, 2011) cross in this region and intermingle with a dense local connectivity (Mesgarani et al., 2014). Among them, the left arcuate fasciculus is larger than the right already early on in life (Dubois et al., 2015). In addition, PPs might also materialize the U-shape fibers which mediate short intralobar connectivity as it might be the case in the central region (Catani et al., 2012; Zhang et al., 2014). Catani et al. (2012) have shown that the fiber connections between the hand-knob motor region and the postcentral gyrus are left lateralized. The left asymmetry we found in the postcentral a b segment is in agreement with this left lateralization. Second, the preferential formation of PPs in the left STAP might be caused by left-right differences in maturational rate, which is thought to play a decisive role in creating structural and functional lateralization in the human brain (de Kovel et al., 2017). Indeed, the right STS appears earlier during gyral development than the left STS (Chi et al., 1977) and matures faster (Leroy et al., 2011). Finally, we cannot exclude a difference in neuronal proliferation in left and right STS progenitors leading to a differential growth between grey and white matter (de Juan Romero et al., 2015; Tallinen et al., 2016) and thus to supplementary tertiary folds when synaptic trees develop. The observation in adult post-mortem brains that the superficial layers of the left superior temporal cortex contain a greater number of large pyramidal cells than the right (Hutsler, 2003) might be part of this specific gyral conformation.

What is the relation between this anatomical pattern and human cognitive functions? The STS is a key structure in voice and face recognition, biological motion, theory of mind, audio-visual integration and language (Deen et al., 2015; Hein and Knight, 2008) with robust functional asymmetries. Although a clear functional subdivision along the sulcus is still debated, the location of the STAP at the basis of Heschl's gyrus points towards a role in vocal stimuli processing (Deen et al., 2015), voice recognition in the right hemisphere (Belin et al., 2000; Moerel et al., 2012) and speech processing in the left hemisphere (DeWitt and Rauschecker, 2012). Since heritability was found only in the left hemisphere, genetic constraints would be stronger on the structural organization of speech network, either within the auditory domain or within the auditory-visual connections. Indeed, the middle STS is the first linguistic step in converting acoustic features into phonemes (DeWitt and Rauschecker, 2012; Liebenthal et al., 2010; Mesgarani et al., 2014) and entering the hierarchy of areas sensitive to increasing levels of linguistic structures (Dehaene-Lambertz et al., 2006; Pallier et al., 2011). It is also the site of auditory and visual cross-modal integration (lip-reading (Calvert et al., 1997; Nath and Beauchamp, 2012; Paulesu et al., 2003), communicative gestures (Redcay et al., 2016), sign language (Moreno et al., 2018; Neville et al., 1998), as well as grapheme-phoneme conversion (Dehaene et al., 2010)). We tentatively explored the structure-function relationship by taking into account the functional tasks tested in the HCP. We observed a significant and large correlation between the activations in the story and math tasks and the asymmetry index in the middle-posterior STS. Again, this asymmetry driven by the left hemisphere indicates that the linguistic component of these tasks might be the crucial factor related to the STAP (**SFig. 9-10**).

The larger heritability in the left STS implicates genes involved in language circuits as the first candidates, such as FOXP2, linked to language lateralization (Ocklenburg et al., 2013), and KIAA0319, whose haplotypes have been shown to correlated with asymmetry of activation in the STS (Pinel et al., 2012). Genome wide association studies of these phenotypes (GWAS) have yielded few significant results because they require enough statistical power to detect variants with small effect sizes. Another interesting approach to identify genes involved in language lateralization would be to focus on genes expressed asymmetrically in both hemispheres (Karlebach and Francks, 2015; Sun and Walsh, 2006). In particular, those differentially expressed in perisylvian speech and language regions during fetal development should be considered (Johnson et al., 2009). Epigenetic modifications in gene expression, such as DNA methylation, histone modification, as well as modulation of expression, such as microRNA post-transcriptional regulation, also need to be examined (Güntürkün and Ocklenburg, 2017). Our pipeline, which robustly and automatically extracts brain asymmetrical features, such as *plis de passage*, should help in investigating the implicated biological pathways in large cohorts.

Other hemispheric asymmetries

The other asymmetries that our results revealed are in agreement with neuro-anatomical descriptions in the STS (Ochiai et al., 2004), the postcentral sulcus (Zlatkina and Petrides, 2010) and the intraparietal sulcus (Zlatkina and Petrides, 2014). In 40 subjects, Zlatkina and Petrides closely delineated the postcentral sulcus segments corresponding to the those of the sulcal roots theory (Régis et al., 2005). We found that the left postcentral sulcus contained more interrupting gyri, notably in its dorsal part, which is concordant with their report. Looking at their drawing of the postcentral and adjacent sulci, we speculate that the asymmetric interruption we quantified might be due to the ascending (marginal) branch of the cingulate sulcus that merges in the postcentral sulcus superior part. In their second study, these authors emphasized that the intraparietal sulcus is divided by a submerged gyrus into two branches, the anterior ramus and the posterior ramus (Zlatkina and Petrides, 2014). They confirmed the trend we found by underlining that the gyral passage occurred more often in the right hemisphere. Third, Shen et al. (2018) reported a significant rightward sulcal depth asymmetry in the anterior cingulate sulcus in normal elderly individuals. This asymmetry is confirmed both by our vertex-wise analysis (**Fig. 6**) and by a 7.9% increase in the amount of left PPs between anterior cingulate pits a and b. Fourth, we did not find any PP asymmetry in the collateral sulcus, as reported in a manual neuroanatomical study (Huntgeburth and Petrides, 2012). Finally, we underlined new findings which need to be further investigated. First, there are more sulcal interruptions in the left infero-temporal region and the right precentral region than in the contralateral hemisphere; asymmetry size is larger than 10%, which is a commonly used threshold to assess brain asymmetry (Galaburda et al., 1987). Second, we reported significant heritability of sulcal interruptions in the left collateral sulcus, the right calcarine fissure, the right collateral sulcus, as well as in the right postcentral sulcus. Our asymmetry results were confirmed by our vertex-wise analysis of the sulcal depth asymmetry. This second approach emphasized rightward asymmetries of sulcal depth in the dorsal postcentral, as well as leftward asymmetry in the intraparietal and on precentral gyrus.

It is difficult to compare our study with previous automated studies of cortical asymmetry as they mainly focused on cortical thickness and cortical surface area. Surface based approaches are twofold either using a cortex parcellation (Chiarello et al., 2016; Kang et al., 2015), in particular the automated Freesurfer ones (Destrieux et al., 2010), or considering interhemispheric registration (Maingault et al., 2016) as we did for our vertex-wise analysis. Overall, we agree with the rightward asymmetry of cortical thickness in the superior temporal lobe (Maingault et al., 2016). Sulcal depth asymmetry has rarely been studied cortex-wise, but previous literature has emphasized a rightward asymmetry in the superior temporal sulcus (Maingault et al., 2016; Van Essen, 2005) and a leftward asymmetry for right handers in the precentral area corresponding to the Rolando genu (Maingault et al., 2016) similar to our result (**Fig. 6**). We assume they did not observe the other asymmetries in sulcal depth due to either smaller samples or differences in the methodology such as the registration

technique in (Van Essen, 2005). Moreover, Maingault and colleagues performed a questionable 10 mm FWHM (full width half maximum) Gaussian filter on each subject asymmetry map. This filtering likely blurred out some population asymmetries, keeping only the largest.

Our study is the first to propose an automated extraction of prominent transverse gyri, the so-called plis de passage. Previous related work by Bodin and colleagues extracted the STS stem depth profile by manually defining the anterior and posterior extremities (Bodin et al., 2017). As explained by the authors, defining these extremities automatically was impossible due to the large intersubject variability, particularly at the cross section with the caudal branches of the STS. Using the sulcal pits as landmarks to allow for matching of the sulcus segments across individuals was essential in automatizing the depth profile extraction. It is worth underlining that Leroy et al. (2015) used the planum temporale anterior and medial tip as landmarks to identify the STAP. Using the sulcal pits within the STS is certainly more reliable and does not need a manual step. Existing methods quantifying the depth profile were usually applied on the central sulcus of human or non-human primates (Cykowski et al., 2008; Hopkins et al., 2014). They relied on the automatic extraction of the sulci as 3D-morphological objects (Perrot et al., 2011), which sometimes lead to the fusion of adjacent sulci. This problem occurred particularly in the STS due to its various ramifications and frequent interruption by a PP, preventing the extraction of a topologically simple morphological object. Thus, the STS is often seen as segmented in several unconnected pieces (Ochiai et al., 2004) which do not necessarily correspond across individuals. In this context, our method appeared most suitable both to mark off the STAP with sulcal landmarks and quantify the depth profile across individuals without any manual input. Furthermore, the flexibility of our pipeline enabled us to study the presence of PPs splitting other main sulci. Although the sulci of most brain regions were analyzed, we were not able to detect PPs in a few sulci which were either too short to host a pair of sulcal pits or too variable across subjects. For example, we should emphasize the poor group areal boundaries in the occipito-temporal regions (27, 28 , 29 **Fig. 2**), which did not allow us to extract PPs robustly and certainly led to the crossing of true gyri by the SP_{DPF}. Thus, we were not able to investigate further sulcal interruptions in this brain region, which have been reported as being related to reading performance in normal readers and dyslexic subjects (Borst et al., 2016; Im et al., 2016).

7. Conclusion

The contribution of this chapter is twofold. *First*, we defined an automated pipeline composed of sulcal pit extraction on the cortical surface at the individual level, computation of sulcal a pit atlas, geodesic path delineation between any given pair of pits, computation of the depth profile along the bottom of the sulcus, and *pli de passage* detection. We demonstrated the feasibility of such a pipeline in a large dataset to detect PPs and found significant asymmetries in the STAP, dorsal postcentral, rostral intraparietal, and dorsal precentral sulci. *Second*, we demonstrated the genetic influence on PPs located in the left STAP region. Because the STAP is a recent asymmetry appearing in the primate

lineage (Leroy et al., 2015), our result confirms that this recent evolutionary change might be related to the emergence of the linguistic network in the left perisylvian region.

8. Supplementary method

8.1. SMethod 1 Exploratory analysis for correlations between STAP asymmetry and task fMRI activations, as well as cognitive scores

We performed an exploratory analysis to link the asymmetry of the STAP with functional findings. To this aim, we defined the asymmetry index AI_{DPF}(or AI_{GD}) $= 2\frac{L-R}{L+R}$, where L and R are the average values of SP_{DPF} (or SP_{GD}) in the left and right hemisphere STAP.

We considered the HCP Language task functional MRI (tfMRI), which includes story and math blocks. Briefly, the HCP Language task was developed by Binder and colleagues (Binder et al., 2011). In the story blocks, participants were presented with brief auditory stories adapted from Aesop's fables, followed by a 2-alternative forced-choice question to check the participants' understanding of the story topic. The example provided in the original chapter is *"For example, after a story about an eagle that saves a man who had done him a favor, participants were asked, 'Was that about revenge or reciprocity?'".* The math task also presented trials auditorily and required subjects to perform addition and subtraction problems. The trials presented subjects with a series of arithmetic operations (e.g., "fourteen plus twelve"), followed by "equals" and then two choices (e.g., "twenty-nine or twenty-six")". **SFig. 8** presents the brain regions activated by the story and math blocks separately.

We decomposed our analysis on the HCP multi-modal parcellation (Glasser et al., 2016) and considered the median parameter estimates (β) in each areal of the parcellation. Then, we computed the Pearson correlation of the β with AI_{DPF} (and AI_{GD}) for the story and math blocks separately.

Additionally, we explored the correlation between the HCP cognitive scores (see **STable 7** for details on these scores) with AI_{DPF} (and AI_{GD}).

9. Supplementary Figures

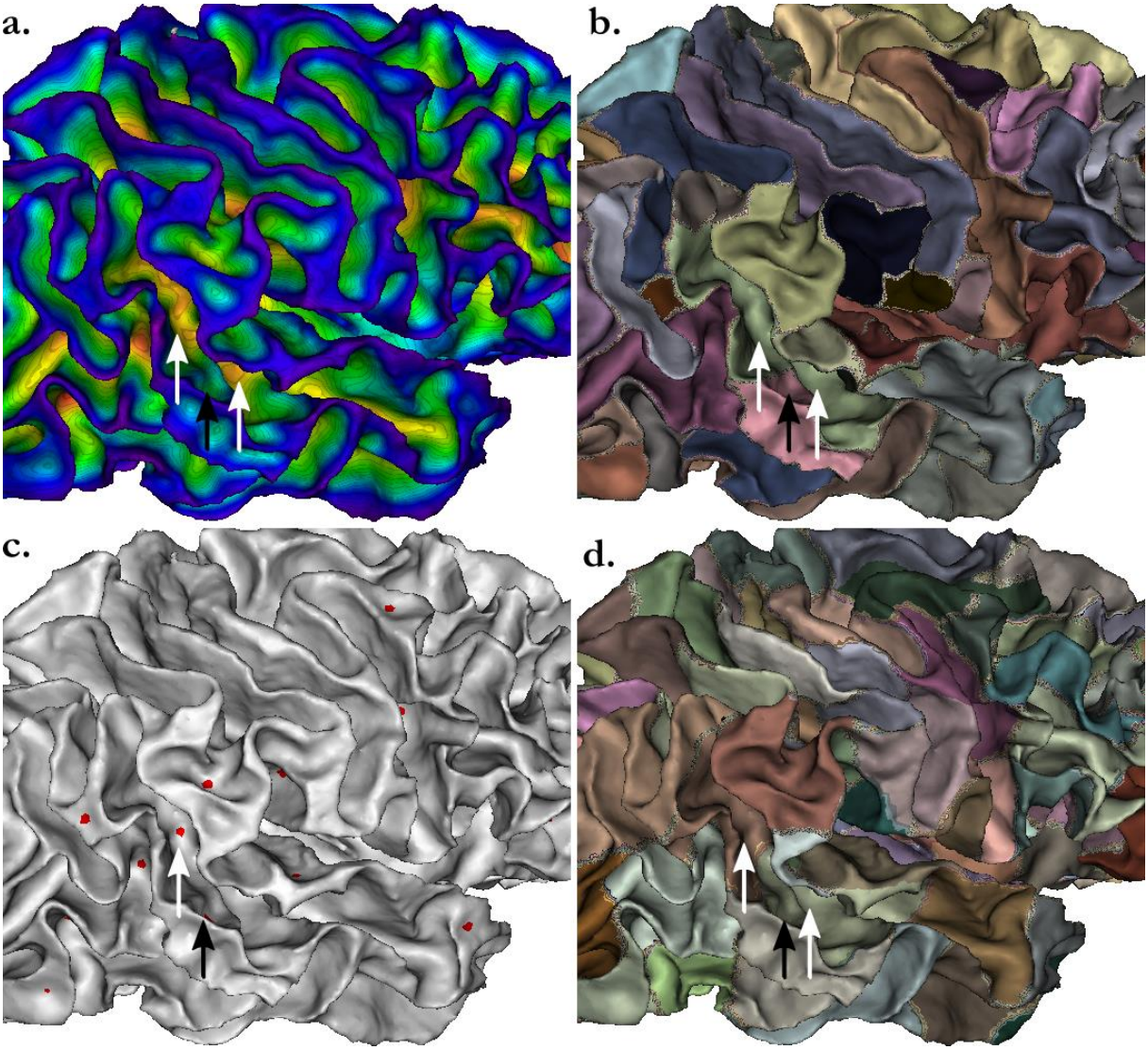

SFig. 1. Example of a subject for whom no deep sulcal pits were extracted by the watershed algorithm in one group areal in the STS (in this case the green areal STS c). **a)** DPF map of the subject's right white matter mesh. **b)** Subject's sulcal basins extracted using a watershed. **c)** Single sulcal pits extracted in each subject's sulcal basin. **d)** Group areal projected from the group template to the subject native mesh. The **black arrow** shows a "superficial" sulcal pit extracted in a cavity in the STS gyral wall. The **two white arrows** point to the zones of the DPF local maxima in the two group areals STS d (brown) and STS c (green). The algorithm did not extract the deep sulcal pit in the group areal STS c because the subject's sulcal basin (in green on **c)**) encompassed the two group areals at the bottom, likely due to the presence of the sulcal basin that encompassed the cavity in the STS wall (in pink on **c)**).

Thus, as extremities of our geodesic path to extract the depth profil between any pair of adjacent pits in any sulci, we chose the deepest vertex. This vertex corresponded in most cases to the sulcal pit, but, in rare cases, as on **SFig. 1.** this point was not the sulcal pit extracted by the algorithm.

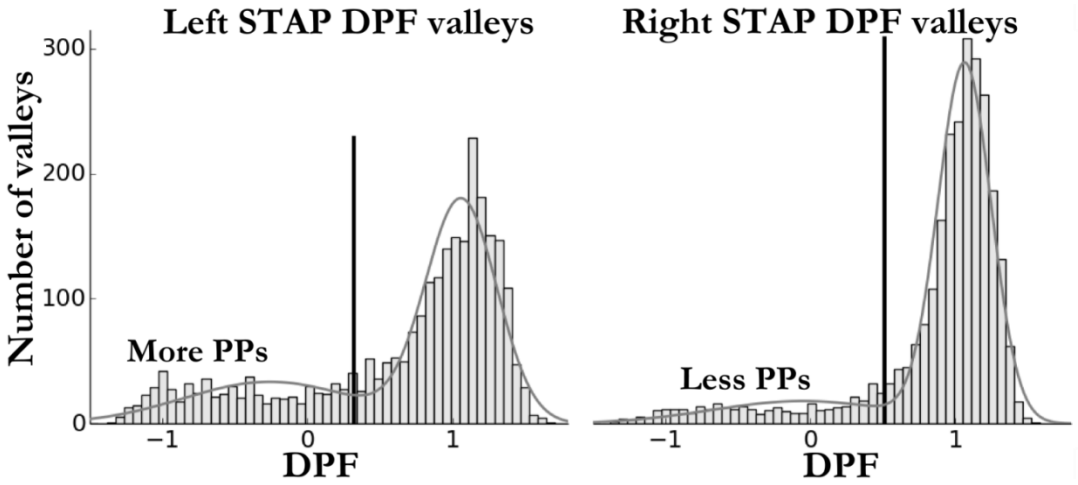

SFig. 2. Presentation of all detected valleys, with a constraint on the minimum distance between two valleys, in the STAP depth profile. The left side presents the left hemisphere DPF distribution of these valleys; we noticed that there are more valleys with low DPF compared to the right hemisphere, corresponding to the preponderance of PPs in the left STAP. The grey curve corresponds to the fit of a mixture of two Gaussians. The dark bar represents the threshold at 3σ from the mean of the main Gaussian.

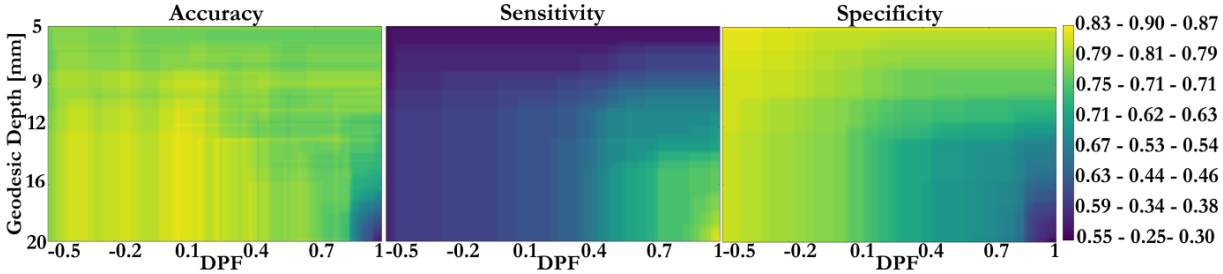

SFig. 3. Accuracy, sensitivity, and specificity obtained for different sets of parameters (DPF vs Geodesic Depth) on 196 hemispheres for which PPs were labelled manually in the STAP from (Leroy et al., 2015).

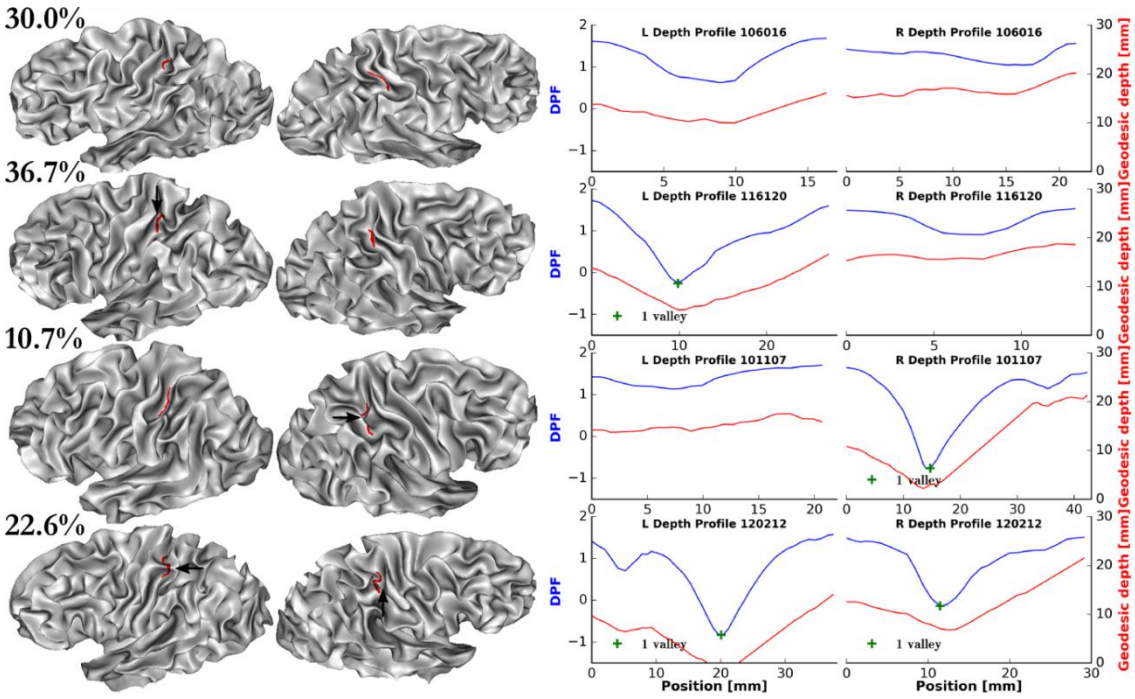

SFig. 4. Typical postcentral a b (13, 14 Fig. 2) patterns with either a symmetric configuration with no PPs on either side (1st line: 30.0% of HCP Caucasians subjects) or one PP on each side (4th line: 22.6%), or asymmetric with only one PP on the left (2nd line: 36.7%) or on the right (3rd line: 10.7%). The associated depth profiles in the postcentral a b (13, 14) segment are shown on the right of the figure. Black arrows indicate the pli de passage position on the mesh.

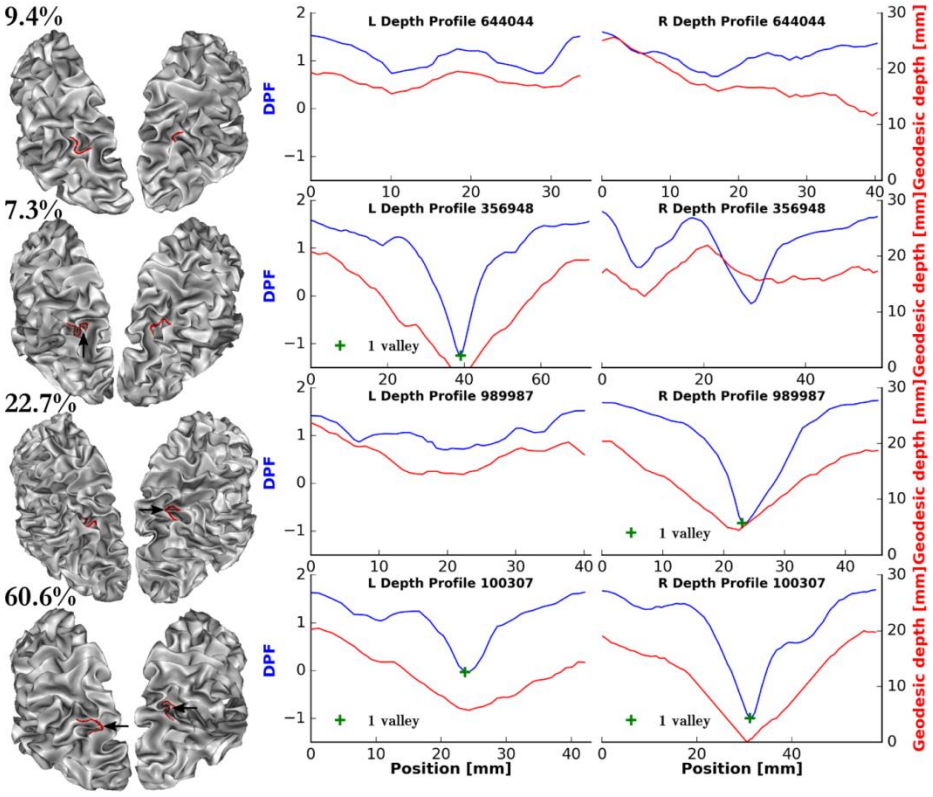

SFig. 5. Typical intraparietal a b (16, 17 Fig. 2) patterns with either a symmetric configuration with no PPs on both either side (1st line: 9.4% of HCP Caucasians subjects) or one PP on each side (4th line: 60.6%), or asymmetric with only one PP on the left (2nd line: 7.3%) or on the right (3rd line: 22.7%). The associated depth profiles in the intraparietal a b (16, 17) segment are shown on the right of the figure. Black arrows indicate the pli de passage position on the mesh.

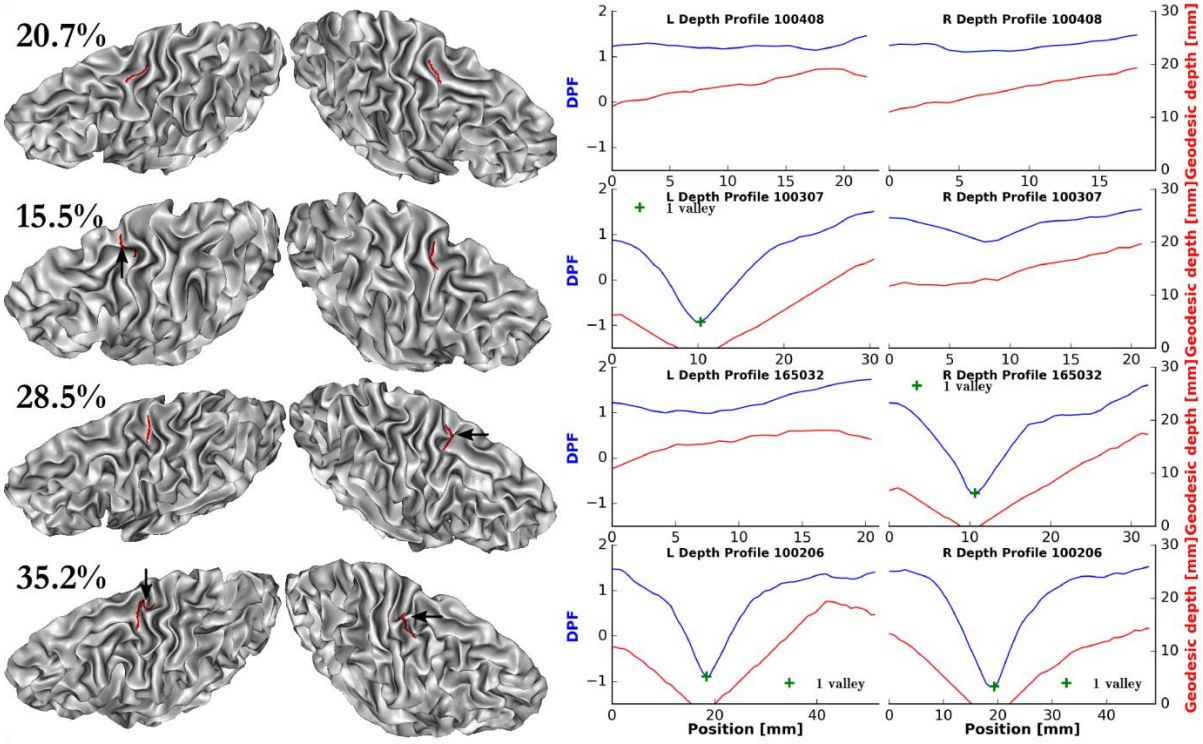

SFig. 6. Typical precentral a b (8, 9 Fig. 2) patterns with either a symmetric configuration with no PPs on either side (1st line: 20.7% of HCP Caucasians subjects) or one PP on each side (4th line: 15.5%), or asymmetric with only one PP on the left (2nd line: 28.5%) or on the right (3rd line: 35.2%). The associated depth profiles in the precentral a b (8, 9) segment are shown on the right of the figure. Black arrows indicate the pli de passage position on the mesh.

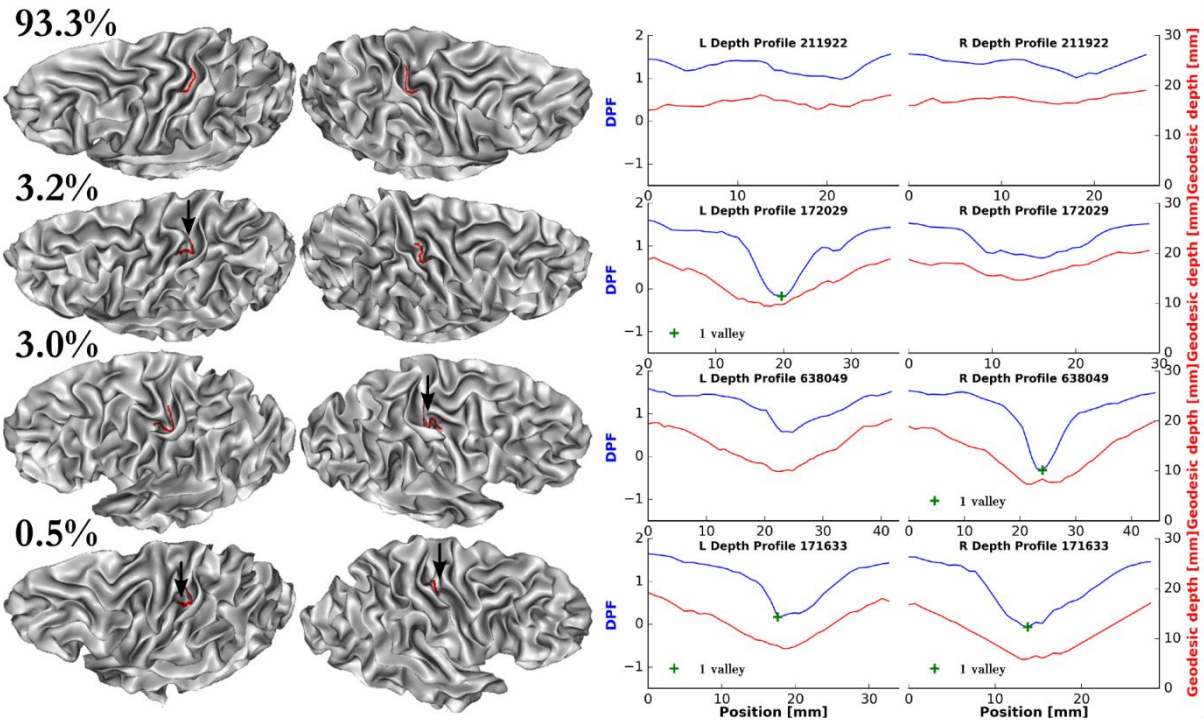

SFig. 7. Typical central a b (10, 11 Fig. 2) patterns with either a symmetric configuration with no PPs on either side (1st line: 93.3% of HCP Caucasians subjects) or one PP on each side (4th line: 0.5%), or asymmetric with only one PP on the left (2nd line: 3.2%) or on the right (3rd line: 3.0%). The associated depth profiles in the central a b (10, 11) segment are shown on the right of the figure. Black arrows indicate the pli de passage position on the mesh.

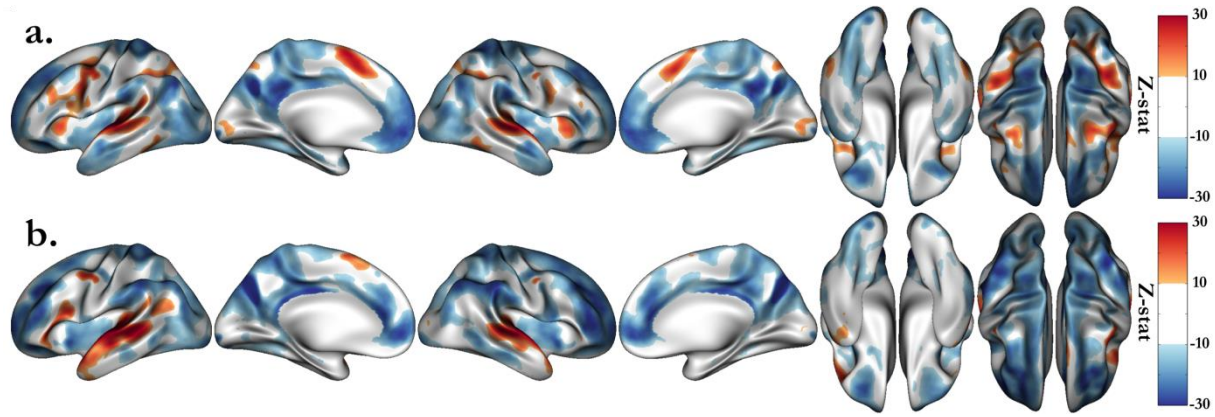

SFig. 8. Group level analysis on the HCP subjects showing activations for the MATH (**a.**) and STORY (**b.**) tasks.

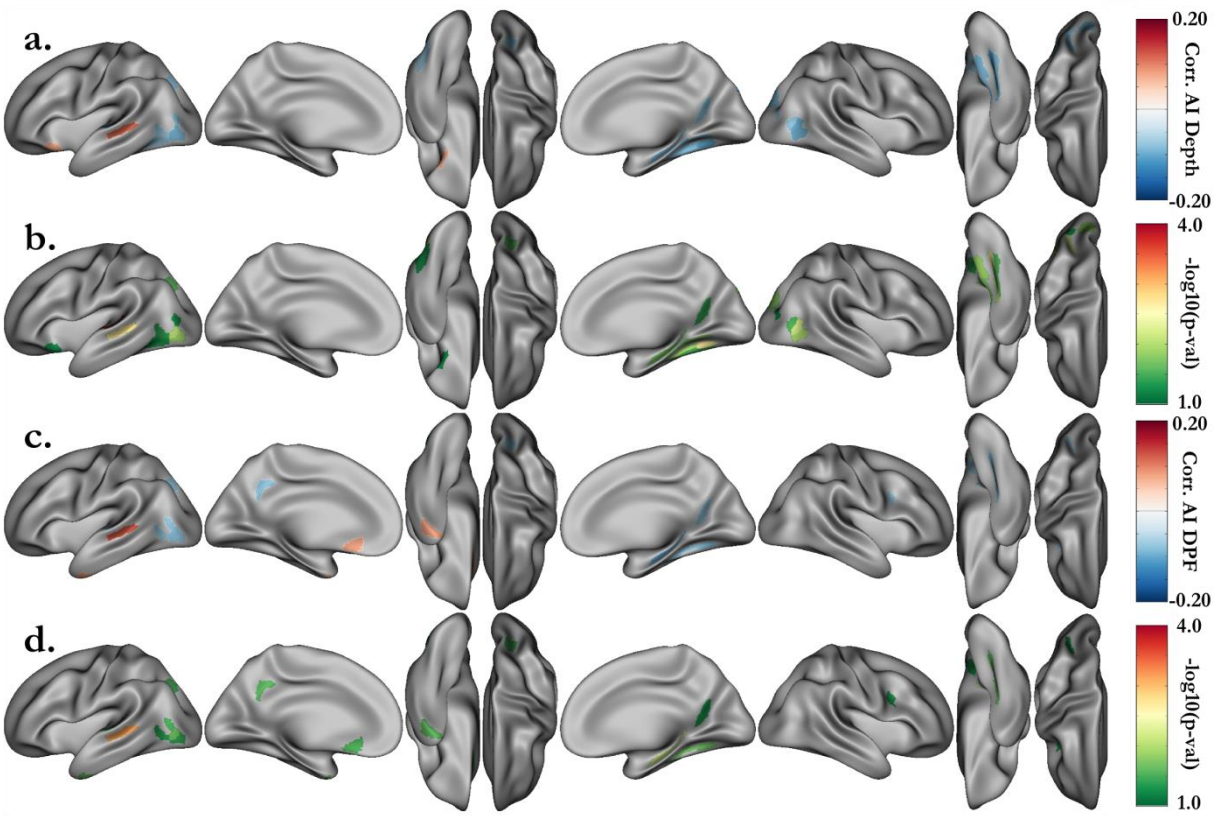

SFig. 9. Pearson correlation between the MATH task activation in each areal and the asymmetry index in the STAP, for the Geodesic Depth (**a., b.**) and the DPF (**c., d.**) profiles. Only areals with $p < 0.05$ (uncorrected) are displayed.

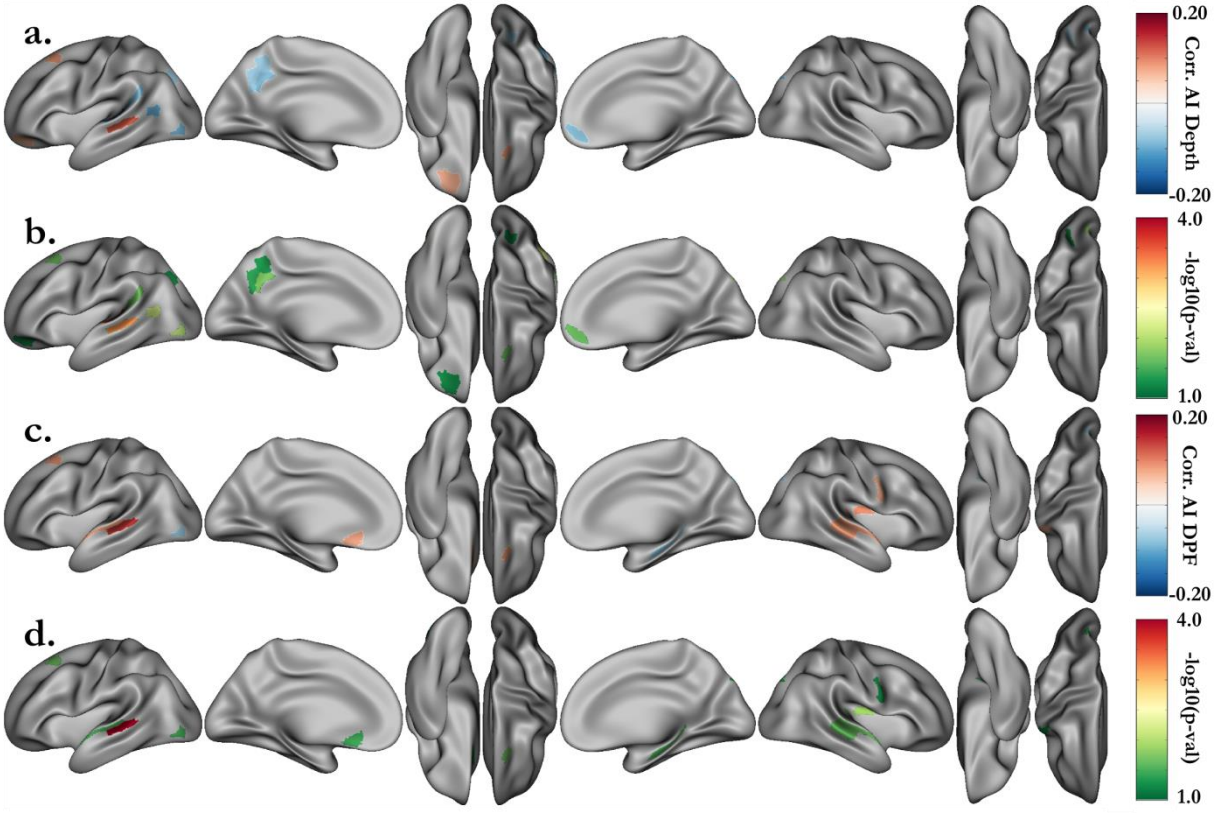

SFig. 10. Pearson correlation between the STORY task activation in each areal and the asymmetry index in the STAP, for the Geodesic Depth (**a., b.**) and the DPF (**c., d.**) profiles. Only areals with $p < 0.05$ (uncorrected) are displayed.

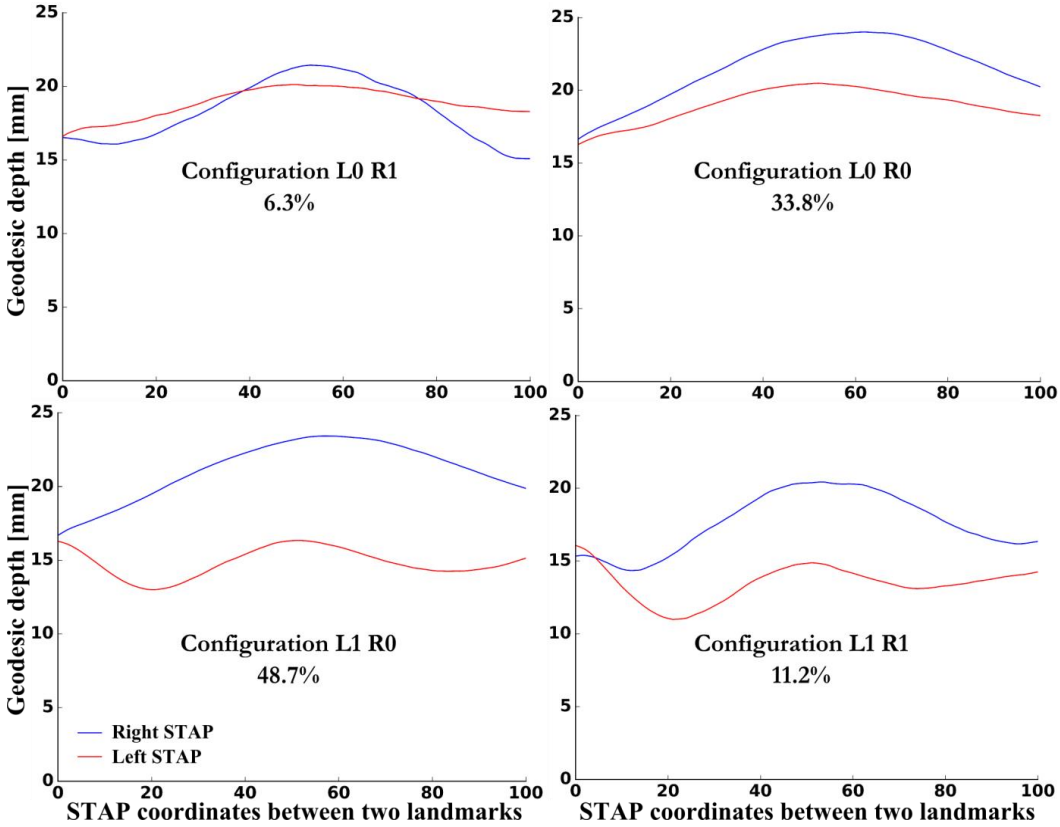

SFig. 11. Average Geodesic Depth Profile in the STAP over the 820 HCP subjects, for each configuration of plis de passage. L0 R1: subjects with a PP only on the right hemisphere; L1 R0: subjects with a PP only on the left; L0 R0: subjects without PPs; L1 R1: subjects with PPs in both hemispheres.

STable 1. Configuration percentages corresponding to Fig 4.

	L1 R1	**L0 R0**	**L1 R0**	**L0 R1**
STAP	11.2%	33.8%	48.7%	6.3%
calcarine a b (34, 35)	8.9%	55.1%	17.3%	18.7%
calcarine b c (35, 36)	31.0%	32.2%	17.3%	19.5%
central a b (10, 11)	0.5%	93.3%	3.2%	3.0%
central b c (11, 12)	0.1%	92.6%	3.8%	3.5%
cingulate a b (37, 38)	34.4%	15.0%	29.3%	21.3%
cingulate b c (38, 39)	21.2%	28.5%	26.8%	23.4%
cingulate c d (39, 40)	21.6%	30.5%	21.1%	26.8%
cingulate d e (40, 41)	1.3%	85.5%	4.6%	8.5%
cingulate e f (41, 42)	0.6%	88.0%	4.3%	7.1%
collateral a b (30, 31)	53.9%	20.9%	12.8%	12.4%
collateral b c (31, 32)	12.1%	49.9%	18.9%	19.1%
collateral c d (32, 33)	53.0%	11.2%	15.7%	20.0%
inf frontal a b (5, 6)	52.7%	9.6%	19.1%	18.5%
inf frontal b c (6, 7)	50.7%	14.9%	15.6%	18.8%
inf temporal a b (23, 24)	61.0%	6.3%	21.8%	10.9%
inf temporal b c (24, 25)	57.4%	6.6%	17.0%	19.0%
inf temporal c d (25, 26)	73.4%	2.0%	12.1%	12.6%
intraparietal a b (16, 17)	60.6%	9.4%	7.3%	22.7%
intraparietal b c (17, 18)	3.8%	75.1%	6.7%	14.4%
occipito temporal a b (27, 28)	83.8%	1.1%	9.4%	5.7%
occipito temporal b c (28, 29)	47.8%	10.2%	17.9%	24.0%

postcentral a b (13, 14)	22.6%	30.0%	36.7%	10.7%
postcentral b c (14, 15)	7.2%	58.9%	17.7%	16.2%
precentral a b (8, 9)	35.2%	20.7%	15.5%	28.5%
sup frontal a b (1, 2)	54.1%	9.6%	16.0%	20.2%
sup frontal b c (2, 3)	45.1%	13.9%	20.5%	20.5%
sup frontal c d (3, 4)	49.9%	12.1%	16.7%	21.3%
sup temporal a b (19, 20)	29.5%	24.4%	26.1%	20.0%
sup temporal b c (20, 21)	4.0%	60.4%	30.7%	4.9%
sup temporal c d (21, 22)	16.6%	37.6%	33.2%	12.7%

L1 R1: proportion of subjects with a pli de passage in both hemispheres for this section; **L0 R0:** without a pli de passage; **L1 R0:** a pli de passage solely in the left hemisphere; **L0 R1:** solely in the right hemisphere.

STable 2. Pli de passage configuration percentages in all considered segments between any pair of pits in the main sulci.

	Asym PP (pval t-test)	**L PP**	**R PP**
STAP	37.3%* ($2.7 \cdot 10^{-19}$)	48.4%	11.1%
calcarine a b (34, 35)	3.5% (0.28)	15.7%	12.2%
calcarine b c (35, 36)	-3.5% (0.21)	38.4%	42.0%
central a b (10, 11)	0.4% (1.0)	2.0%	1.6%
central b c (11, 12)	-0.5% (1.0)	2.6%	3.0%
cingulate a b (37, 38)	8.3% (0.02)	54.4%	46.1%
cingulate b c (38, 39)	3.2% (0.45)	38.7%	35.5%
cingulate c d (39, 40)	-4.6% (0.24)	31.3%	36.0%
cingulate d e (40, 41)	-2.8% (0.31)	2.9%	5.7%
cingulate e f (41, 42)	-2.0% (0.71)	3.9%	5.9%
collateral a b (30, 31)	0.1% (1.0)	59.9%	59.8%
collateral b c (31, 32)	-0.4% (1.0)	25.5%	25.9%
collateral c d (32, 33)	-3.5% (0.18)	63.4%	67.0%
inf frontal a b (5, 6)	-0.1% (1.0)	65.9%	66.0%
inf frontal b c (6, 7)	-4.6% (0.07)	57.1%	61.7%
inf temporal a b (23, 24)	13.2%* ($3.0 \cdot 10^{-7}$)	77.6%	64.4%
inf temporal b c (24, 25)	-0.4% (0.9)	72.0%	72.3%
inf temporal c d (25, 26)	-0.1% (1.0)	82.4%	82.6%
intraparietal a b (16, 17)	-19.1%* ($1.6 \cdot 10^{-15}$)	58.8%	77.9%
intraparietal b c (17, 18)	-6.3% (0.02)	7.4%	13.8%
occipito temporal a b (27, 28)	4.3% (0.02)	86.1%	81.8%
occipito temporal b c (28, 29)	-5.9% (0.05)	60.5%	66.3%
postcentral a b (13, 14)	23.4%* ($1.8 \cdot 10^{-11}$)	51.1%	27.7%
postcentral b c (14, 15)	2.4% (0.61)	22.0%	19.5%
precentral a b (8, 9)	-12.4%* ($2.3 \cdot 10^{-5}$)	45.0%	57.4%
sup frontal a b (1, 2)	-6.1% (0.05)	57.1%	63.2%
sup frontal b c (2, 3)	-1.2% (0.74)	56.5%	57.7%
sup frontal c d (3, 4)	-5.4% (0.05)	58.5%	63.9%
sup temporal a b (19, 20)	3.5% (0.3)	46.6%	43.0%
sup temporal b c (20, 21)	21.7%* ($3.3 \cdot 10^{-8}$)	28.2%	6.5%
sup temporal c d (21, 22)	18.5%* ($1.2 \cdot 10^{-6}$)	40.5%	22.0%

Asym PP: hemispheric asymmetry of plis de passage in this section; **L PP:** proportion of subjects with a pli de passage in the left hemisphere in the considered section; **R PP:** respectively in the right hemisphere;
* significant asymmetry for Fisher exact test with $p < 0.001 \approx 0.05/31$ (Bonferroni correction).

STable 3. Heritability estimates for the presence of a *pli de passage* in the considered sulcal segments in the *left hemisphere*. Significant estimates after stringent Bonferroni correction ($p < 0.0008$) are marked with *.

Sulcal segment	h^2±SE(p)	Age	Age²	Sex	Age*Sex	Age²*Sex	Hispanic	eTIV	Hand
		p-val							
STAP	0.53±0.09 ($1.0\cdot10^{-7}$)*	0.49	0.19	0.06	0.73	0.76	0.4	0.21	0.3
calcarine a b (34, 35)	0.0±0.0 (0.5)	0.86	0.85	0.73	0.34	0.81	0.03	0.34	0.48
calcarine b c (35, 36)	0.3±0.1 ($1.2\cdot10^{-3}$)	0.59	0.12	0.68	0.92	0.07	0.65	0.7	0.76
central a b (10, 11)	0.0±0.0 (0.5)	0.65	0.33	0.19	0.39	0.67	0.67	0.06	0.76
central b c (11, 12)	0.37±0.43 (0.09)	0.27	0.75	0.45	$2.7\cdot10^{-3}$	0.12	0.62	0.53	0.38
cingulate a b (37, 38)	0.21±0.01 (0.02)	0.1	0.39	0.9	0.04	0.56	0.65	0.46	0.3
cingulate b c (38, 39)	0.05±0.0 (0.29)	0.19	0.23	0.43	0.33	0.92	0.88	0.86	0.64
cingulate c d (39, 40)	0.0±0.09 (0.48)	0.97	0.33	0.72	0.73	0.67	0.84	0.62	0.83
cingulate d e (40, 41)	0.14±0.22 (0.26)	0.06	0.09	0.27	0.83	0.36	0.75	0.54	0.7
cingulate e f (41, 42)	0.13±0.14 (0.34)	0.59	0.22	0.94	0.64	0.05	0.44	0.81	0.26
collateral a b (30, 31)	0.33±0.12 ($3.5\cdot10^{-4}$)*	0.48	0.59	0.9	0.78	0.93	0.34	0.47	0.74
collateral b c (31, 32)	0.17±7.91 (0.04)	0.65	0.99	0.04	0.02	0.72	0.25	0.86	0.38
collateral c d (32, 33)	0.26±0.11 ($5.3\cdot10^{-3}$)	0.19	0.48	0.3	0.06	0.21	0.03	0.51	0.84
inf frontal a b (5, 6)	0.0±0.0 (0.5)	0.16	0.12	0.86	0.02	0.04	0.56	0.82	0.6
inf frontal b c (6, 7)	0.14±0.04 (0.09)	0.41	0.93	0.02	0.1	0.73	0.95	0.89	0.39
inf temporal a b (23, 24)	0.08±0.13 (0.27)	0.37	0.04	0.04	0.18	0.02	0.25	0.02	0.1
inf temporal b c (24, 25)	0.12±0.12 (0.14)	0.64	0.98	0.76	0.91	0.73	0.36	0.47	0.78
inf temporal c d (25, 26)	0.17±0.14 (0.11)	0.62	0.8	0.81	0.68	0.28	0.88	0.09	0.91
intraparietal a b (16, 17)	0.28±0.04 ($5.1\cdot10^{-3}$)	0.3	0.18	0.01	0.42	0.34	0.8	0.23	0.16
intraparietal b c (17, 18)	0.21±0.05 (0.07)	0.38	0.83	0.5	0.14	0.46	0.58	0.84	0.79
occipito temporal a b (27, 28)	0.0±0.0 (0.5)	0.24	1.0	0.02	0.45	0.73	0.44	0.23	0.52
occipito temporal b c (28, 29)	0.0±0.0 (0.5)	0.13	0.79	0.93	0.31	0.62	0.26	0.19	0.43
postcentral a b (13, 14)	0.22±0.1 (0.01)	0.16	0.96	0.11	0.22	0.48	1.0	0.02	0.32
postcentral b c (14, 15)	0.0±0.0 (0.5)	0.55	0.67	0.38	0.75	0.2	0.48	0.87	0.15
precentral a b (8, 9)	0.17±0.05 (0.04)	0.34	0.15	0.16	0.25	0.46	0.85	0.92	0.35
sup frontal a b (1, 2)	0.12±0.06 (0.13)	0.8	0.74	0.75	0.72	0.36	0.46	0.82	0.56
sup frontal b c (2, 3)	0.09±0.08 (0.18)	0.61	0.83	0.07	0.29	0.54	0.43	0.72	0.23
sup frontal c d (3, 4)	0.12±0.11 (0.12)	0.27	0.25	0.58	0.12	0.21	0.49	0.43	0.24
sup temporal a b (19, 20)	0.2±0.08 (0.02)	0.51	0.27	0.41	0.44	0.69	0.73	0.12	0.94
sup temporal b c (20, 21)	0.33±0.08 ($5.9\cdot10^{-4}$)*	0.7	0.28	0.3	0.92	0.93	0.09	0.51	0.99
sup temporal c d (21, 22)	0.16±0.1 (0.05)	0.59	0.62	0.07	0.81	0.76	0.51	0.53	0.07

STable 4. Heritability estimates for the presence of a *pli de passage* in the considered sulcal segments in the *right hemisphere*. Significant estimates after stringent Bonferroni correction ($p < 0.0008$) are marked with *.

Sulcal segment	h^2±SE(p)	Age	Age²	Sex	Age*Sex	Age²*Sex	Hisp.	eTIV	Hand
		p-val							
STAP	0.27±0.15 (0.03)	1.0	0.69	0.85	0.92	0.93	0.8	0.36	0.33
calcarine a b (34, 35)	0.15±0.11 (0.1)	0.72	0.76	0.43	0.7	0.1	0.53	0.06	0.5
calcarine b c (35, 36)	0.48±0.1 ($1.8\cdot10^{-6}$)*	0.02	0.01	0.07	0.02	0.08	0.54	0.88	0.67
central a b (10, 11)	0.59±0.21 ($6.6\cdot10^{-3}$)	0.52	0.55	0.4	0.39	0.86	0.43	0.85	0.39
central b c (11, 12)	0.19±0.21 (0.26)	0.93	0.8	0.78	0.9	0.51	0.74	0.64	0.75
cingulate a b (37, 38)	0.03±0.06 (0.36)	0.89	0.46	0.96	0.15	0.66	0.21	0.16	0.78
cingulate b c (38, 39)	0.17±0.42 (0.04)	0.55	0.56	0.09	0.44	0.81	0.11	0.41	0.23
cingulate c d (39, 40)	0.04±0.01 (0.32)	0.38	0.78	0.25	0.66	0.84	0.7	0.44	0.72
cingulate d e (40, 41)	0.35±0.08 (0.02)	0.21	0.39	0.41	0.81	0.24	0.94	0.95	0.64
cingulate e f (41, 42)	0.0±0.0 (0.5)	0.19	0.82	0.49	0.89	0.62	0.63	0.28	0.54
collateral a b (30, 31)	0.33±0.05 ($8.5\cdot10^{-4}$)	0.61	0.75	$9.5\cdot10^{-4}$	0.94	0.09	0.64	0.85	0.91
collateral b c (31, 32)	0.04±0.1 (0.35)	0.57	0.67	0.95	0.55	0.19	0.76	0.08	1.0
collateral c d (32, 33)	0.4±0.11 ($1.7\cdot10^{-4}$)*	0.43	0.29	0.01	0.2	0.07	0.86	0.24	0.01
inf frontal a b (5, 6)	0.17±0.11 (0.05)	0.1	0.26	$9.3\cdot10^{-3}$	0.04	0.14	0.92	0.57	0.42
inf frontal b c (6, 7)	0.23±0.1 (0.01)	0.22	0.07	0.5	0.69	0.18	0.04	0.08	0.26
inf temporal a b (23, 24)	0.15±0.11 (0.08)	0.13	$4.7\cdot10^{-3}$	0.14	0.53	0.02	0.09	0.09	0.44
inf temporal b c (24, 25)	0.04±0.12 (0.35)	0.1	0.1	0.2	0.28	$8.4\cdot10^{-3}$	0.63	0.04	0.38
inf temporal c d (25, 26)	0.31±0.13 ($9.0\cdot10^{-3}$)	0.08	0.51	0.13	0.37	0.04	0.85	0.4	0.47
intraparietal a b (16, 17)	0.06±0.14 (0.34)	0.17	0.37	0.02	0.04	0.04	0.77	0.11	0.08
intraparietal b c (17, 18)	0.12±0.13 (0.18)	0.57	0.09	$1.2\cdot10^{-3}$	0.57	0.1	0.22	0.94	0.17
occipito temporal a b (27, 28)	0.35±0.17 (0.02)	0.42	0.15	0.43	0.84	0.25	0.67	0.21	0.05
occipito temporal b c (28, 29)	0.16±0.0 (0.07)	0.37	0.43	0.22	0.2	0.45	0.93	0.3	0.32
postcentral a b (13, 14)	0.04±0.08 (0.35)	0.73	0.24	0.32	0.98	0.76	0.48	0.81	$5.5\cdot10^{-3}$
postcentral b c (14, 15)	0.37±0.1 ($3.2\cdot10^{-4}$)*	0.55	0.04	0.18	0.63	0.61	0.89	0.85	0.85
precentral a b (8, 9)	0.19±0.1 (0.03)	0.68	$8.0\cdot10^{-3}$	$5.6\cdot10^{-3}$	0.61	$1.8\cdot10^{-4}$	0.8	0.56	0.41
sup frontal a b (1, 2)	0.11±0.11 (0.17)	0.61	0.53	0.34	0.82	0.45	0.55	0.05	0.01
sup frontal b c (2, 3)	0.0±0.0 (0.5)	0.08	0.04	0.53	$6.6\cdot10^{-3}$	0.03	0.88	1.0	0.04
sup frontal c d (3, 4)	0.25±0.09 (0.02)	0.4	0.73	0.69	0.93	0.78	0.52	0.48	0.99
sup temporal a b (19, 20)	0.28±0.3 ($1.9\cdot10^{-3}$)	0.27	0.12	0.32	0.32	0.4	0.99	0.83	0.98
sup temporal b c (20, 21)	0.0±0.0 (0.5)	0.9	0.43	$3.0\cdot10^{-3}$	0.32	0.6	0.32	0.1	0.92
sup temporal c d (21, 22)	0.01±0.11 (0.45)	0.94	0.63	$6.6\cdot10^{-4}$	0.29	0.03	0.81	0.89	0.02

STable 5. Pearson correlations between the MATH task activation in each areal and the asymmetry index in the STAP and for the DPF and Geodesic Depth profiles. Activations are considered separately in the Left and Right hemispheres. Only areals with at least one significant correlation are displayed. (** $p < 0.005$, * $p < 0.05$, uncorrected).

Areals – HCP parcellation	Corr. AI_{DPF} vs activations		Corr. AI_{GD} vs activations	
	Left	**Right**	**Left**	**Right**
Area 25	0.079 (0.03)*	0.028 (0.43)	0.052 (0.15)	0.005 (0.9)
Area 31pd	-0.076 (0.03)*	-0.05 (0.16)	-0.057 (0.11)	-0.036 (0.31)
Area FST	-0.068 (0.06)	-0.059 (0.1)	-0.073 (0.04)*	-0.088 (0.01)*
Area IFJp	0.027 (0.45)	-0.08 (0.03)*	0.01 (0.78)	-0.078 (0.03)*
Area IntraParietal 0	-0.035 (0.33)	-0.072 (0.04)*	-0.054 (0.13)	-0.095 ($8 \cdot 10^{-3}$)*
Area Lateral Occipital 2	-0.067 (0.06)	-0.015 (0.68)	-0.08 (0.02)*	-0.032 (0.37)
Area PGp	-0.031 (0.39)	-0.061 (0.09)	-0.037 (0.3)	-0.073 (0.04)*
Area PH	-0.065 (0.07)	-0.051 (0.16)	-0.077 (0.03)*	-0.058 (0.1)
Area STSd posterior	0.118 ($9 \cdot 10^{-4}$)**	0.056 (0.12)	0.105 ($3 \cdot 10^{-3}$)**	0.023 (0.52)
Area TG Ventral	0.075 (0.04)*	0.022 (0.53)	0.069 (0.05)	-0.014 (0.7)
Area Temporo-Parieto-Occipital Junction 1	0.072 (0.04)*	0.047 (0.19)	0.032 (0.36)	0.021 (0.56)
Area V3A	-0.038 (0.29)	-0.061 (0.09)	-0.043 (0.23)	-0.081 (0.02)*
Area V4t	-0.075 (0.03)*	-0.045 (0.21)	-0.086 (0.02)*	-0.057 (0.11)
Area V6A	-0.019 (0.59)	-0.051 (0.15)	-0.021 (0.56)	-0.071 (0.05)*
Area dorsal 23 a+b	0.071 (0.05)*	0.038 (0.28)	0.067 (0.06)	0.035 (0.33)
Auditory 4 Complex	-0.022 (0.54)	0.01 (0.77)	-0.08 (0.02)*	-0.021 (0.56)
Hippocampus	-0.023 (0.52)	-0.086 (0.02)*	-0.01 (0.79)	-0.078 (0.03)*
IntraParietal Sulcus Area 1	-0.071 (0.05)*	-0.027 (0.46)	-0.076 (0.03)*	-0.041 (0.25)
Medial Superior Temporal Area	-0.059 (0.1)	-0.067 (0.06)	-0.055 (0.12)	-0.093 ($9 \cdot 10^{-3}$)*
Middle Temporal Area	-0.078 (0.03)*	-0.041 (0.25)	-0.068 (0.06)	-0.075 (0.03)*
Para-Insular Area	-0.033 (0.36)	-0.037 (0.29)	-0.036 (0.31)	-0.082 (0.02)*
ParaBelt Complex	-0.077 (0.03)*	-0.007 (0.85)	-0.131 ($2 \cdot 10^{-4}$)**	-0.026 (0.47)
ParaHippocampal Area 1	-0.027 (0.46)	-0.045 (0.2)	-0.049 (0.17)	-0.075 (0.04)*
ParaHippocampal Area 3	-0.003 (0.94)	-0.086 (0.02)*	-0.039 (0.27)	-0.088 (0.01)*
Ventral Visual Complex	-0.027 (0.45)	-0.054 (0.13)	-0.043 (0.23)	-0.091 (0.01)*
VentroMedial Visual Area 1	0.015 (0.67)	-0.054 (0.13)	0.009 (0.8)	-0.087 (0.01)*
VentroMedial Visual Area 3	-0.055 (0.12)	-0.081 (0.02)*	-0.067 (0.06)	-0.108 ($2 \cdot 10^{-3}$)**

STable 6. Pearson correlations between the STORY task activation in each areal and the asymmetry index in the STAP and for the DPF and Geodesic Depth profiles. Activations are considered separately in the Left and Right hemispheres. Only areals with at least one significant correlation are displayed. (** $p < 0.005$, * $p < 0.05$, uncorrected).

Areals – HCP parcellation	**Corr. AI_{DPF} vs activations**		**Corr. AI_{GD} vs activations**	
	Left	**Right**	**Left**	**Right**
Area 1	-0.012 (0.74)	0.072 (0.04)*	-0.003 (0.92)	0.038 (0.29)
Area 10r	-0.015 (0.68)	-0.058 (0.11)	-0.016 (0.66)	-0.077 (0.03)*
Area 11l	0.071 (0.05)*	-0.008 (0.83)	0.076 (0.03)*	-0.029 (0.42)
Area 31pd	-0.067 (0.06)	-0.062 (0.08)	-0.082 (0.02)*	-0.062 (0.08)
Area IntraParietal 0	-0.013 (0.73)	-0.037 (0.3)	-0.028 (0.43)	-0.073 (0.04)*
Area Lateral Occipital 2	-0.07 (0.05)*	0.002 (0.96)	-0.088 (0.01)*	-0.036 (0.32)
Area STSd posterior	$0.14\ (8\cdot10^{-5})$**	0.085 (0.02)*	$0.117\ (1\cdot10^{-3})$**	0.044 (0.22)
Area Temporo-Parieto-Occipital Junction 1	0.074 (0.04)*	0.06 (0.09)	0.029 (0.42)	0.028 (0.44)
Area Temporo-Parieto-Occipital Junction 2	-0.061 (0.09)	0.019 (0.6)	$-0.101\ (5\cdot10^{-3})$**	0.004 (0.92)
Area V3CD	-0.048 (0.18)	-0.055 (0.12)	-0.04 (0.27)	-0.07 (0.05)*
Area V6A	-0.027 (0.46)	-0.071 (0.05)*	-0.035 (0.33)	-0.089 (0.01)*
Area dorsal 23 a+b	0.069 (0.05)	0.06 (0.09)	0.073 (0.04)*	0.064 (0.07)
Auditory 5 Complex	0.067 (0.06)	0.076 (0.03)*	0.043 (0.23)	0.023 (0.52)
Hippocampus	-0.004 (0.9)	-0.076 (0.03)*	0.019 (0.6)	-0.047 (0.19)
Insular Granular Complex	0.012 (0.74)	0.074 (0.04)*	0.003 (0.94)	0.042 (0.24)
IntraParietal Sulcus Area 1	-0.066 (0.06)	-0.033 (0.36)	-0.072 (0.04)*	-0.048 (0.18)
ParaBelt Complex	-0.074 (0.04)*	-0.008 (0.83)	$-0.129\ (3\cdot10^{-4})$**	-0.023 (0.52)
PeriSylvian Language Area	-0.024 (0.51)	0.028 (0.44)	-0.082 (0.02)*	0.006 (0.86)
Primary Auditory Cortex	0.049 (0.17)	0.077 (0.03)*	0.04 (0.27)	0.045 (0.2)
Seventh Visual Area	-0.049 (0.17)	-0.047 (0.19)	-0.063 (0.08)	-0.071 (0.05)*
Superior 6-8 Transitional Area	0.088 (0.01)*	0.009 (0.8)	0.085 (0.02)*	0.011 (0.76)
Ventral Area 6	0.004 (0.9)	0.083 (0.02)*	-0.013 (0.71)	0.033 (0.36)

STable 7. Pearson correlations between the HCP cognitive scores and the asymmetry index in the STAP and for the DPF and Geodesic Depth profiles. (* $p < 0.05$, uncorrected).

Cognitive Scores	AI_{DPF}	AI_{GD}
Cognitive Flexibility	-0.016 (0.65)	-0.007 (0.84)
Inhibition	-0.015 (0.67)	0.004 (0.91)
Verbal Episodic Memory RTC	0.078 (0.03)*	0.078 (0.03)*
Verbal Episodic Memory TOT	-0.048 (0.17)	-0.044 (0.2)
Working Memory	0.015 (0.66)	0.04 (0.25)
Fluid Intelligence CR	0.004 (0.92)	-0.01 (0.77)
Fluid Intelligence RTCR	0.011 (0.74)	0.0 (0.99)
Fluid Intelligence SI	-0.007 (0.83)	-0.001 (0.98)
Episodic Memory	0.019 (0.6)	0.009 (0.8)
Vocabulary Comprehension	0.016 (0.65)	-0.005 (0.89)
Processing Speed	-0.017 (0.62)	-0.02 (0.57)
Reading Decoding	0.022 (0.53)	-0.002 (0.95)
Language Task Acc	0.011 (0.75)	-0.028 (0.43)
Language Task Math Acc	-0.018 (0.62)	-0.064 (0.07)
Language Task Math Avg Difficulty Level	-0.035 (0.33)	-0.04 (0.26)
Language Task Math Median RT	-0.025 (0.49)	-0.007 (0.85)
Language Task Median RT	-0.02 (0.57)	-0.019 (0.6)
Language Task Story Acc	0.041 (0.25)	0.031 (0.38)
Language Task Story Avg Difficulty Level	-0.014 (0.7)	-0.048 (0.18)
Language Task Story Median RT	-0.009 (0.81)	-0.024 (0.51)

All scores have been measured by the HCP. They followed protocols described in the NIH toolbox.
Fluid Intelligence: measured by the Penn Progressive Matrices Test (CR: Number of Correct Responses, SI: Total Skipped Items, RT: Median Reaction Time for CR)
Language/Vocabulary Comprehension: measured by the Picture Vocabulary Test
Processing Speed: measured by the Pattern Comparison Processing Speed Test
Verbal Episodic Memory: measured by the Penn Word Memory Test (CR: Number of Correct Responses, RT: Median Reaction Time for CR)
Working memory: measured by the List Sorting Working Memory Test
Episodic Memory: measured by the Picture Sequence Memory Test
Executive Function/Cognitive Flexibility: measured by the Dimensional Change Card Sort Test
Executive Function/Inhibition: measured by the Flanker Inhibitory Control and Attention Test
Language/Reading Decoding: measured by the Oral Reading Recognition Test
More details can be found at:
https://wiki.humanconnectome.org/display/PublicData/HCP+Data+Dictionary+Public-+500+Subject+Release
Language Task Acc: Average accuracy during the task fMRI HCP Language (MATH & STORY)
Language Task Math Acc: Accuracy during MATH task fMRI
Language Task Math Avg Difficulty Level: Average difficulty level during MATH task fMRI
Language Task Math Median RT: Median reaction time during MATH task fMRI
Language Task Median RT: Average median RT during the task fMRI HCP Language (MATH & STORY)
Language Task Story Acc: Accuracy during STORY task fMRI
Language Task Story Avg Difficulty Level: Average difficulty level during STORY task fMRI
Language Task Story Median RT: Median reaction time during STORY task fMRI

Chapter 3. Shared genetic variance between cognitive performance and brain activations in language and math tasks

1. Introduction to the chapter

In the two previous chapters, we underlined a possibly asymmetric genetic control on the temporal lobe asymmetric structures, namely the sulcal pits and *plis de passage*.

In neuroscience, a frequently asked question is the relationship between structure and function. Therefore, in this chapter, we proposed to indirectly address this theme by investigating the heritability of functional activation during language tasks also in the HCP cohorts and their correlation with human cognitive performance. Additionally, we assessed the shared genetic between these brain activations and cognitive ability, quantified by fluid intelligence, working memory and language standard tests.

2. Abstract

Cognitive performance is highly heritable. However, little is known about common genetic influences on cognitive ability and brain activation when engaged in a cognitive task. The Human Connectome Project (HCP) offers a unique opportunity to study this shared genetic etiology with an extended pedigree of 785 individuals. To investigate this common genetic origin, we took advantage of the HCP dataset, which includes both language and mathematics activation tasks. Using the HCP multimodal parcellation, we identified areals in which inter-individual functional MRI (fMRI) activation variance was significantly explained by genetics. Then, we performed bivariate genetic analyses between the neural activations and behavioral scores, corresponding to the fMRI task accuracies, fluid intelligence, working memory and language performance. We observed that several parts of the language network along the superior temporal sulcus, as well as the angular gyrus belonging to the math processing network, are significantly genetically correlated with these indicators of cognitive performance. This shared genetic etiology provides insights into the brain areas where the human-specific genetic repertoire is expressed. Studying the association of polygenic risk scores, using variants associated with human cognitive ability and brain activation, would provide an opportunity to better understand where these variants are influential.

3. Introduction

Language and math functions in humans are extensively studied in fundamental neuroscience as distinctive abilities of human lineage. They are frequently assessed through neuroimaging to provide endophenotypes (Peterson and Pennington, 2012; Price and Ansari, 2013). They are used as a way to classify the broad behavioral symptoms of language impairments into stable phenotypes that in turn are candidates to search for potential associations with either medical treatment responses or genetic profiles (Docherty et al., 2010; Mascheretti et al., 2017). Structural properties observed using magnetic resonance imaging (MRI) or activations observed with functional MRI (fMRI) have been used to produce such endophenotypes (Männel et al., 2015). These can reveal differences between control and disease groups in language-specific regions (Friederici, 2006) or distinguish disorder subtypes such as grammatical-SLI (specific language impairment) (van der Lely and Pinker, 2014).

Imaging-genetics resources, such as the Human Connectome Project (HCP) provide an unprecedented opportunity to study the variability of such endophenotypes in control subjects, as well as to determine their potential heritability or association with genetics. Following up on these ideas, we first proposed to study the additive genetic variance involved in fMRI activation differences among typically developed individuals. We used the pedigree data from the HCP language comprehension and verbal math fMRI tasks. These tasks recruit regions directly implicated in brain disorders, such as Broca's area in SLI (Leonard, 2003), the angular gyrus in developmental dyslexia (Peterson and Pennington, 2012) and the intraparietal in dyscalculia (Price and Ansari, 2013). A few studies have already attempted to estimate the narrow sense heritability of brain activations for various tasks. They notably include digit and n-back working memory (Blokland et al., 2011; Koten et al., 2009), visual math subtraction (Pinel and Dehaene, 2013), and stimuli such as written words, faces and spoken language (Pinel et al., 2015). However, these studies had relatively small sample sizes for reliably detecting heritability estimates ranging between 25 and 50%. The previous samples included 30 subjects (10 triplets of male monozygotic (MZ) twins with one additional brother) (Koten et al., 2009), 64 subjects (19 MZ and 13 dizygotic (DZ) pairs) (Pinel et al., 2015; Pinel and Dehaene, 2013) or 319 subjects (75 MZ and 66 DZ pairs, 37 unpaired) (Blokland et al., 2011). In addition to including a larger sample size, the HCP data were processed using state of the art methods, providing 2-mm isotropic resolution and finer inter-individual registration. In particular, the so-called grayordinate activations are computed on the surface of the cortex (Barch et al., 2013) for each individual, and inter-subject fMRI alignment is performed using areal-feature-based registration (Robinson et al., 2014). The grayordinate approach refers to fMRI analyses performed on the cortical surface, as opposed to a volume-based approach. The same idea was applied to build the multimodal parcellation of the human cerebral cortex (Glasser et al., 2016) onto which we decomposed our heritability analyses, enabling us to map the genetic influence on fMRI activations on a very fine scale.

Furthermore, it is known that neural activation endophenotypes from MRI may reflect not only impairments in language but also differences in cognitive scores. For example, weaker left-lateralizations have been reported for some developmental language disorders (Bishop, 2013), and in normal populations, fMRI activations during simple tasks correlate with various cognitive scores. Notably, single digit calculation fMRI activations are predictive of high school math scores (Price et al., 2013), and the fronto-parietal functional connectivity in children performing a task that required them to match Arabic numbers to an array of dots correlated with their score on a standardized math test (Emerson and Cantlon, 2012). Using HCP data and in line with these approaches, we show in this chapter how variations in language related fMRI activations correlate with cognitive abilities assessed by the median reaction time (RT), average accuracy and difficulty level during the HCP language and math tasks. Remarkably, recent studies have shown that, beyond the age-related heritability of general cognitive ability (Davies et al., 2011; Plomin and Deary, 2015) and of various indicators of academic performance (Haworth et al., 2008), these scores are highly pleiotropic (Plomin and Deary, 2015; Rimfeld et al., 2015) [pleiotropy occurs when one gene regulates one or more phenotypic traits].

This raises the question of the potential pleiotropy between neural activations and cognitive abilities. Thus, as a second contribution, we studied the shared genetic variance of fMRI activations and cognitive performance scores measured during the MRI session or behavioral scores acquired independently from the task. We studied behavioral variables measured by the HCP using standardized tests from the National Institute of Health (NIH): fluid intelligence, working memory, and language assessments such as vocabulary comprehension and oral reading decoding. Details of these variables and their heritability estimates can be found in **Table S1**, and how well they correlate phenotypically and genetically with the behavioral scores measured during the task is reported in **Table S2**.

Recent genome wide association studies have unveiled new loci and genes influencing human cognitive performance (e.g. human intelligence (Sniekers et al., 2017), general cognitive function (Davies et al., 2016; Trampush et al., 2017) and educational attainment (Davies et al., 2016)) and possibly intelligence as a construct in differential psychology (Plomin and Deary, 2015). However, for these human-specific characteristics, little is known about the underlying integration mechanism of molecular functions or the brain areas where they are most influential. The shared genetic etiology investigated in this work provides new perspectives to decipher the basis of cognitive abilities such as language in humans. This study had two major aims: (1) to estimate the heritability of fMRI activations during story comprehension and math tasks; and (2) to determine the shared genetic etiology between these activations and cognitive performance.

4. Material and Methods

4.1. The language task

The HCP language task was developed by Binder and colleagues (Binder et al., 2011). In the story blocks, participants were presented with brief auditory stories adapted from Aesop's fables, followed by a 2-alternative forced-choice question to check the participants' understanding of the story topic. The example provided in the original chapter is *"For example, after a story about an eagle that saves a man who had done him a favor, participants were asked, "Was that about revenge or reciprocity?""*. In the math blocks, participants were also presented auditory series of addition and subtraction (e.g., "fourteen plus twelve"), followed by "equals" and then two choices (e.g., "twenty-nine or twenty-six"). To ensure similar level of difficulty across participants, math trials automatically adapted to the participants responses. As shown by Binder and colleagues (Binder et al., 2011), the story and math trials were well matched in terms of duration, auditory and phonological input, and attention demand. Furthermore, they were likely to elicit distinct brain activation – on the one hand, anterior temporal lobes classically involved in semantic processing, and parietal cortex on the other hand, classically involved in numerical processing, thus spanning a broad set of regions involved in conceptual semantic processing.

4.2. HCP task fMRI analysis

The analysis of fMRI data was carried out by the HCP consortium and we describe briefly their pipeline (Barch et al., 2013). The Story predictor covered the variable duration of a short story, question, and response period (~30 s). The Math predictor covered the duration of a set of math questions designed to roughly match the duration of the story blocks. The grayordinate data for individual task runs were processed in a level 1 analysis. Activity estimates were computed for the preprocessed functional time series from each run using a general linear model (GLM) implemented in FSL's FILM (FMRIB's Improved Linear Model with autocorrelation correction) (Woolrich et al., 2001). Predictors were convolved with a double gamma "canonical" hemodynamic response function (Glover, 1999) to generate the main model regressors. The two runs for each task and subject were then combined in a level 2 fixed-effects analysis (Barch et al., 2013), which we used as our phenotype. Fixed-effects analyses were conducted using FEAT (fMRI Expert Analysis Tool) to estimate the average effects across runs within-subjects, and then mixed-effects analyses treating subjects as random effects were conducted using FLAME (FMRIB's Local Analysis of Mixed Effects) to estimate the average effects of interest for the group third-level analysis. For the following genetic analyses, the FEAT outputs are used to form our phenotypes.

4.3. Phenotype definitions

To define our phenotypes, we consider separately the regression analyses on STORY and MATH tasks, and the contrast STORY-MATH. We used the beta values (pe1.dtseries.nii files) of the results of the level 2 analysis, which essentially average the level 1, i.e., the individual, runs. The contrasts were defined by the HCP in level 1 and averaged for level 2: thus, the grayordinate values of the beta and contrast values (cope1.dtseries.nii) are identical in this case, as they did not define any "new" contrasts specifically at level 2. Therefore, we could have used the cope1.dtseries.nii.files with no difference in results. We used the MSMAll registered the functional analysis results from HCP and the HCP multimodal parcellation (Glasser et al., 2016). We analyzed each of the 180 areals separately. We computed the median beta values in each areal for both hemispheres. These phenotypes constitute our proxy to estimate the activation in each part of the brain.

Moreover, we also included in our phenotypes the accuracy, reaction time and average difficulty level for the MATH and STORY tasks. We called these "behavioral scores", as opposed to the grayordinate activation phenotypes previously defined.

4.4. Bivariate genetic analyses

To assess the relationship between math dexterity/language comprehension and activation in brain areas, we computed the Pearson correlation between the median activation in each of the 180 areals of both hemispheres, and the behavioral scores.

Furthermore, we assessed the degree of shared genetic variance in the areals for which activation was significantly correlated with the behavioral scores; we performed a genetic correlation analysis using SOLAR, relying on the following model:

$\rho_p = \sqrt{h_a^2}\sqrt{h_b^2}\cdot\rho_g + \sqrt{1-h_a^2}\sqrt{1-h_b^2}\cdot\rho_e$, where Pearson's phenotypic correlation ρ_p is decomposed into ρ_g and ρ_e. ρ_g is the proportion of variability due to shared genetic effects and ρ_e that due to the environment, while h_a^2 and h_b^2 correspond to the previously defined narrow sense heritability for phenotypes *a* and *b*, respectively. In our case, one corresponds to the heritability of fMRI activation in one areal, while the second is the heritability of one of our behavioral scores.

5. Results

5.1. Task fMRI Activations in MATH and STORY tasks

Figure 1 shows the activations for MATH (vs the intercept of the general linear model (GLM) being considered as baseline), STORY and the contrast STORY - MATH. The intercept reflects the mean of the residual BOLD time series after removing variance explained by all other regressors. Both tasks show clear activations in the planum temporale and Heschl's gyrus area, reflecting the fact that the stimuli were presented in the auditory modality. The MATH task, in which participants were

requested to perform addition and subtraction, activates areas traditionally implicated in mathematical calculations, that is, the intraparietal sulcus, the middle frontal and the inferior temporal regions (Amalric and Dehaene, 2016; Rickard et al., 2000). The story listening task activates the language understanding network, encompassing bilateral temporal regions and left frontal regions (Pallier et al., 2011; Skeide and Friederici, 2016). As expected, the group activations for the STORY task are more left lateralized, notably in the left posterior superior temporal and inferior frontal regions, which correspond to Wernicke's and Broca's areas, respectively. Moreover, regions implicated in inhibition networks are also activated by these tasks (Erika-Florence et al., 2014; Simmonds et al., 2008), notably the middle frontal gyrus in the math task and the medial prefrontal cortex, implicated in motivation and execution, and above the anterior cingulate cortex, controlling selective attention (Etkin et al., 2011; Leisman et al., 2012). In addition, both tasks activate complementary networks; in particular, the math task deactivates the semantic and episodic memory processes, known as the default mode network, which is also active in resting or passive states (Binder et al., 2011). This last remark makes the STORY-MATH contrast particularly relevant for studying the genetic influence on activation specifically elicited by math and story tasks.

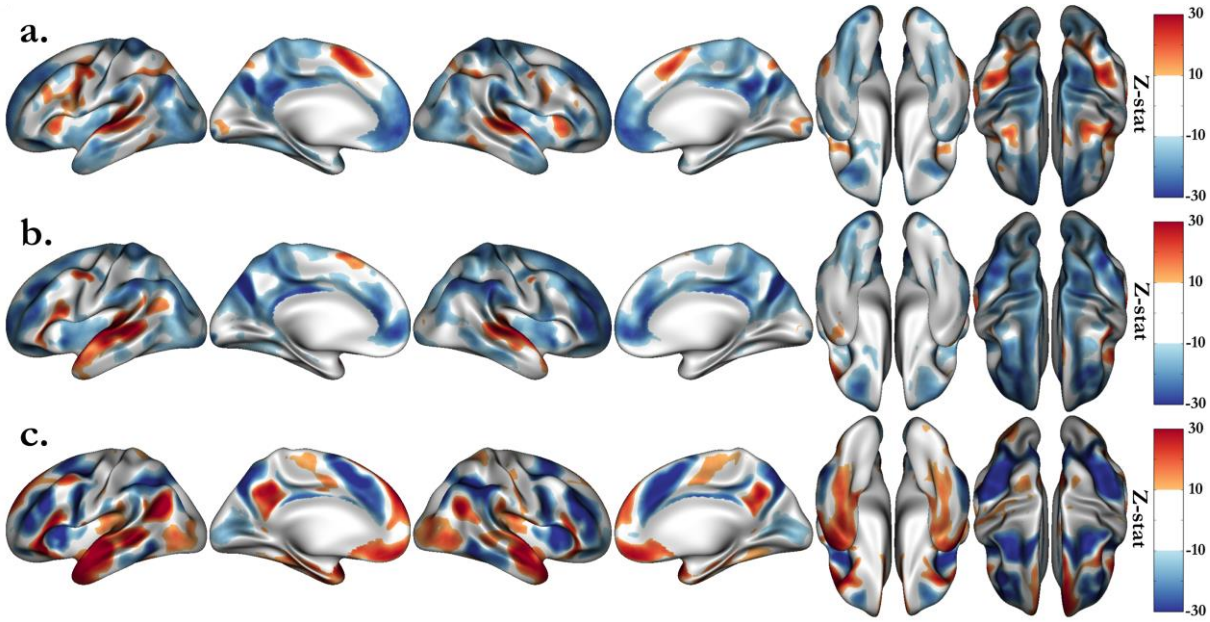

Figure 1. Group average activations for the HCP language tasks, including MATH a. and STORY b. blocks, and the STORY-MATH contrast c. Group maps are shown with a lower threshold of z = ± 10 and saturation from z = 30 to introduce the main areas activated by the tasks. Due to the large number of subjects, the associated p-values are significant; we arbitrarily set the thresholds to emphasize the regions that are known to be recruited by these tasks.

5.2. Univariate Genetic Analyses

We performed a cortex-wise heritability analysis on the median activation (β-value) in the 360 areals of the HCP multi-modal parcellation. After stringent Bonferroni correction ($p < 0.05/360 \approx 1.4 \cdot 10^{-4}$), we found 54 regions whose activations during the MATH task are heritable and 46 regions for the STORY task. These results are summarized in **Figure 2** and heritability estimates are included

in **Tables S3-S6**. The details and names of the areals can be found in the Supplementary Information of the chapter describing the multimodal parcellation of the human cerebral cortex (Glasser et al., 2016). For the MATH (resp. STORY) task, the heritability estimates range from 0.23 to 0.45, with the maximum in the left "Area PGp" corresponding to the angular gyrus (resp. 0.22 to 0.55, with the maximum in the left "PeriSylvian Language Area"). In addition, we performed heritability analysis using the median z-stat value in each areal instead of the median parameter estimate (β-value) and obtained similar results (**Fig S1**).

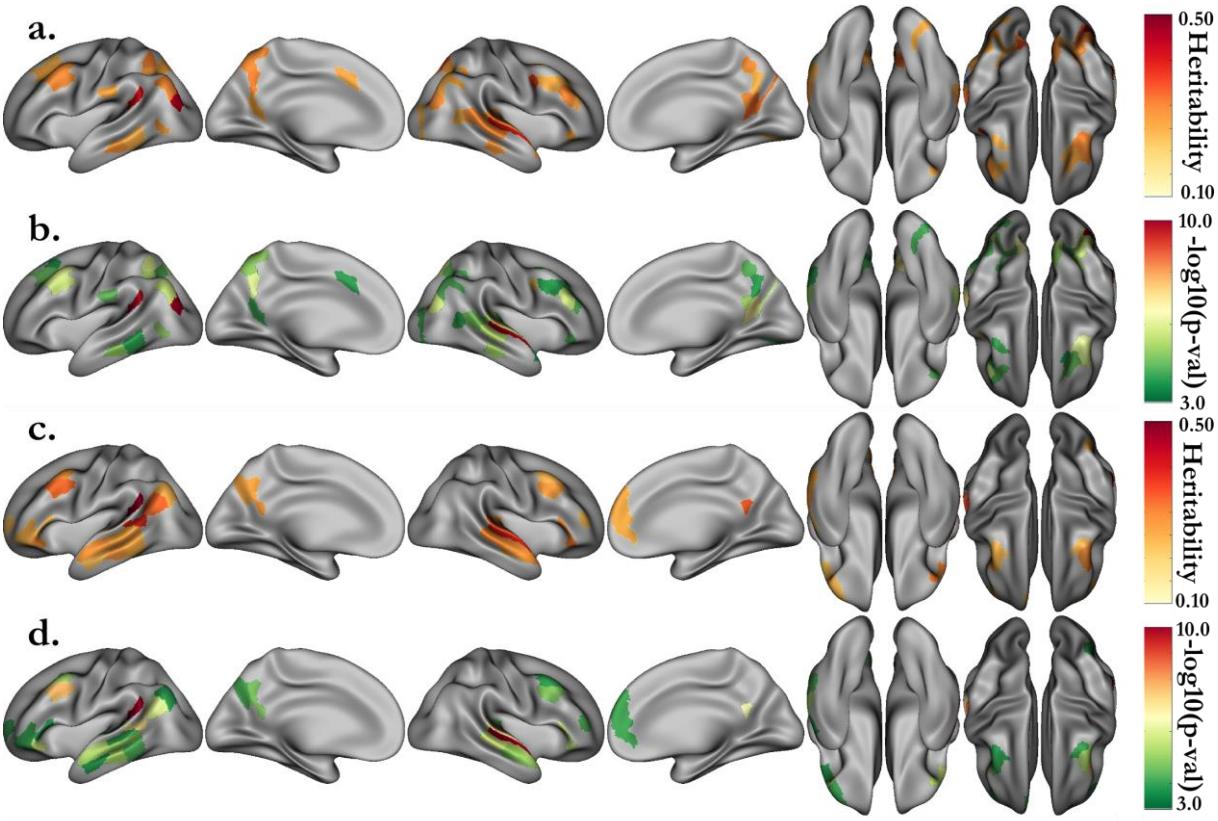

Figure 2. Heritability estimates for the activations of the MATH a. and STORY c. tasks, and their associated p-values (respectively, b. and d.). Only the estimates significant after correction ($p < 0.05/360$, with 180 areals in each hemisphere) are displayed. Activations correspond to the median parameter estimate (β) in each areal of the HCP multimodal parcellation.

The univariate genetic analysis of the activations associated with verbal math emphasizes mainly areals spanning the math network, including the intraparietal sulcus, middle frontal, inferior temporal and angular gyri. The analysis of activations associated with story comprehension distinctively underlines regions of the language network as bilaterally heritable. Among these regions are the superior temporal sulcus dorsal and ventral parts, Brodmann area (BA) 47 in Broca's area, and the middle frontal gyrus at the junction with the precentral sulcus. Interestingly, the heritability networks of the MATH and STORY tasks overlap very little except in the auditory cortex, around the planum temporale, in the frontal cortex (BA 8), and in the inferior temporal region.

Table 1 presents the heritability estimates of the behavioral scores gathered during the MRI scans. The global accuracy on the HCP language tasks, averaging the scores in the MATH and STORY tasks, was significantly heritable, with $h^2 = 0.34$, close to the traditionally high heritability

estimate of cognitive performance (Krapohl et al., 2014; Shakeshaft et al., 2013). The heritability estimates for the median reaction time (RT) were approximately 0.2. Furthermore, RT Story and RT Math were significantly correlated (phenotypic correlation: $\rho_p = 0.34$, genetic correlation: $\rho_g = 0.45$, **Table S2**). Regarding the accuracy and average difficulty level of the HCP language task, we observed that the MATH task variables have higher heritability estimates than those of the STORY task. This result might indicate a higher genetic influence on performance during simple arithmetic tasks than during language comprehension. However, this result needs to be considered in light of the different distribution patterns of MATH and STORY accuracies. The STORY accuracy reported by the HCP displays discrete values and might not be sufficiently informative (**Fig S2**). **Table S2** underlines a significant correlation between math and story accuracies ($\rho_p = 0.15$, $\rho_g = 0.27$). The discrete distribution of STORY accuracy likely occurs because each story lasted approximately 20-30s, few story questions were presented to the subjects, and most subjects tended to choose the correct answer in the two-alternative forced-choice question.

Table 1. Heritability estimates for the behavioral scores associated with the tasks. Language accuracy and reaction time (RT) correspond to the average of the respective MATH and STORY variables. The p-values associated with the covariates related to age and sex, ethnic group and education level are also displayed.

Trait	h^2±SE (p)	Age	Age²	Sex	Age*Sex	Age²*Sex	Hispanic	Educ	h^2_{cov}%
		p-val							
Language Accuracy	0.34 ± 0.06 ($2.3\cdot10^{-8}$)	0.49	0.75	0.01	0.96	0.22	0.97	$1.2\cdot10^{-7}$	7.2
Language RT	0.22 ± 0.07 ($8.4\cdot10^{-4}$)	0.44	0.91	0.69	0.85	0.95	0.71	0.04	0.5
Math Accuracy	0.4 ± 0.06 ($1.6\cdot10^{-10}$)	0.5	0.96	$9.2\cdot10^{-4}$	0.81	0.39	0.76	$1.9\cdot10^{-6}$	7.2
Math Difficulty Level	0.33 ± 0.07 ($1.0\cdot10^{-6}$)	0.53	0.17	0.02	0.61	0.05	0.42	$8.7\cdot10^{-8}$	7.9
Math Median RT	0.17 ± 0.07 ($7.4\cdot10^{-3}$)	0.6	0.41	0.78	0.82	0.69	0.26	0.01	1.1
Story Accuracy	0.18 ± 0.06 ($1.6\cdot10^{-3}$)	0.78	0.48	0.86	0.76	0.23	0.61	$2.2\cdot10^{-3}$	1.4
Story Difficulty Level	0.33 ± 0.07 ($1.3\cdot10^{-6}$)	0.66	0.43	0.81	0.44	0.28	0.91	0.11	0.0
Story Median RT	0.2 ± 0.07 ($1.4\cdot10^{-3}$)	0.41	0.63	0.39	0.59	0.68	0.45	0.39	0.0

5.3. Bivariate Genetic Analyses

We performed bivariate genetic analyses to quantify the shared genetic influence between intellectual performance, represented by the behavioral measures, and the neural activation in each areal. The genetic correlation estimates are usually subject to substantial sampling errors and therefore inaccurate. The large sample size of the HCP offers the opportunity to reduce the standard errors. The distribution of STORY accuracy values is concentrated on a small number of values (**Fig S2**), thus, we chose to use the average of the STORY and MATH accuracies as the behavioral score to characterize the individual performance. Thus, the results presented here concern the relationship between this average score and the activations or deactivations revealed by the contrast STORY-MATH (activation

map shown in **Figure 1.c**. As a first step of our analysis and to filter out the areals for which the neural activation was not significantly correlated with the behavioral score, we computed the phenotypic correlation between these two variables in each areal of the HCP multi-modal parcellation. **Figure 3. (a, b)** summarizes the phenotypic correlation and associated p-values, for areals significant after Bonferroni correction ($p < 0.05/360$). The language network is clearly encompassed along the left superior temporal sulcus (STS) and Broca's area, as well as in the anterior part of the right STS. The activations in the angular gyrus (area PGp), supporting the manipulation of numbers in verbal form(Dehaene et al., 2003), were also significantly correlated with the behavioral scores.

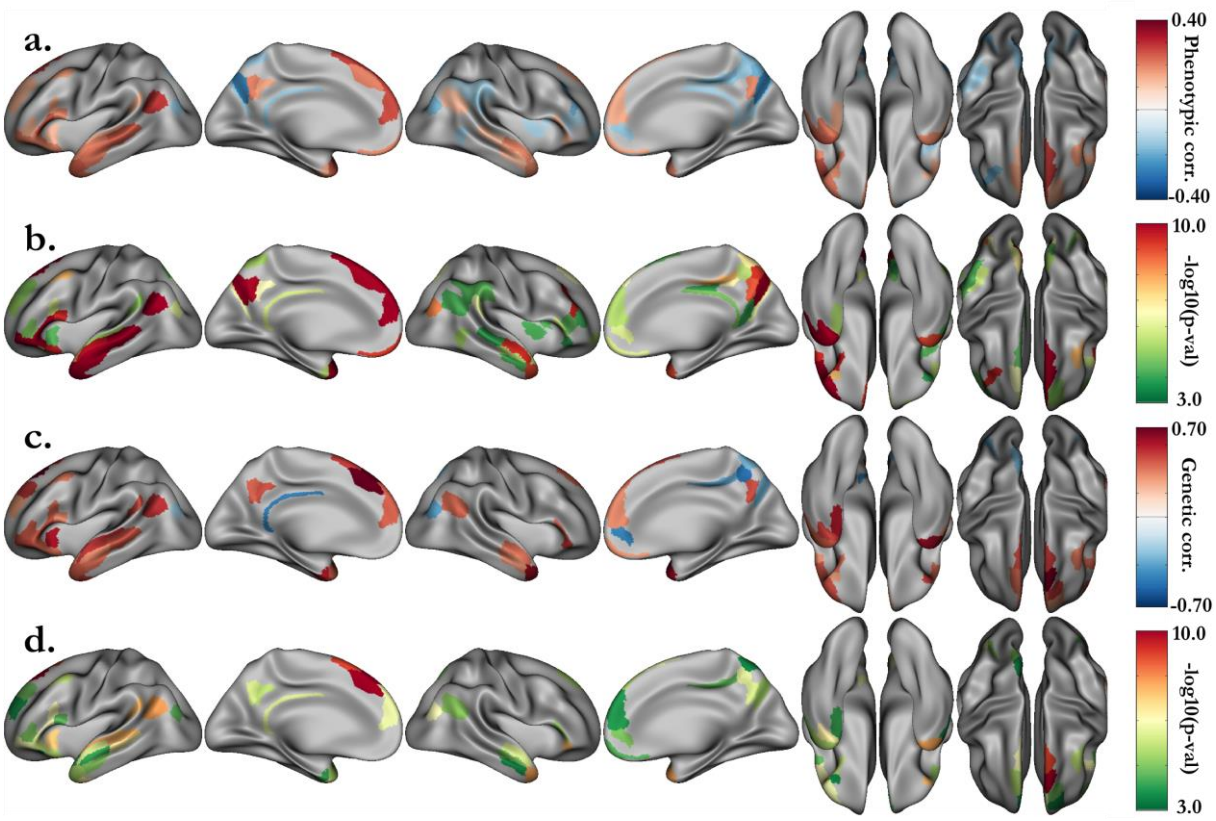

Figure 3. Bivariate genetic analysis results between HCP LANGUAGE task accuracy and activation for the STORY-MATH contrast in each areal. **a.** After strict Bonferroni correction ($p < 0.05/360$), significant phenotypic correlations between the language task accuracy (average of story and math accuracies) and the median activation of the contrast STORY-MATH in each areal, **b.** with their associated p-values. **c.** Proportion of variability due to shared genetic effects with **d.** their associated uncorrected p-values < 0.05.

Among the 360 areals of the HCP multimodal parcellation, 39 (resp. 38) were significantly phenotypically correlated and were kept for the bivariate analysis in the right (resp. left) hemisphere. The shared genetic variance estimates for these areals are presented **Figure 3 (c, d)** ($p < 0.05$ without correction), and detailed values can be found in **Tables S7 and S8**. With stringent Bonferroni correction the p-value threshold for ρ_g is $p < 0.05/(39+38) \approx 6.5 \cdot 10^{-4}$. Among the areals with significant shared genetic variance, we found the left anterior ventral insular area (AVI, $\rho_g = 0.61$) and the right angular gyrus (PGp, $\rho_g = -0.40$). Noticeably, in the left hemisphere areals, parts of the language network in the posterior STS had activations that shared significant genetic variance with language accuracy. These include the posterior ventral (STSv posterior, $\rho_g = 0.47$) and dorsal (STSd

posterior, ρ_g = 0.45) parts of the STS, adjacent to the auditory 5 complex area (A5, ρ_g = 0.54), the perisylvian language area (PSL, ρ_g = 0.47) and the temporo-intraparietal junction (PGi, ρ_g = 0.54). On the left hemisphere internal face, we also found the superior frontal language area (SFL, ρ_g = 0.61) and, adjacent to this areal the Brodmann 8 decomposed into medial (8Bm, ρ_g = 0.75) and lateral (8Bl, ρ_g = 0.73) parts. Additionally, we noted two right hemisphere regions implicated in language processing and significantly genetically correlated with the fMRI task average score: the temporal pole (area TG dorsal, TGd, ρ_g = 0.65) and the lateral part of Brodmann area 47 (47l, ρ_g = 0.51). The latter is adjacent to Brodmann areas 44 and 45 in the inferior frontal, which are connected through the arcuate fasciculus with the language temporal regions.

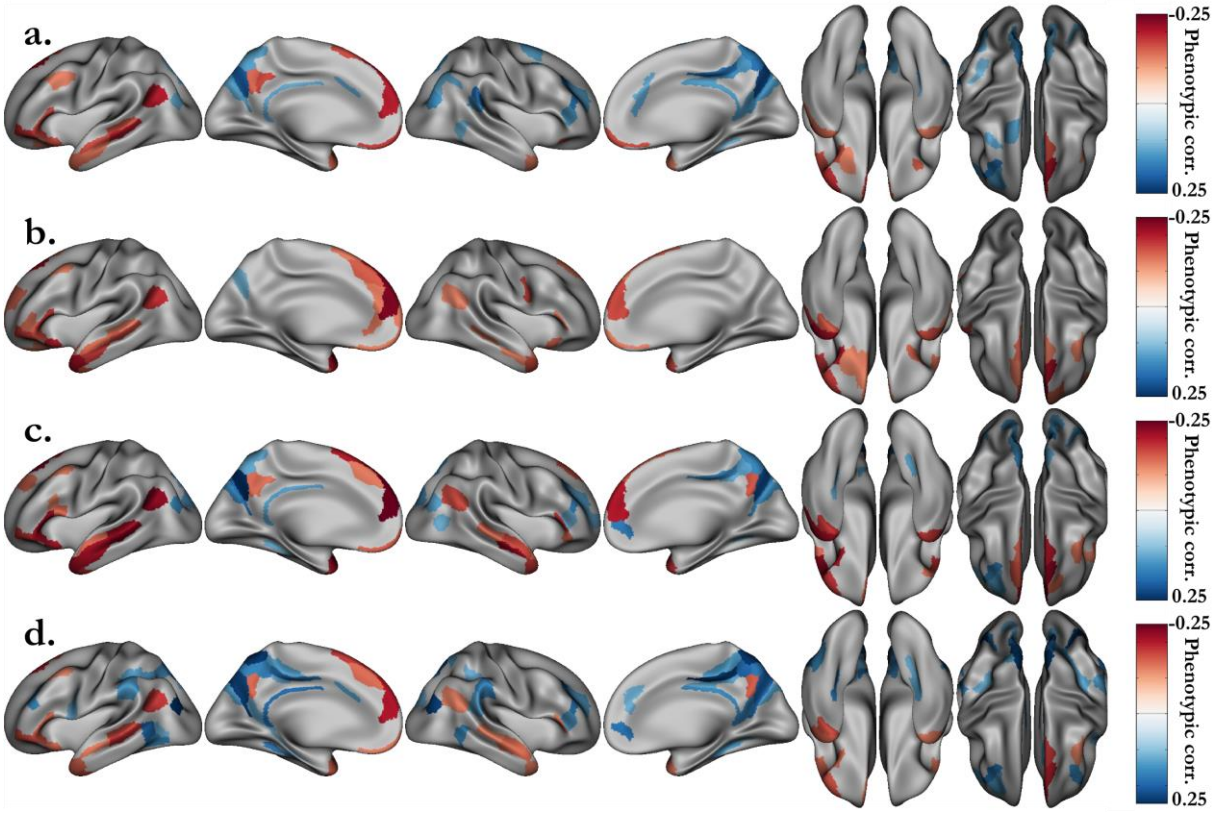

Figure 4. Significant phenotypic correlations between the grayordinate activations of the STORY-MATH contrast and the NIH behavioral scores. **a.** Fluid intelligence (PMAT24_A_CR). **b.** Working memory (ListSort). **c.** Vocabulary comprehension (PicVocab). **d**. Reading decoding (ReadEng). Associated p-values ($p < 0.05/360$, Bonferroni correction) can be found Fig S3.

Additionally, we extended our analysis to behavioral variables measured by the HCP following a standardized NIH protocol. Among these, we selected the variables that are most likely to reflect cognitive performance. Then, we estimated their heritability (**Table S1**) and correlations with the behavioral scores measured during the fMRI task (**Table S2**). In this set of variables, fluid intelligence (heritability: h^2=0.43, correlations with language accuracy: ρ_p = 0.36, ρ_g = 0.61), working memory (h^2=0.52, ρ_p = 0.34, ρ_g = 0.50), vocabulary comprehension (h^2=0.64, ρ_p = 0.40, ρ_g = 0.57) and oral reading decoding (h^2=0.67, ρ_p = 0.46, ρ_g = 0.67) were the ones with the highest heritability estimates and correlations with the average accuracy of the two fMRI tasks. Thus, we performed a

bivariate genetic analysis between the STORY-MATH activations (difference between β_{STORY} and β_{MATH}) and these four variables. Regardless of whether one considers the NIH scores or the ones directly related to the fMRI tasks, the study of shared genetic influence with the median activation yields approximately the same set of regions (**Figures 4, 5**). This observation reinforces our claim that these regions have common genetic roots with the parts of general cognitive performance accounted for by the four cognitive variables under scrutiny, namely fluid intelligence, working memory, vocabulary comprehension and reading decoding.

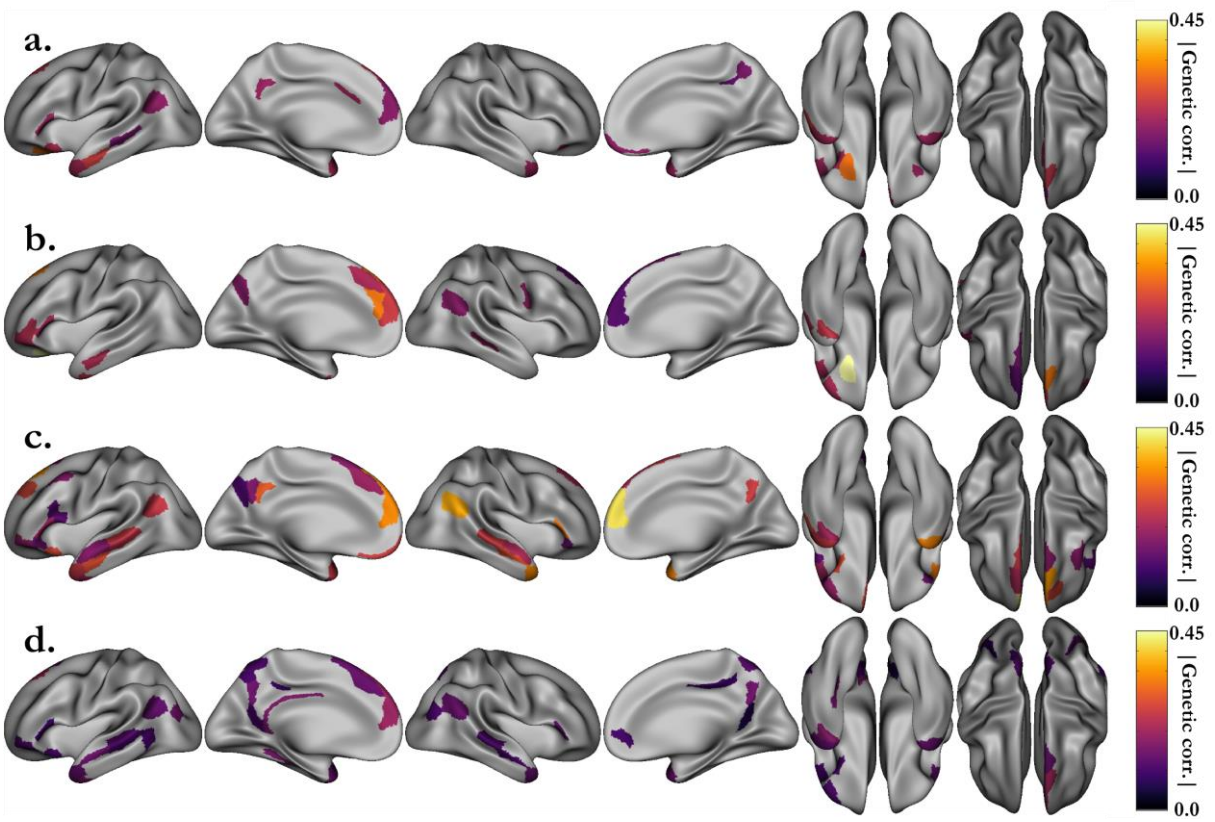

Figure 5. Shared genetic variance (absolute value) between the grayordinate activations of the STORY-MATH contrast and the NIH behavioral scores. a. Fluid intelligence (PMAT24_A_CR). **b.** Working memory (ListSort). **c.** Vocabulary comprehension (PicVocab). **d.** Reading decoding (ReadEng). Associated p-values ($p < 0.05$, uncorrected) can be found in Fig S4. Genetic correlation was investigated only for areals that were significantly phenotypically correlated (**Figure 4**).

6. Discussion

In this chapter, we have shown that brain activation pattern in the language and math networks are heritable. Additionally, we highlighted a particular set of regions along the superior temporal sulcus and in the inferior frontal whose activations share a common genetic basis with some aspects of general cognitive ability, assessed through fMRI task accuracy and behavioral scores.

We must emphasize that these results correspond to fMRI activations associated with verbal math and semantic comprehension tasks. Thus, regions not recruited by the tasks cannot be found to be significantly correlated with cognitive ability in our case, because activations in these regions are incoherent across individuals. Notably, the visual word form area, related to literacy, is not activated in our oral tasks because they did not require word reading.

Furthermore, combining data from various cohorts is unfeasible, because neural activations from different tasks are not comparable when estimating inter-individual variance. This highlights the necessity of utilizing large cohorts with standardized fMRI protocols to perform such genetic analyses. To our knowledge, this is the first study to address the heritability of fMRI activation cortex-wise on a multimodal parcellation of the human cerebral cortex. Our results confirm the genetic influence on the formation of neural circuits implicated in language (Vernes and Fisher, 2013) and math (Pinel and Dehaene, 2013). Using the HCP fine scale parcellation (Glasser et al., 2016) allowed us, for instance, to distinguish the genetic effects on the temporo-parietal junction implicated in language (Pallier et al., 2011) (area PGi) and on the adjacent angular gyrus (area PGp), which is particularly involved in the manipulation of numbers in verbal form (Dehaene et al., 2003). Indeed, these two areas, part of BA 39, present different cytoarchitectonic properties, such as a slightly broader layer II for PGi (Caspers et al., 2006), which might explain their involvement in different tasks. In a previous work, Pinel and Dehaene also found the left angular gyrus and the posterior superior parietal lobule bilaterally to be heritable (Pinel and Dehaene, 2013). Adding to these observations, our results underline a left hemisphere intraparietal specificity, with more heritable areals and slightly higher heritability compared to the right for the MATH contrast. This finding is consistent with results reported by Vogel and colleagues demonstrating a correlation of activations in the left intraparietal sulcus modulated by age, which was not observed in the right intraparietal l (Vogel et al., 2015). Heritability represents the proportion of observed inter-individual phenotypic variance that is explained by genetics. Thus, it might be that inter-individual variance is not sufficiently pronounced in the right hemisphere, whereas activations have evolved over one's lifetime in the left hemisphere. Overall, the heritability maps for the STORY and MATH tasks pinpoint regions known to be disrupted in neurodevelopmental disorders. For instance, the inferior frontal area and the temporo-parietal junction activations are impaired in developmental dyslexia (Eicher and Gruen, 2013; Peterson and Pennington, 2012), and the intraparietal region activations are less modulated by the numerical distance between two numbers being compared in developmental dyscalculia (Ashkenazi et al., 2012; Price and Ansari, 2013; Price et al., 2007). Highlighted areas might provide new insights into brain regions where normal gene expression might be disrupted, leading to brain dysfunction and neurodevelopmental disorders. Frequently replicated genes associated with neurobehavioral disorders, such as developmental dyslexia or SLI, likely play such a role in structural brain maturation by interfering with neuronal migration and neurite growth (Mascheretti et al., 2017).

Several studies have already described some phenotypic correlations between cognitive abilities and neural activations in language (Booth et al., 2003; Skeide et al., 2016; van Ettinger-Veenstra et al., 2010) and math (Bugden et al., 2012; Emerson and Cantlon, 2015, 2012; Price et al., 2013). Our study replicates these observations, notably the correlation with language processing regions, including Broca's area and the posterior superior temporal gyrus (Skeide et al., 2016). Moreover, we estimated the genetic proportion in these phenotypic correlations. Hence, we

demonstrated a shared genetic etiology between brain activations and cognitive performance, assessed in our study by the following tests: fluid intelligence, working memory, vocabulary comprehension and reading decoding. Interestingly, in the right hemisphere, mainly the anterior STS was found to be genetically correlated with the language task accuracy. This result seems consistent with the hypothesized role of the right anterior STS in the processing of prosody or figurative language, likely involved in the Aesop's fable metaphors presented to the subjects (Diaz and Hogstrom, 2011).

The observed genetic correlations shed light on the genetic links between cognitive performance and activation level in cognitive task-related fMRI. These links might be related to the development and maturation of myelin, enhancing brain connectivity. In children with difficulties processing syntactically complex sentences, arcuate fasciculus maturation was incomplete compared to adults (Brauer et al., 2011; Friederici and Gierhan, 2013). Thus, we could look for additive genetic effects implicated in the various levels of fiber tract maturation, which improves brain connectivity and efficiency. Indeed, Skeide and colleagues reported an example of such a genetic risk variant for dyslexia. They showed that this variant is related to the functional connectivity of left fronto-temporal phonological processing areas during the resting state (Skeide et al., 2015). Similarly, children with higher arithmetic scores present a more mature response modulation in their left intraparietal lobe (Bugden et al., 2012). Our study suggests that a proportion of the observed inter-individual variance in cognitive performance partly results from the same additive genetic effects as those contributing to brain activation variance. The moderate shared genetic basis suggests that a crucial interaction occurs between the environment and gene networks to enable the brain to develop to its full potential.

Recently, with the emergence of large cohorts, such as UKBiobank, new loci and genes influencing human cognitive ability have been discovered (Davies et al., 2016; Sniekers et al., 2017; Trampush et al., 2017). However, little is known about how these genes contribute to this human-specific trait. Our study pinpoints brain regions where activations genetically correlate with global cognition scores. These regions might help elucidate the mechanism in which these genes are implicated. When the HCP genotyping data are released, a polygenic score of these newly discovered variants could be used to determine the explained proportion of the neural activation variance in these regions.

7. Supplementary Figures

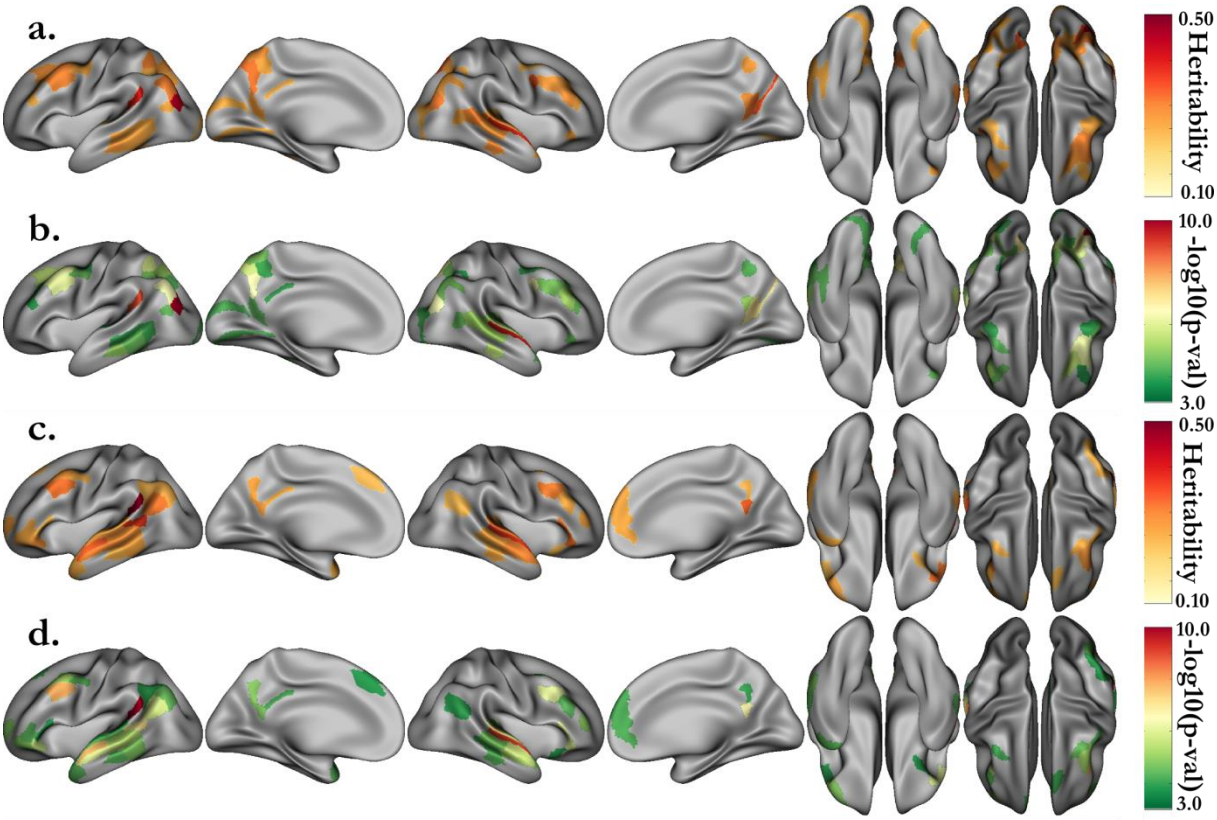

S1 Fig. Heritability estimates for the activations of the contrasts MATH (a.) and STORY (c.), and their associated p-values (respectively b., d.), using median z-stat per areal. Only the estimates significant after correction ($p < 0.05/360$, with 180 areals in each hemisphere) are displayed. Activations correspond to the median z-stat in each areal of the HCP multimodal parcellation. There is almost no difference with Fig. 2, when using the median parameter estimate (β) as a proxy for the activation in each areal.

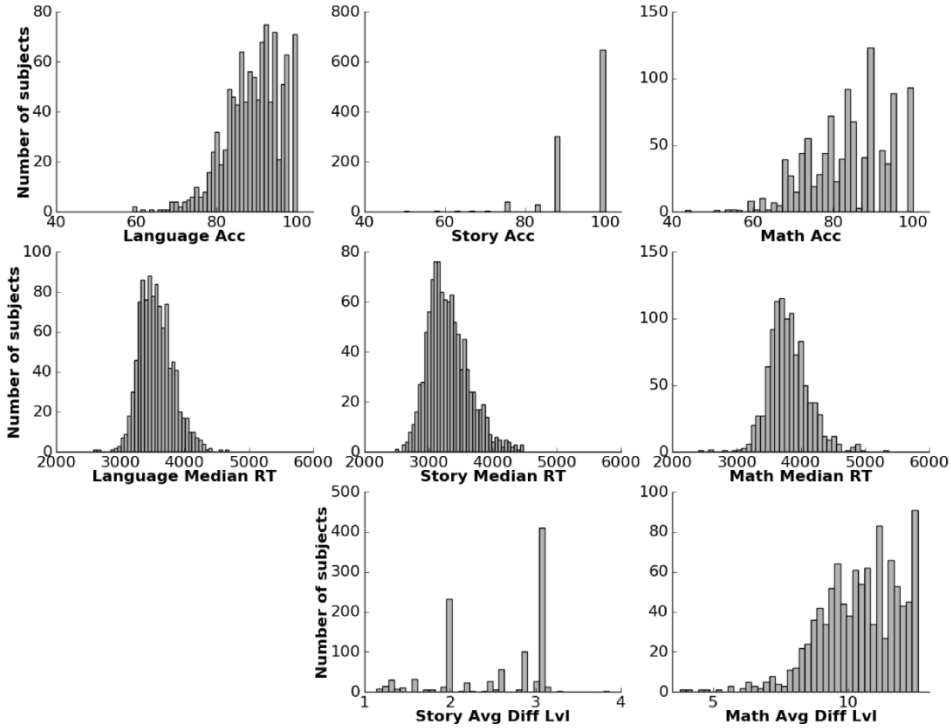

S2 Fig. Distribution of behavioral scores collected by HCP during the language fMRI task, composed of math and story tasks.

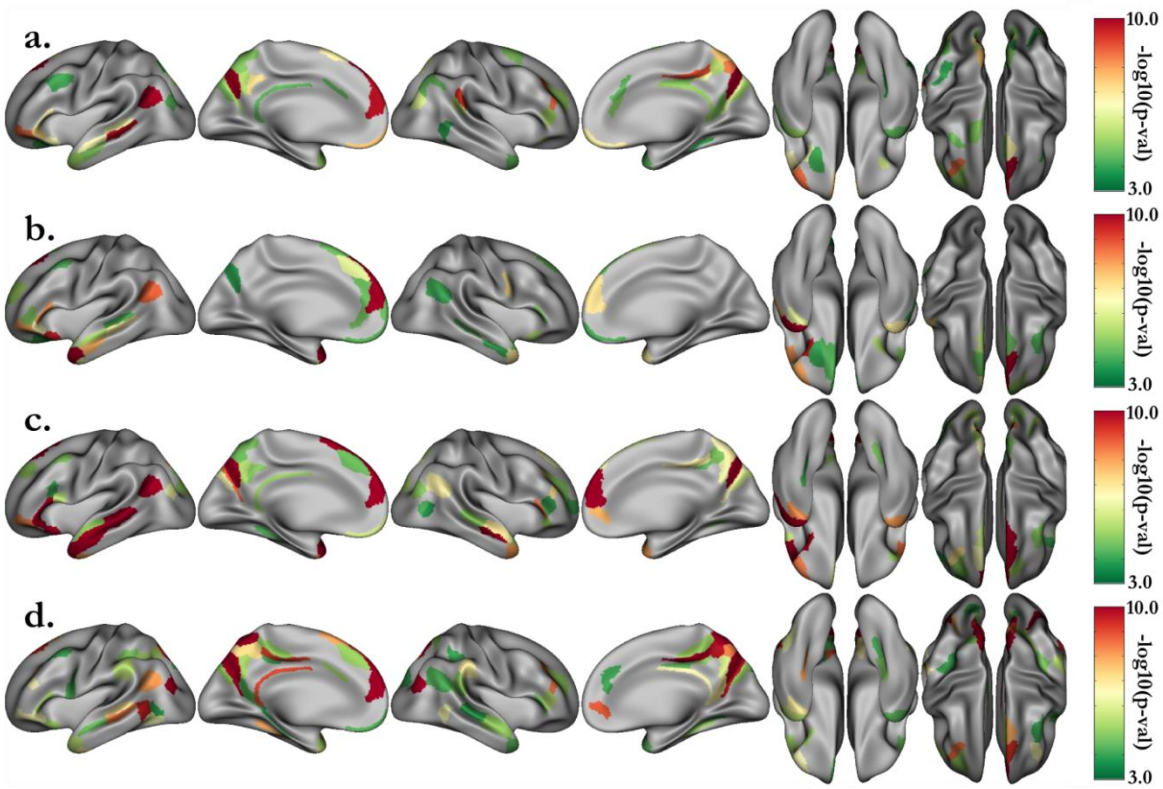

S3 Fig. P-values associated to the phenotypic correlation (Figure 4) between the grayordinates activations of the STORY-MATH contrast and the NIH behavioral scores. **a.** Fluid Intelligence (PMAT24_A_CR). **b.** Working Memory (ListSort). **c.** Vocabulary Comprehension (PicVocab). **d.** Reading Decoding (ReadEng). All p-values < 0.05/360, Bonferroni correction.

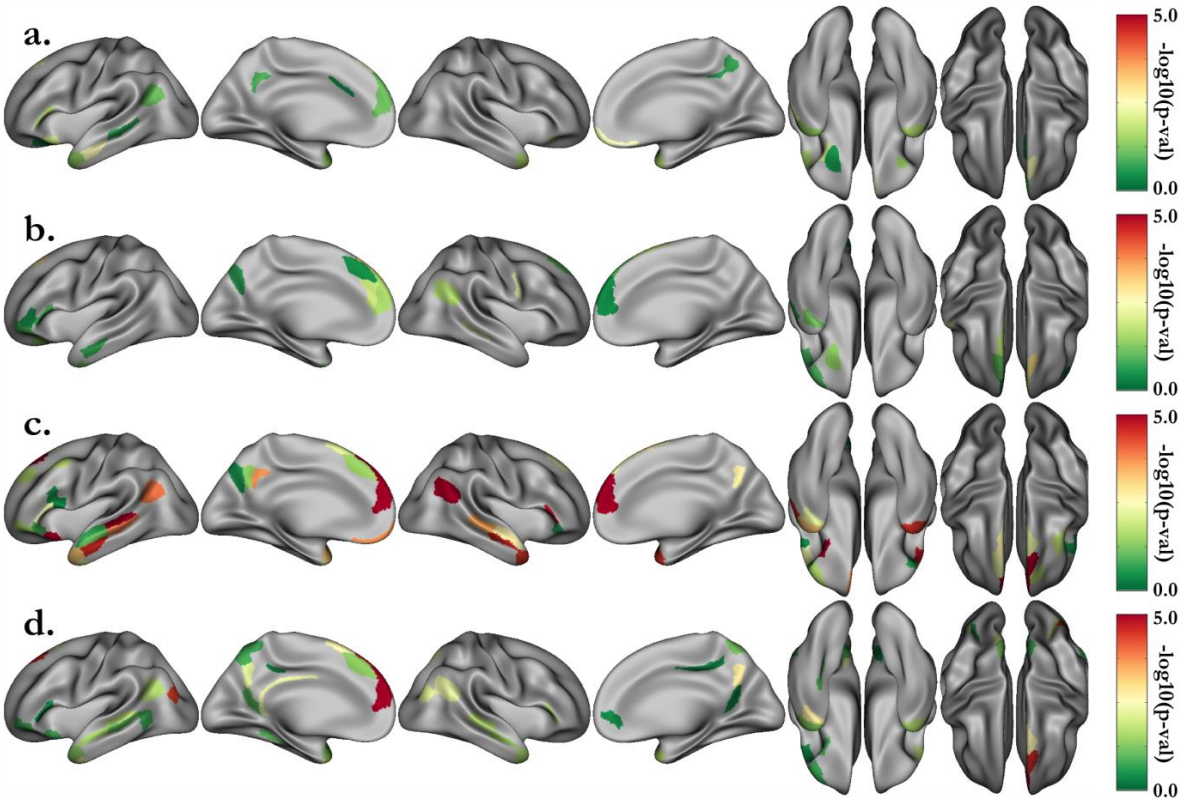

S4 Fig. P-values associated to the genetic correlation (Figure 5) between the grayordinates activations of the STORY-MATH contrast and the NIH behavioral scores. a. Fluid Intelligence (PMAT24_A_CR). **b.** Working Memory (ListSort). **c.** Vocabulary Comprehension (PicVocab). **d.** Reading Decoding (ReadEng). All p-values p < 0.05, uncorrected.

8. Supplementary Tables

S1 Table. Heritability estimates for the NIH behavioral variables. see Methods for description of the analysis.

Trait	h^2±SE (p)	Age	Age^2	Sex	Age*Sex	Age^2*Sex	Hispanic	Educ	h^2cov%
		p-val							
Fluid Intelligence CR	0.43±0.06 ($5.8\cdot10^{-13}$)	0.2	0.48	$3.6\cdot10^{-5}$	0.21	0.24	0.55	$1.0\cdot10^{-10}$	9.1
Fluid Intelligence RT	0.22±0.06 ($1.0\cdot10^{-4}$)	0.94	0.3	$1.5\cdot10^{-6}$	0.11	0.1	0.97	$2.6\cdot10^{-6}$	5.7
Fluid Intelligence SI	0.29±0.06 ($3.0\cdot10^{-7}$)	0.03	0.22	$9.2\cdot10^{-5}$	0.12	0.24	0.91	$3.3\cdot10^{-9}$	7.7
Vocabulary Comprehension	0.64±0.04 ($2.7\cdot10^{-30}$)	0.68	0.45	$3.5\cdot10^{-5}$	0.24	0.79	0.71	$1.7\cdot10^{-25}$	16.5
Processing Speed	0.33±0.06 ($1.0\cdot10^{-7}$)	0.65	0.36	0.24	0.1	0.19	0.53	0.13	0.0
Verbal Episodic Memory CR	0.46±0.06 ($2.6\cdot10^{-13}$)	$3.2\cdot10^{-3}$	0.3	0.4	0.55	0.1	0.72	0.21	3.2
Verbal Episodic Memory RT	0.33±0.06 ($4.3\cdot10^{-8}$)	0.24	0.76	0.21	0.4	0.97	0.48	$1.1\cdot10^{-5}$	2.6
Working memory	0.52±0.05 ($1.1\cdot10^{-18}$)	$6.0\cdot10^{-3}$	0.06	0.53	$6.1\cdot10^{-3}$	0.1	0.29	$4.1\cdot10^{-7}$	4.8
Episodic Memory	0.44±0.06 ($3.8\cdot10^{-14}$)	0.21	0.03	$1.3\cdot10^{-4}$	0.93	0.11	0.97	$1.7\cdot10^{-7}$	5.2
Cognitive Flexibility	0.38±0.06 ($1.2\cdot10^{-10}$)	0.26	0.43	0.27	0.56	0.3	0.97	$7.9\cdot10^{-3}$	1.0
Inhibition	0.31±0.06 ($3.0\cdot10^{-7}$)	0.14	0.32	0.02	0.11	0.49	0.27	0.32	1.7
Reading Decoding	0.67±0.04 ($1.2\cdot10^{-30}$)	0.32	0.8	0.01	0.14	0.29	0.63	$1.1\cdot10^{-24}$	15.7

All scores have been measured by HCP. They follow protocols described in the NIH toolbox.

Fluid Intelligence: measured by the Penn Progressive Matrices Test (CR: Number of Correct Responses, SI: Total Skipped Items, RT: Median Reaction Time for CR)

Language/Vocabulary Comprehension: measured by the Picture Vocabulary Test

Processing Speed: measured by the Pattern Comparison Processing Speed Test

Verbal Episodic Memory: measured by the Penn Word Memory Test (CR: Number of Correct Responses, RT: Median Reaction Time for CR)

Working memory: measured by the List Sorting Working Memory Test

Episodic Memory: measured by the Picture Sequence Memory Test

Executive Function/Cognitive Flexibility: measured by the Dimensional Change Card Sort Test

Executive Function/Inhibition: measured by the Flanker Inhibitory Control and Attention Test

Language/Reading Decoding: measured by the Oral Reading Recognition Test

More details can be found at: https://wiki.humanconnectome.org/display/PublicData/HCP+Data+Dictionary+Public-+500+Subject+Release

S2 Table. Genetic (ρ_p (p) / $\rho_g \pm \sigma_g$ (p)) (above diagonal) and phenotypic (below diagonal) correlations for the NIH standard behavioral scores and task variables.

	Language Acc	Language Median RT	Story Acc	Story Median RT	Story Avg Diff level	Math Acc	Math Median RT	Math Avg Diff level	PMAT24 A CR	PMAT24 A SI	PMAT24 A RTCR	PicVocab	ProcSpeed	IWRD TOT	IWRD RTC	ListSort	PicSeq	CardSort	Flanker	ReadEng
Language Acc	*	-0.41 ±0.19 (0.03)	0.66 ±0.11 (10^{-3})	-0.06 ±0.19 (0.74)	0.88 ±0.07 (10^{-8})	0.9 ±0.04 (10^{-9})	-0.73 ±0.23 (10^{-4})	0.67 ±0.11 (10^{-5})	0.61 ±0.14 (10^{-5})	-0.53 ±0.16 (10^{-3})	0.22 ±0.17 (0.18)	0.57 ±0.10 (10^{-8})	0.44 ±0.16 (10-3)	0.32 ±0.15 (0.04)	-0.24 ±0.13 (0.07)	0.50 ±0.12 (10^{-5})	0.76 ±0.14 (10^{-9})	0.61 ±0.15 (10^{-5})	0.55 ±0.15 (10^{-4})	0.67 ±0.10 (10^{-10})
Language Median RT	-0.15 (10^{-7})	*	-0.18 ±0.27 (0.49)	0.9 ±0.06 (10^{-3})	-0.41 ±0.2 (0.04)	-0.46 ±0.16 (10^{-3})	0.85 ±0.08 (10^{-3})	-0.39 ±0.24 (0.07)	-0.42 ±0.17 (0.01)	0.4 ±0.2 (0.05)	-0.05 ±0.22 (0.8)	-0.2 ±0.15 (0.17)	-0.49 ±0.2 (0.02)	-0.54 ±0.2 (10-3)	0.3 ±0.16 (0.08)	-0.13 ±0.16 (0.41)	-0.27 ±0.17 (0.1)	-0.13 ±0.19 (0.5)	-0.1 ±0.21 (0.62)	0.0 ±0.14 (0.99)
Story Acc	0.71 (10^{-160})	-0.01 (0.67)	*	-0.22 ±0.27 (0.39)	0.25 ±0.2 (0.22)	0.27 ±0.18 (0.13)	-0.09 ±0.28 (0.75)	0.98 ±0.12 (10^{-6})	0.33 ±0.18 (0.06)	-0.27 ±0.22 (0.19)	0.18 ±0.23 (0.41)	0.65 ±0.15 (10^{-6})	0.26 ±0.22 (0.22)	0.59 ±0.21 (10-3)	-0.15 ±0.18 (0.38)	0.17 ±0.17 (0.3)	0.52 ±0.21 (10^{-3})	0.45 ±0.2 (0.02)	0.49 ±0.22 (0.02)	0.60 ±0.16 (10^{-5})
Story Median RT	-0.06 (0.07)	0.83 (10^{-264})	-0.02 (0.53)	*	0.01 ±0.2 (0.97)	-0.01 ±0.18 (0.95)	0.54 ±0.21 (0.05)	-0.42 ±0.26 (0.06)	-0.27 ±0.17 (0.12)	0.28 ±0.21 (0.17)	0.11 ±0.22 (0.61)	-0.14 ±0.14 (0.33)	-0.37 ±0.2 (0.07)	-0.41 ±0.2 (0.04)	0.2 ±0.17 (0.25)	-0.03 ±0.16 (0.85)	-0.01 ±0.17 (0.94)	-0.12 ±0.19 (0.55)	-0.01 ±0.21 (0.98)	0.17 ±0.13 (0.21)
Story Avg Diff level	0.6 (10^{-105})	-0.12 (10^{-5})	0.13 (10^{-5})	-0.07 (0.03)	*	0.98 ±0.05 (10^{-9})	-0.88 ±0.28 (10^{-5})	0.29 ±0.16 (0.09)	0.51 ±0.14 (10^{-4})	-0.55 ±0.17 (10^{-3})	0.14 ±0.18 (0.44)	0.31 ±0.11 (100)	0.31 ±0.16 (0.06)	0.32 ±0.16 (0.05)	-0.24 ±0.14 (0.09)	0.47 ±0.12 (10^{-4})	0.47 ±0.13 (10^{-4})	0.70 ±0.14 (10^{-6})	0.25 ±0.16 (0.14)	0.46 ±0.11 (10^{-5})
Math Acc	0.81 (10^{-243})	-0.2 (10^{-11})	0.15 (10^{-7})	-0.06 (0.04)	0.73 (10^{-178})	*	-0.86 ±0.19 (10^{-6})	0.31 ±0.14 (0.03)	0.59 ±0.13 (10^{-6})	-0.57 ±0.15 (10^{-4})	0.21 ±0.16 (0.18)	0.35 ±0.10 (10^{-4})	0.41 ±0.15 (10-3)	0.1 ±0.14 (0.48)	-0.22 ±0.12 (0.07)	0.54 ±0.11 (10^{-6})	0.67 ±0.11 (10^{-8})	0.50 ±0.14 (10^{-4})	0.44 ±0.14 (10^{-3})	0.51 ±0.09 (10^{-7})
Math Median RT	-0.19 (10^{-10})	0.81 (10^{-250})	-0.0 (0.95)	0.34 (10^{-31})	-0.13 (10^{-5})	-0.27 (10^{-19})	*	-0.19 ±0.23 (0.4)	-0.49 ±0.19 (10^{-3})	0.43 ±0.22 (0.05)	-0.23 ±0.23 (0.32)	-0.16 ±0.16 (0.29)	-0.46 ±0.23 (0.04)	-0.55 ±0.23 (0.01)	0.34 ±0.17 (0.06)	-0.21 ±0.17 (0.23)	-0.49 ±0.19 (10^{-3})	-0.1 ±0.21 (0.65)	-0.19 ±0.22 (0.39)	-0.22 ±0.15 (0.14)
Math Avg Diff level	0.44 (10^{-50})	0.1 (10^{-3})	0.48 (10^{-62})	0.18 (10^{-9})	0.28 (10^{-20})	0.21 (10^{-12})	-0.02 (0.51)	*	0.16 ±0.14 (0.26)	-0.12 ±0.17 (0.49)	-0.19 ±0.18 (0.3)	0.57 ±0.10 (10^{-7})	0.07 ±0.17 (0.67)	0.32 ±0.16 (0.05)	-0.36 ±0.15 (0.01)	0.38 ±0.13 (10^{-3})	0.39 ±0.14 (10^{-3})	0.22 ±0.16 (0.16)	0.45 ±0.17 (10-3)	0.28 ±0.11 (0.01)
PMAT24 A CR	0.36 (10^{-33})	-0.12 (10^{-4})	0.16 (10^{-7})	-0.06 (0.05)	0.3 (10^{-24})	0.37 (10^{-35})	-0.13 (10^{-5})	0.17 (10^{-8})	*	-0.97 ±0.02 (10^{-10})	0.62 ±0.09 (10^{-4})	0.51 ±0.08 (10-8)	0.16 ±0.14 (0.26)	0.34 ±0.12 (10-3)	-0.22 ±0.11 (0.05)	0.61 ±0.10 (10^{-9})	0.4 ±0.11 (10^{-4})	0.33 ±0.12 (10^{-3})	0.22 ±0.13 (0.09)	0.44 ±0.08 (10^{-6})
PMAT24 A SI	-0.32 (10^{-27})	0.1 (10^{-3})	-0.14 (10^{-5})	0.05 (0.08)	-0.28 (10^{-20})	-0.34 (10^{-30})	0.11 (10^{-4})	-0.15 (10^{-6})	-0.97 (10^{-300})	*	-0.73 ±0.08 (10^{-4})	-0.54 ±0.10 (10^{-7})	-0.21 ±0.17 (0.21)	-0.36 ±0.15 (0.02)	0.3 ±0.13 (0.03)	-0.75 ±0.13 (10^{-9})	-0.36 ±0.13 (10^{-3})	-0.35 ±0.14 (0.02)	-0.23 ±0.16 (0.14)	-0.44 ±0.10 (10^{-5})
PMAT24 A RTCR	0.17(10^{-8})	0.01 (0.78)	0.08 (10^{-3})	0.04 (0.17)	0.12 (10^{-4})	0.17 (10^{-8})	-0.03 (0.35)	0.01 (0.73)	0.72 (10^{-193})	-0.7 (10^{-178})	*	0.13 ±0.13 (0.3)	-0.22 ±0.19 (0.24)	0.26 ±0.19 (0.16)	-0.05 ±0.16 (0.77)	0.37 ±0.15 (0.01)	0.06 ±0.15 (0.7)	0.07 ±0.17 (0.68)	-0.07 ±0.18 (0.72)	0.28 ±0.13 (0.03)
PicVocab	0.4 (10^{-42})	-0.13 (10^{-5})	0.27 (10^{-19})	-0.09 (10^{-3})	0.32 (10^{-26})	0.33 (10^{-29})	-0.13 (10^{-5})	0.28 (10^{-21})	0.5 (10^{-76})	-0.47 (10^{-67})	0.26 (10^{-19})	*	0.11 ±0.1 (0.31)	0.36 ±0.09 (10^{-4})	-0.24 ±0.09 (10^{-3})	0.39 ±0.08 (10^{-6})	0.08 ±0.09 (0.37)	0.14 ±0.10 (0.13)	0.18 ±0.11 (0.09)	Rhog ERROR
ProcSpeed	0.17 (10^{-8})	-0.15 (10^{-7})	0.07 (0.02)	-0.13 (10^{-5})	0.21 (10^{-11})	0.17 (10^{-8})	-0.13 (10^{-5})	0.17 (10^{-8})	0.15 (10^{-7})	-0.14 (10^{-6})	-0.04 (0.18)	0.16 (10^{-8})	*	0.06 ±0.16 (0.72)	-0.46 ±0.12 (10^{-4})	0.22 ±0.12 (0.07)	0.25 ±0.13 (0.06)	0.48 ±0.11 (10^{-3})	0.30 ±0.14 (0.07)	0.01 ±0.11 (0.95)
IWRD TOT	0.2 (10^{-11})	-0.08 (0.01)	0.12 (10^{-5})	-0.01 (0.65)	0.18 (10^{-9})	0.18 (10^{-9})	-0.12 (10^{-4})	0.13 (10^{-5})	0.23 (10^{-15})	-0.21 (10^{-13})	0.13 (10^{-6})	0.26 (10^{-20})	0.14 (10^{-7})	*	-0.48 ±0.11 (10^{-4})	0.2 ±0.11 (0.1)	0.47 ±0.12 (10^{-4})	0.3 ±0.14 (0.03)	0.49 ±0.16 (10^{-3})	0.38 ±0.09 (10^{-4})
IWRD RTC	-0.1 (10^{-4})	0.21 (10^{-11})	-0.01 (0.77)	0.14 (10^{-6})	-0.16 (10^{-7})	-0.14 (10^{-6})	0.2 (10^{-11})	-0.13 (10^{-5})	-0.09 (10^{-3})	0.08 (10^{-3})	0.08 (10^{-3})	-0.18 (10^{-10})	-0.25 (10^{-19})	-0.28 (10^{-22})	*	-0.35 ±0.10 (10^{-4})	-0.26 ±0.11 (0.02)	-0.15 ±0.12 (0.24)	-0.14 ±0.13 (0.31)	-0.24 ±0.09 (10^{-3})
ListSort	0.34 (10^{-30})	-0.12 (10^{-4})	0.16 (10^{-7})	-0.05 (0.09)	0.3 (10^{-23})	0.34 (10^{-30})	-0.14 (10^{-6})	0.2 (10^{-11})	0.36 (10^{-37})	-0.34 (10^{-34})	0.14 (10^{-7})	0.34 (10^{-33})	0.18 (10^{-10})	0.16 (10^{-8})	-0.1 (10^{-4})	*	0.54 ±0.09 (10^{-8})	0.26 ±0.11 (0.02)	0.13 ±0.12 (0.29)	0.38 ±0.08 (10^{-6})
PicSeq	0.26 (10^{-18})	-0.11 (10^{-4})	0.14 (10^{-5})	-0.03 (0.38)	0.21 (10^{-12})	0.25 (10^{-17})	-0.16 (10^{-7})	0.17 (10^{-8})	0.3 (10^{-25})	-0.28 (10^{-22})	0.12 (10^{-5})	0.2 (10^{-12})	0.2 (10^{-13})	0.24 (10^{-17})	-0.12 (10^{-5})	0.34 (10^{-35})	*	0.29 ±0.12 (0.02)	0.35 ±0.14 (10^{-2})	0.16 ±0.09 (0.06)
CardSort	0.25 (10^{-16})	-0.17 (10^{-8})	0.12 (10^{-4})	-0.12 (10^{-4})	0.26 (10^{-17})	0.25 (10^{-16})	-0.16 (10^{-7})	0.14 (10^{-6})	0.22 (10^{-14})	-0.22 (10^{-15})	0.04 (0.22)	0.19 (10^{-11})	0.42 (10^{-53})	0.15 (10^{-7})	-0.14 (10^{-7})	0.21 (10^{-13})	0.21 (10^{-13})	*	0.50 ±0.11 (10^{-4})	0.30 ±0.09 (10^{-3})
Flanker	0.16 (10^{-7})	-0.13 (10-5)	0.07 (0.03)	-0.11 (10^{-4})	0.17 (10^{-8})	0.17 (10^{-8})	-0.11 (10^{-4})	0.13 (10^{-5})	0.13 (10^{-6})	-0.12 (10^{-5})	-0.01 (0.61)	0.2 (10^{-13})	0.39 (10^{-46})	0.08 (10^{-3})	-0.16 (10^{-8})	0.14 (10^{-6})	0.15 (10^{-7})	0.52 (10^{-83})	*	0.14 ±0.11 (0.18)
ReadEng	0.46 (10^{-56})	-0.1 (10-3)	0.23 (10^{-13})	-0.01 (0.83)	0.39 (10^{-40})	0.45 (10^{-54})	-0.16 (10^{-7})	0.23 (10^{-14})	0.48 (10^{-70})	-0.45 (10^{-62})	0.3 (10^{-26})	0.7 (10^{-178})	0.16 (10^{-8})	0.28 (10^{-22})	-0.15 (10^{-7})	0.36 (10^{-38})	0.21 (10^{-13})	0.25 (10^{-18})	0.18 (10^{-10})	*

S3 Table. Heritability estimates for MATH activations in the left hemisphere and associated p-values for covariates. Only significant estimates after Bonferroni correction, $p < 1.4 \cdot 10^{-4}$, are presented.

Trait	$h^2 \pm SE(p)$	Age	Age^2	Sex	Age*Sex	Age^2*Sex	Ethni	Educ
		p-val						
Area 7m	0.3 ± 0.06 ($1.0 \cdot 10^{-6}$)	0.55	0.76	0.55	0.58	0.9	0.17	0.49
Area 8Ad	0.26 ± 0.07 ($3.2 \cdot 10^{-5}$)	0.54	0.44	0.89	0.75	0.41	0.52	$9.8 \cdot 10^{-3}$
Area 8Av	0.29 ± 0.06 ($1.2 \cdot 10^{-6}$)	0.94	0.48	0.02	0.86	0.04	0.11	0.15
Area 8C	0.29 ± 0.06 ($1.6 \cdot 10^{-6}$)	0.68	0.25	$3.8 \cdot 10^{-3}$	0.58	0.01	0.65	0.15
Area FST	0.27 ± 0.06 ($1.0 \cdot 10^{-5}$)	0.18	0.37	0.33	0.57	0.1	0.41	0.48
Area IntraParietal 0	0.33 ± 0.07 ($6.0 \cdot 10^{-7}$)	0.62	0.13	0.01	0.73	0.02	0.23	0.59
Area IntraParietal 1	0.29 ± 0.06 ($2.1 \cdot 10^{-6}$)	0.61	0.02	0.04	0.74	$8.8 \cdot 10^{-3}$	$6.1 \cdot 10^{-5}$	0.09
Area Lateral IntraParietal dorsal	0.27 ± 0.06 ($5.5 \cdot 10^{-6}$)	0.83	0.25	0.16	0.72	0.09	$1.2 \cdot 10^{-3}$	0.91
Area Lateral IntraParietal ventral	0.3 ± 0.06 ($1.4 \cdot 10^{-6}$)	0.77	0.64	0.97	0.58	0.51	0.35	0.55
Area PF opercular	0.26 ± 0.06 ($3.3 \cdot 10^{-5}$)	0.12	0.44	0.21	0.83	0.3	0.62	0.33
Area PGp	0.45 ± 0.06 ($5.2 \cdot 10^{-13}$)	0.73	0.78	0.03	0.9	0.52	0.84	0.64
Area PGs	0.3 ± 0.07 ($2.4 \cdot 10^{-6}$)	0.88	0.9	0.55	0.78	0.51	0.17	0.07
Area TE1 Middle	0.28 ± 0.07 ($1.1 \cdot 10^{-5}$)	0.85	0.55	0.41	0.66	0.8	0.05	0.1
Area TE1 posterior	0.25 ± 0.07 ($1.1 \cdot 10^{-4}$)	0.94	0.28	$1.4 \cdot 10^{-3}$	0.92	$4.5 \cdot 10^{-3}$	0.1	0.01
Area p32 prime	0.25 ± 0.07 ($1.0 \cdot 10^{-4}$)	0.59	0.39	0.4	0.79	0.23	0.8	0.69
Inferior 6-8 Transitional Area	0.3 ± 0.06 ($6.0 \cdot 10^{-7}$)	0.72	0.39	0.03	0.99	0.04	0.13	$2.6 \cdot 10^{-4}$
Lateral Area 7P	0.29 ± 0.06 ($2.9 \cdot 10^{-6}$)	0.89	0.36	0.21	0.73	0.1	0.55	0.04
Medial Area 7A	0.29 ± 0.07 ($1.1 \cdot 10^{-5}$)	0.56	0.69	0.85	0.48	0.64	0.93	0.25
Medial Area 7P	0.29 ± 0.07 ($1.1 \cdot 10^{-5}$)	0.51	0.18	0.74	0.23	0.04	0.46	0.89
Medial IntraParietal Area	0.25 ± 0.07 ($5.6 \cdot 10^{-5}$)	0.55	0.49	$7.2 \cdot 10^{-3}$	0.94	0.1	0.16	0.41
Parieto-Occipital Sulcus Area 1	0.26 ± 0.07 ($7.4 \cdot 10^{-5}$)	0.47	0.53	0.27	0.43	0.41	0.94	0.59
PeriSylvian Language Area	0.42 ± 0.06 ($1.5 \cdot 10^{-10}$)	0.3	0.09	0.42	0.83	$5.3 \cdot 10^{-3}$	0.03	0.35
Superior 6-8 Transitional Area	0.23 ± 0.07 ($1.3 \cdot 10^{-4}$)	0.39	0.64	0.13	0.5	0.64	0.49	$5.4 \cdot 10^{-3}$

S4 Table. Heritability estimates for MATH activations in the right hemisphere and associated p-values for covariates. Only significant estimates after Bonferroni correction, $p < 1.4 \cdot 10^{-4}$, are presented.

Trait	h^2±SE(p)	Age	Age^2	Sex	Age*Sex	Age^2*Sex	Ethni	Educ
		p-val						
Area 46	0.25±0.07 ($4.9 \cdot 10^{-5}$)	0.51	0.49	0.68	0.9	0.15	0.81	0.79
Area 47l	0.25±0.07 ($5.4 \cdot 10^{-5}$)	0.81	0.45	0.96	0.7	0.43	0.76	0.42
Area 7m	0.24±0.07 ($1.1 \cdot 10^{-4}$)	0.7	0.43	0.27	0.87	0.29	0.01	0.41
Area 8C	0.25±0.07 ($1.3 \cdot 10^{-4}$)	0.18	0.84	0.28	0.35	0.6	0.21	0.9
Area IntraParietal 0	0.26±0.07 ($2.5 \cdot 10^{-5}$)	0.87	0.7	0.74	0.08	0.05	0.55	0.76
Area Lateral IntraParietal dorsal	0.27±0.07 ($5.5 \cdot 10^{-5}$)	0.82	0.82	0.33	0.49	0.16	0.03	0.44
Area PGp	0.29±0.06 ($1.6 \cdot 10^{-6}$)	0.28	0.76	$5.6 \cdot 10^{-3}$	0.81	0.22	0.64	0.32
Area PGs	0.25±0.07 ($4.8 \cdot 10^{-5}$)	0.5	0.66	$3.8 \cdot 10^{-3}$	0.55	0.99	0.53	0.75
Area STGa	0.26±0.07 ($1.4 \cdot 10^{-4}$)	0.93	0.69	0.98	0.55	0.35	0.17	0.14
Area STSd posterior	0.3±0.07 ($3.2 \cdot 10^{-6}$)	0.11	0.55	0.07	0.55	0.91	0.66	0.45
Area TA2	0.28±0.07 ($1.2 \cdot 10^{-5}$)	0.4	0.9	0.25	0.25	0.8	0.75	0.59
Area TE1 Middle	0.28±0.06 ($6.6 \cdot 10^{-6}$)	0.6	0.44	0.31	0.21	0.83	0.82	0.81
Area TemporoParietoOccipital Junction 1	0.29±0.07 ($2.1 \cdot 10^{-5}$)	0.53	0.18	0.07	0.52	0.92	0.27	0.97
Area TemporoParietoOccipital Junction 2	0.24±0.07 ($1.0 \cdot 10^{-4}$)	0.18	0.62	0.14	0.52	0.44	0.93	0.36
Area posterior 9-46v	0.3±0.06 ($1.7 \cdot 10^{-6}$)	0.68	0.09	$6.7 \cdot 10^{-3}$	0.97	0.02	0.54	0.63
Area ventral 23 a+b	0.29±0.07 ($7.4 \cdot 10^{-6}$)	0.92	0.77	$6.7 \cdot 10^{-3}$	0.51	0.63	0.21	0.54
Auditory 4 Complex	0.28±0.06 ($3.4 \cdot 10^{-6}$)	0.78	0.63	0.01	0.68	0.8	0.41	0.3
Auditory 5 Complex	0.39±0.06 ($1.3 \cdot 10^{-10}$)	0.22	0.11	0.05	0.42	0.07	0.19	0.99
Dorsal Transitional Visual Area	0.31±0.07 ($1.7 \cdot 10^{-6}$)	0.33	0.62	0.02	0.96	0.53	0.55	0.79
Fourth Visual Area	0.25±0.07 ($6.8 \cdot 10^{-5}$)	0.15	0.07	0.89	0.84	0.02	0.3	0.22
Inferior 6-8 Transitional Area	0.24±0.06 ($7.9 \cdot 10^{-5}$)	0.08	0.51	0.32	0.1	0.05	0.15	0.92
Lateral Area 7P	0.35±0.07 ($1.0 \cdot 10^{-7}$)	0.59	0.26	0.55	0.56	0.13	0.68	$5.6 \cdot 10^{-3}$
Lateral Belt Complex	0.29±0.07 ($2.3 \cdot 10^{-6}$)	0.71	0.1	0.55	0.53	0.12	0.5	0.75
Medial IntraParietal Area	0.26±0.07 ($3.5 \cdot 10^{-5}$)	0.53	0.98	0.94	0.06	0.41	0.17	0.25
ParaBelt Complex	0.35±0.06 ($2.5 \cdot 10^{-8}$)	0.65	0.43	0.49	0.68	0.16	0.23	0.74
Parieto-Occipital Sulcus Area 1	0.32±0.06 ($1.0 \cdot 10^{-7}$)	0.98	0.61	$7.0 \cdot 10^{-3}$	0.31	0.95	0.56	0.43
PreCuneus Visual Area	0.29±0.07 ($3.8 \cdot 10^{-5}$)	0.2	0.78	$7.3 \cdot 10^{-3}$	0.78	0.87	0.16	0.35
Premotor Eye Field	0.36±0.06 ($2.6 \cdot 10^{-8}$)	0.74	0.64	0.82	0.82	0.46	0.72	0.36
Primary Auditory Cortex	0.26±0.07 ($4.5 \cdot 10^{-5}$)	0.99	0.11	0.58	0.6	0.06	$1.1 \cdot 10^{-3}$	0.36

S5 Table. Heritability estimates for STORY activations in the left hemisphere and associated p-values for covariates. Only significant estimates after Bonferroni correction, $p < 1.4 \cdot 10^{-4}$, are presented.

Trait	h^2±SE(p)	Age	Age^2	Sex	Age*Sex	Age^2*Sex	Ethni	Educ
		p-val						
Area 45	0.22 ± 0.06 ($1.4 \cdot 10^{-4}$)	0.98	0.04	0.59	0.24	0.04	0.49	0.08
Area 47l	0.29 ± 0.06 ($1.5 \cdot 10^{-6}$)	0.76	0.29	0.01	0.17	0.1	0.92	0.37
Area 7m	0.26 ± 0.07 ($2.0 \cdot 10^{-5}$)	0.2	0.64	$4.4 \cdot 10^{-3}$	0.11	0.64	0.46	0.7
Area 8Av	0.28 ± 0.06 ($4.9 \cdot 10^{-6}$)	0.75	0.14	0.83	0.68	0.02	0.43	0.56
Area 8C	0.32 ± 0.06 ($2.1 \cdot 10^{-8}$)	0.32	0.88	0.03	0.46	0.05	0.96	0.83
Area PGi	0.32 ± 0.07 ($9.0 \cdot 10^{-7}$)	0.21	0.31	0.41	0.86	0.11	0.05	0.11
Area PGs	0.24 ± 0.07 ($1.2 \cdot 10^{-4}$)	0.48	0.35	0.55	0.36	0.12	0.16	0.1
Area STSd anterior	0.28 ± 0.06 ($3.0 \cdot 10^{-6}$)	0.42	0.01	0.13	0.43	$2.7 \cdot 10^{-3}$	0.51	0.02
Area STSd posterior	0.25 ± 0.07 ($7.9 \cdot 10^{-5}$)	0.33	0.29	0.64	0.59	0.04	0.1	0.12
Area STSv anterior	0.28 ± 0.06 ($5.5 \cdot 10^{-6}$)	0.47	0.03	0.5	0.87	0.02	0.22	0.07
Area STSv posterior	0.27 ± 0.06 ($1.0 \cdot 10^{-5}$)	0.35	0.43	0.25	0.42	0.19	0.08	0.39
Area TA2	0.31 ± 0.07 ($1.2 \cdot 10^{-6}$)	0.17	0.08	$1.8 \cdot 10^{-3}$	0.97	0.03	0.54	0.49
Area TE1 Middle	0.28 ± 0.06 ($6.0 \cdot 10^{-6}$)	0.33	0.96	0.93	0.62	0.6	0.28	0.04
Area TE1 anterior	0.23 ± 0.06 ($1.2 \cdot 10^{-4}$)	0.02	0.49	0.04	1.0	0.94	0.02	0.93
Area TE1 posterior	0.25 ± 0.07 ($5.1 \cdot 10^{-5}$)	0.92	0.18	0.07	0.37	$6.7 \cdot 10^{-3}$	0.27	0.07
Area TemporoParietoOccipital Junction 1	0.39 ± 0.07 ($1.0 \cdot 10^{-7}$)	0.16	0.01	0.46	0.63	$1.4 \cdot 10^{-4}$	0.2	0.03
Area anterior 47r	0.24 ± 0.06 ($7.8 \cdot 10^{-5}$)	0.61	0.4	0.02	0.65	0.05	0.44	0.04
Area posterior 10p	0.22 ± 0.06 ($9.5 \cdot 10^{-5}$)	0.61	0.79	0.57	0.14	0.87	0.43	0.18
Area posterior 47r	0.25 ± 0.07 ($9.5 \cdot 10^{-5}$)	0.12	0.45	0.01	0.22	0.21	0.75	0.5
Area ventral 23 a+b	0.28 ± 0.07 ($1.4 \cdot 10^{-5}$)	0.5	0.95	0.04	0.2	0.45	0.05	0.05
Inferior 6-8 Transitional Area	0.23 ± 0.06 ($8.4 \cdot 10^{-5}$)	0.97	0.2	0.11	0.37	0.05	0.71	$6.0 \cdot 10^{-3}$
ParaBelt Complex	0.24 ± 0.07 ($1.2 \cdot 10^{-4}$)	0.02	0.1	0.63	0.59	0.05	0.3	0.51
Parieto-Occipital Sulcus Area 2	0.26 ± 0.07 ($5.7 \cdot 10^{-5}$)	0.15	0.56	0.12	0.56	0.29	0.59	0.01
PeriSylvian Language Area	0.55 ± 0.05 ($1.3 \cdot 10^{-17}$)	0.48	0.16	0.89	0.8	0.07	0.06	0.85

S6 Table. Heritability estimates for STORY activations in the *right hemisphere* and associated p-values for covariates. Only significant estimates after Bonferroni correction, $p < 1.4 \cdot 10^{-4}$, are presented.

Trait	h^2±SE(p)	Age	Age^2	Sex	Age*Sex	Age^2*Sex	Ethni	Educ
		p-val						
Area 45	0.3±0.07 ($1.8 \cdot 10^{-6}$)	0.76	0.92	0.31	0.9	0.93	0.21	0.18
Area 47l	0.31±0.07 ($2.6 \cdot 10^{-6}$)	0.14	0.59	0.22	0.35	0.75	0.84	0.74
Area 8Av	0.24±0.07 ($1.0 \cdot 10^{-4}$)	0.46	0.97	0.13	0.69	0.17	0.38	0.15
Area 8C	0.27±0.07 ($1.5 \cdot 10^{-5}$)	0.09	0.54	0.24	0.12	0.56	0.52	0.94
Area 9 Middle	0.25±0.07 ($7.2 \cdot 10^{-5}$)	0.13	0.75	0.06	0.3	0.75	0.1	0.45
Area STGa	0.3±0.07 ($8.1 \cdot 10^{-6}$)	0.93	0.2	0.59	0.99	0.17	0.88	0.06
Area STSd anterior	0.28±0.07 ($7.4 \cdot 10^{-6}$)	0.57	0.29	0.02	0.61	0.41	0.91	0.03
Area STSd posterior	0.29±0.06 ($1.6 \cdot 10^{-6}$)	0.1	0.77	0.11	0.97	0.81	0.85	0.09
Area STSv anterior	0.26±0.06 ($1.7 \cdot 10^{-5}$)	0.2	0.02	0.63	0.87	0.17	0.2	0.16
Area TA2	0.36±0.06 ($1.8 \cdot 10^{-8}$)	0.08	0.33	$1.6 \cdot 10^{-3}$	0.36	0.43	0.12	0.09
Area anterior 9-46v	0.24±0.06 ($5.2 \cdot 10^{-5}$)	0.14	0.5	0.01	0.61	0.1	0.52	0.05
Area p32	0.25±0.07 ($7.0 \cdot 10^{-5}$)	0.93	0.77	0.25	0.46	0.48	0.69	0.24
Area ventral 23 a+b	0.34±0.07 ($3.0 \cdot 10^{-7}$)	0.55	0.95	$8.1 \cdot 10^{-4}$	0.27	0.89	0.14	0.43
Auditory 4 Complex	0.33±0.06 ($2.0 \cdot 10^{-7}$)	0.62	0.8	0.06	0.48	0.9	0.49	0.87
Auditory 5 Complex	0.39±0.06 ($9.1 \cdot 10^{-11}$)	0.22	0.09	0.22	0.64	0.08	0.34	0.76
Inferior 6-8 Transitional Area	0.24±0.07 ($1.2 \cdot 10^{-4}$)	0.34	0.54	0.11	0.07	0.21	0.1	0.85
Lateral Belt Complex	0.25±0.07 ($3.3 \cdot 10^{-5}$)	0.58	0.05	0.92	0.63	0.08	0.97	0.67
Medial Belt Complex	0.27±0.07 ($9.2 \cdot 10^{-5}$)	0.92	0.06	0.2	1.0	0.23	0.25	0.83
ParaBelt Complex	0.38±0.06 ($1.8 \cdot 10^{-9}$)	0.38	0.38	0.98	0.46	0.09	0.43	0.34
Primary Auditory Cortex	0.27±0.07 ($1.4 \cdot 10^{-5}$)	0.96	0.05	0.45	0.53	0.07	$9.7 \cdot 10^{-3}$	0.56

S7 Table. Bivariate genetic analysis results for areals in the *left hemisphere* with the STORY-MATH contrast median activation and the HCP language task accuracy. ρ_p: phenotypic correlation, ρ_g: shared genetic variance, ρ_e: environment correlation

Trait	ρ_p (p)	$\rho_g \pm$SE (p)	ρ_e (p)
Anterior Ventral Insular Area	0.13 ($4.8\cdot10^{-5}$)	0.61±0.17 ($3.0\cdot10^{-4)}$	-0.12 (0.11)
Area 10v	0.19 ($6.6\cdot10^{-10}$)	0.23±0.15 (0.13)	0.11 (0.12)
Area 31pd	0.16 ($3.0\cdot10^{-7}$)	0.47±0.15 ($3.4\cdot10^{-3}$)	0.01 (0.88)
Area 44	0.19 ($4.1\cdot10^{-10}$)	0.35±0.13 (0.02)	0.12 (0.08)
Area 45	0.25 ($8.0\cdot10^{-16}$)	0.46±0.13 ($9.4\cdot10^{-4}$)	0.11 (0.14)
Area 47l	0.2 ($2.1\cdot10^{-11}$)	0.43±0.14 ($2.6\cdot10^{-3}$)	-0.0 (1.0)
Area 47m	0.17 ($3.2\cdot10^{-8}$)	0.29±0.14 (0.04)	0.07 (0.28)
Area 47s	0.19 ($2.8\cdot10^{-10}$)	0.4±0.13 ($3.6\cdot10^{-3}$)	0.01 (0.93)
Area 7m	0.2 ($1.4\cdot10^{-10}$)	0.44±0.14 ($2.2\cdot10^{-3}$)	0.02 (0.75)
Area 8Av	0.17 ($2.1\cdot10^{-8}$)	0.39±0.12 ($3.5\cdot10^{-3}$)	0.01 (0.88)
Area 8BM	0.2 ($1.2\cdot10^{-10}$)	0.75±0.14 ($8.9\cdot10^{-7}$)	-0.08 (0.27)
Area 8B Lateral	0.28 ($4.5\cdot10^{-20}$)	0.73±0.14 ($5.2\cdot10^{-7}$)	0.02 (0.72)
Area 9 Middle	0.26 ($1.5\cdot10^{-17}$)	0.44±0.13 ($1.4\cdot10^{-3}$)	0.08 (0.29)
Area 9 Posterior	0.13 ($1.5\cdot10^{-5}$)	0.52±0.21 (0.01)	-0.02 (0.76)
Area 9 anterior	0.14 ($8.6\cdot10^{-6}$)	0.3±0.14 (0.04)	0.03 (0.68)
Area IFSp	0.15 ($1.6\cdot10^{-6}$)	0.42±0.12 ($9.4\cdot10^{-4}$)	-0.04 (0.58)
Area IntraParietal 0	-0.13 ($1.9\cdot10^{-5}$)	-0.21±0.12 (0.1)	0.0 (0.97)
Area PGi	0.28 ($9.8\cdot10^{-21}$)	0.54±0.13 ($1.4\cdot10^{-4}$)	0.11 (0.14)
Area PGp	-0.15 ($9.0\cdot10^{-7}$)	-0.27±0.11 (0.01)	0.06 (0.47)
Area STGa	0.18 ($9.2\cdot10^{-9}$)	0.34±0.15 (0.03)	0.08 (0.26)
Area STSd anterior	0.19 ($2.1\cdot10^{-10}$)	0.52±0.16 ($1.9\cdot10^{-3}$)	0.06 (0.39)
Area STSd posterior	0.24 ($7.8\cdot10^{-15}$)	0.47±0.11 ($1.9\cdot10^{-4}$)	0.09 (0.22)
Area STSv anterior	0.22 ($1.0\cdot10^{-12}$)	0.35±0.15 (0.03)	0.12 (0.1)
Area STSv posterior	0.23 ($4.3\cdot10^{-14}$)	0.45±0.12 ($6.5\cdot10^{-4}$)	0.05 (0.45)
Area TE1 anterior	0.21 ($5.5\cdot10^{-12}$)	0.41±0.15 ($8.5\cdot10^{-3}$)	0.1 (0.15)
Area TG Ventral	0.21 ($6.2\cdot10^{-12}$)	0.51±0.14 ($6.6\cdot10^{-4}$)	0.01 (0.92)
Area TG dorsal	0.23 ($1.5\cdot10^{-14}$)	0.44±0.15 ($5.1\cdot10^{-3}$)	0.06 (0.37)
Area anterior 47r	0.21 ($1.9\cdot10^{-11}$)	0.48±0.14 ($1.2\cdot10^{-3}$)	-0.02 (0.82)
Area posterior 47r	0.13 ($1.6\cdot10^{-5}$)	0.44±0.17 (0.01)	-0.03 (0.63)
Auditory 5 Complex	0.14 ($7.8\cdot10^{-6}$)	0.54±0.14 ($2.0\cdot10^{-4}$)	-0.05 (0.45)
Dorsal Transitional Visual Area	-0.15 ($4.9\cdot10^{-7}$)	-0.16±0.16 (0.33)	-0.05 (0.43)
Lateral Area 7P	-0.13 ($4.4\cdot10^{-5}$)	-0.04±0.12 (0.74)	-0.04 (0.54)
Medial Area 7A	-0.14 ($5.6\cdot10^{-6}$)	-0.14±0.14 (0.33)	-0.06 (0.43)
Parieto-Occipital Sulcus Area 2	-0.26 ($1.5\cdot10^{-17}$)	-0.19±0.12 (0.11)	-0.15 (0.03)
PeriSylvian Language Area	0.13 ($1.2\cdot10^{-5}$)	0.47±0.12 ($2.0\cdot10^{-4}$)	-0.13 (0.09)
Perirhinal Ectorhinal Cortex	0.14 ($5.2\cdot10^{-6}$)	0.59±0.3 (0.03)	0.0 (0.97)
RetroSplenial Complex	-0.15 ($1.6\cdot10^{-6}$)	-0.5±0.16 ($1.9\cdot10^{-3}$)	0.02 (0.71)
Superior Frontal Language Area	0.27 ($4.8\cdot10^{-19}$)	0.52±0.11 ($3.4\cdot10^{-5}$)	0.07 (0.37)

S8 Table. Bivariate genetic analysis results for areals in the *right hemisphere* with the STORY-MATH contrast median activation and the HCP language task accuracy. ρ_p: phenotypic correlation, ρ_g: shared genetic variance, ρ_e: environment correlation

Trait	ρ_p (p)	ρ_g±SE (p)	ρ_e (p)
Area 10v	0.15 ($1.3\cdot10^{-6}$)	0.32±0.13 (0.02)	0.03 (0.66)
Area 23c	-0.17 ($2.0\cdot10^{-8}$)	-0.38±0.15 (0.01)	-0.01 (0.91)
Area 23d	-0.12 ($8.8\cdot10^{-5}$)	-0.31±0.17 (0.07)	-0.01 (0.92)
Area 31a	-0.16 ($2.2\cdot10^{-7}$)	-0.19±0.14 (0.18)	-0.07 (0.32)
Area 45	0.14 ($2.5\cdot10^{-6}$)	0.42±0.15 ($7.1\cdot10^{-3}$)	-0.0 (0.98)
Area 46	-0.19 ($3.5\cdot10^{-10}$)	-0.14±0.15 (0.36)	-0.12 (0.08)
Area 47l	0.12 ($1.1\cdot10^{-4}$)	0.51±0.14 ($2.3\cdot10^{-4}$)	-0.04 (0.56)
Area 7m	0.18 ($1.7\cdot10^{-9}$)	0.48±0.15 ($1.9\cdot10^{-3}$)	0.0 (0.95)
Area 8B Lateral	0.16 ($3.3\cdot10^{-7}$)	0.41±0.14 ($4.6\cdot10^{-3}$)	0.0 (0.98)
Area 9 Middle	0.14 ($3.9\cdot10^{-6}$)	0.35±0.16 (0.03)	-0.01 (0.9)
Area IFSa	-0.13 ($3.6\cdot10^{-5}$)	-0.2±0.14 (0.15)	0.01 (0.9)
Area IntraParietal 0	-0.16 ($2.6\cdot10^{-7}$)	-0.33±0.12 ($9.3\cdot10^{-3}$)	0.0 (0.98)
Area IntraParietal 2	-0.15 ($2.3\cdot10^{-6}$)	-0.29±0.15 (0.05)	-0.02 (0.8)
Area PF Complex	-0.13 ($3.7\cdot10^{-5}$)	-0.22±0.13 (0.1)	-0.03 (0.72)
Area PFm Complex	-0.12 ($5.5\cdot10^{-5}$)	-0.09±0.15 (0.55)	-0.08 (0.28)
Area PGi	0.12 ($6.5\cdot10^{-5}$)	0.42±0.15 ($8.0\cdot10^{-3}$)	0.02 (0.76)
Area PGp	-0.18 ($5.1\cdot10^{-9}$)	-0.4±0.12 ($9.6\cdot10^{-4}$)	0.11 (0.13)
Area PHT	-0.14 ($7.3\cdot10^{-6}$)	-0.18±0.14 (0.21)	-0.01 (0.85)
Area STGa	0.15 ($2.0\cdot10^{-6}$)	0.24±0.16 (0.14)	0.06 (0.38)
Area STSd anterior	0.19 ($4.6\cdot10^{-10}$)	0.4±0.12 ($2.0\cdot10^{-3}$)	0.05 (0.51)
Area STSd posterior	0.12 ($1.0\cdot10^{-4}$)	0.27±0.14 (0.05)	0.03 (0.68)
Area STSv anterior	0.14 ($2.8\cdot10^{-6}$)	0.36±0.13 (0.01)	-0.0 (0.95)
Area TE1 anterior	0.12 ($6.8\cdot10^{-5}$)	0.32±0.15 (0.04)	0.07 (0.32)
Area TG dorsal	0.19 ($9.8\cdot10^{-10}$)	0.65±0.17 ($1.5\cdot10^{-4}$)	-0.02 (0.81)
Area anterior 10p	-0.14 ($5.2\cdot10^{-6}$)	-0.21±0.18 (0.24)	-0.05 (0.45)
Area anterior 9-46v	-0.12 ($7.7\cdot10^{-5}$)	0.05±0.15 (0.73)	-0.1 (0.13)
Area p32	-0.15 ($1.2\cdot10^{-6}$)	-0.49±0.2 ($9.7\cdot10^{-3}$)	0.04 (0.5)
Dorsal Transitional Visual Area	-0.15 ($7.4\cdot10^{-7}$)	-0.2±0.15 (0.2)	-0.02 (0.73)
Frontal OPercular Area 4	-0.12 ($4.9\cdot10^{-5}$)	0.02±0.19 (0.93)	-0.09 (0.18)
Lateral Area 7P	-0.15 ($9.8\cdot10^{-7}$)	-0.32±0.12 ($9.9\cdot10^{-3}$)	0.08 (0.29)
Medial Area 7A	-0.16 ($1.2\cdot10^{-7}$)	-0.34±0.17 (0.05)	0.02 (0.76)
Medial Area 7P	-0.19 ($6.0\cdot10^{-10}$)	-0.21±0.15 (0.18)	-0.05 (0.45)
Middle Insular Area	-0.12 ($5.9\cdot10^{-5}$)	-0.0±0.19 (0.98)	-0.1 (0.12)
Parieto-Occipital Sulcus Area 1	-0.12 ($1.0\cdot10^{-4}$)	-0.17±0.12 (0.15)	0.04 (0.59)
Parieto-Occipital Sulcus Area 2	-0.26 ($7.7\cdot10^{-18}$)	-0.34±0.12 ($5.5\cdot10^{-3}$)	-0.06 (0.39)
PeriSylvian Language Area	-0.15 ($6.4\cdot10^{-7}$)	-0.34±0.18 (0.05)	-0.03 (0.67)
PreCuneus Visual Area	-0.14 ($2.8\cdot10^{-6}$)	-0.54±0.18 ($1.5\cdot10^{-3}$)	0.1 (0.13)
RetroSplenial Complex	-0.13 ($2.0\cdot10^{-5}$)	-0.28±0.16 (0.07)	0.01 (0.88)
Superior Frontal Language Area	0.13 ($3.6\cdot10^{-5}$)	0.49±0.15 ($1.1\cdot10^{-3}$)	-0.05 (0.5)

Chapter 4. eQTL of KCNK2 regionally influences the brain sulcal widening: evidence from 15,597 UK Biobank participants with neuroimaging data

1. Introduction to the chapter

Previous chapters were interested in the heritability of brain-based phenotypes or their shared genetic with cognitive ability. Using HCP data, we could not look for causal genetic variants, because we only had the filial relationship between individuals and not their genetic material.

In this chapter, we take advantage of the recent release of 20,000 subjects (15,500 from main Bristish ancestry and with successful imaging processing) to perform an exploratory analysis looking for genome-wide genetic association with sulcal grey matter thickness or sulcal width (reflecting the cerebrospinal fluid extent between gyri). For the readers of this thesis, I should note that we did start to explore the genetic associations with sulcal pit DPF or pli de passage occurrence (see Chapter 5). However, for these phenotypes we used Freesurfer white meshes obtain from T1 and T2 nifti images only. Our number subject was thus limited to ~11,000 after applying our processing pipelines. In this case, our GWAS results are not yet genome wide significant and/or replicated

2. Abstract

The grey and white matter volumes are known to decline with age. This cortical shrinkage is visible on magnetic resonance images and is conveniently identified by the increased volume of cerebrospinal fluid in the sulci between two gyri. Here, we replicated this finding using the UK Biobank dataset and studied the genetic influence on these cortical features of aging. We divided all individuals genetically confirmed of British ancestry into two sub-cohorts (12,162 and 3,435 subjects for discovery and replication samples, respectively). We found that the heritability of the sulcal opening ranges from 15 to 45% (s.e.= 4.8%). We identified 4 new loci that contribute to this opening, including one that also affects the sulci grey matter thickness. We identified the most significant variant (rs864736) on this locus as being an expression quantitative trait locus (eQTL) for the KCNK2 gene. This gene regulates the immune-cell into the central nervous system (CNS) and controls the CNS inflammation, which is implicated in cortical atrophy and cognitive decline. These results expand our knowledge of the genetic contribution to cortical shrinking and promote further investigation into these variants and genes in pathological context such as Alzheimer's disease in which brain shrinkage is a key biomarker.

3. Introduction

The brain structure aspect alters throughout life. In particular, grey and white matter volumes are known to shrink with age in diseased and normal brains (Fjell and Walhovd, 2010; Ge et al., 2002; Lockhart and DeCarli, 2014). Numerous cross-sectional and longitudinal studies have confirmed this

trend by either studying grey matter volume changes (Lemaitre et al., 2012) or cortical sulci widening (Kochunov et al., 2005; Shen et al., 2018). Importantly, the magnitude of brain shrinkage varies across regions and individuals, and increases with age (Raz et al., 2005). Multiple factors related to the environment or to genetics likely play a role in these changes. Such genetic effect is characterized in the hippocampus atrophy with the apolipoprotein E, ε4 allele (ApoE-ε4), which is also associated with an increased risk for developing late onset Alzheimer's disease (AD) (Moffat et al., 2000). However, the genetic underpinnings of the brain sulcal features have not been investigated, except a few studies that were interested in the heritability of sulcal depth in extended pedigrees of young adults (Le Guen et al., 2018a) or non-human primates (Kochunov et al., 2010). To the best of our knowledge, no genome wide association studies (GWAS) in imaging genetics with a sample size above 10,000 subjects were conducted on the brain sulcal features. In imaging-genetics, previous GWAS with such sample sizes have looked into the hippocampal and intracranial volumes (Stein et al., 2012), or the human subcortical brain structures (Hibar et al., 2015). These studies traditionally used meta-analyses which pooled subjects scanned in different centers with various scanners and from different age ranges. Such a meta-analysis initiative is best exemplified by the ENIGMA (Thompson et al., 2014) and CHARGE (Psaty et al., 2009) consortia. The UK Biobank project (Allen et al., 2012) offers a remarkable opportunity to address these issues by gathering data from a fairly homogenous population of subjects, and acquiring magnetic resonance images (MRI) on identical scanners operated at the same location. Additionally, it enables researchers to directly access a cohort with numerous participants while alleviating the uncertainty of meta-analyses.

In this chapter, we consider ten prominent brain sulci that are automatically extracted and labelled using the Brainvisa cortical sulci recognition pipeline (Perrot et al., 2011; Rivière et al., 2009). These sulci are the central, the anterior and posterior cingulate, the inferior and superior temporal, the intraparietal, the subparietal, the superior and inferior frontal sulci and the Sylvian fissure (Mangin et al., 2015; Shen et al., 2018). Even though the subparietal sulcus is not as prominent as the others, it was included in our analysis because it lies in the precuneus which is a major target for atrophy in AD (Bailly et al., 2015; Karas et al., 2007). First, we replicated the known trends of cortical shrinking with age in a large sample of individuals from the UK Biobank, considering the grey matter thickness and sulcal opening. Second, we estimated the genetic influence on these features with the genome wide complex trait analysis (GCTA)(Yang et al., 2011). In this method, the genetic relationship (kinship) matrix between subjects is computed to estimate the variance of an observed phenotype, which can be explained by the single nucleotide polymorphisms (SNPs), referred to as the heritability. Finally, we performed a genome wide association study (GWAS) of the phenotypes with the genotyped variants using PLINK (Purcell et al., 2007). A functional annotation of the phenotype-associated variants was then performed using the gene expression level published by the Genotype-Tissue Expression (GTEx) consortium (GTEx Consortium, 2017), allowing the identification of expression quantitative trait loci (eQTLs).

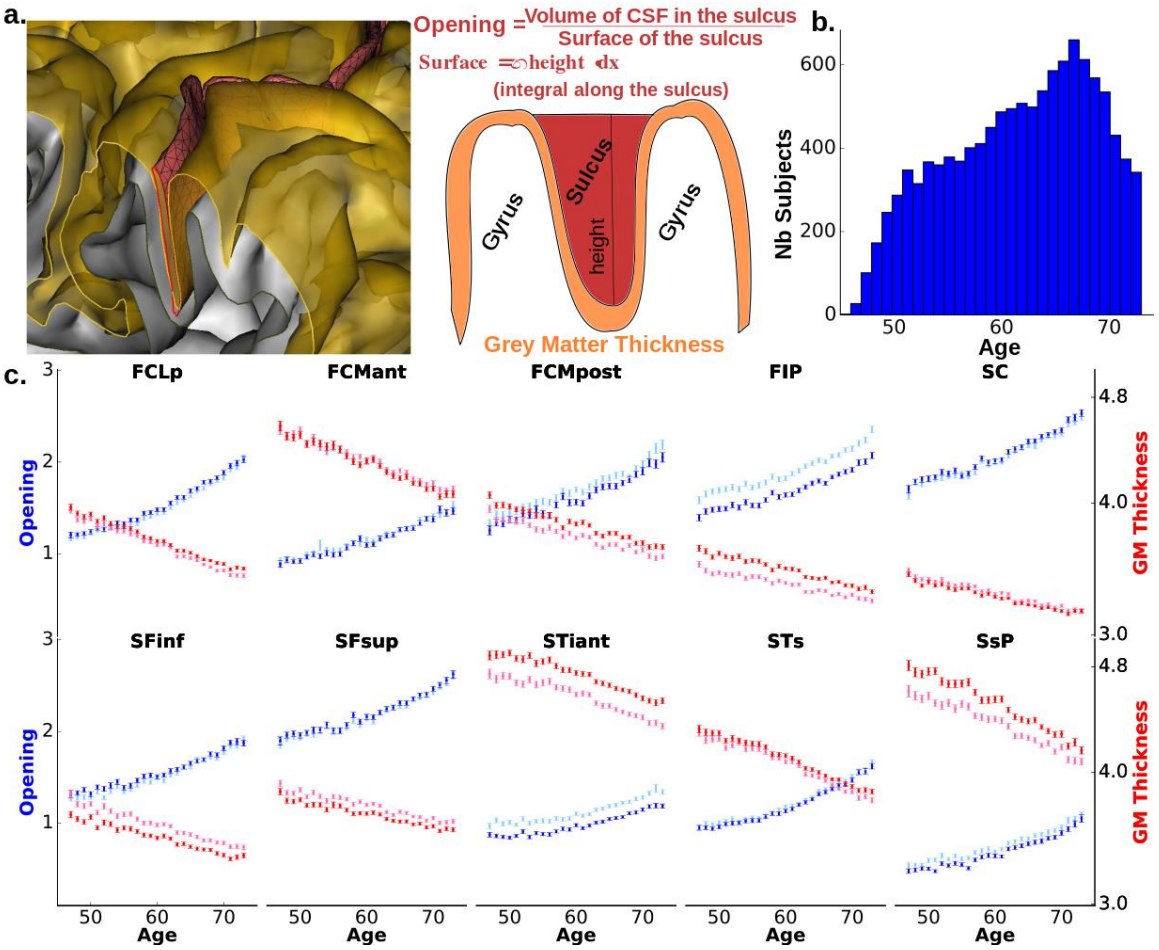

Figure 1. Evolution of sulcal opening and grey matter thickness with age in the main brain sulci. **a.** Schematic definition of the opening and grey matter thickness for the Brainvisa sulci. **b.** Age distribution in the UK Biobank sample with MR Imaging. **c.** Mean opening (red) and mean grey matter thickness (blue) vs age. (light blue and light red represent left hemisphere values; dark blue and red represent right hemisphere values).

4. Methods

4.1. Cortical sulci extraction

The cortical sulci were extracted from T1-weighted images via the following steps. First, the brain mask was obtained with an automated skull stripping procedure based on the SPM8 skull-cleanup tool (Ashburner, 2009). Second, the images were segmented into grey matter, white matter and cerebrospinal fluid using histogram scale-space analysis and mathematical morphology (Mangin et al., 2004). Third, individual sulci were segmented and labelled using Morphologist, the sulci identification pipeline from Brainvisa (version 4.5.1, (Rivière et al., 2009)). For segmentation, a kind of crevasse detector was used to reconstruct each fold geometry as the medial surface from the two opposing gyral banks that spanned from the most internal point of the fold to the convex hull of the cortex (Mangin et al., 2004). A Bayesian inspired pattern recognition approach relying on Statistical Probabilistic Anatomy Maps and multiscale spatial normalization was used to label the folds using a nomenclature of 125 sulci (Mangin et al., 2015; Perrot et al., 2011). For each sulcus, the average distance between both banks of the pial surface was used to quantify the sulcus width. This average distance was computed as the ratio between 1) the volume of CSF filling up the sulcus from the brain

hull to the fold bottom and 2) the surface area of the sulcus estimated by half the sum of the areas of the triangles making up a mesh of the corresponding medial surface (**Figure 1a**). The average thickness of the cortical mantle on both sides of the sulcus was computed using a fast marching algorithm applied to a voxel-based binary representation of the cortex grey matter (Perrot et al., 2011).

4.2. Age and sulci features relationship

In our discovery sample, to quantify the influence of age, we computed the mean of each sulcal feature for each age across the subjects with the same age. It is worth noting that the age at MRI scan is provided by UK Biobank with a one year precision. We excluded 45 and 46 year old subjects due to their small sample sizes. We can robustly estimate the mean feature per year after 50 years, because there are more than 200 subjects per 1-year interval. Last, using linear regression, we estimated the slope of a linear model adjusted between sulcal features and age (**Table S1**).

The heritability estimation using the Genome wide complex trait analyses (GCTA) software is described in the introduction.

4.3. Genetic univariate association analyses

The genotype-phenotype association analyses were performed using PLINKv1.9 (Purcell et al., 2007), with the following thresholds: missing genotype = 10% (32.938 variants excluded), hwe = 10^{-6} (12.301), and maf = 1,0% (117.165), in total 621.852 variants passed the genetics QC for the discovery sample. Note that the missing genotype threshold is traditionally more stringent to estimate the kinship in GCTA analysis than to perform GWAS. The genome wide significant threshold for the discovery sample was set to $p < 5 \cdot 10^{-8}$ and $p < 0.05$ in the replication sample for variants that passed the first threshold.

5. Results

5.1. Age-related cortical shrinking

The UK Biobank large sample size enabled us to precisely estimate the mean of sulcal opening and grey matter (GM) thickness per age with a 1-year precision. **Figure 1** (**c, d**) underlines a strong correlation between the age and these two cortical features in the discovery sample. Between 47 and 73 years old, the sulcal opening increases on average of 0.025 mm/year, while the GM thickness decreases on average of 0.015 mm/year (**Table S1**). The Sylvian fissure and the subparietal sulcus show the maximum increase of opening and decrease of GM thickness, respectively, while the inferior temporal and left intraparietal have the minimum.

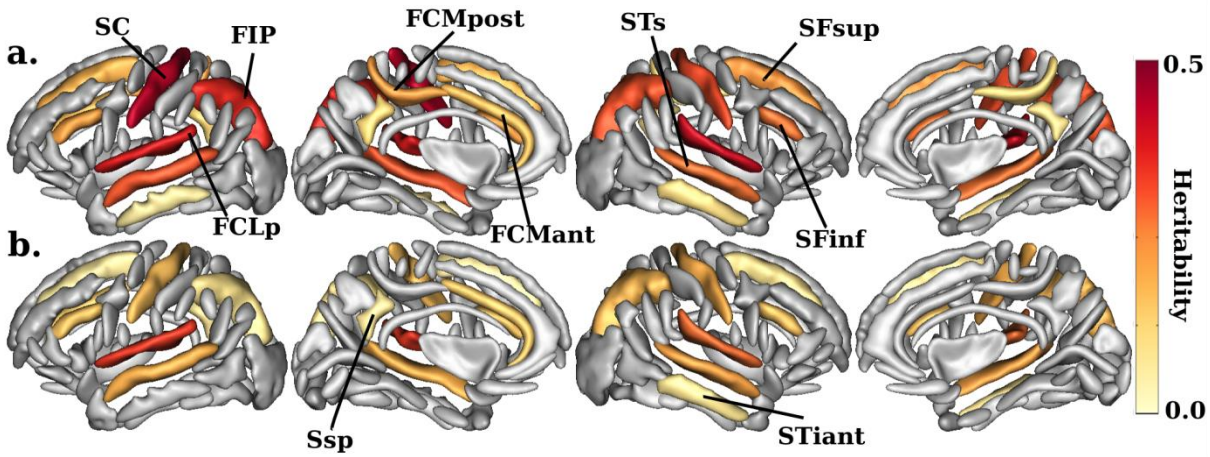

Figure 2. Heritability estimates of the sulcal opening (a.) and sulcal grey matter thickness (b.). ($p < 0.00125$ Bonferroni corrected). Main sulci have been annotated using Brainvisa abbreviation (**SC**: Central, **FIP**: Intraparietal, **FCLp**: Sylvian fissure, **FCMpost**: Posterior Cingulate, **FCMant**: Anterior Cingulate, **STs**: Superior Temporal, **STiant**: Inferior Temporal, **SFsup**: Superior Frontal, **SFinf**: Inferior Frontal, **Ssp**: Subparietal). The sulci are displayed using the Statistical Probability Anatomy Map (SPAM) representation, which represents the average sulci shape and position on the reference base of the Brainvisa sulci extraction pipeline (Perrot et al., 2011).

5.2. Heritability of sulcal opening and grey matter thickness around the sulci

In the discovery sample, we estimated the heritability ($\mathbf{h^2_{SNPs}}$) of the sulcal opening and GM thickness using the GCTA method (Yang et al., 2011), i.e. the variance explained by all the SNPs (**Figure 2**). Significant $\mathbf{h^2_{SNPs}}$ estimates for the sulcal opening range from 0.15 to 0.45, with a minimum in the left inferior temporal and a maximum in the left central sulcus (**Table S2**). Significant $\mathbf{h^2_{SNPs}}$ estimates for the GM thickness range from 0.15 to 0.37, with a minimum in the left superior frontal and a maximum in the left Sylvian fissure. Note that the sulcal opening heritability values are all higher than the ones of the GM thickness.

5.3. Genome-wide association study (GWAS) of the cortical features

We performed a genome-wide association study on the genotyped data for the sulcal opening and GM thickness in the ten sulci. Manhattan and QQ plots are shown in the supplementary materials (**Figures S1-4**). **Table 1** summarizes the 24 phenotype-SNP associations that were genome-wide significant in the discovery sample and nominally significant in the replication sample. Among these associations, 12 SNPs were unique at 5 different loci. The most represented locus, with 17 replicated association hits, is on chromosome 1, 27kb before the transcription start site of the KCNK2. Within this locus, the two main associated SNPs are rs59084003 and rs864736 with 7 and 4 significant hits respectively. It should be noted that these two SNPs are not in strong linkage disequilibrium (LD) and other significant SNPs on this locus are either in LD with the first or the second one (**Figure S5**). The second most represented locus, with 4 significant associations, is on chromosome 16. This locus lies in the starting region of the non-coding RNA LOC101928708, in the vicinity of the protein coding gene

C16orf95, followed by FBXO31. On this locus, the main associated SNP is rs9933149 with 3 hits. The three other loci each include a single significant replicated phenotype-SNP association. On chromosome 8, rs11774568, associated with the GM thickness in the left Sylvian fissure, is in a region with a high density of genes, between the genes DEFB136 and DEFB135. On chromosome 9, rs10980645, associated with the central sulcus opening, is an intronic variant of the LPAR1 gene. On chromosome 12, rs12146713, associated with the right STs opening, is an intronic variant of the NUAK1 gene.

Table 1. Significant genome wide association hit SNPs (discovery $p < 5 \cdot 10^{-8}$ and replication $p < 0.05$). Bold rsid correspond to variants that are further investigated in **Figure 3**, the remainders are in **Figures S7-S8**.

Feature	Sulcus	chr	Pos (GRCh37)	rsid	β	p-val	β	p-val	Nearest Gene
					Discovery (≈ 12150)		Replication (≈ 3430)		
Opening	**FCMpost left**	1	215134722	rs755576	-0.101	$1.7 \cdot 10^{-9}$	-0.075	0.02	KCNK2
	FCMpost left	1	215135752	rs6667184	-0.052	$2.6 \cdot 10^{-9}$	-0.046	$6.2 \cdot 10^{-3}$	KCNK2
	FCMpost left	1	215140283	rs504473	0.053	$2.2 \cdot 10^{-8}$	0.043	0.02	KCNK2
	FCMpost left	1	215150260	**rs864736**	0.063	$2.3 \cdot 10^{-14}$	0.064	$3.2 \cdot 10^{-5}$	KCNK2
	FCMpost right				0.061	$3.8 \cdot 10^{-14}$	0.061	$4.7 \cdot 10^{-5}$	
	FCMpost left	1	215154276	**rs59084003**	-0.121	$3.0 \cdot 10^{-14}$	-0.083	$5.1 \cdot 10^{-3}$	KCNK2
	FCMpost right				-0.116	$7.9 \cdot 10^{-14}$	-0.073	0.01	
	FIP left				-0.071	$9.7 \cdot 10^{-10}$	-0.044	0.04	
	FIP right				-0.072	$3.4 \cdot 10^{-11}$	-0.062	$1.8 \cdot 10^{-3}$	
	SC right				-0.074	$2.7 \cdot 10^{-9}$	-0.058	0.01	
	SsP left				-0.061	$5.6 \cdot 10^{-9}$	-0.042	0.02	
	FCMpost left	1	215186121	rs2841614	-0.093	$4.1 \cdot 10^{-9}$	-0.084	$5.1 \cdot 10^{-3}$	KCNK2
	FCMpost left	1	215191552	rs1452608	-0.054	$5.2 \cdot 10^{-11}$	-0.044	$4.7 \cdot 10^{-3}$	KCNK2
	FCMpost right	1	215135752	rs6667184	-0.058	$1.5 \cdot 10^{-11}$	-0.046	$4.0 \cdot 10^{-3}$	KCNK2
	SC left	9	113699603	rs10980645	0.038	$4.5 \cdot 10^{-8}$	0.033	0.01	LPAR1
	STs right	12	106476805	rs12146713	0.05	$9.3 \cdot 10^{-10}$	0.031	0.03	NUAK1
	SFinf left	16	87226206	rs9933149	-0.031	$5.0 \cdot 10^{-8}$	-0.05	$1.7 \cdot 10^{-6}$	C16orf95
	STs left				-0.033	$2.6 \cdot 10^{-11}$	-0.019	0.03	
	STs right				-0.031	$2.2 \cdot 10^{-10}$	-0.024	$8.2 \cdot 10^{-3}$	
	SFinf left	16	87237863	rs4843549	-0.033	$5.5 \cdot 10^{-9}$	-0.047	$5.9 \cdot 10^{-6}$	C16orf95
GM thickness	**FCMpost left**	1	215150260	**rs864736**	-0.023	$8.3 \cdot 10^{-10}$	-0.02	$6.2 \cdot 10^{-3}$	KCNK2
	FCMpost right				-0.024	$9.6 \cdot 10^{-10}$	-0.019	0.01	
	FIP right	1	215154276	**rs59084003**	0.037	$7.3 \cdot 10^{-10}$	0.037	$5.6 \cdot 10^{-4}$	KCNK2
	FCLp left	8	11836318	rs11774568	0.018	$4.2 \cdot 10^{-8}$	0.017	$4.9 \cdot 10^{-3}$	DEFB135

5.4. Regional significance and direction of effect of the hit variants

DNA region upward KCNK2 harbors significant SNP association with the sulcal opening (**Figure 3**) and GM thickness (**Figure S6**) of the posterior cingulate, the central and intraparietal sulci.

In addition, the implicated SNPs show near genome-wide significant influence on the sulcal features in the superior temporal, inferior frontal and subparietal sulci. Overall, this suggests a brain wide regulation for this genomic region. The sulcal opening is increased in carriers of the minor allele of rs864736 (maf = 46%, in our discovery sample), while it is decreased in carriers of the minor allele of rs59084003 (maf = 7%). The locus on chromosome 16 displays a more specific spatial control over the temporal and frontal lobes, with significant sulci including the inferior frontal, the superior and inferior temporal and the Sylvian fissure (**Figures S7-8 a.**). The sucal opening of these sulci is decreased in carriers of the minor allele rs9933149 (maf = 38%). It should be noted that the SNPs of these two loci have a significant pleiotropic influence on sulcal opening and GM thickness.

Regarding the three remaining loci, they preferentially influence one out of the two sulcal features. The intronic variant (rs12146713) of NUAK1 significantly influences the sulcal opening in the temporal region (Sylvian fissure, superior and inferior temporal sulci), as well as in the inferior frontal and intraparietal sulci (**Figures S7-8 b.**). The intronic variant (rs10980645) of LPAR1 significantly affects the sulcal opening of the central sulcus, and moderately affects the posterior cingulate (**Figures S7-8 c.**). The variant (rs11774568) chromosome 8, near DEFB136, appears to be linked with the GM thickness of the Sylvian fissure and superior temporal sulcus (**Figures S7-8 d.**).

5.5. Functional annotation of the loci

To obtain information on the role of the region upstream of KCNK2, we investigated the gene expression QTL using the GTEx database (GTEx Analysis Release V7 (dbGaP Accession phs000424.v7.p2)) (GTEx Consortium, 2017). We found that the variants rs864736 and rs14526008, which are in LD, are significant eQTLs for the KCNK2 gene expression, with significant multi-tissue meta-analysis RE2 (random-effects model 2) (Han and Eskin, 2011) p-values of $9.7 \cdot 10^{-6}$ and $5.7 \cdot 10^{-9}$, respectively. **Figure 4** presents the effect size in various tissues of rs864736 allelic configuration on KCNK2 gene expression. Even though the association barely reaches nominal significance in single brain tissue due to low sample sizes (~80-140 subjects), it overall emphasizes strong effects across brain tissues. The other significantly associated SNP near KCNK2 (rs59084003) was not reported as a significant eQTL in GTEx possibly for technical reasons because of its small minor allele frequency (7%). Indeed, the effect of allelic configurations cannot be well observed in the relative small GTEx sample. **Table S3** summarizes the other eQTLs found in GTEx for the different loci.

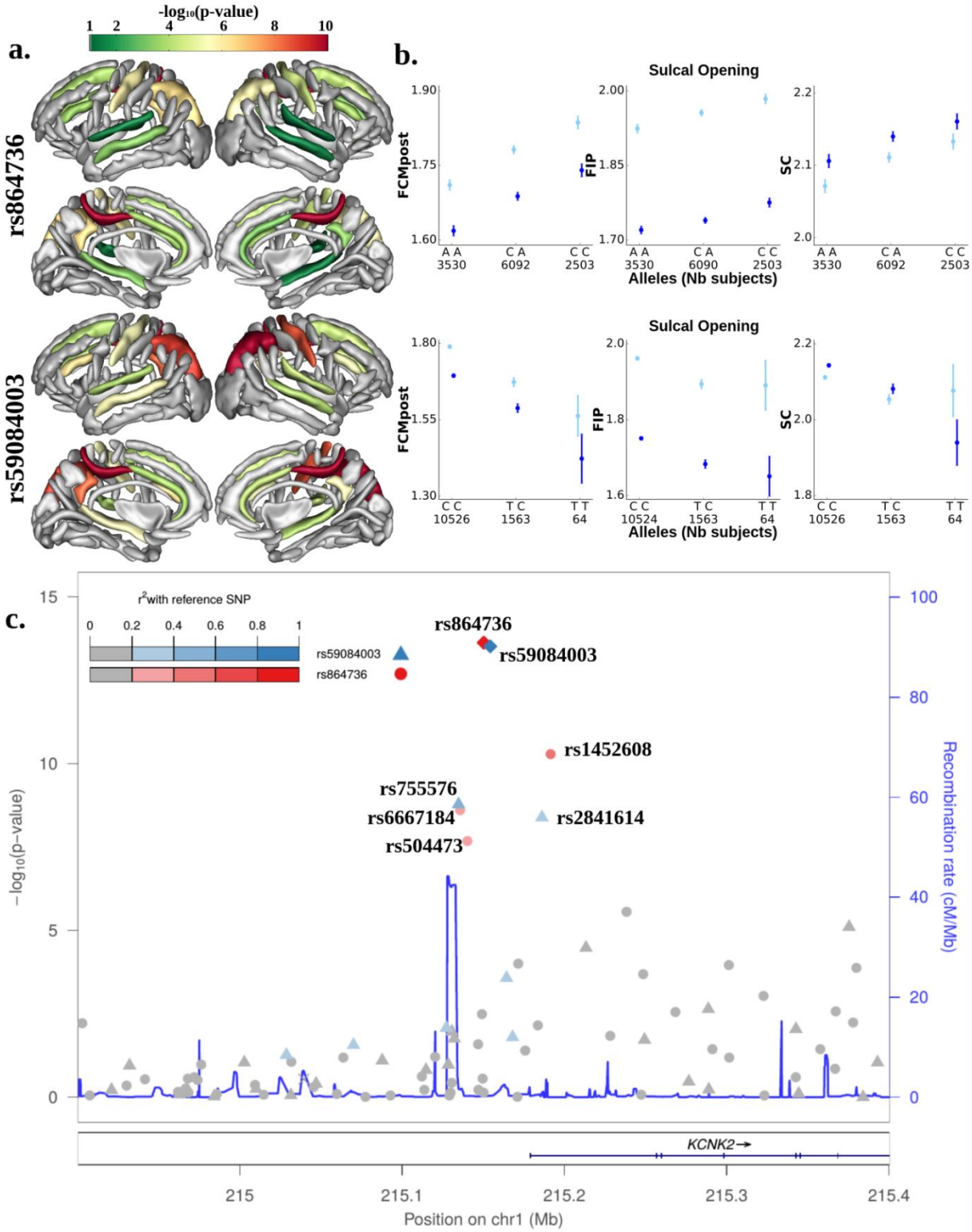

Figure 3. GWAS hits upstream of KCNK2 regulating the sulcal opening. First and second lines correspond to rs864736 and rs59084003, respectively. Lines represents respectively: **a)** the log10(p-value) of each SNPs mapped onto the nominally significant sulci among the ten considered; **b)** the mean sulcal opening and standard error for each configuration of variants in the most significant sulci; **c)** Locuszoom display (Pruim et al., 2011) of the phenotype-variants association for the region upstream of KCNK2 with the left posterior cingulate sulcus opening as a phenotype.

6. Discussion

The bulk of participants in the UK Biobank are older than 50 years old and results have to be discussed within this interval. In order to scrutinize certain genetic effects on brain features, it is important to understand the effect of age. Indeed, some genetic influences may only be revealed in a relatively aged cohort such as the UK Biobank. In this study, we emphasized a steady age effect on the sulcal opening and GM thickness between 45 and 75 years of age. Furthermore, we showed that these brain features are genetically controlled by estimating their heritability in ten prominent sulci and we also identified several of their causal variants.

It is well known that with age, the GM and white matter (WM) volumes decreases (Raz et al., 2005), while the amount of cerebrospinal fluid (CSF) in the cortical folds increases (Good et al., 2001). In our analysis, we confirmed the well-established results regarding the GM thickness decrease and sulcal opening increase with age in the UK Biobank cohort. The assessment of cortical sulci opening is well described and correlates with neurocognitive decline in mild cognitive impairment and dementia disorders (Bastos Leite et al., 2004). In addition, the CSF opening is probably a better biomarker than the GM thickness because the contrast in MRI images is stable with age. The cortical sulci widening with age is likely related to the reduction of gyral thickness resulting in the dilatation of the sulci (Magnotta, 1999; Symonds et al., 1999), but could also account for neurodegenerative processes occurring in the underlying white matter (Gunning-Dixon et al., 2009). While, the GM thickness and sulcal widening are correlated (Kochunov et al., 2008; Liu et al., 2013), the robustness of the two measures might differ. We obtained less significant variant-phenotype associations in GM thickness, because the sulcal opening might be more consistently measured across individuals than the GM thickness. This might be due to the fact that the MRI contrast between GM and CSF remains more stable across the lifespan than the GM / WM contrast (Kochunov et al., 2005). Thus, sulcal widening is commonly used by radiologists as a surrogate of cortical atrophy in clinical settings (Shen et al., 2018). It could also reflect a higher sensitivity to the primal effects of aging because of the consequences of grey and white matter atrophy. Note that the opening of larger sulci like the Sylvian valley could also be impacted by global mechanical compensation for aging processes.

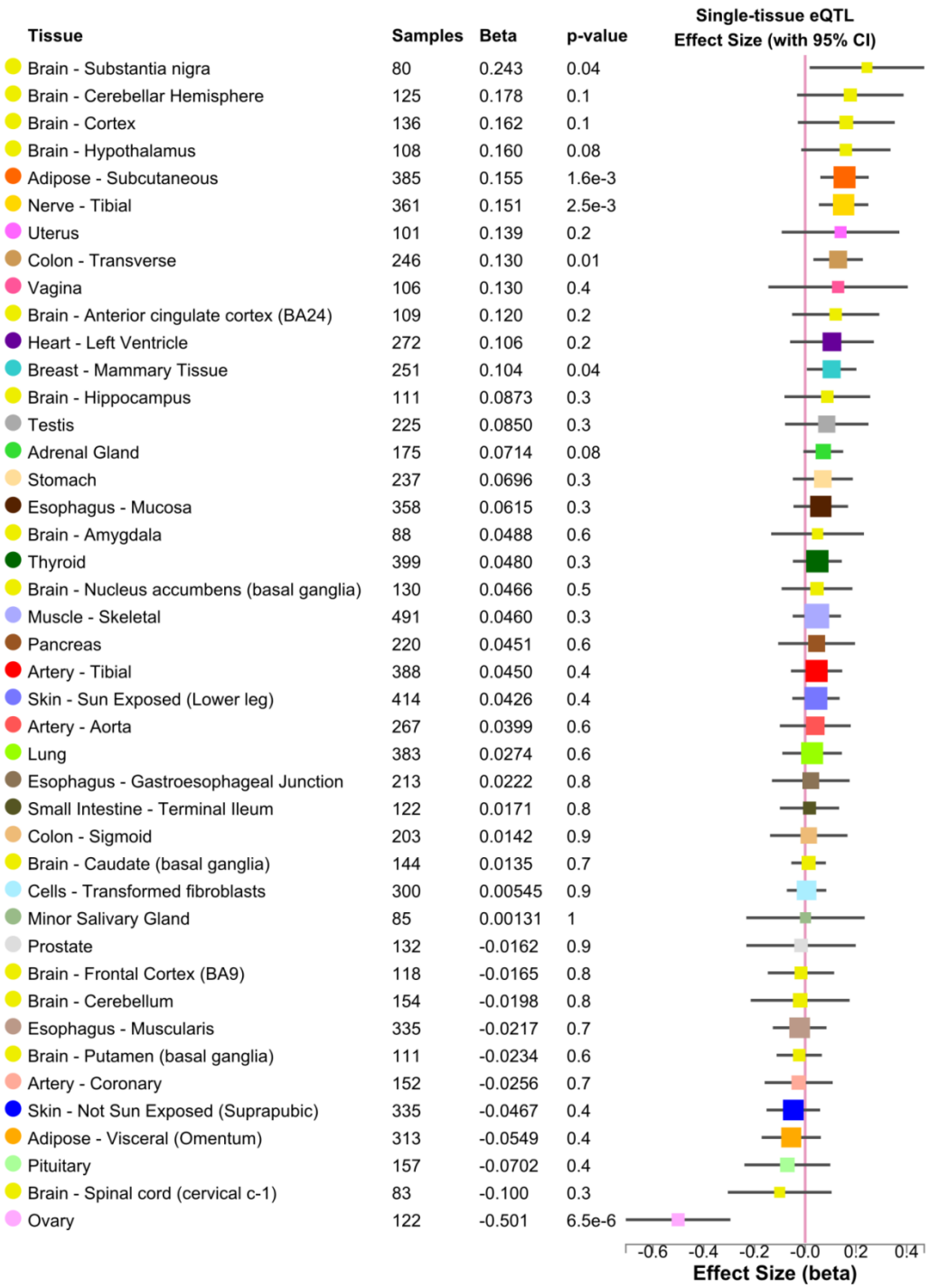

Figure 4. Multi-tissue eQTLs comparison for gene KCNK2 and variant rs864736 (ENSG00000082482.9 KCNK2 and 1_215150260_C_A_b37 eQTL). Meta-Analysis Random Effect Model2 (Han and Eskin, 2011) p-val = $9.7 \cdot 10^{-6}$. (Data Source: GTEx Analysis Release V7, dbGaP Accession phs000424.v7.p2)

The main finding of this chapter is that the locus upstream of the KCNK2 transcription start site influences the sulcal opening and GM thickness. Additionally, the tissue specific gene expression (eQTL) analysis of the GTEx consortium emphasizes that overall (meta-analysis of all tissues), and particulary in the brain, this DNA region regulates the expression of KCNK2 (GTEx Consortium, 2017). Thus, we can legitimately assume a link between the regulation of KCNK2 expression and the amplitude of sulcal opening. In other words, depending on the allelic configurations in the region

upstream of KCNK2, an individual will have his sulci comparatively enlarged. Because sulcal widening is a marker of cortical atrophy as we pinpointed in the previous paragraph, there is a potential link between KCNK2 expression level and brain atrophy. The KCNK2 gene, also known as TREK1, is a member of the two-pore-domain potassium channel family which is expressed predominantly in the brain (Hervieu et al., 2001). Previous literature emphasized several functions for KCNK2 gene in the brain. First, the KCNK2 regulates the blood-brain barrier function and inflammation in the brain of mice (Bittner et al., 2013) and humans (Bittner et al., 2014). The inhibition or deletion of KCNK2 facilitates lymphocytes migration into the central nervous system (CNS) and promotes autoimmune CNS inflammation (Bittner et al., 2013). Second, in mice, the knockdown of KCNK2 gene impairs the neuronal migration of late-born cortical excitatory neurons, which are precursors of Layer II/III neurons (Bando et al., 2014). Third, in rat hippocampal astrocytes, the increase of KCNK2 expression mediates neuroprotection during ischemia (Banerjee et al., 2016). The mechanism might involve KCNK2 blockade, inhibiting neuronal apoptosis and protecting the brain from cerebral ischemic injury (Wang et al., 2018). Finally, KCNK2 over expression was shown to exacerbate memory impairment in middle-age mice (Cai et al., 2017). To summarize, KCNK2 controls several major cellular responses involved in memory formation and is believed to participate in neuroinflammation, cerebral ischemia and blood-brain barrier dysfunction (Bittner et al., 2014; Cai et al., 2017; Wang et al., 2018).

The first role suggests the most promising direction of future work, because previous studies have proposed that neuroinflammation is involved in cognitive decline in midlife (Marsland et al., 2015) and implicated in pathological age-related changes and AD (McGeer and McGeer, 2001). Throughout life, stress, recurrent inflammation and subclinical cerebrovascular events potentially contribute to brain aging (Raz and Rodrigue, 2006). The link between our findings and inflammation indicates a potential mediation role for KCNK2. Finally, it is difficult to disentangle whether or not brain inflammation has a deleterious role on cognitive functions, since there is no clear consensus. A recent study however emphasizes a slower progression of AD in patients with early neuroinflammation (Hamelin et al., 2016).

In conclusion, in a sample of 15,597 subjects representative of the general population of British ancestry, we have shown that an eQTL of KCNK2 influences sulcal widening. This appears coherent with the role of KCNK2, which affects the regulation of inflammation response in the brain.

7. Supplementary Figures

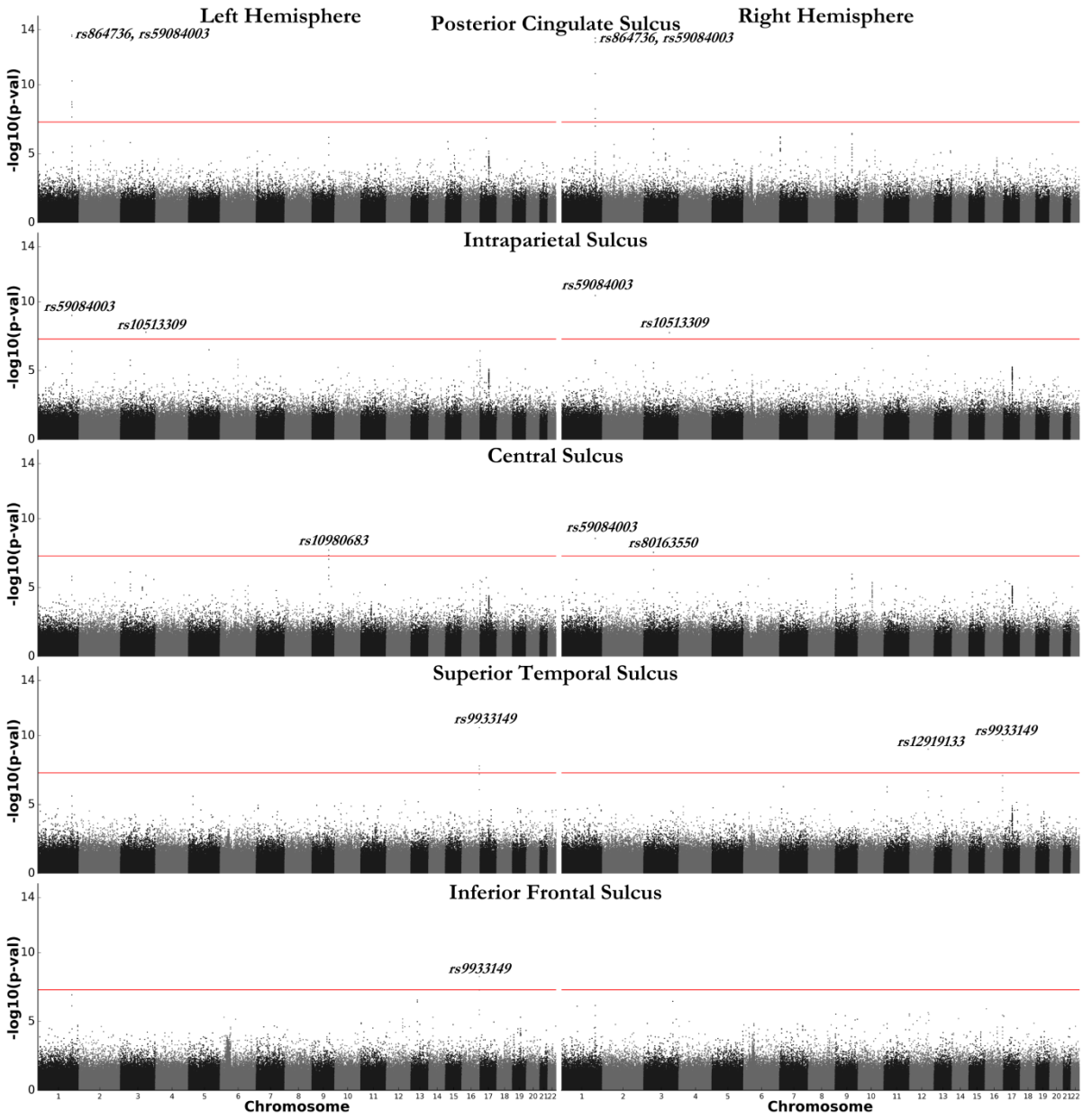

Figure S1. Manhattan plots for five sulci considering their opening as the phenotype for the GWAS.

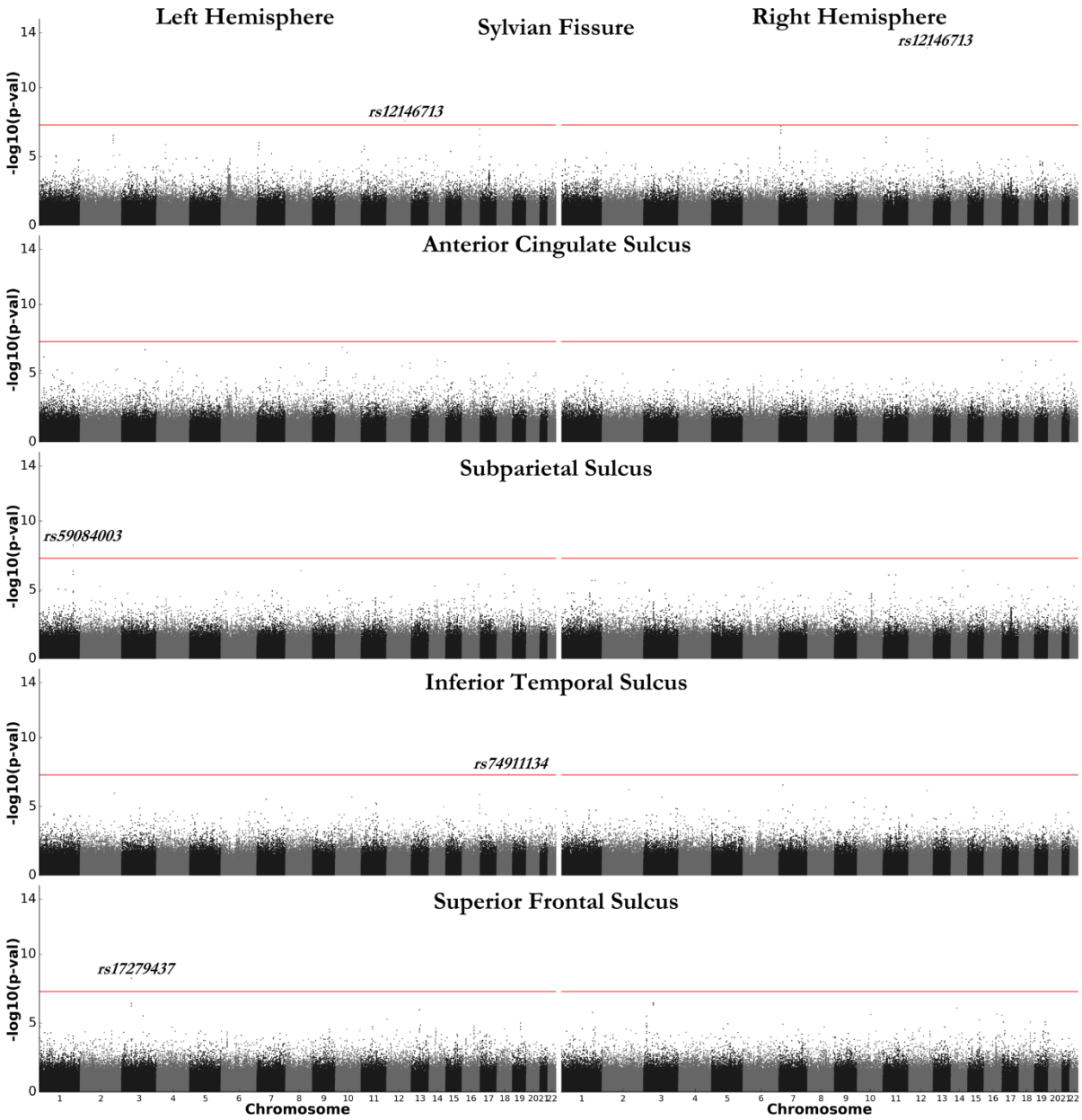

Figure S2. Manhattan plots for five sulci considering their opening as the phenotype for the GWAS.

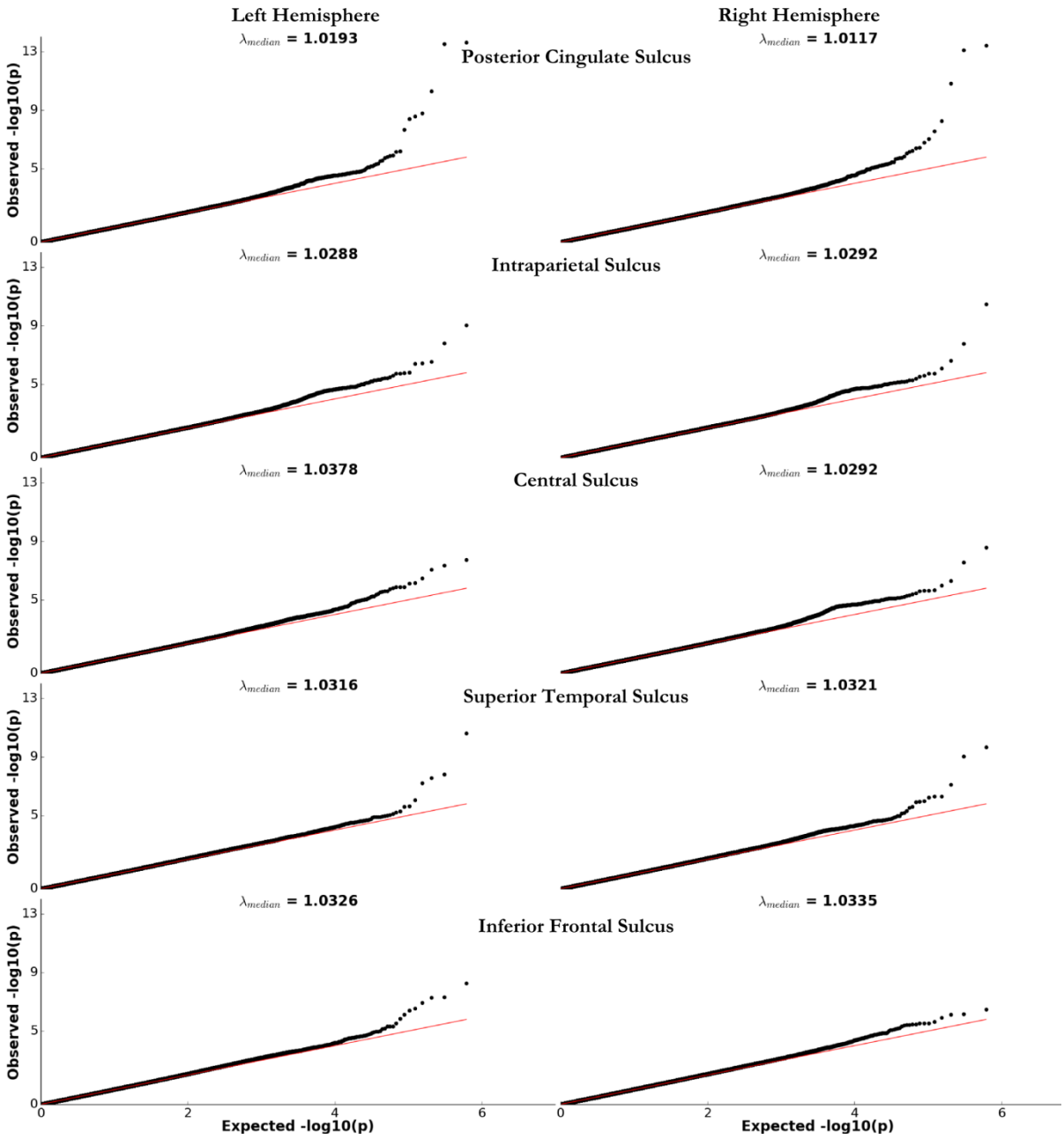

Figure S3. QQ plots for five sulci considering their opening as the phenotype for the GWAS.

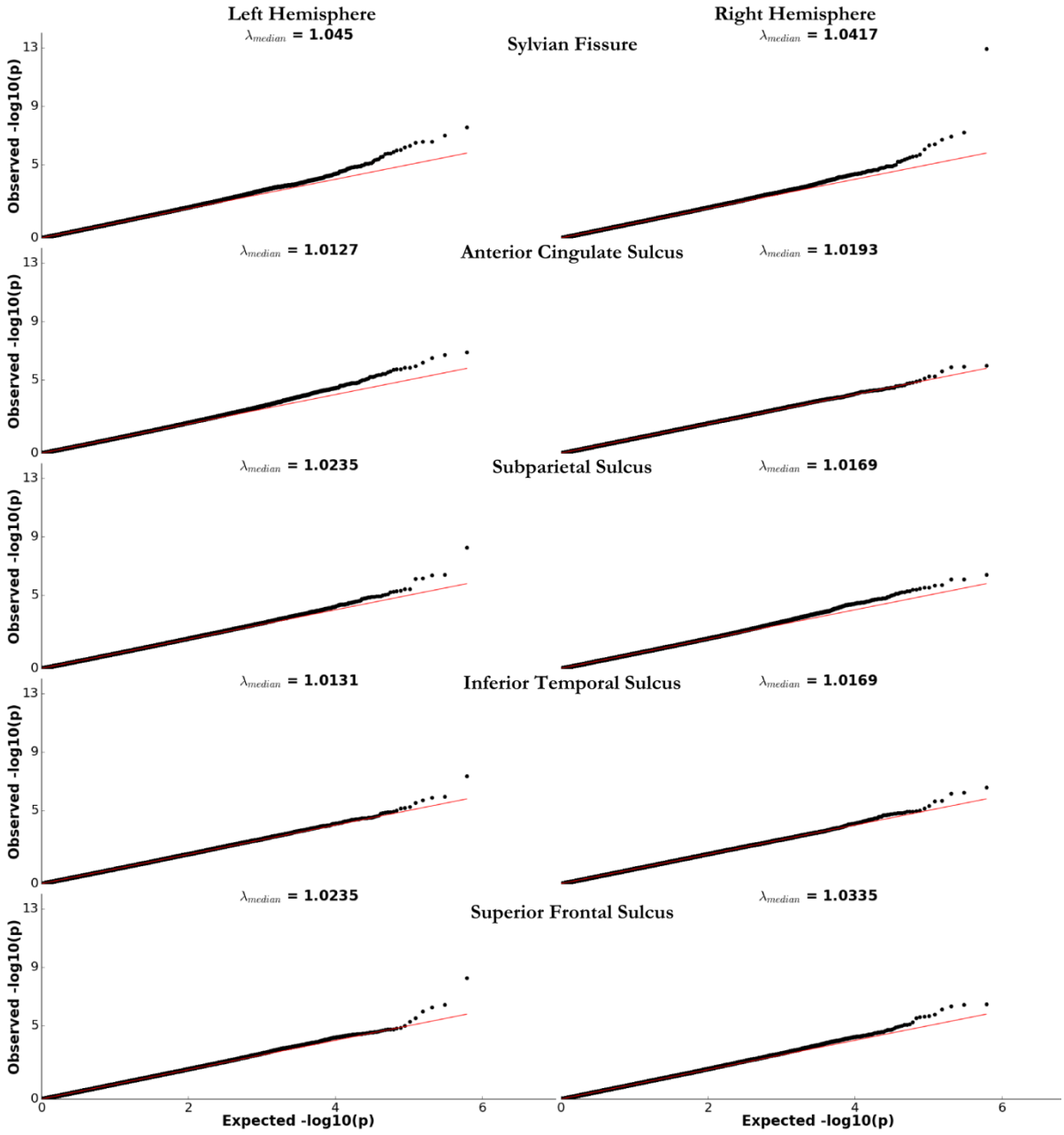

Figure S4. QQ plots for five sulci considering their opening as the phenotype for the GWAS.

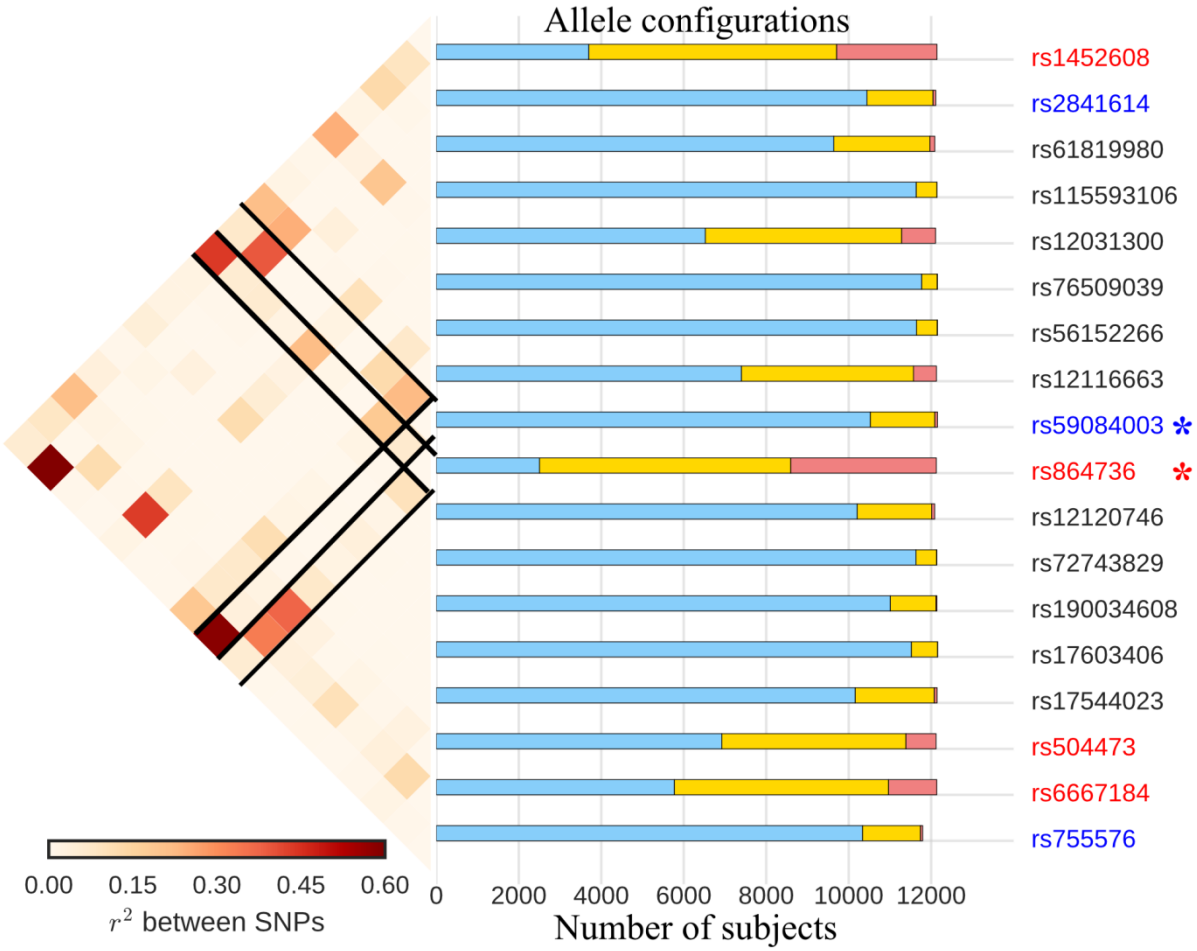

Figure S5. Linkage disequilibrium (r^2 computed with PLINK) for SNPs in the significant locus upward of KCNK2. The number of subjects for the different allelic configurations is displayed (number of subjects homozygote major allele in blue, heterozygote in yellow, homozygote minor allele in red). The significant variants in GWAS (**Tab. 1**) in LD with rs864736 and rs59084003 are in red and blue, respectively.

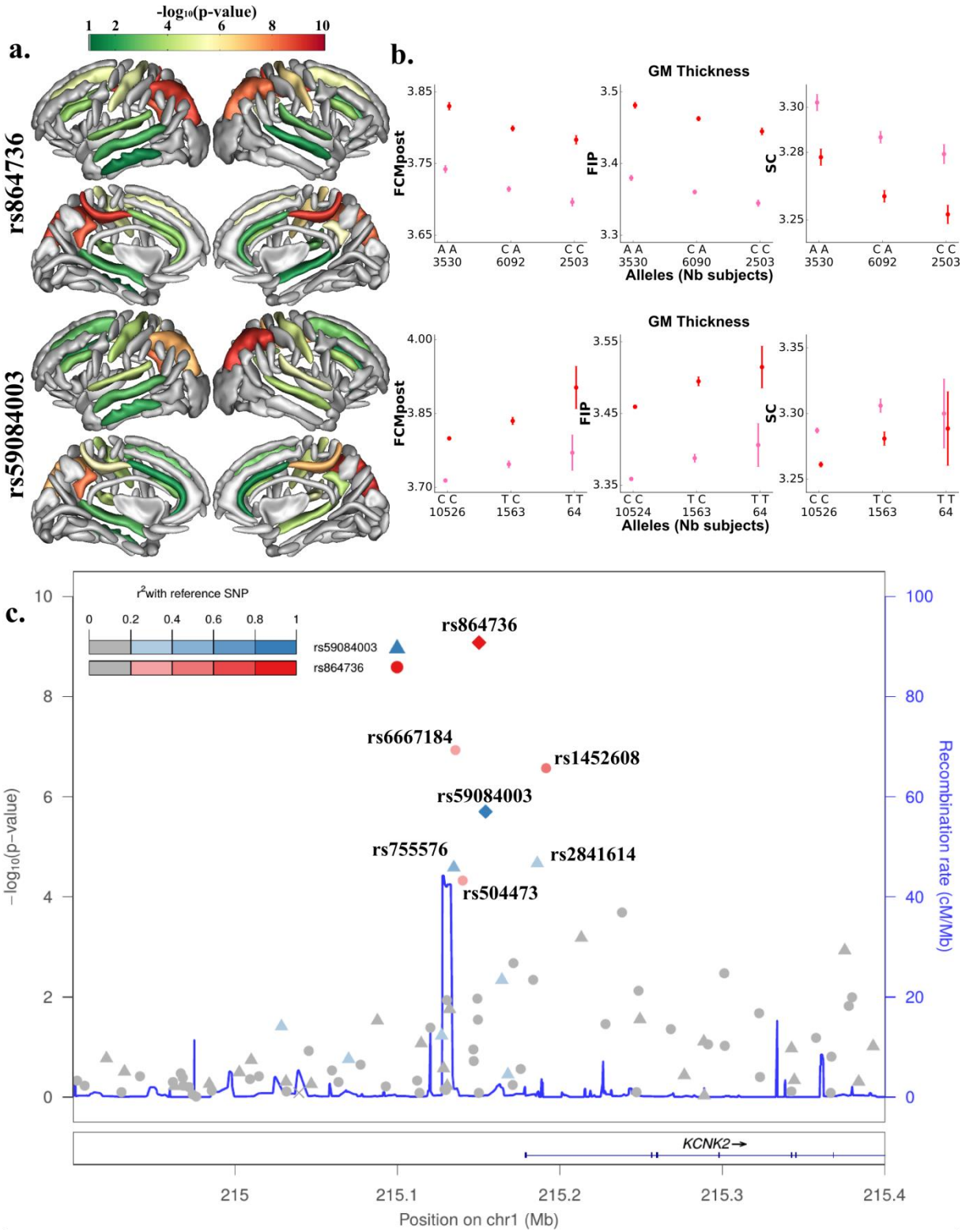

Figure S6. Most significant GWAS hits on KCNK2 regulating the GM thickness. First and second lines correspond to rs864736 and rs59084003, respectively. Lines represents respectively: **a.** the log10(p-value) of each SNPs mapped onto the nominally significant sulci among the ten considered; **b.** the mean GM thickness and standard error for each configuration of variants in the most significant sulci; **c.** Locuszoom display (Pruim et al., 2011) of the phenotype-variants association for the region upward to KCNK2 with the left posterior cingulate sulcus opening as a phenotype..

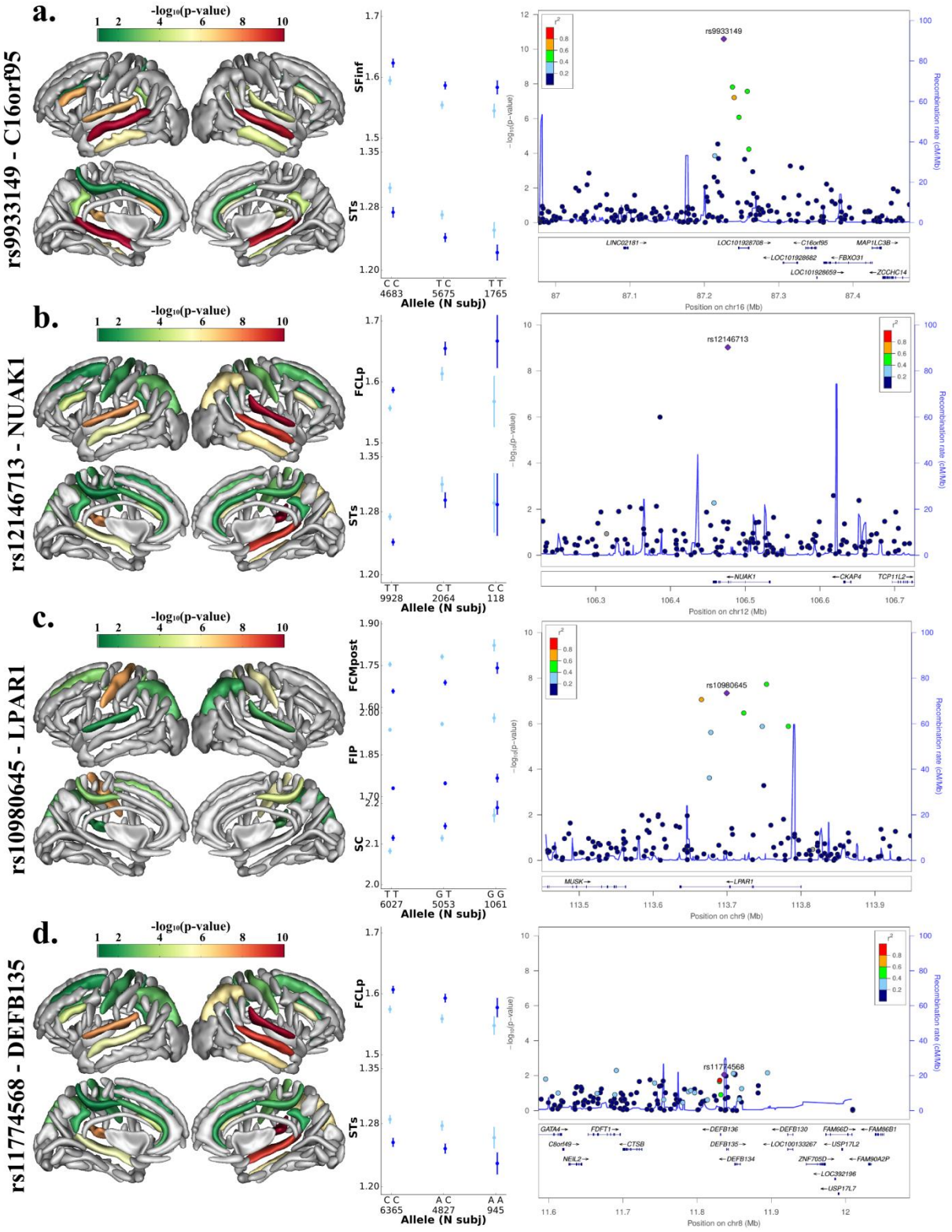

Figure S7. Four significant GWAS hits on the sulcal opening. Lines correspond to the SNPs presented in the following order rs9933149 (**a.**), rs12146713 (**b.**) rs10980645 (**c.**) rs11774568 (**d.**). Columns represents respectively the log10(p-value) of each SNPs mapped onto the nominally significant sulci among the ten considered; the mean sulcal opening and standard error for each configuration of variants in the most significant sulci; Locuszoom display (Pruim et al., 2011) for each variant with the associated most significant phenotype.

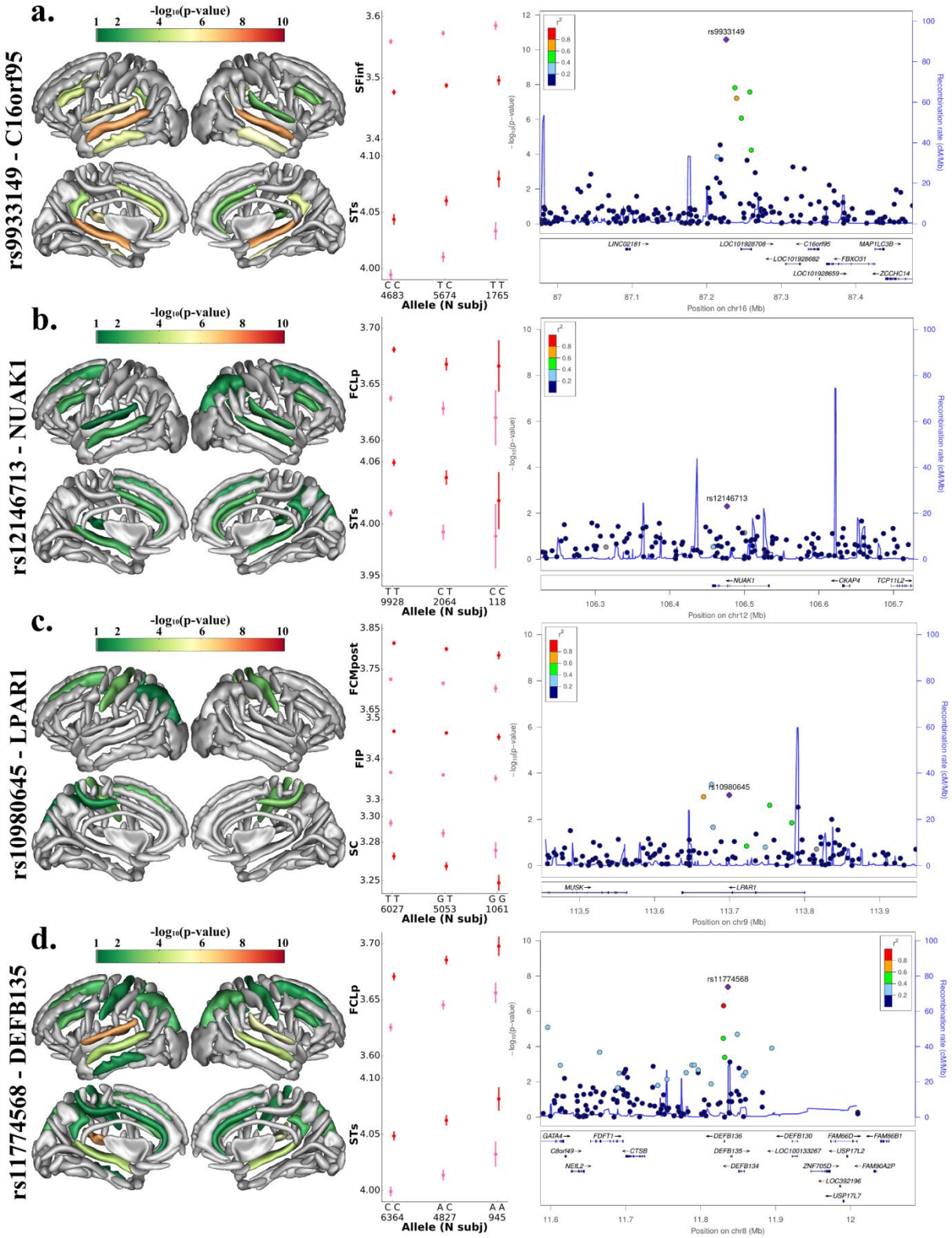

Figure S8. Four significant GWAS hits on the grey matter thickness of the sulci. Lines correspond to the SNPs presented in the following order rs9933149 (**a.**), rs12146713 (**b.**) rs10980645 (**c.**) rs11774568 (**d.**). Columns represents respectively: the log10(p-value) of each SNPs mapped onto the nominally significant sulci among the ten considered; the mean sulci grey matter thickness and standard error for each configuration of variants in the most significant sulci; Locuszoom display (Pruim et al., 2011) for each variant with the associated most significant phenotype.

8. Supplementary Tables

Table S1. Associated slopes for the Figure 1. (c)

Feature	Sulcus	Hemisphere	Slope
Opening	Sylvian Fissure	left	0.0322
		right	0.0325
	Anterior Cingulate	left	0.0217
		right	0.0228
	Posterior Cingulate	left	0.0282
		right	0.0277
	Intraparietal	left	0.0252
		right	0.0232
	Central	left	0.029
		right	0.0293
	Inferior Frontal	left	0.0244
		right	0.0225
	Superior Frontal	left	0.0254
		right	0.0252
	Inferior Temporal	left	0.0145
		right	0.014
	Superior Temporal	left	0.0259
		right	0.0261
	Subparietal	left	0.02
		right	0.0206
Grey Matter Thickness	Sylvian Fissure	left	-0.019
		right	-0.0183
	Anterior Cingulate	left	-0.0181
		right	-0.0199
	Posterior Cingulate	left	-0.0125
		right	-0.0139
	Intraparietal	left	-0.0095
		right	-0.012
	Central	left	-0.0111
		right	-0.0105
	Inferior Frontal	left	-0.0145
		right	-0.0126
	Superior Frontal	left	-0.0105
		right	-0.0099
	Inferior Temporal	left	-0.0154
		right	-0.0156
	Superior Temporal	left	-0.0199
		right	-0.0194
	Subparietal	left	-0.0207
		right	-0.0244

Table S2. Heritability estimates and their associated p-values corresponding to Figure 2.

Feature	Sulcus	Left Hemisphere	Right Hemisphere
Opening	Sylvian Fissure	0.4 ± 0.048 ($5.3 \cdot 10^{-18}$)	0.423 ± 0.049 ($5.3 \cdot 10^{-19}$)
	Anterior Cingulate	0.23 ± 0.049 ($1.1 \cdot 10^{-6}$)	0.099 ± 0.048 (0.02)
	Posterior Cingulate	0.275 ± 0.049 ($7.2 \cdot 10^{-9}$)	0.19 ± 0.049 ($4.9 \cdot 10^{-5}$)
	Intraparietal	0.388 ± 0.049 ($1.6 \cdot 10^{-15}$)	0.345 ± 0.049 ($4.8 \cdot 10^{-13}$)
	Central	0.445 ± 0.049 ($1.7 \cdot 10^{-19}$)	0.349 ± 0.049 ($6.7 \cdot 10^{-13}$)
	Inferior Frontal	0.269 ± 0.049 ($1.2 \cdot 10^{-8}$)	0.317 ± 0.048 ($9.7 \cdot 10^{-12}$)
	Superior Frontal	0.246 ± 0.049 ($3.2 \cdot 10^{-7}$)	0.285 ± 0.049 ($2.4 \cdot 10^{-9}$)
	Inferior Temporal	0.151 ± 0.049 ($9.2 \cdot 10^{-4}$)	0.184 ± 0.049 ($6.6 \cdot 10^{-5}$)
	Superior Temporal	0.342 ± 0.048 ($2.4 \cdot 10^{-13}$)	0.318 ± 0.049 ($1.2 \cdot 10^{-11}$)
	Subparietal	0.198 ± 0.049 ($2.8 \cdot 10^{-5}$)	0.175 ± 0.048 ($1.1 \cdot 10^{-4}$)
Grey Matter Thickness	Sylvian Fissure	0.371 ± 0.048 ($2.8 \cdot 10^{-16}$)	0.323 ± 0.048 ($1.5 \cdot 10^{-12}$)
	Anterior Cingulate	0.218 ± 0.049 ($3.1 \cdot 10^{-6}$)	0.079 ± 0.048 (0.05)
	Posterior Cingulate	0.144 ± 0.049 ($1.3 \cdot 10^{-3}$)	0.127 ± 0.048 ($3.4 \cdot 10^{-3}$)
	Intraparietal	0.173 ± 0.048 ($1.0 \cdot 10^{-4}$)	0.239 ± 0.048 ($2.0 \cdot 10^{-7}$)
	Central	0.232 ± 0.048 ($4.2 \cdot 10^{-7}$)	0.253 ± 0.049 ($5.6 \cdot 10^{-8}$)
	Inferior Frontal	0.223 ± 0.048 ($1.2 \cdot 10^{-6}$)	0.224 ± 0.049 ($1.6 \cdot 10^{-6}$)
	Superior Frontal	0.151 ± 0.048 ($6.3 \cdot 10^{-4}$)	0.167 ± 0.048 ($2.0 \cdot 10^{-4}$)
	Inferior Temporal	0.1 ± 0.048 (0.02)	0.166 ± 0.049 ($2.6 \cdot 10^{-4}$)
	Superior Temporal	0.254 ± 0.048 ($2.9 \cdot 10^{-8}$)	0.266 ± 0.048 ($7.4 \cdot 10^{-9}$)
	Subparietal	0.159 ± 0.049 ($5.7 \cdot 10^{-4}$)	0.123 ± 0.048 ($4.9 \cdot 10^{-3}$)

Table S3. Summary GTEx information on the significant loci (GTEx Analysis Release V7 (dbGaP Accession phs000424.v7.p2))

chr	rsid	maf in ~12k subjects	Nearest gene(s)	eQTLs GTEx (meta p-val)
1	rs864736	0.45765	KCNK2	KCNK2 (multi-tissue 9.7*10^-6; significant tissue: ovary)
1	rs59084003	0.06957	KCNK2	No significant eQTLs (maf probably too low)
8	rs11774568	0.27672	DEFB136; DEFB135	Highly intergenic regions, notably significant eQTLs in brain tissues with genes ['CTSB', 'RP11-481A20.10', 'RP11-481A20.11', 'RP11-351I21.7', 'RP11-351I21.6', 'FAM66A']
9	rs10980645	0.29548	Intron of LPAR1	No significant eQTLs
12	rs12146713	0.09496	Intron of NUAK1	ENSG00000257890.1 (lincRNA) (multi-tissue 4.1*10^-28; significant tissues: skin-lower_leg; artery-tibial; adipose-subcutaneous)
16	rs9933149	0.37965	LOC101928708; C16orf95; FBXO31	ENSG00000261651.1 (antisense RNA) (p-val computed only in testis tissue 3.0*10^-7)

Chapter 5. Replication of the sulcal pits and plis de passage results in the UK Biobank

1. Introduction

In this brief chapter, we propose to replicate the heritability results obtained in the first two chapters. For these analyses, we considered the UK Biobank release in NIFTI format in January 2018 accounting for 15,040 subjects. Additionally, we restricted our analysis to the subsample using the same criteria as in the previous chapter (i.e. identified by UK Biobank as belonging to the white British ancestry, without genotyping outliers (high missing rates, heterozygosity or sex mismatch)). We then applied the Freesurfer 6 processing pipeline (Fischl, 2012) to subjects having T1 and T2 MR images folder labelled as usable by UK Biobank. Finally, we performed the GCTA analysis described in the previous chapter on the 11,237 remaining subjects.

For the sulcal pits analysis, we used the parcellation of Chapter 1 obtained on the HCP subjects in order to have the exact same areals for our replication analysis.

Similarly, in the plis de passage analysis, we used the same pipeline as described in Chapter 2 on the same corresponding parcellation.

2. Results and Discussion

Figure 1 is obtained in the UK Biobank using unrelated individuals with GCTA method to estimate the heritability as opposed to Figure 3 in Chapter 1 obtained in related subjects using the SOLAR method. Overall, the sulcal pit frequencies and median DPF are close to the ones obtained on HCP data with similar regional pattern distribution. The areals, which have a significant ($p < 0.05$, uncorrected) heritability estimate for the sulcal pits DPF, are listed **Tables 1 and 2** for the left and right hemispheres, respectively. Even though the heritability estimates obtained with UK Biobank are lower than the ones in HCP the general trend of heritability values is respected. Notably, the highest heritability value is found for the pit in the left hemisphere *collateral a* areal ($h^2_{HCP} = 0.46$, $h^2_{UKB} = 0.35$) and the *superior temporal b, c* areals are found significantly heritable in the left hemisphere but not in right, similar to result obtained with HCP pedigree data (in the left hemisphere h^2_{HCP} (STs b) = 0.26, h^2_{UKB} (STs b) = 0.10; h^2_{HCP} (STs c) = 0.38, h^2_{UKB} (STs c) = 0.14). The *olfactory* pit DPF remains the second highest heritable areal bilaterally (h^2_{HCP} (olfactory left) = 0.42, h^2_{UKB} (olfactory left) = 0.29; h^2_{HCP} (olfactory right) = 0.41, h^2_{UKB} (olfactory right) = 0.26). Other areals are found significantly heritable bilaterally in both UK Biobank and HCP, these include *below subparietal and cingulate, collateral a, b, junction collateral and calcarine a*, and only the left hemisphere: *lateral occipital b* ($h^2_{HCP} = 0.32$, $h^2_{UKB} = 0.14$), *subparietal* ($h^2_{HCP} = 0.22$, $h^2_{UKB} = 0.11$), or only in the right hemisphere: *cingulate d* ($h^2_{HCP} = 0.38$, $h^2_{UKB} = 0.15$).

The discrepancies between UK Biobank and HCP estimates, approximately systematically 0.1 to 0.15 higher in HCP, are caused by two main phenomena: (i) the unaccounted shared environment in HCP families' likely lead to overestimating the heritability in that case, (ii) the UK Biobank estimates are based on a genetic relationship matrix built only from common variants and thus does not include information about rare variants, which often have larger effect than common ones. Additionally, the standard errors obtained for these heritability estimates are similar in both cases: 0.06 to 0.09 for HCP (820 related subjects, with pedigree information) and 0.05 to 0.07 for UK Biobank (11,237 unrelated subjects, with genotyped information). The true heritability value in each areal certainly lies between the heritability estimates obtained separately on UK Biobank and HCP for these areals. Remarkably, as underlined in the previous paragraph the regional patterns of heritability remained consistent in the two cohorts and make us confident in the ones that reproduce this trend. **Figure 2** illustrates the correlation (Pearson corr. = 0.63, $p = 5.4 \cdot 10^{-6}$) between heritability estimates of sulcal pits in UK Biobank and HCP for areals with associated p-values < 0.05 (uncorrected) in both cohorts.

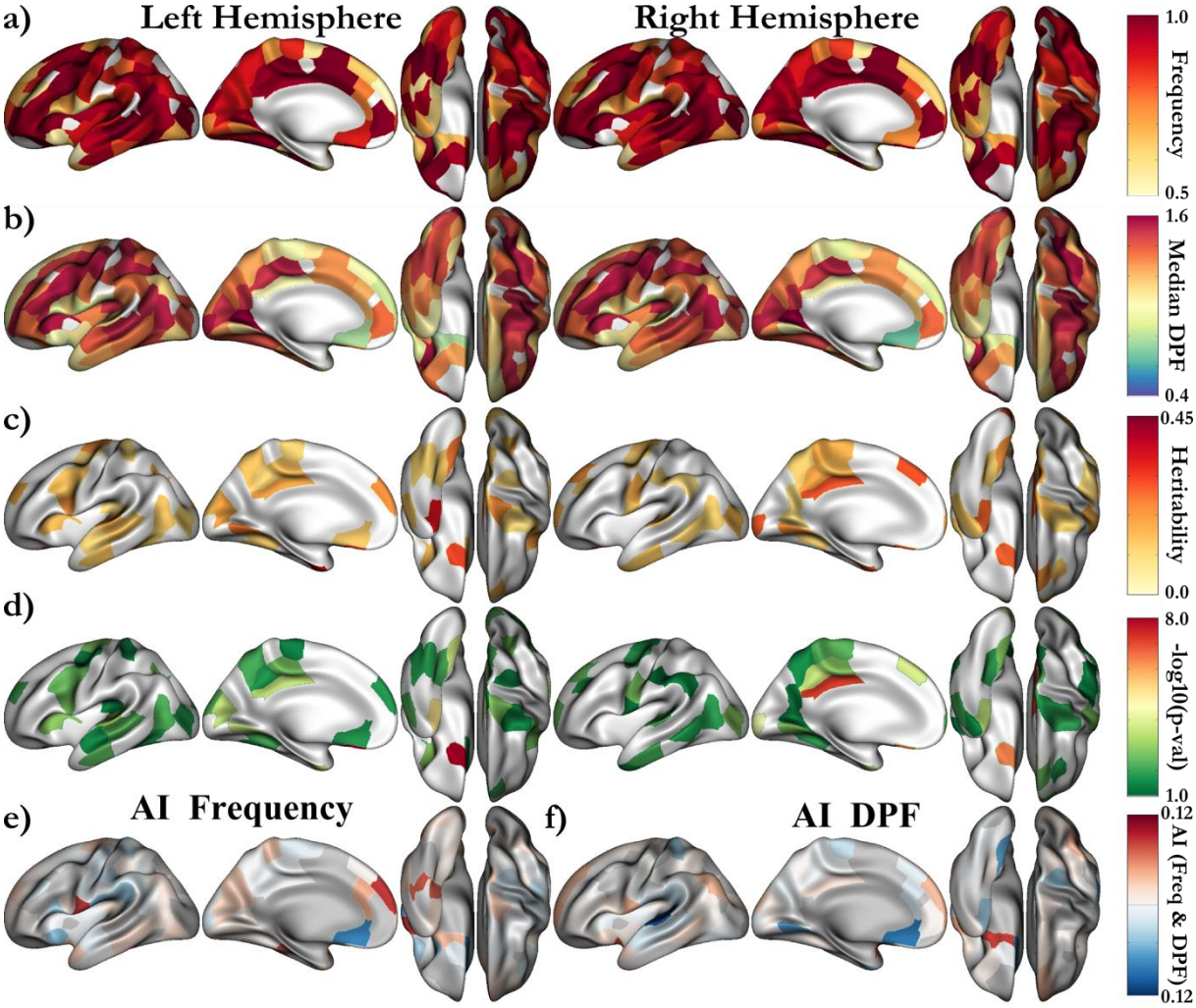

Figure 1. (a) Deep pits frequency and **(b)** median DPF of the pits selected as phenotypes in each areal. **(c)** Heritability and **(d)** associated –log10(p-values) for all the areals being significant without correction ($p < 0.05$). The areals which are significant after strict Bonferroni are shown with a color above yellow. Both left and right hemisphere results **(a, b, c, d)** are presented on the symmetrized (left) template. **(e)** Asymmetry Index frequency. **(f)** Asymmetry Index median DPF.

Table 1. Results of the additive analysis for the DPF of the pits in the *left hemisphere*: heritability estimate and associated p-value.

Trait	h^2±SE(p)	Subjects
below subparietal and cingulate	0.175±0.052 ($2.7\cdot10^{-4}$)	10863
calcarine b	0.181±0.054 ($2.8\cdot10^{-4}$)	10102
cingulate d	0.143±0.051 ($2.2\cdot10^{-3}$)	11108
circular insular a	0.09±0.052 (0.04)	10753
circular insular d	0.145±0.049 ($1.4\cdot10^{-3}$)	11102
collateral a	0.353±0.082 ($7.2\cdot10^{-6}$)	6801
collateral b	0.126±0.051 ($7.2\cdot10^{-3}$)	10943
inf temporal a	0.131±0.052 ($4.3\cdot10^{-3}$)	10591
inf temporal d	0.131±0.052 ($5.6\cdot10^{-3}$)	10816
intraparietal b	0.152±0.053 ($2.0\cdot10^{-3}$)	10421
junct collateral and calcarine a	0.239±0.068 ($2.0\cdot10^{-4}$)	8280
junct precentral and inf frontal	0.138±0.05 ($3.0\cdot10^{-3}$)	11190
junct sup frontal and precentral	0.098±0.051 (0.03)	11146
lateral occipital a	0.113±0.051 (0.01)	11075
lateral occipital b	0.137±0.053 ($4.7\cdot10^{-3}$)	10679
occipito temporal b	0.113±0.051 (0.01)	11194
olfactory	0.287±0.052 ($8.6\cdot10^{-9}$)	10690
planum temporale area	0.17±0.056 ($1.0\cdot10^{-3}$)	9903
postcentral a	0.104±0.055 (0.03)	10296
precentral	0.21±0.072 ($1.5\cdot10^{-3}$)	7716
subparietal	0.105±0.05 (0.02)	11021
subparietal b	0.134±0.055 ($7.0\cdot10^{-3}$)	9977
sup temporal b	0.103±0.053 (0.03)	10489
sup temporal c	0.135±0.051 ($4.5\cdot10^{-3}$)	11103
supplementary motor area	0.105±0.058 (0.03)	9611

Table 2. Results of the additive analysis for the DPF of the pits in the *right hemisphere*: heritability estimate and associated p-value.

Trait	h^2±SE(p)	Subjects
below subparietal and cingulate	0.272±0.052 ($7.0\cdot10^{-8}$)	10801
calcarine a	0.093±0.051 (0.03)	10874
calcarine c	0.265±0.068 ($4.8\cdot10^{-5}$)	8160
central c	0.167±0.058 ($1.8\cdot10^{-3}$)	9631
cingulate d	0.15±0.05 (1.2·10-3)	11033
cingulate e	0.17±0.066 ($4.7\cdot10^{-3}$)	8450
collateral a	0.261±0.079 ($3.2\cdot10^{-4}$)	7024
collateral b	0.118±0.051 (0.01)	11093
inf temporal a	0.13±0.053 ($6.9\cdot10^{-3}$)	10522
inf temporal c	0.112±0.052 (0.02)	10662
inf temporal d	0.115±0.051 (0.01)	11046
junct collateral and calcarine a	0.204±0.068 ($1.5\cdot10^{-3}$)	8420
junct sup frontal and precentral	0.112±0.05 (0.01)	11122
lateral occipital a	0.154±0.051 ($1.3\cdot10^{-3}$)	11076
mid frontal b	0.129±0.058 (0.01)	9742
olfactory	0.262±0.054 ($4.7\cdot10^{-7}$)	10456
parieto occipital a	0.094±0.054 (0.04)	10284
planum temporale area	0.132±0.055 ($7.2\cdot10^{-3}$)	10113
postcentral c	0.105±0.062 (0.05)	9019
precentral	0.144±0.068 (0.02)	8186
subparietal	0.179±0.052 ($2.7\cdot10^{-4}$)	10855
subparietal b	0.114±0.056 (0.02)	9983
sup frontal a	0.162±0.06 ($3.2\cdot10^{-3}$)	9376
supplementary motor area	0.158±0.06 ($4.5\cdot10^{-3}$)	9344
supra marginal gyrus	0.095±0.053 (0.03)	10532
temporale pole	0.131±0.07 (0.03)	7892

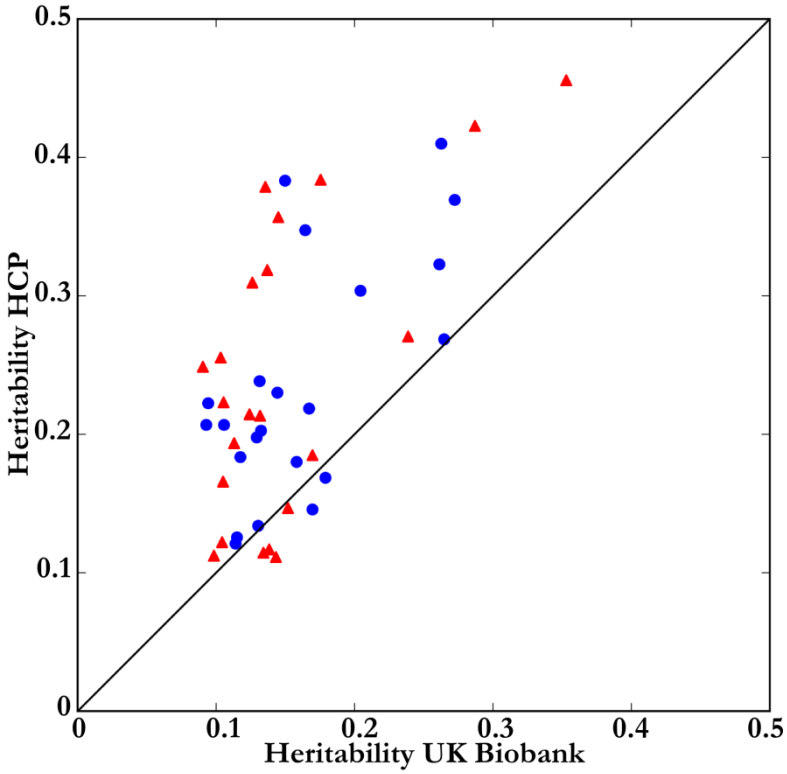

Figure 2. Heritability of sulcal pits DPF in UK Biobank vs HCP. Only areals with associated p-values < 0.05 (uncorrected) in both cohorts have their heritability estimate display (red triangles represent left hemisphere areals, and blue disks represent right hemisphere areals). The Pearson correlation between the heritability estimates of UK Biobank and HCP is $\rho = 0.63$ ($p = 5.4 \cdot 10^{-6}$).

Table 3 presents the heritability estimate, for the UK Biobank cohort, of the presence of a *pli de passage* (PP) in the superior temporal asymmetrical pit area (STAP), whose extraction method has been described in Chapter 2. Remarkably, we obtained as for the HCP cohort that the formation of a PP in the left hemisphere is under genetic control, while it does not appear to be in the right hemisphere. This last statement need to be moderated due to the low PP frequency in the right hemisphere (15.5%) compare to the left (57.3%). The discrepancies in heritability estimates are larger in that case compare to the sulcal pits differences in estimates (h^2_{HCP} (left STAP PP) = 0.53, h^2_{UKB} (left STAP PP) = 0.17; h^2_{HCP} (right STAP PP) = 0.27, h^2_{UKB} (right STAP PP) = 0.00). It should be noted that in this case the model used by GCTA for discrete trait gives standard error comparable to the ones obtained for quantitative trait (about ±0.05), while the discrete trait model of SOLAR gave standard error ranging between ±0.09 to 0.15, suggesting more uncertain fits. The symmetric heritability estimates for the geodesic depth in UK Biobank (**Table 3**) might suggest that this phenotype does not take into account the particular local shape (convexity) as the DPF does. Therefore, the geodesic depth might be more related to the brain volume than to the STAP area geometry.

Table 3. Results of the additive analysis (heritability estimate and associated p-value) for the STAP phenotypes: presence or absence of a transverse sulcal interruption (PP) and average DPF along the STAP.

Trait	h^2±SE (p)	Subjects	Frequency
PP in the Left STAP	0.1714±0.0493 ($1.9\cdot10^{-4}$)	11237	0.573
PP in the Right STAP	0.0000±0.0490 (0.5)	11237	0.155
Left STAP average DPF	0.1823±0.0499 ($1.0\cdot10^{-4}$)	11237	Not applicable
Right STAP average DPF	0.0754±0.0496 (0.064)	11237	Not applicable
Asymmetry index STAP average DPF	0.1155±0.0497 (0.009)	11237	Not applicable
Left STAP average geodesic depth	0.2023±0.0498 ($1.7\cdot10^{-5}$)	11237	Not applicable
Right STAP average geodesic depth	0.1935±0.0496 ($7.6\cdot10^{-5}$)	11237	Not applicable
Asymmetry index STAP average geodesic depth	0.1080±0.0494 (0.013)	11237	Not applicable

Overall, our results suggest that there is a stronger genetic influence on the interindividual variability in the left hemisphere compare to the right in the shape (depth, convexity, presence of sulcal interruption) in areals superior temporal c and to a lesser extent areal superior temporal b.

Conclusion

The initial goal of this thesis was to identify genetic variants that regulate the structural asymmetries observed in the human temporal lobe. These genetic factors hold promise to understand the genetic construct underlying what makes us human for two main reasons. First, the temporal lobe is the most implicated region in the production and understanding of language and is almost always lateralized in the left hemisphere. Second, the brain structural asymmetries in this region appear to be human-specific, because they are weakly observed in non-human primates.

In the literature, previous approaches that were successful in identifying genetic variants whose mutations affect the language production mostly resulted from family genetic linkage studies. This type of study looks for genetic difference between affected and unaffected family members and if the disorder phenotype occurs specifically for a given allelic combination then the genetic linked is established. The main requirement is to consider a family over a few generations and large enough to reach statistical significance, generally less than 100 individuals. As opposed to genetic linkage studies, ours include unrelated individuals this leads to a larger number of differences in the genome to be considered. These differences of a single nucleotide, named SNP, occur at specific positions in the genome. There are genotyped using chips able to measure 500,000 to 1,000,000 SNPs. Thus, a genome-wide univariate association on each of these SNPs imposes setting a stringent significant threshold at $p < 5 \cdot 10^{-8}$. Common genetic variants in the general population often have small effect size and thus require an extremely large sample (> 10,000-100,000) to have enough statistical power to detect an effect significantly.

Taking into account this requirement, we first needed to design automated methods to extract our asymmetric phenotypes from brain images. As a consequence, an essential part of my work was to identify and extend existing brain features extraction techniques that were able to reliably scale on such sample size. In this aim, we used the sulcal pits extraction algorithm from Auzias et al. (2015) and identify the presence of transverse sulcal interruptions in the superior temporal sulcus (Le Guen et al., 2018b). Second, an important point was to assess if these two originals biomarkers were heritable. Thus, we applied these pipelines to the 1,000 subjects Human Connectome Project dataset and found various regional heritability levels ranging from 20% to 50% for the sulcal pits DPF (Le Guen et al., 2018a) and pli de passage formation (Le Guen et al., 2018b). These results were later replicated in the UK Biobank, using genotyping information from unrelated individuals. In this latter case, even though the pattern of heritability remained consistent in areals that were significant after correction, the heritability estimates were lower with differences ranging from 10 to 35%. These discrepancies between h^2_{PED} and h^2_{SNP} were expected and already observed for other phenotypes in the literature, such as the height (Yang et al., 2010). There are mainly due to two reasons: first, the unaccounted shared environment in case of pedigree, and second, the smaller variance captured by common variants as opposed to the whole genome.

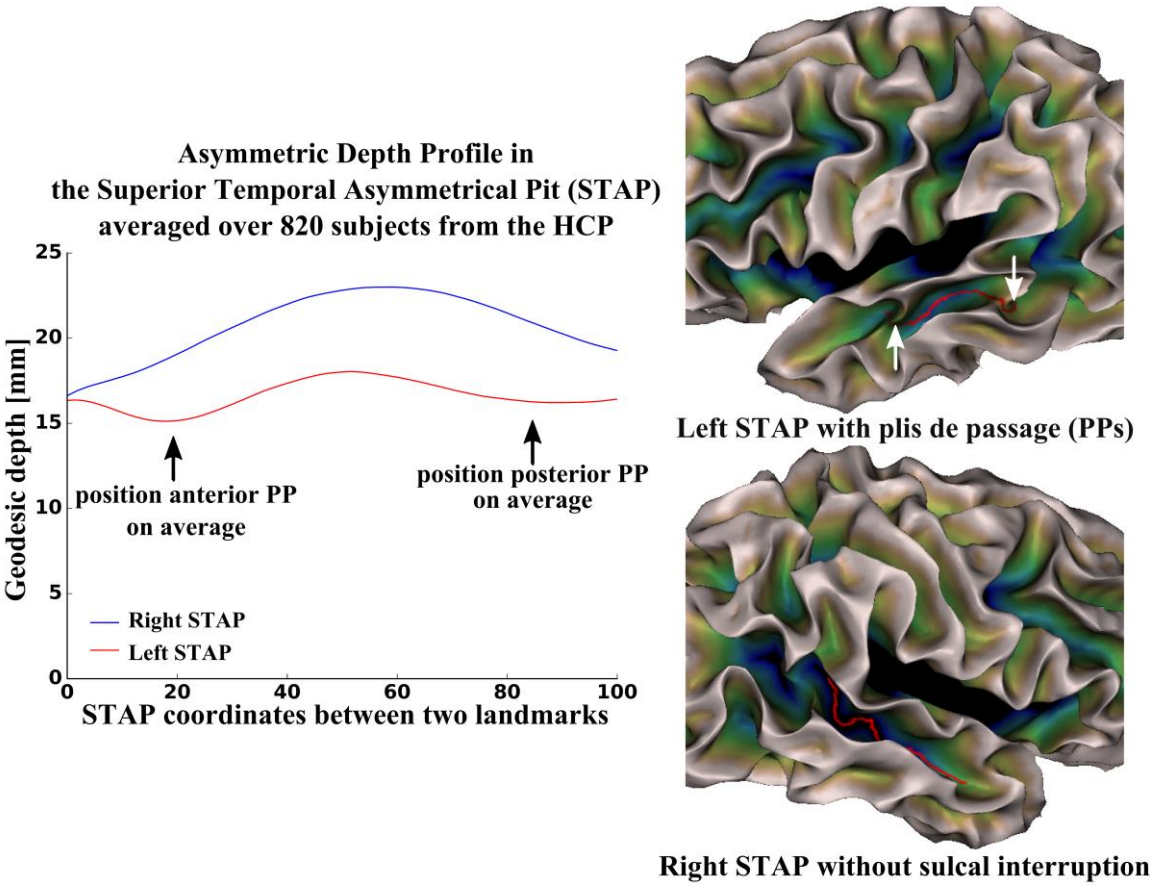

Figure 1. (Left) Asymmetric depth profile in the superior temporal asymmetrical pit (STAP) area averaged over 820 Caucasians HCP subjects**. (Right)** Example subject with transverse sulcal interruptions, which border the STAP anteriorly and posteriorly in the left hemisphere, and without such interruption in the right hemisphere.

Given the initial goal, the most interesting results of this thesis are related to the superior temporal sulcus (STS):

- The rightward depth asymmetry was confirmed in large cohorts as HCP and UK Biobank.
- A significant leftward asymmetry of pli de passage (PP) was observed in this sulcus.
- In both cohorts, the DPF of sulcal pits *STS b and c* present higher and more significant heritability estimates in the left hemisphere compare to the right.
- Similarly, the formation of PP appears under moderate genetic control in the left hemisphere for both cohorts, but not in the right hemisphere.

These findings suggest asymmetric genetic constraints on the structure supporting the linguistic network. **Figure 1** exemplifies the configuration of the STS around sulcal pits STS b-c, which roughly delimit the boundaries of the STAP area defined by Leroy et al., (2015). The STAP area had a strong rightward depth asymmetry in all human groups considered, but this asymmetry was not observed in chimpanzees (Leroy et al., 2015). The concrete correlate of this asymmetry is the preferentially leftward formation of white matter bumps transverse to the sulcus in this region. The potential cognitive advantages have been discussed in depth in the corresponding chapter. Briefly, it is hypothesized that plis de passage are composed of short-range U fibers, whose density in this area is

increased to improve the efficiency of the intra-hemispheric neural signal transmission related to language processing happening along the STS. The asymmetric heritability estimates likely reflect asymmetric genetic cues, which support the fiber density and the asymmetry of other temporal lobe structures. In turn, these structural asymmetries are widely hypothesized to support the human left hemisphere language lateralization. Finding asymmetric heritability estimates suggest a genetic blueprint that favors the formation of a specific brain cytoarchitecture in the left temporal lobe that is later used during language processing. Our result towards a more pronounced genetic influence in the left temporal region interindividual variability contrasts with previous hypotheses. Due to the earlier appearance (Dubois et al., 2008) and maturation (Leroy et al., 2011) of the right STS region compare to the left, it was assumed that genetic constraints should be higher in the right hemisphere and that the left could be more susceptible to environmental influence. The heritability estimates obtained seem to contradict this hypothesis. Another hypothesis might be that the maturation of the left temporal region is longer due to a prolonged exposure to genetic cues in this hemisphere.

The causal genetic variants regulating the formation of this specific brain architecture in every human remain to be investigated. Our preliminary genome-wide association study on STAP phenotypes did not yet lead any genome-wide significant and replicable hits, using the sample of 11,000 UK Biobank subjects included to estimate the heritability of STAP pli de passage. One reason might be that the late availability of UK Biobank data (end January 2018) prevented us to examine the results in depth at the time of writing and thus we will continue exploring potential causal association. Another reason could be that the genetic mechanism regulating the STAP asymmetry cannot be identified by simple univariate association. In this aim, we have started looking for haplotypes association, but other types of association should also be investigated. Finally, we should also underline that because the STAP depth asymmetry and left language lateralization are observed in almost every human, the causal genetic variants supporting this asymmetry might be rare variants. Therefore, the UK Biobank genotyping data mostly composed of common variants might lack the causal rare variants of interest or contain too few individuals with mutations on these SNPs.

A second part of this thesis consisted in studying the genetic underlying the functional activations during language task. To this aim, we took advantage of the unique HCP dataset, which includes a task fMRI related to language performed by over a thousand related subjects in the same scanner. To the best of our knowledge only one existing cohort had reached an equivalent sample size, but for a working memory task (Blokland et al., 2011). Additionally, our phenotypes, used as proxy for neural activations, were defined using state of the art fMRI methods. Notably, the parameter estimates (β) were defined on the surface of cortex using a grayordinate approach, as opposed to volume based approaches that perform unconstrained smoothing in the volume potentially mixing signals from non-adjacent neurons on the cortex. Besides, we split the cortex in 180 areals, in each hemisphere, obtained from the newly released HCP multimodal parcellation, which finely delineates

various areas of the cortex based on structural, myelin, and resting-state and task activations information. The significant heritability estimates for the math and story tasks span the range 22 to 45% and particularly included brain regions involved in semantic comprehension. Furthermore, we investigated the shared genetic etiology between cognitive performance, assessed by performance to the fMRI tasks and standard cognitive tests, and the neural activations in heritable brain regions. The main finding of this study is that the region, whose activations shared the stronger common genetic grounds with behavioral scores, was composed of the angular gyrus and temporo-parietal junction. The behavioral scores with the highest significance of shared genetic variance included: language task accuracy, fluid intelligence, vocabulary comprehension and reading decoding. This region is interesting due to its particular role in semantic comprehension, as well as its adjacency with the intraparietal and superior temporal sulci implicated in human high cognitive functions, respectively mathematics operation and language processing.

The last part of this thesis is the most promising in term of genetic causal links. Our replicated GWAS results demonstrate that a region upstream of the KCNK2 gene is significantly associated with sulcal opening and gray matter thickness. Besides, the two investigated phenotypes significantly correlate with age and are thus markers of brain ageing. Additionally, in a gene tissue expression database (GTEx Consortium, 2017) the most associated SNP variant rs864736 is found to be in a cis-regulating region of the KCKN2 gene. This gene regulates the immune-cell response into the central nervous system (CNS) and controls the CNS inflammation, which is implicated in cortical atrophy and cognitive decline. Our results expand our knowledge of the genetic contribution to brain features related to ageing. Our study promotes further investigation into the associated variants obtained and their nearby genes in pathological context such as Alzheimer's disease in which brain shrinkage is a key biomarker.

First, our findings (or no findings) confirmed the overall small effect size (< 0.5%) of common variants. Thus, the question of the relevance of these SNPs associations explaining a small percentage of the phenotypic variance in the general population needs to be addressed. Imaging-genetic studies with a focus on pathologies or syndromes yield more interpretable and usable outcomes. Notably, in the disease context, the associated SNPs are often used to form polygenic risk scores, enabling to more precisely assess the susceptibility of any individual. These polygenic scores are also used to test the association of group of variants with non-disease traits. The effect size of these scores on the phenotypic variance corresponds to the sum of effects of each variant and is thus more significant than single SNP association. Second, rare variants often have larger effect size on phenotypes than common variants. Thus, we should promote whole genome sequencing to allow the study of rare variant association. Finally, the systematic post processing of GWAS results could also yield additional results (de Leeuw et al., 2015; Watanabe et al., 2017), using for instance tissue enrichment information.

Résumé de la thèse

Introduction

La découverte récente de la région de la STAP (superior temporal asymmetrical pit area) par Leroy et al. (2015) a motivé nos recherches en imagerie génétique de variations génétiques responsables des asymétries propres au cerveau humain. En effet, Leroy et al. ont mis en évidence que cette région du lobe temporal contenait une asymétrie inter-hémisphères de profondeur chez l'homme dès la naissance, mais que cette asymétrie n'était quasiment pas observée chez le chimpanzé. Pour identifier les variations génétiques impliquées dans la formation de ces asymétries, nous devions premièrement sélectionner et extraire de façon robuste des phénotypes qui caractérisent ces asymétries. En accord avec les pratiques actuelles en imagerie génétique (D. Hibar, Imaging-genetics workshop OHBM 2016), nous n'avons pas adopté une approche considérant des gènes candidats mais considéré le génome entier (genome wide association study, GWAS). En effet, les résultats dans la littérature d'étude utilisant des gènes candidats contiennent souvent des résultats non reproductibles, avec des faux positifs dus à une diminution artificielle du seuil de significativité. Par ailleurs, compte tenu que la plupart des variants communs impliqués dans la variance du phénotype ont une taille d'effet très petite, nous avions besoin d'une cohorte suffisamment large pour avoir la puissance statistique nécessaire. Pour cette raison, la méthode d'extraction de notre phénotype devait être automatisée pour pouvoir être appliquée sur un grand nombre de sujets.

À notre connaissance, dans les études précédentes les structures du lobe temporal comme le planum temporale, le gyrus de Heschl ou même la STAP ont toutes été manuellement ou semi automatiquement délimitées et extraites. La première contribution de cette thèse fut donc de trouver des marqueurs anatomiques intermédiaires reflétant ces asymétries et extractibles par des processus automatisés.

Les sulcal pits constituent de premiers marqueurs intermédiaires. Ce sont les localisations supposées des premiers plissements du cerveau. Quatre raisons justifient ce choix : (i) les point les plus profonds des sillons du cerveau semblent moins sensible au bruit, (ii) ces structures étant formées tôt lors du développement du cerveau elles seraient moins susceptible à l'influence de l'environnement, (iii) un groupe partenaire avait récemment développé un algorithme permettant leur extraction automatique dans une centaine de sujets (Auzias et al., 2015), (iv) la densité des sulcal pits semble asymétrique dans le sillon temporale supérieur (STS) (Im et al., 2010).

Un second marqueur intéressant est le pli de passage, qui est un gyrus transverse – plissement tertiaire – séparant un sillon en deux parties. En particulier, cette structure a été observée par des neuroanatomistes comme étant plus fréquente dans le STS gauche que dans son homologue de l'autre hémisphère (Ochiai et al., 2004). La présence de ce pli de passage plus fréquente dans l'hémisphère gauche contribue à l'asymétrie de profondeur de la STAP (Leroy et al., 2015). Toutefois, les pipelines

de traitement d'images existant n'ont jamais adressé la problématique de l'extraction de ces plissements tertiaires. Nous avons proposé une méthode de novo pour les extraire par un processus automatisé.

Dès lors que ces structures du cerveau ont été extraites nous avons examiné si leurs variations interindividuelles étaient sous contrôle génétique. Comme seconde contribution de cette thèse, nous avons estimé l'héritabilité (i.e. la contribution génétique à la variance phénotypique). Jusqu'à la mise à disposition des données UK Biobank ou des données de génotypage de HCP, le nombre limité de sujet dans la cohorte IMAGEN ne nous a pas permis d'effectuer une analyse GWAS avec suffisamment de puissance statistique pour obtenir une association significative. Pour cette raison, dans un premier temps, nous avons restreint nos analyses génétiques à l'héritabilité.

Un phénotype additionnel disponible était les activations d'IRM fonctionnelle (fMRI), qui a été très rarement étudié, la tâche fMRI de langage de HCP nous a offert une opportunité unique d'examiner l'héritabilité des activations asymétriques dans les zones du cerveau impliquées dans la perception des signaux auditifs et la compréhension sémantique. De plus, la mise à disposition de données comportementales nous a permis d'étudier la variance génétique partagée entre ces activations du cerveau et les capacités cognitives humaines. Cette étude constitue la troisième contribution de cette thèse.

Finalement, lorsque les données UK Biobank ont été mises à disposition de notre groupe, nous avons étudié l'influence génétique sur les sillons du cerveau et recherché les variations génétiques qui contribuent à la largeur sulcal et à l'épaisseur corticale au fond du sillon. Nous avons découvert et répliqué plusieurs variants causaux qui sont associés à ces caractéristiques, dont nous avons aussi confirmé qu'elles sont des marqueurs du vieillissement du cerveau.

Conclusion

L'objectif initial de cette thèse était d'identifier des variations génétiques qui régulent la formation des asymétries de structure observées dans le lobe temporal humain. Ces facteurs génétiques sont prometteurs pour comprendre la construction génétique sous-jacente de ce qui nous différencie des chimpanzés pour deux raisons. Premièrement, le lobe temporal est la région la plus impliquée dans la production et la compréhension du langage et les activations associées sont presque toujours latéralisées dans l'hémisphère gauche. Deuxièmement, les asymétries de structure dans cette région semblent être propres à l'homme, car elles sont faiblement observées chez les primates non-humains.

Dans la littérature, les approches précédentes qui ont réussi à identifier des variants génétiques dont les mutations affectent la production du langage, résultent essentiellement d'études de liaisons génétiques dans des familles étendues. Ce type d'étude recherche les différences génétiques entre les membres de la famille affectés et non affectés. Si le trouble cognitif apparaît spécifiquement pour une combinaison allélique donnée alors la causalité génétique est établie. La contrainte principale est qu'il faut disposer d'une famille élargie et sur plusieurs générations, mais dans ce cas le nombre d'individus

nécessaire pour une association significative peut être de moins de 100 individus. Contrairement aux études de liaisons, nos travaux incluent des personnes non apparentées avec un nombre très important de différences génétiques entre leurs génomes. Ces différences d'un seul nucléotide, appelée single nucleotid polymorphism (SNP), se produisent à des positions spécifiques du génome. Elles sont génotypées avec des puces capables de mesurées généralement entre 500 000 et 1 000 000 de SNPs. Pour cette raison, si l'on teste l'association de chacun de ces SNPs (étude GWAS), alors le seuil de significativité doit rigoureusement être fixé à $p < 5 \cdot 10\text{-}8$. Les variants génétiques communs dans la population générale ont souvent de petites tailles d'effet sur la variation phénotypique. Pour cette raison, nous avons besoins d'un échantillon d'individus extrêmement large (> 10 000-100 000) pour avoir suffisamment de puissance statistique pour détecter un effet significatif.

En prenant en compte cette condition, nous avons donc premièrement construit des méthodes d'extraction automatisées des structures asymétriques de la région de la STAP. Par conséquent, une part essentielle de mon travail a consisté à identifier et étendre des processus d'extraction de caractéristiques du cerveau qui pouvaient passer à l'échelle sur de telles tailles de cohortes. Dans cette optique, nous avons utilisé l'algorithme d'extraction des racines sulcales proposé par Auzias et al. (2015), puis identifier la présence d'interruption transverse du STS (Le Guen et al., 2018b). Ensuite, une étape importante fût de confirmer que ces deux biomarqueurs originaux étaient héritables. Ainsi, nous avons appliqué ces pipelines de traitement aux 1000 sujets du Human Connectome Project et avons obtenu des niveaux d'héritabilité régionaux variants entre 20 et 50% pour la profondeur et convexité (= DPF) des sulcal pits (Le Guen et al., 2018a) et la formation de plis de passage (Le Guen et al., 2018b). Ces résultats furent par la suite répliqués dans la cohorte UK Biobank, en utilisant des données de génotypages des individus non apparentés par opposition aux données de pédigrées de HCP. Dans le cas des données UK Biobank, les valeurs estimées d'héritabilité sont plus faibles de l'ordre de 10 à 35%, bien que la distribution régionale de l'héritabilité reste consistante dans les régions significatives après correction. Ces différences entre h^2_{PED} et h^2_{SNP} étaient attendues et déjà observées pour d'autres phénotypes dans la littérature, comme la taille (Yang et al., 2010). Elles sont principalement dues à deux raisons : premièrement, l'environnement partagé est mal pris en compte dans les études de pédigrées, et deuxièmement, la variance génétique expliquée par les variants communs génotypés est plus petite que celle de l'ensemble du génome.

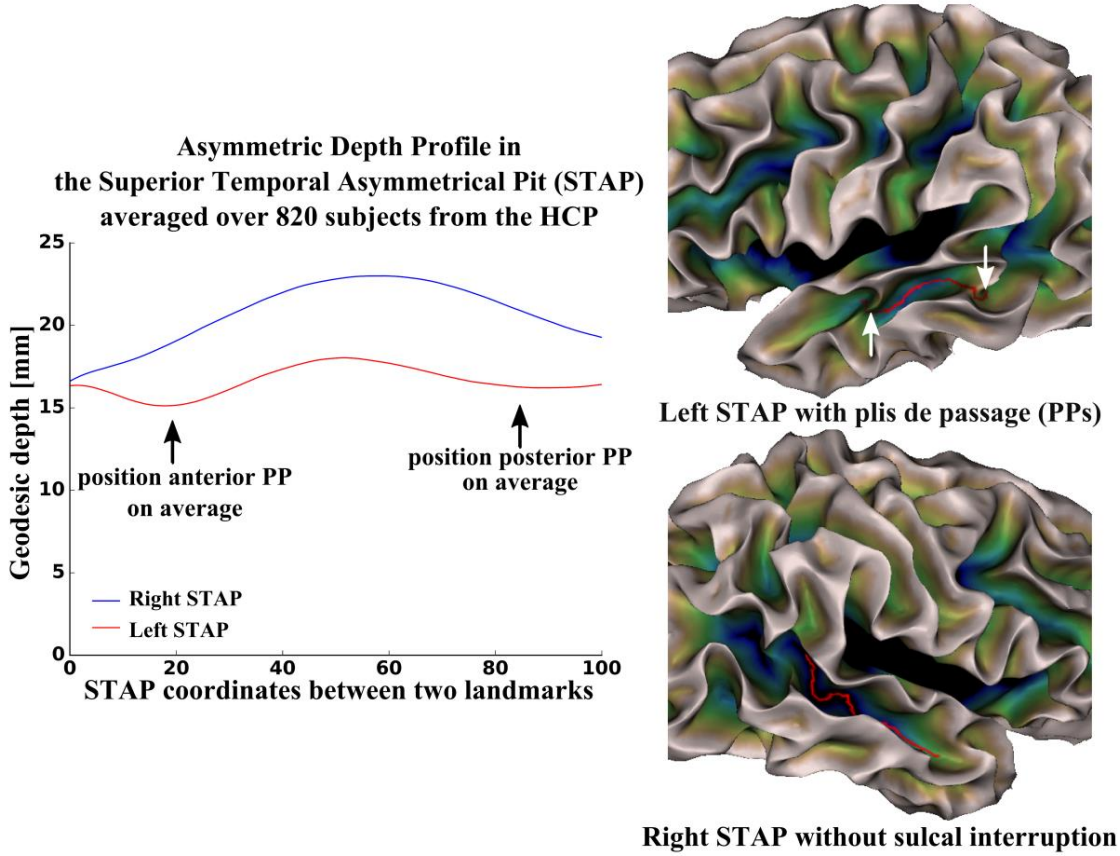

Figure 1. (Gauche) Profils de profondeur asymétriques dans la région du superior temporal asymmetrical pit (STAP) moyennés sur 820 sujets caucasiens du HCP**. (Droite)** Exemple d'un sujet avec : deux interruptions sulcales transverses dans son STS gauche, ces deux interruptions correspondent approximativement aux limites antérieures et postérieures de la STAP, et pas d'interruption dans son STS droit.

Compte tenu de l'objectif initial de cette thèse, les résultats les plus intéressants de cette thèse concernent le sillon temporal supérieur (STS) :

1) L'asymétrie de profondeur du STS a été confirmée dans deux larges cohortes (HCP et UK Biobank).
2) Une fréquence significativement plus importante de plis de passage (PPs) à gauche a été observée.
3) Dans les deux cohortes, la DPF des sulcal pits STS b et c présente des niveaux d'héritabilité plus élevés et plus significatifs dans l'hémisphère gauche.
4) Également, la formation de PP apparaît sous contrôle génétique modéré dans les deux cohortes dans la STAP à gauche, mais pas dans l'hémisphère droit.

Ces résultats suggèrent des contraintes génétiques asymétriques sur les structures supportant les réseaux linguistiques. La **Figure 1** donne un exemple de la configuration du STS autour des sulcal pits STS b-c, qui délimitent approximativement les frontières de la STAP définie par Leroy et al. (2015). La région de la STAP présente une asymétrie de profondeur vers la droite dans tous les groupes d'humain considérés, mais cette asymétrie n'est pas observée chez les chimpanzés (Leroy et al., 2015). Le corrélat concret de cette asymétrie est la formation latéralisée vers la gauche de bosses

de matière blanche, transverse au STS dans cette région. Les avantages cognitifs potentiels ont été discutés en détails dans le chapitre correspondant. Brièvement, il est supposé que les plis de passage sont composés de fibre en U courtes, dont la densité dans cette zone est augmentée pour améliorer l'efficacité des connections intra-hémisphériques facilitant la transmission de signaux neuronaux impliqués dans les processus du langage se produisant le long du STS. Les valeurs asymétriques d'héritabilité obtenues reflètent probablement des signaux génétiques asymétriques, qui contribuent à la densité des fibres et à l'asymétrie des autres structures du lobe temporal. Réciproquement, ces asymétries structurelles sont largement supposées comme le support de la latéralisation du langage dans l'hémisphère gauche du cerveau humain. Cette asymétrie d'héritabilité suggère un schéma génétique directeur qui favorise la formation d'une architecture cellulaire spécifique dans le lobe temporal gauche, qui est plus tard utilisé dans le traitement du langage. Nos résultats suggèrent un contrôle génétique plus prononcé dans l'hémisphère gauche, ces résultats contrastent avec les hypothèses précédemment postulées. Du fait de la formation (Dubois et al., 2008) et maturation (Leroy et al., 2011) antérieures du STS droit comparé au STS gauche, il était postulé que les contraintes génétiques étaient plus importantes dans l'hémisphère droit et que le gauche était donc plus susceptible à l'influence de l'environnement. Les estimations d'héritabilité obtenues semblent contredire cette hypothèse. Une autre hypothèse pourrait être que la maturation de la région temporale gauche est plus tardive due à une exposition prolongée à gauche aux signaux génétiques contribuant à la formation de ces structures.

Les variants causaux régulant la formation de cette architecture cérébrale spécifique dans la population générale reste à être examinés. Nos résultats préliminaires d'association sur l'ensemble du génome avec nos phénotypes de la STAP n'ont pour l'instant produit aucun résultat significatif et réplicable. Dans ce cas, nous avons considéré un échantillon de 11 000 sujets UK Biobank aussi utilisés pour estimer l'héritabilité de ces structures. Une des raisons est la disponibilité tardive au cours de la thèse des données UK Biobank (janvier 2018) qui nous a empêché d'examiner plus en détails les associations GWAS non significatives au moment d'écrire ce manuscrit. Ainsi, nous allons continuer à chercher des associations génétiques avec ces structures en raffinant nos méthodes. Une autre raison de cette absence de résultat est peut-être que les mécanismes génétiques régulant l'asymétrie de la STAP ne peuvent pas être exhibés par une association univariée simple. Dans ce but, nous avons commencé à étudier les associations haplotypiques, mais d'autres types d'association doivent aussi être analysés. Finalement, nous devons aussi souligner que l'asymétrie de profondeur de la STAP et la latéralisation du langage sont observées chez presque tous les êtres humains et par conséquent les variants génétiques causaux supportant ces asymétries sont probablement rares. Par conséquent, les données génotypées d'UK Biobank contenant principalement des variants communs manquent probablement les variants rares causaux d'intérêt ou contiennent une trop petite proportion d'individus avec une mutation sur ces SNPs.

Une seconde partie de cette thèse consistait à étudier la contribution génétique sous-jacente aux activations fonctionnelles durant une tâche de langage. Dans cette perspective, nous avons tiré parti de la ressource exceptionnelle du jeu de données HCP, qui inclue une tâche fMRI liée au langage, exécutée par plus de 1000 sujets dans le même scanner. À notre connaissance, seulement une autre cohorte à ce jour réunit autant de sujet mais pour une tâche de mémoire de travail (Blokland et al., 2011). De plus, nos phénotypes utilisés comme intermédiaires aux activations neuronales ont été définis en utilisant des méthodes d'analyse fMRI à l'état de l'art. En particulier, l'estimation paramétrique (β) a été définie sur la surface du cortex en utilisant une approche « grayordinate », par opposition aux approches dans le volume qui utilisent des lissages non contraints et qui mélangent des signaux dans le volume de neurones non adjacents à la surface du cortex. Par ailleurs, nous avons utilisé une parcellation multimodale du cortex (Glasser et al., 2016), qui délimite finement diverses régions du cortex en utilisant des informations de topologies, myelin, resting-state, et d'activations durant les tâches fMRI. Les estimations d'héritabilité pour les tâches de maths et de fables d'Esope sont comprises entre 22 et 45% et incluent particulièrement des régions du cerveau impliquées dans la compréhension sémantique. D'autre part, nous avons étudié la variance génétique partagée entre les activations neuronales dans les régions héritables et la performance cognitive, mesurée par les résultats obtenus durant les tâches fMRI et par des tests cognitifs standards. Cette étude montre que la région dont les activations partagent les origines génétiques communes les plus fortes avec les scores cognitifs est composée du gyrus angulaire et de la jonction temporo-pariétale. Les scores comportementaux avec la plus grande significativité de variance génétique partagée incluent : l'exactitude des réponses durant les tâches fMRI, l'intelligence fluide, la compréhension du vocabulaire, la lecture/déchiffrage. Cette région est intéressante du fait de son rôle particulier dans la compréhension sémantique, et de sa proximité avec les sillons temporal et intrapariétal impliqués dans les fonctions cognitives humaines de haut niveaux, respectivement les processus du langage et les opérations mathématiques.

La dernière partie de cette thèse est la plus prometteuse en termes de variations génétiques causales. Nous avons découverts et répliqués une association GWAS entre une région antérieure au gène KCNK2 et l'ouverture des sillons, et avec l'épaisseur corticale autour des sillons. Ces deux phénotypes examinés corrèlent très significativement avec l'âge et sont donc des marqueurs du vieillissement du cerveau. De plus, une base de donnée (GTEx Consortium, 2017) de gene-tissue expression montre que le SNP le plus associé rs864736 dans notre analyse est dans une région cis-régulatrice du gène KCNK2. Ce gène régule la réponse des cellules immunitaires dans le système nerveux centrale (CNS) et contrôle l'inflammation du CNS, qui est impliquée dans l'atrophie corticale et le déclin cognitif. Notre étude encourage une enquête plus approfondie des variants associés et des gènes voisins dans un contexte pathologique comme la maladie d'Alzheimer pour laquelle l'atrophie est un biomarqueur clé.

Premièrement, nos résultats ou absences de résultats confirment la taille d'effet généralement petite (< 0.5%) des variants communs. Pour cette raison, il est important de s'interroger sur la pertinence et l'intérêt d'associations avec des SNPs qui expliquent un pourcentage infime de la variance phénotypique dans la population générale. Les études d'imageries génétiques qui se concentrent sur des pathologies semblent produire des résultats plus interprétables et utilisables.En particulier, dans un contexte pathologique, les SNPs associés sont souvent utilisés pour former des scores polygéniques de risque, qui sont utilisés pour évaluer la susceptibilité de tout individu à une maladie. Ces scores polygéniques commencent aussi à être utilisés pour tester des associations de groupes de variants avec des traits non liés à une maladie. La taille d'effet de ces scores dans la variance phénotypique correspond alors à la somme des tailles d'effets de chaque variant et permet ainsi d'obtenir une association plus significative qu'avec un unique SNP. Secondement, les variants rares ont souvent des tailles d'effet plus larges sur les phénotypes comparés aux variants communs. Ainsi, nous devrions promouvoir le séquençage du génome entier en imagerie génétique pour permettre l'étude des associations avec des variants rares. Finalement, le post traitement systématique des résultats de GWAS peut aussi conduire à des résultats supplémentaires (de Leeuw et al., 2015; Watanabe et al., 2017), par exemple en utilisant une information d'enrichissement de tissues.

References

Allen, N., Sudlow, C., Downey, P., Peakman, T., Danesh, J., Elliott, P., Gallacher, J., Green, J., Matthews, P., Pell, J., Sprosen, T., Collins, R., 2012. UK Biobank: Current status and what it means for epidemiology. Heal. Policy Technol. 1, 123–126. doi:10.1016/j.hlpt.2012.07.003

Almasy, L., Blangero, J., 1998. Multipoint Quantitative-Trait Linkage Analysis in General Pedigrees. Am. J. Hum. Genet. 62, 1198–211. doi:10.1086/301844

Amalric, M., Dehaene, S., 2016. Origins of the brain networks for advanced mathematics in expert mathematicians. Proc. Natl. Acad. Sci. 113, 4909–4917. doi:10.1073/pnas.1603205113

Amunts, K., Schleicher, A., Burgel, U., Mohlberg, H., Uylings, H.B.M., Zilles, K., 1999. Broca's region revisited: Cytoarchitecture and intersubject variability. J. Comp. Neurol. 412, 319–341. doi:10.1002/(SICI)1096-9861(19990920)412:2<319::AID-CNE10>3.0.CO;2-7

Ashburner, J., 2009. Computational anatomy with the SPM software. Magn. Reson. Imaging 27, 1163–1174. doi:10.1016/j.mri.2009.01.006

Ashkenazi, S., Rosenberg-Lee, M., Tenison, C., Menon, V., 2012. Weak task-related modulation and stimulus representations during arithmetic problem solving in children with developmental dyscalculia. Dev. Cogn. Neurosci. 2, S152–S166. doi:10.1016/j.dcn.2011.09.006

Auzias, G., Brun, L., Deruelle, C., Coulon, O., 2015. Deep sulcal landmarks: Algorithmic and conceptual improvements in the definition and extraction of sulcal pits. Neuroimage 111, 12–25. doi:10.1016/j.neuroimage.2015.02.008

Bae, B. Il, Tietjen, I., Atabay, K.D., Evrony, G.D., Johnson, M.B., Asare, E., Wang, P.P., Murayama, A.Y., Im, K., Lisgo, S.N., Overman, L., Šestan, N., Chang, B.S., Barkovich, A.J., Grant, P.E., Topçu, M., Politsky, J., Okano, H., Piao, X., Walsh, C.A., 2014. Evolutionarily dynamic alternative splicing of GPR56 Regulates regional cerebral cortical patterning. Science (80-.). 343, 764–768. doi:10.1126/science.1244392

Bailly, M., Destrieux, C., Hommet, C., Mondon, K., Cottier, J.-P., Beaufils, E., Vierron, E., Vercouillie, J., Ibazizene, M., Voisin, T., Payoux, P., Barré, L., Camus, V., Guilloteau, D., Ribeiro, M.-J., 2015. Precuneus and Cingulate Cortex Atrophy and Hypometabolism in Patients with Alzheimer's Disease and Mild Cognitive Impairment: MRI and 18 F-FDG PET Quantitative Analysis Using FreeSurfer. Biomed Res. Int. 2015, 1–8. doi:10.1155/2015/583931

Bando, Y., Hirano, T., Tagawa, Y., 2014. Dysfunction of KCNK potassium channels impairs neuronal migration in the developing mouse cerebral cortex. Cereb. Cortex 24, 1017–1029. doi:10.1093/cercor/bhs387

Banerjee, A., Ghatak, S., Sikdar, S.K., 2016. l-Lactate mediates neuroprotection against ischaemia by increasing TREK1 channel expression in rat hippocampal astrocytes in vitro. J. Neurochem. 265–281. doi:10.1111/jnc.13638

Barch, D.M., Burgess, G.C., Harms, M.P., Petersen, S.E., Schlaggar, B.L., Corbetta, M., Glasser, M.F., Curtiss, S., Dixit, S., Feldt, C., Nolan, D., Bryant, E., Hartley, T., Footer, O., Bjork, J.M., Poldrack, R., Smith, S., Johansen-Berg, H., Snyder, A.Z., Van Essen, D.C., 2013. Function in the human connectome: Task-fMRI and individual differences in behavior. Neuroimage 80, 169–189. doi:10.1016/j.neuroimage.2013.05.033

Barrick, T.R., Mackay, C.E., Prima, S., Maes, F., Vandermeulen, D., Crow, T.J., Roberts, N., 2005. Automatic analysis of cerebral asymmetry: An exploratory study of the relationship between brain torque and planum temporale asymmetry. Neuroimage 24, 678–691. doi:10.1016/j.neuroimage.2004.09.003

Barron, D.H., 1950. An experimental analysis of some factors involved in the development of the fissure pattern of the cerebral cortex. J. Exp. Zool. 113, 553–581. doi:10.1002/jez.1401130304

Bartley, A.J., Jones, D.W., Weinberger, D.R., 1997. Genetic variability of human brain size and cortical gyral patterns. Brain 120, 257–269. doi:10.1093/brain/120.2.257

Bastos Leite, A.J., Scheltens, P., Barkhof, F., 2004. Pathological Aging of the Brain. Top. Magn. Reson. Imaging 15, 369–389. doi:10.1097/01.rmr.0000168070.90113.dc

Belin, P., Zatorre, R.J., Lafaille, P., Ahad, P., Pike, B., 2000. Voice-selective areas in human auditory cortex. Nature 403, 309–312. doi:10.1038/35002078

Binder, J.R., Gross, W.L., Allendorfer, J.B., Bonilha, L., Chapin, J., Edwards, J.C., Grabowski, T.J., Langfitt, J.T., Loring, D.W., Lowe, M.J., Koenig, K., Morgan, P.S., Ojemann, J.G., Rorden, C., Szaflarski, J.P., Tivarus, M.E., Weaver, K.E., 2011. Mapping anterior temporal lobe language areas with fMRI: A multicenter normative study. Neuroimage 54, 1465–1475. doi:10.1016/j.neuroimage.2010.09.048

Bishop, D.V.M., 2013. Cerebral Asymmetry and Language Development: Cause, Correlate, or Consequence? Science (80-.). 340, 1230531–1230531. doi:10.1126/science.1230531

Bittner, S., Ruck, T., Fernández-Orth, J., Meuth, S.G., 2014. TREK-king the blood-brain-barrier. J. Neuroimmune Pharmacol. 9, 293–301. doi:10.1007/s11481-014-9530-8

Bittner, S., Ruck, T., Schuhmann, M.K., Herrmann, A.M., Maati, H.M.O., Bobak, N., G??bel, K., Langhauser, F., Stegner, D., Ehling, P., Borsotto, M., Pape, H.C., Nieswandt, B., Kleinschnitz, C., Heurteaux, C., Galla, H.J., Budde, T., Wiendl, H., Meuth, S.G., 2013. Endothelial TWIK-related potassium channel-1 (TREK1) regulates immune-cell trafficking into the CNS. Nat. Med. 19, 1161–1165. doi:10.1038/nm.3303

Blokland, G. a, McMahon, K.L., Thompson, P.M., Martin, N.G., de Zubicaray, G.I., Wright, M.J., 2011. Heritability of working memory brain activation. J Neurosci 31, 10882–10890. doi:10.1523/JNEUROSCI.5334-10.2011

Bodin, C., Takerkart, S., Belin, P., Coulon, O., 2017. Anatomo-functional correspondence in the superior temporal sulcus. Brain Struct. Funct. 1–12. doi:10.1007/s00429-017-1483-2

Boemio, A., Fromm, S., Braun, A., Poeppel, D., 2005. Hierarchical and asymmetric temporal sensitivity in human auditory cortices. Nat. Neurosci. 8, 389–395. doi:10.1038/nn1409

Bogdan, R., Salmeron, B.J., Carey, C.E., Agrawal, A., Calhoun, V.D., Garavan, H., Hariri, A.R., Heinz, A., Hill, M.N., Holmes, A., Kalin, N.H., Goldman, D., 2017. Imaging Genetics and Genomics in Psychiatry: A Critical Review of Progress and Potential. Biol. Psychiatry 82, 165–175. doi:10.1016/j.biopsych.2016.12.030

Bond, J., Roberts, E., Mochida, G.H., Hampshire, D.J., Scott, S., Askham, J.M., Springell, K., Mahadevan, M., Crow, Y.J., Markham, A.F., Walsh, C.A., Geoffrey Woods, C., 2002. ASPM is a major determinant of cerebral cortical size. Nat. Genet. 32, 316–320. doi:10.1038/ng995

Booth, J.R., Burman, D.D., Meyer, J.R., Gitelman, D.R., Parrish, T.B., Mesulam, M.M., 2003. Relation between brain activation and lexical performance. Hum. Brain Mapp. 19, 155–169. doi:10.1002/hbm.10111

Borrell, V., 2018. How Cells Fold the Cerebral Cortex. J. Neurosci. 38, 776–783. doi:10.1523/JNEUROSCI.1106-17.2017

Borrell, V., Reillo, I., 2012. Emerging roles of neural stem cells in cerebral cortex development and evolution. Dev. Neurobiol. 72, 955–971. doi:10.1002/dneu.22013

Borst, G., Cachia, A., Tissier, C., Ahr, E., Simon, G., Houd?, O., 2016. Early Cerebral Constraints on Reading Skills in School-Age Children: An MRI Study. Mind, Brain, Educ. 10, 47–54. doi:10.1111/mbe.12098

Boucher, M., Whitesides, S., Evans, A., 2009. Depth potential function for folding pattern representation, registration and analysis. Med. Image Anal. 13, 203–214. doi:10.1016/j.media.2008.09.001

Brauer, J., Anwander, A., Friederici, A.D., 2011. Neuroanatomical prerequisites for language functions in the maturing brain. Cereb. Cortex 21, 459–466. doi:10.1093/cercor/bhq108

Büchel, C., Raedler, T., Sommer, M., Sach, M., Weiller, C., 2004. White Matter Asymmetry in the Human Brain : A Diffusion Tensor MRI Study. Cereb. Cortex 14, 945–951. doi:10.1093/cercor/bhh055

Bugden, S., Price, G.R., McLean, D.A., Ansari, D., 2012. The role of the left intraparietal sulcus in the relationship between symbolic number processing and children's arithmetic competence. Dev. Cogn. Neurosci. 2, 448–457. doi:10.1016/j.dcn.2012.04.001

Buxhoeveden, D.P., Casanova, M.F., 2002. The minicolumn hypothesis in neuroscience. Brain 125, 935–951. doi:10.1093/brain/awf110

Buxhoeveden, D.P., Switala, A.E., Litaker, M., Roy, E., Casanova, M.F., 2001. Lateralization of minicolumns in human planum temporale is absent in nonhuman primate cortex. Brain. Behav. Evol. 57, 349–358. doi:10.1159/000047253

Bycroft, C., Freeman, C., Petkova, D., Band, G., Elliott, L.T., Sharp, K., Motyer, A., Vukcevic, D.,

Delaneau, O., O'Connell, J., Cortes, A., Welsh, S., McVean, G., Leslie, S., Donnelly, P., Marchini, J., 2017. Genome-wide genetic data on ~500,000 UK Biobank participants. bioRxiv 166298. doi:10.1101/166298

Cai, Y., Peng, Z., Guo, H., Wang, F., Zeng, Y., 2017. TREK-1 pathway mediates isoflurane-induced memory impairment in middle-aged mice. Neurobiol. Learn. Mem. 145, 199–204. doi:10.1016/j.nlm.2017.10.012

Calvert, G.A., Bullmore, E.T., Brammer, M.J., Campbell, R., Williams, S.C.R., McGuire, P.K., Woodruff, P.W.R., Iversen, S.D., David, A.S., 1997. Activation of Auditory Cortex During Silent Lipreading. Science (80-.). 276, 593–596. doi:10.1126/science.276.5312.593

Cantalupo, C., Hopkins, W.D., 2001. Asymmetric Broca's area in great apes. Nature 414, 505–505. doi:10.1038/35107134

Caspers, S., Geyer, S., Schleicher, A., Mohlberg, H., Amunts, K., Zilles, K., 2006. The human inferior parietal cortex: Cytoarchitectonic parcellation and interindividual variability. Neuroimage 33, 430–448. doi:10.1016/j.neuroimage.2006.06.054

Catani, M., Dell'Acqua, F., Vergani, F., Malik, F., Hodge, H., Roy, P., Valabregue, R., Thiebaut de Schotten, M., 2012. Short frontal lobe connections of the human brain. Cortex 48, 273–291. doi:10.1016/j.cortex.2011.12.001

Chen, C., Gutierrez, E.D., Thompson, W., Panizzon, M.S., Jernigan, T.L., Eyler, L.T., Fennema-Notestine, C., Jak, A.J., Neale, M.C., Franz, C.E., Lyons, M.J., Grant, M.D., Fischl, B., Seidman, L.J., Tsuang, M.T., Kremen, W.S., Dale, A.M., 2012. Hierarchical Genetic Organization of Human Cortical Surface Area. Science (80-.). 335, 1634–1636. doi:10.1126/science.1215330

Cheverud, J.M., Falk, D., Vannier, M., Konigsberg, L., Helmkamp, R.C., Hildebolt, C., 1990. Heritability of Brain Size and Surface Features in Rhesus Macaques (Macaca mulatta). J. Hered. 819012, 51–57.

Chi, J.G., Dooling, E.C., Gilles, F.H., 1977. Gyral development of the human brain. Ann. Neurol. 1, 86–93. doi:10.1002/ana.410010109

Chiarello, C., Vazquez, D., Felton, A., McDowell, A., 2016. Structural asymmetry of the human cerebral cortex: Regional and between-subject variability of surface area, cortical thickness, and local gyrification. Neuropsychologia 93, 365–379. doi:10.1016/j.neuropsychologia.2016.01.012

Coren, S., 1992. The left-hander syndrome: The causes and consequences of left-handedness., The left-hander syndrome: The causes and consequences of left-handedness. Free Press, New York, NY, US.

Crosson, B., Saclek, J.R., Bobholz, J.A., Gökçay, D., Mohr, C.M., Leonard, C.M., Maron, L., Auerbach, E.J., Browd, S.R., Freeman, A.J., Briggs, R.W., 1999. Activity in the paracingulate and cingulate sulci during word generation: An fMRI study of functional anatomy. Cereb. Cortex 9, 307–316. doi:10.1093/cercor/9.4.307

Cykowski, M.D., Coulon, O., Kochunov, P. V, Amunts, K., Lancaster, J.L., Laird, A.R., Glahn, D.C., Fox, P.T., 2008. The central sulcus: an observer-independent characterization of sulcal landmarks and depth asymmetry. Cereb. Cortex 18, 1999–2009. doi:10.1093/cercor/bhm224

Davies, G., Marioni, R.E., Liewald, D.C., Hill, W.D., Hagenaars, S.P., Harris, S.E., Ritchie, S.J., Luciano, M., Fawns-Ritchie, C., Lyall, D., Others, 2016. Genome-wide association study of cognitive functions and educational attainment in UK Biobank (N= 112 151). Mol. Psychiatry 21, 1–10. doi:10.1038/mp.2016.45

Davies, G., Tenesa, A., Payton, A., Yang, J., Harris, S.E., Liewald, D., Ke, X., Le Hellard, S., Christoforou, A., Luciano, M., McGhee, K., Lopez, L., Gow, A.J., Corley, J., Redmond, P., Fox, H.C., Haggarty, P., Whalley, L.J., McNeill, G., Goddard, M.E., Espeseth, T., Lundervold, A.J., Reinvang, I., Pickles, A., Steen, V.M., Ollier, W., Porteous, D.J., Horan, M., Starr, J.M., Pendleton, N., Visscher, P.M., Deary, I.J., 2011. Genome-wide association studies establish that human intelligence is highly heritable and polygenic. Mol. Psychiatry 16, 996–1005. doi:10.1038/mp.2011.85

de Juan Romero, C., Bruder, C., Tomasello, U., Sanz-Anquela, J.M., Borrell, V., Romero, C.D.J., Bruder, C., Tomasello, U., Sanz-Anquela, J.M., 2015. Discrete domains of gene expression in germinal layers distinguish the development of gyrencephaly. EMBO J. 34, 1–16. doi:10.15252/embj.201591176

de Kovel, C.G.F., Lisgo, S., Karlebach, G., Ju, J., Cheng, G., Fisher, S.E., Francks, C., 2017. Left-

right asymmetry of maturation rates in human embryonic neural development. Biol. Psychiatry. doi:10.1016/j.biopsych.2017.01.016
de Leeuw, C.A., Mooij, J.M., Heskes, T., Posthuma, D., 2015. MAGMA: Generalized Gene-Set Analysis of GWAS Data. PLoS Comput. Biol. 11, 1–19. doi:10.1371/journal.pcbi.1004219
Deen, B., Koldewyn, K., Kanwisher, N., Saxe, R., 2015. Functional Organization of Social Perception and Cognition in the Superior Temporal Sulcus. Cereb. Cortex 25, 4596–4609. doi:10.1093/cercor/bhv111
Dehaene-Lambertz, G., Hertz-Pannier, L., Dubois, J., Meriaux, S., Roche, A., Sigman, M., Dehaene, S., 2006. Functional organization of perisylvian activation during presentation of sentences in preverbal infants. Proc. Natl. Acad. Sci. 103, 14240–14245. doi:10.1073/pnas.0606302103
Dehaene-Lambertz, G., Spelke, E.S., 2015. The Infancy of the Human Brain. Neuron 88, 93–109. doi:10.1016/j.neuron.2015.09.026
Dehaene, S., Pegado, F., Braga, L.W., Ventura, P., Filho, G.N., Jobert, A., Dehaene-Lambertz, G., Kolinsky, R., Morais, J., Cohen, L., 2010. How Learning to Read Changes the Cortical Networks for Vision and Language. Science (80-.). 330, 1359–1364. doi:10.1126/science.1194140
Dehaene, S., Piazza, M., Pinel, P., Cohen, L., 2003. THREE PARIETAL CIRCUITS FOR NUMBER PROCESSING. Cogn. Neuropsychol. 20, 487–506. doi:10.1080/02643290244000239
Destrieux, C., Fischl, B., Dale, A., Halgren, E., 2010. Automatic parcellation of human cortical gyri and sulci using standard anatomical nomenclature. Neuroimage 53, 1–15. doi:10.1016/j.neuroimage.2010.06.010
DeWitt, I., Rauschecker, J.P., 2012. Phoneme and word recognition in the auditory ventral stream. Proc. Natl. Acad. Sci. 109, E505–E514. doi:10.1073/pnas.1113427109
Diaz, M.T., Hogstrom, L.J., 2011. The influence of context on hemispheric recruitment during metaphor processing. J. Cogn. Neurosci. 23, 3586–3597. doi:10.1162/jocn_a_00053
Docherty, A.R., Kremen, W.S., Panizzon, M.S., Prom-Wormley, E.C., Franz, C.E., Lyons, M.J., Eaves, L.J., Neale, M.C., 2015. Comparison of Twin and Extended Pedigree Designs for Obtaining Heritability Estimates. Behav. Genet. 45, 461–466. doi:10.1007/s10519-015-9720-z
Docherty, S.J., Davis, O.S.P., Kovas, Y., Meaburn, E.L., Dale, P.S., Petrill, S.A., Schalkwyk, L.C., Plomin, R., 2010. A genome-wide association study identifies multiple loci associated with mathematics ability and disability. Genes, Brain Behav. 9, 234–247. doi:10.1111/j.1601-183X.2009.00553.x
Dorsaint-Pierre, R., Penhune, V.B., Watkins, K.E., Neelin, P., Lerch, J.P., Bouffard, M., Zatorre, R.J., 2006. Asymmetries of the planum temporale and Heschl's gyrus: Relationship to language lateralization. Brain 129, 1164–1176. doi:10.1093/brain/awl055
Dubois, J., Benders, M., Cachia, a., Lazeyras, F., Ha-Vinh Leuchter, R., Sizonenko, S. V., Borradori-Tolsa, C., Mangin, J.F., Hüppi, P.S., 2008. Mapping the early cortical folding process in the preterm newborn brain. Cereb. Cortex 18, 1444–1454. doi:10.1093/cercor/bhm180
Dubois, J., Benders, M., Lazeyras, F., Borradori-Tolsa, C., Leuchter, R.H.V., Mangin, J.F., Hüppi, P.S., 2010. Structural asymmetries of perisylvian regions in the preterm newborn. Neuroimage 52, 32–42. doi:10.1016/j.neuroimage.2010.03.054
Dubois, J., Germanaud, D., Angleys, H., Leroy, F., Fischer, C., Lebenberg, J., Lazeyras, F., Dehaene-Lambertz, G., Hertz-Pannier, L., Mangin, J.F., Huppi, P., Lefevre, J., 2016. Exploring the successive waves of cortical folding in the developing brain using MRI and spectral analysis of gyrification. Proc. - Int. Symp. Biomed. Imaging 2016–June, 261–264. doi:10.1109/ISBI.2016.7493259
Dubois, J., Poupon, C., Thirion, B., Simonnet, H., Kulikova, S., Leroy, F., Hertz-Pannier, L., Dehaene-Lambertz, G., 2015. Exploring the Early Organization and Maturation of Linguistic Pathways in the Human Infant Brain. Cereb. Cortex 1–16. doi:10.1093/cercor/bhv082
Echevarría, D., Vieira, C., Gimeno, L., Martínez, S., 2003. Neuroepithelial secondary organizers and cell fate specification in the developing brain. Brain Res. Rev. 43, 179–191. doi:10.1016/j.brainresrev.2003.08.002
Eicher, J.D., Gruen, J.R., 2013. Imaging-genetics in dyslexia: Connecting risk genetic variants to brain neuroimaging and ultimately to reading impairments. Mol. Genet. Metab. 110, 201–212. doi:10.1016/j.ymgme.2013.07.001
Emerson, R.W., Cantlon, J.F., 2015. Continuity and change in children's longitudinal neural responses

to numbers. Dev. Sci. 18, 314–326. doi:10.1111/desc.12215
Emerson, R.W., Cantlon, J.F., 2012. Early math achievement and functional connectivity in the fronto-parietal network. Dev. Cogn. Neurosci. 2, S139–S151. doi:10.1016/j.dcn.2011.11.003
Erika-Florence, M., Leech, R., Hampshire, a, 2014. A functional network perspective on response inhibition and attentional control. Nat Commun 5, 4073. doi:10.1038/ncomms5073
Etkin, A., Egner, T., Kalisch, R., 2011. Emotional processing in anterior cingulate and medial prefrontal cortex. Trends Cogn. Sci. 15, 85–93. doi:10.1016/j.tics.2010.11.004
Fischl, B., 2012. FreeSurfer. Neuroimage 62, 774–781. doi:10.1016/j.neuroimage.2012.01.021
Fischl, B., Rajendran, N., Busa, E., Augustinack, J., Hinds, O., Yeo, B.T.T., Mohlberg, H., Amunts, K., Zilles, K., 2008. Cortical folding patterns and predicting cytoarchitecture. Cereb. Cortex 18, 1973–1980. doi:10.1093/cercor/bhm225
Fjell, A.M., Walhovd, K.B., 2010. Structural Brain Changes in Aging: Courses, Causes and Cognitive Consequences. Rev. Neurosci. 21, 187–221. doi:10.1515/REVNEURO.2010.21.3.187
Florio, M., Albert, M., Taverna, E., Namba, T., Brandl, H., Lewitus, E., Haffner, C., Sykes, A., Wong, F.K., Peters, J., Guhr, E., Klemroth, S., Prufer, K., Kelso, J., Naumann, R., Nusslein, I., Dahl, A., Lachmann, R., Paabo, S., Huttner, W.B., 2015. Human-specific gene ARHGAP11B promotes basal progenitor amplification and neocortex expansion. Science (80-.). 347, 1465–1470. doi:10.1126/science.aaa1975
Florio, M., Borrell, V., Huttner, W.B., 2017. Human-specific genomic signatures of neocortical expansion. Curr. Opin. Neurobiol. 42, 33–44. doi:10.1016/j.conb.2016.11.004
Foubet, O., Trejo, M., Toro, R., 2018. Mechanical morphogenesis and the development of neocortical organisation. Cortex 1–15. doi:10.1016/j.cortex.2018.03.005
Friederici, A.D., 2006. The Neural Basis of Language Development and Its Impairment. Neuron 52, 941–952. doi:10.1016/j.neuron.2006.12.002
Friederici, A.D., Gierhan, S.M., 2013. The language network. Curr. Opin. Neurobiol. 23, 250–254. doi:10.1016/j.conb.2012.10.002
Frith, C.D., Frith, U., 2007. Social Cognition in Humans. Curr. Biol. 17, R724–R732. doi:10.1016/j.cub.2007.05.068
Galaburda, A.M., Corsiglia, J., Rosen, G.D., Dana, C.A., Sherman, F., Sherman, G.F., 1987. Planum temporale asymmetry, reappraisal since Geschwind and Levitsky. Neuropsychologia 25, 853–868. doi:https://doi.org/10.1016/0028-3932(87)90091-1
Galli, R., Fiocco, R., De Filippis, L., Muzio, L., Gritti, A., Mercurio, S., Broccoli, V., Pellegrini, M., Mallamaci, A., Vescovi, A.L., 2002. Emx2 regulates the proliferation of stem cells of the adult mammalian central nervous system. Development 129, 1633–1644.
Ganjgahi, H., Winkler, A.M., Glahn, D.C., Blangero, J., Kochunov, P., Nichols, T.E., 2015. Fast and powerful heritability inference for family-based neuroimaging studies. Neuroimage 115, 256–268. doi:10.1016/j.neuroimage.2015.03.005
Ge, T., Nichols, T.E., Lee, P.H., Holmes, A.J., Roffman, J.L., Buckner, R.L., Sabuncu, M.R., Smoller, J.W., 2015. Massively expedited genome-wide heritability analysis (MEGHA). Proc. Natl. Acad. Sci. 112, 2479–2484. doi:10.1073/pnas.1415603112
Ge, Y., Grossman, R.I., Babb, J.S., Rabin, M.L., Mannon, L.J., Kolson, D.L., 2002. Age-related total gray matter and white matter changes in normal adult brain. Part I: volumetric MR imaging analysis. Am. J. Neuroradiol. 23, 1327–33.
Germanaud, D., Lefèvre, J., Toro, R., Fischer, C., Dubois, J., Hertz-Pannier, L., Mangin, J.F., 2012. Larger is twistier: Spectral analysis of gyrification (SPANGY) applied to adult brain size polymorphism. Neuroimage 63, 1257–1272. doi:10.1016/j.neuroimage.2012.07.053
Geschwind, D.H., Miller, B.L., 2001. Molecular approaches to cerebral laterality: Development and neurodegeneration. Am. J. Med. Genet. 101, 370–381. doi:10.1002/1096-8628(20010715)101:4<370::AID-AJMG1223>3.0.CO;2-G
Geschwind, D.H., Miller, B.L., DeCarli, C., Carmelli, D., 2002. Heritability of lobar brain volumes in twins supports genetic models of cerebral laterality and handedness. Proc. Natl. Acad. Sci. 99, 3176–3181. doi:10.1073/pnas.052494999
Geschwind, N., Levitsky, W., 1968. Human Brain: Left-Right Asymmetries in Temporal Speech Region. Science (80-.). 161, 186–187. doi:10.1126/science.161.3837.186
Glahn, D.C., Knowles, E.E.M., Mckay, D.R., Sprooten, E., Raventós, H., Blangero, J., Gottesman, I.I.,

Almasy, L., 2014. Arguments for the sake of endophenotypes: Examining common misconceptions about the use of endophenotypes in psychiatric genetics. Am. J. Med. Genet. Part B Neuropsychiatr. Genet. 165, 122–130. doi:10.1002/ajmg.b.32221
Glahn, D.C., Thompson, P.M., Blangero, J., 2007. Neuroimaging endophenotypes: Strategies for finding genes influencing brain structure and function. Hum. Brain Mapp. 28, 488–501. doi:10.1002/hbm.20401
Glasel, H., Leroy, F., Dubois, J., Hertz-Pannier, L., Mangin, J.F., Dehaene-Lambertz, G., 2011. A robust cerebral asymmetry in the infant brain: The rightward superior temporal sulcus. Neuroimage 58, 716–723. doi:10.1016/j.neuroimage.2011.06.016
Glasser, M.F., Coalson, T.S., Robinson, E.C., Hacker, C.D., Harwell, J., Yacoub, E., Ugurbil, K., Andersson, J., Beckmann, C.F., Jenkinson, M., Smith, S.M., Van Essen, D.C., 2016. A multi-modal parcellation of human cerebral cortex. Nature 536, 171–8. doi:10.1038/nature18933
Glasser, M.F., Sotiropoulos, S.N., Wilson, J.A., Coalson, T.S., Fischl, B., Andersson, J.L., Xu, J., Jbabdi, S., Webster, M., Polimeni, J.R., Van Essen, D.C., Jenkinson, M., 2013. The minimal preprocessing pipelines for the Human Connectome Project. Neuroimage 80, 105–124. doi:10.1016/j.neuroimage.2013.04.127
Glover, G.H., 1999. Deconvolution of Impulse Response in Event-Related BOLD fMRI1. Neuroimage 9, 416–429. doi:10.1006/nimg.1998.0419
Gómez-Robles, A., Hopkins, W.D., Schapiro, S.J., Sherwood, C.C., 2015. Relaxed genetic control of cortical organization in human brains compared with chimpanzees. Proc. Natl. Acad. Sci. U. S. A. 112, 14799–804. doi:10.1073/pnas.1512646112
Good, C.D., Johnsrude, I., Ashburner, J., Henson, R.N.A., Friston, K.J., Frackowiak, R.S.J., 2001. Cerebral asymmetry and the effects of sex and handedness on brain structure: A voxel-based morphometric analysis of 465 normal adult human brains. Neuroimage 14, 685–700. doi:10.1006/nimg.2001.0857
Gratiolet, P., 1854. Mémoire sur les plis cérébraux de l'homme et des primates, Paris. ed. Arthus Bertrand.
Greve, D.N., Van der Haegen, L., Cai, Q., Stufflebeam, S., Sabuncu, M.R., Fischl, B., Brysbaert, M., 2013. A surface-based analysis of language lateralization and cortical asymmetry. J. Cogn. Neurosci. 25, 1477–92. doi:10.1162/jocn_a_00405
GTEx Consortium, 2017. Genetic effects on gene expression across human tissues. Nature 550, 204–213. doi:10.1038/nature24277
Gunning-Dixon, F.M., Brickman, A.M., Cheng, J.C., Alexopoulos, G.S., 2009. Aging of cerebral white matter: a review of MRI findings. Int. J. Geriatr. Psychiatry 24, 109–117. doi:10.1002/gps.2087
Güntürkün, O., Ocklenburg, S., 2017. Ontogenesis of Lateralization. Neuron. doi:10.1016/j.neuron.2017.02.045
Habas, P.A., Scott, J.A., Roosta, A., Rajagopalan, V., Kim, K., Rousseau, F., Barkovich, A.J., Glenn, O.A., Studholme, C., 2012. Early folding patterns and asymmetries of the normal human brain detected from in utero MRI. Cereb. Cortex 22, 13–25. doi:10.1093/cercor/bhr053
Hamelin, L., Lagarde, J., Dorothée, G., Leroy, C., Labit, M., Comley, R.A., de Souza, L.C., Corne, H., Dauphinot, L., Bertoux, M., Dubois, B., Gervais, P., Colliot, O., Potier, M.C., Bottlaender, M., Sarazin, M., 2016. Early and protective microglial activation in Alzheimer's disease: a prospective study using 18 F-DPA-714 PET imaging. Brain 139, 1252–1264. doi:10.1093/brain/aww017
Han, B., Eskin, E., 2011. Random-effects model aimed at discovering associations in meta-analysis of genome-wide association studies. Am. J. Hum. Genet. 88, 586–598. doi:10.1016/j.ajhg.2011.04.014
Haworth, C.M.A., Dale, P., Plomin, R., 2008. A Twin Study into the Genetic and Environmental Influences on Academic Performance in Science in nine-year-old Boys and Girls. Int. J. Sci. Educ. 30, 1003–1025. doi:10.1080/09500690701324190
Hein, G., Knight, R.T., 2008. Superior temporal sulcus--It's my area: or is it? J. Cogn. Neurosci. 20, 2125–2136. doi:10.1162/jocn.2008.20148
Hervieu, G.J., Cluderay, J.E., Gray, C.W., Green, P.J., Ranson, J.L., Randall, A.D., Meadows, H.J., 2001. Distribution and expression of TREK-1, a two-pore-domain potassium channel, in the

adult rat CNS. Neuroscience 103, 899–919. doi:10.1016/S0306-4522(01)00030-6
Hibar, D.P., Adams, H.H.H., Jahanshad, N., Chauhan, G., Stein, J.L., Hofer, E., Renteria, M.E., Bis, J.C., Arias-Vasquez, A., Ikram, M.K., Desrivières, S., Vernooij, M.W., Abramovic, L., Alhusaini, S., Amin, N., Andersson, M., Arfanakis, K., Aribisala, B.S., Armstrong, N.J., Athanasiu, L., Axelsson, T., Beecham, A.H., Beiser, A., Bernard, M., Blanton, S.H., Bohlken, M.M., Boks, M.P., Bralten, J., Brickman, A.M., Carmichael, O., Chakravarty, M.M., Chen, Q., Ching, C.R.K., Chouraki, V., Cuellar-Partida, G., Crivello, F., Den Braber, A., Doan, N.T., Ehrlich, S., Giddaluru, S., Goldman, A.L., Gottesman, R.F., Grimm, O., Griswold, M.E., Guadalupe, T., Gutman, B.A., Hass, J., Haukvik, U.K., Hoehn, D., Holmes, A.J., Hoogman, M., Janowitz, D., Jia, T., Jørgensen, K.N., Karbalai, N., Kasperaviciute, D., Kim, S., Klein, M., Kraemer, B., Lee, P.H., Liewald, D.C.M., Lopez, L.M., Luciano, M., Macare, C., Marquand, A.F., Matarin, M., Mather, K.A., Mattheisen, M., McKay, D.R., Milaneschi, Y., Muñoz Maniega, S., Nho, K., Nugent, A.C., Nyquist, P., Loohuis, L.M.O., Oosterlaan, J., Papmeyer, M., Pirpamer, L., Pütz, B., Ramasamy, A., Richards, J.S., Risacher, S.L., Roiz-Santiañez, R., Rommelse, N., Ropele, S., Rose, E.J., Royle, N.A., Rundek, T., Sämann, P.G., Saremi, A., Satizabal, C.L., Schmaal, L., Schork, A.J., Shen, L., Shin, J., Shumskaya, E., Smith, A. V., Sprooten, E., Strike, L.T., Teumer, A., Tordesillas-Gutierrez, D., Toro, R., Trabzuni, D., Trompet, S., Vaidya, D., Van der Grond, J., Van der Lee, S.J., Van der Meer, D., Van Donkelaar, M.M.J., Van Eijk, K.R., Van Erp, T.G.M., Van Rooij, D., Walton, E., Westlye, L.T., Whelan, C.D., Windham, B.G., Winkler, A.M., Wittfeld, K., Woldehawariat, G., Wolf, C., Wolfers, T., Yanek, L.R., Yang, J., Zijdenbos, A., Zwiers, M.P., Agartz, I., Almasy, L., Ames, D., Amouyel, P., Andreassen, O.A., Arepalli, S., Assareh, A.A., Barral, S., Bastin, M.E., Becker, D.M., Becker, J.T., Bennett, D.A., Blangero, J., van Bokhoven, H., Boomsma, D.I., Brodaty, H., Brouwer, R.M., Brunner, H.G., Buckner, R.L., Buitelaar, J.K., Bulayeva, K.B., Cahn, W., Calhoun, V.D., Cannon, D.M., Cavalleri, G.L., Cheng, C.-Y., Cichon, S., Cookson, M.R., Corvin, A., Crespo-Facorro, B., Curran, J.E., Czisch, M., Dale, A.M., Davies, G.E., De Craen, A.J.M., De Geus, E.J.C., De Jager, P.L., De Zubicaray, G.I., Deary, I.J., Debette, S., DeCarli, C., Delanty, N., Depondt, C., DeStefano, A., Dillman, A., Djurovic, S., Donohoe, G., Drevets, W.C., Duggirala, R., Dyer, T.D., Enzinger, C., Erk, S., Espeseth, T., Fedko, I.O., Fernández, G., Ferrucci, L., Fisher, S.E., Fleischman, D.A., Ford, I., Fornage, M., Foroud, T.M., Fox, P.T., Francks, C., Fukunaga, M., Gibbs, J.R., Glahn, D.C., Gollub, R.L., Göring, H.H.H., Green, R.C., Gruber, O., Gudnason, V., Guelfi, S., Håberg, A.K., Hansell, N.K., Hardy, J., Hartman, C.A., Hashimoto, R., Hegenscheid, K., Heinz, A., Le Hellard, S., Hernandez, D.G., Heslenfeld, D.J., Ho, B.-C., Hoekstra, P.J., Hoffmann, W., Hofman, A., Holsboer, F., Homuth, G., Hosten, N., Hottenga, J.-J., Huentelman, M., Pol, H.E.H., Ikeda, M., Jack Jr, C.R., Jenkinson, M., Johnson, R., Jönsson, E.G., Jukema, J.W., Kahn, R.S., Kanai, R., Kloszewska, I., Knopman, D.S., Kochunov, P., Kwok, J.B., Lawrie, S.M., Lemaître, H., Liu, X., Longo, D.L., Lopez, O.L., Lovestone, S., Martinez, O., Martinot, J.-L., Mattay, V.S., McDonald, C., McIntosh, A.M., McMahon, F.J., McMahon, K.L., Mecocci, P., Melle, I., Meyer-Lindenberg, A., Mohnke, S., Montgomery, G.W., Morris, D.W., Mosley, T.H., Mühleisen, T.W., Müller-Myhsok, B., Nalls, M.A., Nauck, M., Nichols, T.E., Niessen, W.J., Nöthen, M.M., Nyberg, L., Ohi, K., Olvera, R.L., Ophoff, R.A., Pandolfo, M., Paus, T., Pausova, Z., Penninx, B.W.J.H., Pike, G.B., Potkin, S.G., Psaty, B.M., Reppermund, S., Rietschel, M., Roffman, J.L., Romanczuk-Seiferth, N., Rotter, J.I., Ryten, M., Sacco, R.L., Sachdev, P.S., Saykin, A.J., Schmidt, R., Schmidt, H., Schofield, P.R., Sigursson, S., Simmons, A., Singleton, A., Sisodiya, S.M., Smith, C., Smoller, J.W., Soininen, H., Steen, V.M., Stott, D.J., Sussmann, J.E., Thalamuthu, A., Toga, A.W., Traynor, B.J., Troncoso, J., Tsolaki, M., Tzourio, C., Uitterlinden, A.G., Hernández, M.C.V., Van der Brug, M., van der Lugt, A., van der Wee, N.J.A., Van Haren, N.E.M., van 't Ent, D., Van Tol, M.-J., Vardarajan, B.N., Vellas, B., Veltman, D.J., Völzke, H., Walter, H., Wardlaw, J.M., Wassink, T.H., Weale, M.E., Weinberger, D.R., Weiner, M.W., Wen, W., Westman, E., White, T., Wong, T.Y., Wright, C.B., Zielke, R.H., Zonderman, A.B., Martin, N.G., Van Duijn, C.M., Wright, M.J., Longstreth, W.T., Schumann, G., Grabe, H.J., Franke, B., Launer, L.J., Medland, S.E., Seshadri, S., Thompson, P.M., Ikram, M.A., 2017. Novel genetic loci associated with hippocampal volume. Nat. Commun. 8, 13624. doi:10.1038/ncomms13624
Hibar, D.P., Stein, J.L., Renteria, M.E., Arias-Vasquez, A., Desrivières, S., Jahanshad, N., Toro, R.,

Wittfeld, K., Abramovic, L., Andersson, M., Aribisala, B.S., Armstrong, N.J., Bernard, M., Bohlken, M.M., Boks, M.P., Bralten, J., Brown, A. a., Mallar Chakravarty, M., Chen, Q., Ching, C.R.K., Cuellar-Partida, G., den Braber, A., Giddaluru, S., Goldman, A.L., Grimm, O., Guadalupe, T., Hass, J., Woldehawariat, G., Holmes, A.J., Hoogman, M., Janowitz, D., Jia, T., Kim, S., Klein, M., Kraemer, B., Lee, P.H., Olde Loohuis, L.M., Luciano, M., Macare, C., Mather, K. a., Mattheisen, M., Milaneschi, Y., Nho, K., Papmeyer, M., Ramasamy, A., Risacher, S.L., Roiz-Santiañez, R., Rose, E.J., Salami, A., Sämann, P.G., Schmaal, L., Schork, A.J., Shin, J., Strike, L.T., Teumer, A., van Donkelaar, M.M.J., van Eijk, K.R., Walters, R.K., Westlye, L.T., Whelan, C.D., Winkler, A.M., Zwiers, M.P., Alhusaini, S., Athanasiu, L., Ehrlich, S., Hakobjan, M.M.H., Hartberg, C.B., Haukvik, U.K., Heister, A.J.G. a. M., Hoehn, D., Kasperaviciute, D., Liewald, D.C.M., Lopez, L.M., Makkinje, R.R.R., Matarin, M., Naber, M. a. M., Reese McKay, D., Needham, M., Nugent, A.C., Pütz, B., Royle, N. a., Shen, L., Sprooten, E., Trabzuni, D., van der Marel, S.S.L., van Hulzen, K.J.E., Walton, E., Wolf, C., Almasy, L., Ames, D., Arepalli, S., Assareh, A. a., Bastin, M.E., Brodaty, H., Bulayeva, K.B., Carless, M. a., Cichon, S., Corvin, A., Curran, J.E., Czisch, M., de Zubicaray, G.I., Dillman, A., Duggirala, R., Dyer, T.D., Erk, S., Fedko, I.O., Ferrucci, L., Foroud, T.M., Fox, P.T., Fukunaga, M., Raphael Gibbs, J., Göring, H.H.H., Green, R.C., Guelfi, S., Hansell, N.K., Hartman, C. a., Hegenscheid, K., Heinz, A., Hernandez, D.G., Heslenfeld, D.J., Hoekstra, P.J., Holsboer, F., Homuth, G., Hottenga, J.-J., Ikeda, M., Jack, C.R., Jenkinson, M., Johnson, R., Kanai, R., Keil, M., Kent, J.W., Kochunov, P., Kwok, J.B., Lawrie, S.M., Liu, X., Longo, D.L., McMahon, K.L., Meisenzahl, E., Melle, I., Mohnke, S., Montgomery, G.W., Mostert, J.C., Mühleisen, T.W., Nalls, M. a., Nichols, T.E., Nilsson, L.G., Nöthen, M.M., Ohi, K., Olvera, R.L., Perez-Iglesias, R., Bruce Pike, G., Potkin, S.G., Reinvang, I., Reppermund, S., Rietschel, M., Romanczuk-Seiferth, N., Rosen, G.D., Rujescu, D., Schnell, K., Schofield, P.R., Smith, C., Steen, V.M., Sussmann, J.E., Thalamuthu, A., Toga, A.W., Traynor, B.J., Troncoso, J., Turner, J. a., Valdés Hernández, M.C., van 't Ent, D., van der Brug, M., van der Wee, N.J. a., van Tol, M.-J., Veltman, D.J., Wassink, T.H., Westman, E., Zielke, R.H., Zonderman, A.B., Ashbrook, D.G., Hager, R., Lu, L., McMahon, F.J., Morris, D.W., Williams, R.W., Brunner, H.G., Buckner, R.L., Buitelaar, J.K., Cahn, W., Calhoun, V.D., Cavalleri, G.L., Crespo-Facorro, B., Dale, A.M., Davies, G.E., Delanty, N., Depondt, C., Djurovic, S., Drevets, W.C., Espeseth, T., Gollub, R.L., Ho, B.-C., Hoffmann, W., Hosten, N., Kahn, R.S., Le Hellard, S., Meyer-Lindenberg, A., Müller-Myhsok, B., Nauck, M., Nyberg, L., Pandolfo, M., Penninx, B.W.J.H., Roffman, J.L., Sisodiya, S.M., Smoller, J.W., van Bokhoven, H., van Haren, N.E.M., Völzke, H., Walter, H., Weiner, M.W., Wen, W., White, T., Agartz, I., Andreassen, O. a., Blangero, J., Boomsma, D.I., Brouwer, R.M., Cannon, D.M., Cookson, M.R., de Geus, E.J.C., Deary, I.J., Donohoe, G., Fernández, G., Fisher, S.E., Francks, C., Glahn, D.C., Grabe, H.J., Gruber, O., Hardy, J., Hashimoto, R., Hulshoff Pol, H.E., Jönsson, E.G., Kloszewska, I., Lovestone, S., Mattay, V.S., Mecocci, P., McDonald, C., McIntosh, A.M., Ophoff, R. a., Paus, T., Pausova, Z., Ryten, M., Sachdev, P.S., Saykin, A.J., Simmons, A., Singleton, A., Soininen, H., Wardlaw, J.M., Weale, M.E., Weinberger, D.R., Adams, H.H.H., Launer, L.J., Seiler, S., Schmidt, R., Chauhan, G., Satizabal, C.L., Becker, J.T., Yanek, L., van der Lee, S.J., Ebling, M., Fischl, B., Longstreth, W.T., Greve, D., Schmidt, H., Nyquist, P., Vinke, L.N., van Duijn, C.M., Xue, L., Mazoyer, B., Bis, J.C., Gudnason, V., Seshadri, S., Ikram, M.A., Martin, N.G., Wright, M.J., Schumann, G., Franke, B., Thompson, P.M., Medland, S.E., 2015. Common genetic variants influence human subcortical brain structures. Nature 520, 224–229. doi:10.1038/nature14101

Hilgetag, C.C., Barbas, H., 2006. Role of mechanical factors in the morphology of the primate cerebral cortex. PLoS Comput. Biol. 2, 146–159. doi:10.1371/journal.pcbi.0020022

Hill, J., Dierker, D., Neil, J., Inder, T., Knutsen, a., Harwell, J., Coalson, T., Van Essen, D., 2010. A Surface-Based Analysis of Hemispheric Asymmetries and Folding of Cerebral Cortex in Term-Born Human Infants. J. Neurosci. 30, 2268–2276. doi:10.1523/JNEUROSCI.4682-09.2010

Hopkins, W.D., Meguerditchian, A., Coulon, O., Bogart, S., Mangin, J.-F., Sherwood, C.C., Grabowski, M.W., Bennett, A.J., Pierre, P.J., Fears, S., Woods, R., Hof, P.R., Vauclair, J., 2014. Evolution of the Central Sulcus Morphology in Primates. Brain. Behav. Evol. 84, 19–30. doi:10.1159/000362431

Hopkins, W.D., Pilcher, D.L., MacGregor, L., 2000. Sylvian fissure asymmetries in nonhuman

primates revisited: A comparative MRI study. Brain. Behav. Evol. 56, 293–299. doi:10.1159/000047213
Hopkins, W.D., Taglialatela, J.P., Meguerditchian, A., Nir, T., Schenker, N.M., Sherwood, C.C., 2008. Gray matter asymmetries in chimpanzees as revealed by voxel-based morphometry. Neuroimage 42, 491–497. doi:10.1016/j.neuroimage.2008.05.014
Huntgeburth, S.C., Petrides, M., 2012. Morphological patterns of the collateral sulcus in the human brain. Eur. J. Neurosci. 35, 1295–1311. doi:10.1111/j.1460-9568.2012.08031.x
Hutsler, J.J., 2003. The specialized structure of human language cortex: Pyramidal cell size asymmetries within auditory and language-associated regions of the temporal lobes. Brain Lang. 86, 226–242. doi:10.1016/S0093-934X(02)00531-X
Im, K., Jo, H.J., Mangin, J.F., Evans, A.C., Kim, S.I., Lee, J.M., 2010. Spatial distribution of deep sulcal landmarks and hemispherical asymmetry on the cortical surface. Cereb. Cortex 20, 602–611. doi:10.1093/cercor/bhp127
Im, K., Lee, J.M., Jeon, S., Kim, J.H., Seo, S.W., Na, D.L., Grant, P.E., 2013. Reliable Identification of Deep Sulcal Pits: The Effects of Scan Session, Scanner, and Surface Extraction Tool. PLoS One 8, 1–10. doi:10.1371/journal.pone.0053678
Im, K., Pienaar, R., Lee, J.M., Seong, J.K., Choi, Y.Y., Lee, K.H., Grant, P.E., 2011. Quantitative comparison and analysis of sulcal patterns using sulcal graph matching: A twin study. Neuroimage 57, 1077–1086. doi:10.1016/j.neuroimage.2011.04.062
Im, K., Pienaar, R., Paldino, M.J., Gaab, N., Galaburda, A.M., Grant, P.E., 2012. Quantification and Discrimination of Abnormal Sulcal Patterns in Polymicrogyria. Cereb. Cortex 23, 3007–15. doi:10.1093/cercor/bhs292
Im, K., Raschle, N.M., Smith, S.A., Ellen Grant, P., Gaab, N., 2016. Atypical Sulcal Pattern in Children with Developmental Dyslexia and At-Risk Kindergarteners. Cereb. Cortex 26, 1138–1148. doi:10.1093/cercor/bhu305
Jahanshad, N., Ganjgahi, H., Bralten, J., Braber, A. Den, Patel, B., Ritchie, S., Sprooten, E., Hoogman, M., Rey, M., 2017. Do Candidate Genes Affect the Brain ' s White Matter Microstructure ? Large-Scale Evaluation of 6,165 Diffusion MRI Scans. bioRvix. doi:10.1101/107987
Jenkinson, M., Beckmann, C.F., Behrens, T.E.J., Woolrich, M.W., Smith, S.M., 2012. Fsl. Neuroimage 62, 782–790. doi:10.1016/j.neuroimage.2011.09.015
Johnson, M.B., Kawasawa, Y.I., Mason, C.E., Krsnik, Ž., Coppola, G., Bogdanović, D., Geschwind, D.H., Mane, S.M., State, M.W., Šestan, N., 2009. Functional and Evolutionary Insights into Human Brain Development through Global Transcriptome Analysis. Neuron 62, 494–509. doi:10.1016/j.neuron.2009.03.027
Ju, X.C., Hou, Q.Q., Sheng, A.L., Wu, K.Y., Zhou, Y., Jin, Y., Wen, T., Yang, Z., Wang, X., Luo, Z.G., 2016. The hominoid-specific gene TBC1D3 promotes generation of basal neural progenitors and induces cortical folding in mice. Elife 5, 1–25. doi:10.7554/eLife.18197
Kang, X., Herron, T.J., Ettlinger, M., Woods, D.L., 2015. Hemispheric asymmetries in cortical and subcortical anatomy. Laterality Asymmetries Body, Brain Cogn. 20, 658–684. doi:10.1080/1357650X.2015.1032975
Kao, C.Y., Hofer, M., Sapiro, G., Stern, J., Rehm, K., Rottenberg, D. a., 2007. A geometric method for automatic extraction of sulcal fundi. IEEE Trans. Med. Imaging 26, 530–540. doi:10.1109/TMI.2006.886810
Karas, G., Scheltens, P., Rombouts, S., Van Schijndel, R., Klein, M., Jones, B., Van Der Flier, W., Vrenken, H., Barkhof, F., 2007. Precuneus atrophy in early-onset Alzheimer's disease: A morphometric structural MRI study. Neuroradiology 49, 967–976. doi:10.1007/s00234-007-0269-2
Karlebach, G., Francks, C., 2015. Lateralization of gene expression in human language cortex. Cortex 67, 30–36. doi:10.1016/j.cortex.2015.03.003
Kertesz, A., Black, S.E., Polk, M., Howell, J., 1986. Cerebral Asymmetries on Magnetic Resonance Imaging. Cortex 22, 117–127. doi:https://doi.org/10.1016/S0010-9452(86)80036-3
Kochunov, P., Glahn, D.C., Fox, P.T., Lancaster, J.L., Saleem, K., Shelledy, W., Zilles, K., Thompson, P.M., Coulon, O., Mangin, J.F., Blangero, J., Rogers, J., 2010. Genetics of primary cerebral gyrification: Heritability of length, depth and area of primary sulci in an extended pedigree of Papio baboons. Neuroimage 53, 1126–1134. doi:10.1016/j.neuroimage.2009.12.045

Kochunov, P., Jahanshad, N., Marcus, D., Winkler, A., Sprooten, E., Nichols, T.E., Wright, S.N., Hong, L.E., Patel, B., Behrens, T., Jbabdi, S., Andersson, J., Lenglet, C., Yacoub, E., Moeller, S., Auerbach, E., Ugurbil, K., Sotiropoulos, S.N., Brouwer, R.M., Landman, B., Lemaitre, H., den Braber, A., Zwiers, M.P., Ritchie, S., van Hulzen, K., Almasy, L., Curran, J., deZubicaray, G.I., Duggirala, R., Fox, P., Martin, N.G., McMahon, K.L., Mitchell, B., Olvera, R.L., Peterson, C., Starr, J., Sussmann, J., Wardlaw, J., Wright, M., Boomsma, D.I., Kahn, R., de Geus, E.J.C., Williamson, D.E., Hariri, A., van 't Ent, D., Bastin, M.E., McIntosh, A., Deary, I.J., Hulshoff pol, H.E., Blangero, J., Thompson, P.M., Glahn, D.C., Van Essen, D.C., 2015. Heritability of fractional anisotropy in human white matter: A comparison of Human Connectome Project and ENIGMA-DTI data. Neuroimage 111, 300–301. doi:10.1016/j.neuroimage.2015.02.050

Kochunov, P., Mangin, J.F., Coyle, T., Lancaster, J., Thompson, P., Rivière, D., Cointepas, Y., Régis, J., Schlosser, A., Royall, D.R., Zilles, K., Mazziotta, J., Toga, A., Fox, P.T., 2005. Age-related morphology trends of cortical sulci. Hum. Brain Mapp. 26, 210–220. doi:10.1002/hbm.20198

Kochunov, P., Thompson, P.M., Coyle, T.R., Lancaster, J.L., Kochunov, V., Royall, D., Mangin, J.F., Rivière, D., Fox, P.T., 2008. Relationship among neuroimaging indices of cerebral health during normal aging. Hum. Brain Mapp. 29, 36–45. doi:10.1002/hbm.20369

Koelkebeck, K., Miyata, J., Kubota, M., Kohl, W., Son, S., Fukuyama, H., Sawamoto, N., Takahashi, H., Murai, T., 2014. The contribution of cortical thickness and surface area to gray matter asymmetries in the healthy human brain. Hum. Brain Mapp. 35, 6011–6022. doi:10.1002/hbm.22601

Koran, M.E., Thornton-Wells, T. a, Jahanshad, N., Glahn, D.C., Thompson, P.M., Blangero, J., Nichols, T.E., Kochunov, P., Landman, B. a, 2014. Impact of family structure and common environment on heritability estimation for neuroimaging genetics studies using Sequential Oligogenic Linkage Analysis Routines. J. Med. Imaging 1, 014005. doi:10.1117/1.JMI.1.1.014005

Kostović, I., Judaš, M., 2010. The development of the subplate and thalamocortical connections in the human foetal brain. Acta Paediatr. Int. J. Paediatr. 99, 1119–1127. doi:10.1111/j.1651-2227.2010.01811.x

Koten, J.W., Wood, G., Hagoort, P., Goebel, R., Propping, P., Willmes, K., Boomsma, D.I., 2009. Genetic Contribution to Variation in Cognitive Function: An fMRI Study in Twins. Science (80-.). 323, 1737–1740. doi:10.1126/science.1167371

Krapohl, E., Rimfeld, K., Shakeshaft, N.G., Trzaskowski, M., McMillan, A., Pingault, J.-B.J.-B., Asbury, K., Harlaar, N., Kovas, Y., Dale, P.S., Plomin, R., 2014. The high heritability of educational achievement reflects many genetically influenced traits, not just intelligence. Proc. Natl. Acad. Sci. 111, 15273–15278. doi:10.1073/pnas.1408777111

Kroenke, C.D., Bayly, P. V, 2018. How Forces Fold the Cerebral Cortex. J. Neurosci. 38, 767–775. doi:10.1523/JNEUROSCI.1105-17.2017

Le Floch, É., Guillemot, V., Frouin, V., Pinel, P., Lalanne, C., Trinchera, L., Tenenhaus, A., Moreno, A., Zilbovicius, M., Bourgeron, T., Dehaene, S., Thirion, B., Poline, J.-B., Duchesnay, É., 2012. Significant correlation between a set of genetic polymorphisms and a functional brain network revealed by feature selection and sparse Partial Least Squares. Neuroimage 63, 11–24. doi:10.1016/j.neuroimage.2012.06.061

Le Guen, Y., Auzias, G., Dehaene-Lambertz, G., Leroy, F., Mangin, J.-F., Duchesnay, E., Coulon, O., Frouin, V., 2017. Regional study of the genetic influence on the sulcal pits, in: 2017 IEEE 14th International Symposium on Biomedical Imaging (ISBI 2017). IEEE, pp. 77–80. doi:10.1109/ISBI.2017.7950472

Le Guen, Y., Auzias, G., Leroy, F., Noulhiane, M., Dehaene-Lambertz, G., Duchesnay, E., Mangin, J.-F., Coulon, O., Frouin, V., 2018a. Genetic Influence on the Sulcal Pits: On the Origin of the First Cortical Folds. Cereb. Cortex 28, 1922–1933. doi:10.1093/cercor/bhx098

Le Guen, Y., Leroy, F., Auzias, G., Riviere, D., Grigis, A., Mangin, J.-F., Coulon, O., Dehaene-Lambertz, G., Frouin, V., 2018b. The chaotic morphology of the left superior temporal sulcus is genetically constrained. Neuroimage 174, 297–307. doi:10.1016/j.neuroimage.2018.03.046

Le Troter, A., Auzias, G., Coulon, O., 2012. Automatic sulcal line extraction on cortical surfaces using geodesic path density maps. Neuroimage 61, 941–949. doi:10.1016/j.neuroimage.2012.04.021

Leisman, G., Machado, C., Melillo, R., Mualem, R., 2012. Intentionality and "free-will" from a

neurodevelopmental perspective. Front. Integr. Neurosci. 6, 1–12. doi:10.3389/fnint.2012.00036
Lemaitre, H., Goldman, A.L., Sambataro, F., Verchinski, B.A., Meyer-Lindenberg, A., Weinberger, D.R., Mattay, V.S., 2012. Normal age-related brain morphometric changes: nonuniformity across cortical thickness, surface area and gray matter volume? Neurobiol. Aging 33, 617.e1-617.e9. doi:10.1016/j.neurobiolaging.2010.07.013
Leonard, L.B., 2003. Specific language impairment: Characterizing the deficits, in: Language Competence across Populations: Toward a Definition of Specific Language Impairment.
Leroy, F., Cai, Q., Bogart, S.L., Dubois, J., Coulon, O., Monzalvo, K., Fischer, C., Glasel, H., Van der Haegen, L., Bénézit, A., Lin, C.-P., Kennedy, D.N., Ihara, A.S., Hertz-Pannier, L., Moutard, M.-L., Poupon, C., Brysbaert, M., Roberts, N., Hopkins, W.D., Mangin, J.-F., Dehaene-Lambertz, G., 2015. New human-specific brain landmark: The depth asymmetry of superior temporal sulcus. Proc. Natl. Acad. Sci. 112, 1208–1213. doi:10.1073/pnas.1412389112
Leroy, F., Glasel, H., Dubois, J., Hertz-Pannier, L., Thirion, B., Mangin, J.-F., Dehaene-Lambertz, G., 2011. Early Maturation of the Linguistic Dorsal Pathway in Human Infants. J. Neurosci. 31, 1500–1506. doi:10.1523/JNEUROSCI.4141-10.2011
Li, G., Lin, W., Gilmore, J.H., Shen, D., 2015. Spatial Patterns, Longitudinal Development, and Hemispheric Asymmetries of Cortical Thickness in Infants from Birth to 2 Years of Age. J. Neurosci. 35, 9150–62. doi:10.1523/JNEUROSCI.4107-14.2015
Li, S., Jin, Z., Koirala, S., Bu, L., Xu, L., Hynes, R.O., Walsh, C.A., Corfas, G., Piao, X., 2008. GPR56 Regulates Pial Basement Membrane Integrity and Cortical Lamination. J. Neurosci. 28, 5817–5826. doi:10.1523/JNEUROSCI.0853-08.2008
Liebenthal, E., Desai, R., Ellingson, M.M., Ramachandran, B., Desai, A., Binder, J.R., 2010. Specialization along the Left Superior Temporal Sulcus for Auditory Categorization. Cereb. Cortex 20, 2958–2970. doi:10.1093/cercor/bhq045
Liu, J., Calhoun, V.D., 2014. A review of multivariate analyses in imaging genetics. Front. Neuroinform. 8, 29. doi:10.3389/fninf.2014.00029
Liu, T., Sachdev, P.S., Lipnicki, D.M., Jiang, J., Geng, G., Zhu, W., Reppermund, S., Tao, D., Trollor, J.N., Brodaty, H., Wen, W., 2013. Limited relationships between two-year changes in sulcal morphology and other common neuroimaging indices in the elderly. Neuroimage 83, 12–17. doi:10.1016/j.neuroimage.2013.06.058
Lockhart, S.N., DeCarli, C., 2014. Structural Imaging Measures of Brain Aging. Neuropsychol. Rev. 24, 271–289. doi:10.1007/s11065-014-9268-3
Lohmann, G., Von Cramon, D.Y., Colchester, A.C.F., 2008. Deep sulcal landmarks provide an organizing framework for human cortical folding. Cereb. Cortex 18, 1415–1420. doi:10.1093/cercor/bhm174
Lohmann, G., von Cramon, D.Y., Steinmetz, H., 1999. Sulcal Variability of Twins. Cereb. Cortex 9, 754–763. doi:10.1093/cercor/9.7.754
Lu, Q., Powles, R.L., Abdallah, S., Ou, D., Wang, Q., Hu, Y., Lu, Y., Liu, W., Li, B., Mukherjee, S., Crane, P.K., Zhao, H., 2017. Systematic tissue-specific functional annotation of the human genome highlights immune-related DNA elements for late-onset Alzheimer's disease. PLoS Genet. 13, 1–24. doi:10.1371/journal.pgen.1006933
Lui, J.H., Hansen, D. V., Kriegstein, A.R., 2011. Development and evolution of the human neocortex. Cell 146, 18–36. doi:10.1016/j.cell.2011.06.030
Magnotta, V. a, 1999. Quantitative In Vivo Measurement of Gyrification in the Human Brain: Changes Associated with Aging. Cereb. Cortex 9, 151–160. doi:10.1093/cercor/9.2.151
Mahmoudzadeh, M., Dehaene-Lambertz, G., Fournier, M., Kongolo, G., Goudjil, S., Dubois, J., Grebe, R., Wallois, F., 2013. Syllabic discrimination in premature human infants prior to complete formation of cortical layers. Proc. Natl. Acad. Sci. 110, 4846–4851. doi:10.1073/pnas.1212220110
Maingault, S., Tzourio-Mazoyer, N., Mazoyer, B., Crivello, F., 2016. Regional correlations between cortical thickness and surface area asymmetries: A surface-based morphometry study of 250 adults. Neuropsychologia 93, 350–364. doi:10.1016/j.neuropsychologia.2016.03.025
Mangin, J.-F., Perrot, M., Operto, G., Cachia, a., Fischer, C., Lefèvre, J., Rivière, D., 2015. Sulcus Identification and Labeling, Brain Mapping: An Encyclopedic Reference. Elsevier Inc. doi:10.1016/B978-0-12-397025-1.00307-9

Mangin, J.F., Rivière, D., Cachia, A., Duchesnay, E., Cointepas, Y., Papadopoulos-Orfanos, D., Scifo, P., Ochiai, T., Brunelle, F., Régis, J., 2004. A framework to study the cortical folding patterns. Neuroimage 23, 129–138. doi:10.1016/j.neuroimage.2004.07.019
Männel, C., Meyer, L., Wilcke, A., Boltze, J., Kirsten, H., Friederici, A.D., 2015. Working-memory endophenotype and dyslexia-associated genetic variant predict dyslexia phenotype. Cortex 71, 291–305. doi:10.1016/j.cortex.2015.06.029
Marsland, A.L., Gianaros, P.J., Kuan, D.C.H., Sheu, L.K., Krajina, K., Manuck, S.B., 2015. Brain morphology links systemic inflammation to cognitive function in midlife adults. Brain. Behav. Immun. 48, 195–204. doi:10.1016/j.bbi.2015.03.015
Mascheretti, S., De Luca, A., Trezzi, V., Peruzzo, D., Nordio, A., Marino, C., Arrigoni, F., 2017. Neurogenetics of developmental dyslexia: from genes to behavior through brain neuroimaging and cognitive and sensorial mechanisms. Transl. Psychiatry 7, e987. doi:10.1038/tp.2016.240
Masuda, K., Toda, T., Shinmyo, Y., Ebisu, H., Hoshiba, Y., Wakimoto, M., Ichikawa, Y., Kawasaki, H., 2015. Pathophysiological analyses of cortical malformation using gyrencephalic mammals. Sci. Rep. 5, 1–15. doi:10.1038/srep15370
McGeer, P.L., McGeer, E.G., 2001. Inflammation, autotoxicity and Alzheimer disease. Neurobiol. Aging 22, 799–809. doi:10.1016/S0197-4580(01)00289-5
McKay, D.R., Kochunov, P., Cykowski, M.D., Kent, J.W., Laird, A.R., Lancaster, J.L., Blangero, J., Glahn, D.C., Fox, P.T., 2013. Sulcal depth-position profile is a genetically mediated neuroscientific trait: description and characterization in the central sulcus. J. Neurosci. 33, 15618–25. doi:10.1523/JNEUROSCI.1616-13.2013
Meng, Y., Li, G., Lin, W., Gilmore, J.H., Shen, D., 2014. Spatial distribution and longitudinal development of deep cortical sulcal landmarks in infants. Neuroimage 100, 206–218. doi:10.1016/j.neuroimage.2014.06.004
Mesgarani, N., Cheung, C., Johnson, K., Chang, E.F., 2014. Phonetic Feature Encoding in Human Superior Temporal Gyrus. Science (80-.). 343, 1006–1010. doi:10.1126/science.1245994
Mitchell, J.K., 2015. The Genetic Architecture of Neurodevelopmental Disorders, in: The Genetics of Neurodevelopmental Disorders. Wiley-Blackwell, pp. 1–28. doi:10.1002/9781118524947.ch1
Mitchell, K.J., 2018. Neurogenomics - towards a more rigorous science. Eur. J. Neurosci. 47, 109–114. doi:10.1111/ejn.13801
Moerel, M., De Martino, F., Formisano, E., 2012. Processing of Natural Sounds in Human Auditory Cortex: Tonotopy, Spectral Tuning, and Relation to Voice Sensitivity. J. Neurosci. 32, 14205–14216. doi:10.1523/JNEUROSCI.1388-12.2012
Moffat, S.D., Szekely, C.A., Zonderman, A.B., Kabani, N.J., Resnick, S.M., 2000. Longitudinal change in hippocampal volume as a function of apolipoprotein E genotype. Neurology 55, 134–136. doi:10.1212/WNL.55.1.134
Moreno, A., Limousin, F., Dehaene, S., Pallier, C., 2018. Brain correlates of constituent structure in sign language comprehension. Neuroimage 167, 151–161. doi:10.1016/j.neuroimage.2017.11.040
Mota, B., Herculano-Houzel, S., 2015. Cortical folding scales universally with surface area and thickness, not number of neurons. Science (80-.). 349, 74–77. doi:10.1126/science.aaa9101
Narr, K.L., Bilder, R.M., Kim, S., Thompson, P.M., Szeszko, P., Robinson, D., Luders, E., Toga, A.W., 2004. Abnormal gyral complexity in first-episode schizophrenia. Biol. Psychiatry 55, 859–867. doi:10.1016/j.biopsych.2003.12.027
Nath, A.R., Beauchamp, M.S., 2012. A neural basis for interindividual differences in the McGurk effect, a multisensory speech illusion. Neuroimage 59, 781–787. doi:10.1016/j.neuroimage.2011.07.024
Neale, M.C., Miller, M.B., 1997. The use of likelihood-based confidence intervals in genetic models. Behav. Genet. 27, 113–120. doi:10.1023/A:1025681223921
Neville, H.J., Bavelier, D., Corina, D., Rauschecker, J., Karni, A., Lalwani, A., Braun, A., Clark, V., Jezzard, P., Turner, R., 1998. Cerebral organization for language in deaf and hearing subjects: Biological constraints and effects of experience. Proc. Natl. Acad. Sci. 95, 922–929. doi:10.1073/pnas.95.3.922
Nishikuni, K., Ribas, G.C., 2013. Study of fetal and postnatal morphological development of the brain sulci. J. Neurosurg. Pediatr. 11, 1–11. doi:10.3171/2012.9.PEDS12122

Nonaka-Kinoshita, M., Reillo, I., Artegiani, B., Ángeles Martínez-Martínez, M., Nelson, M., Borrell, V., Calegari, F., 2013. Regulation of cerebral cortex size and folding by expansion of basal progenitors. EMBO J. 32, 1817–1828. doi:10.1038/emboj.2013.96

Ochiai, T., Grimault, S., Scavarda, D., Roch, G., Hori, T., Rivière, D., Mangin, J.-F., Régis, J., 2004. Sulcal pattern and morphology of the superior temporal sulcus. Neuroimage 22, 706–719. doi:10.1016/j.neuroimage.2004.01.023

Ocklenburg, S., Arning, L., Gerding, W.M., Epplen, J.T., Güntürkün, O., Beste, C., 2013. FOXP2 variation modulates functional hemispheric asymmetries for speech perception. Brain Lang. 126, 279–284. doi:10.1016/j.bandl.2013.07.001

Ono, M., Kubik, S., Abernathey, C., 1990. Atlas of the Cerebral Sulci. Georg Thieme Verlag, Stuggart.

Pallier, C., Devauchelle, A.-D., Dehaene, S., 2011. Cortical representation of the constituent structure of sentences. Proc. Natl. Acad. Sci. 108, 2522–2527. doi:10.1073/pnas.1018711108

Paulesu, E., Perani, D., Blasi, V., Silani, G., Borghese, N. a, De Giovanni, U., Sensolo, S., Fazio, F., 2003. A Functional-Anatomical Model for Lipreading. J. Neurophysiol. 90, 2005–2013. doi:10.1152/jn.00926.2002

Paus, T.T., Tomaiuolo, F., Otaky, N.N., Petrides, M., Atlas, J., Morris, R., Evans, A.C., MacDonald, D., 1996. Human cingulate and paracingulate sulci: Pattern, variability, asymmetry and probabilistic map. Cereb. Cortex 6, 207–214. doi:10.1093/cercor/6.2.207

Pelphrey, K.A., Viola, R.J., McCarthy, G., 2004. When strangers pass: processing of mutual and averted social gaze in the superior temporal sulcus. Psychol. Sci. 15, 598–603. doi:10.1111/j.0956-7976.2004.00726.x

Peper, J.S., Brouwer, R.M., Boomsma, D.I., Kahn, R.S., Hulshoff Pol, H.E., 2007. Genetic influences on human brain structure: A review of brain imaging studies in twins. Hum. Brain Mapp. 28, 464–473. doi:10.1002/hbm.20398

Perrot, M., Rivière, D., Mangin, J.-F., 2011. Cortical sulci recognition and spatial normalization. Med. Image Anal. 15, 529–50. doi:10.1016/j.media.2011.02.008

Peterson, R.L., Pennington, B.F., 2012. Developmental dyslexia. Lancet 379, 1997–2007. doi:10.1016/S0140-6736(12)60198-6

Piao, X., Hill, R.S., Bodell, A., Chang, B.S., Basel-Vanagaite, L., Straussberg, R., Dobyns, W.B., Qasrawi, B., Winter, R.M., Innes, A.M., Voit, T., Ross, M.E., Michaud, J.L., Déscarie, J.-C., Barkovich, A.J., Walsh, C.A., 2004. G Protein-Coupled Receptor-Dependent Development of Human Frontal Cortex. Science (80-.). 303, 2033–2036. doi:10.1126/science.1092780

Pinel, P., Dehaene, S., 2013. Genetic and environmental contributions to brain activation during calculation. Neuroimage 81, 306–316. doi:10.1016/j.neuroimage.2013.04.118

Pinel, P., Dehaene, S., 2010. Beyond hemispheric dominance: brain regions underlying the joint lateralization of language and arithmetic to the left hemisphere. J. Cogn. Neurosci. 22, 48–66. doi:10.1162/jocn.2009.21184

Pinel, P., Fauchereau, F., Moreno, A., Barbot, A., Lathrop, M., Zelenika, D., Le Bihan, D., Poline, J.-B., Bourgeron, T., Dehaene, S., 2012. Genetic Variants of FOXP2 and KIAA0319/TTRAP/THEM2 Locus Are Associated with Altered Brain Activation in Distinct Language-Related Regions. J. Neurosci. 32, 817–825. doi:10.1523/JNEUROSCI.5996-10.2012

Pinel, P., Lalanne, C., Bourgeron, T., Fauchereau, F., Poupon, C., Artiges, E., Le Bihan, D., Dehaene-Lambertz, G., Dehaene, S., 2015. Genetic and environmental influences on the visual word form and fusiform face areas. Cereb. Cortex 25, 2478–2493. doi:10.1093/cercor/bhu048

Plomin, R., Deary, I.J., 2015. Genetics and intelligence differences: five special findings. Mol. Psychiatry 20, 98–108. doi:10.1038/mp.2014.105

Polderman, T.J.C., Benyamin, B., de Leeuw, C.A., Sullivan, P.F., van Bochoven, A., Visscher, P.M., Posthuma, D., 2015. Meta-analysis of the heritability of human traits based on fifty years of twin studies. Nat. Genet. 47, 702–9. doi:10.1038/ng.3285

Poluch, S., Juliano, S.L., 2015. Fine-tuning of neurogenesis is essential for the evolutionary expansion of the cerebral cortex. Cereb. Cortex 25, 346–364. doi:10.1093/cercor/bht232

Powell, H.W.R., Parker, G.J.M., Alexander, D.C., Symms, M.R., Boulby, P.A., Wheeler-Kingshott, C.A.M., Barker, G.J., Noppeney, U., Koepp, M.J., Duncan, J.S., 2006. Hemispheric asymmetries in language-related pathways: A combined functional MRI and tractography study. Neuroimage

32, 388–399. doi:10.1016/j.neuroimage.2006.03.011
Price, G., Ansari, D., 2013. Dyscalculia: Characteristics, Causes, and Treatments. Numeracy 6. doi:10.5038/1936-4660.6.1.2
Price, G.R., Holloway, I., Räsänen, P., Vesterinen, M., Ansari, D., 2007. Impaired parietal magnitude processing in developmental dyscalculia. Curr. Biol. 17, 1042–1043. doi:10.1016/j.cub.2007.10.013
Price, G.R., Mazzocco, M.M.M., Ansari, D., 2013. Why Mental Arithmetic Counts: Brain Activation during Single Digit Arithmetic Predicts High School Math Scores. J. Neurosci. 33, 156–163. doi:10.1523/JNEUROSCI.2936-12.2013
Pruim, R.J., Welch, R.P., Sanna, S., Teslovich, T.M., Chines, P.S., Gliedt, T.P., Boehnke, M., Abecasis, G.R., Willer, C.J., Frishman, D., 2011. LocusZoom: Regional visualization of genome-wide association scan results. Bioinformatics 27, 2336–2337. doi:10.1093/bioinformatics/btq419
Psaty, B.M., O'Donnell, C.J., Gudnason, V., Lunetta, K.L., Folsom, A.R., Rotter, J.I., Uitterlinden, A.G., Harris, T.B., Witteman, J.C.M., Boerwinkle, E., 2009. Cohorts for Heart and Aging Research in Genomic Epidemiology (CHARGE) Consortium design of prospective meta-analyses of genome-wide association studies from 5 Cohorts. Circ. Cardiovasc. Genet. 2, 73–80. doi:10.1161/CIRCGENETICS.108.829747
Pujol, J., Deus, J., Losilla, J.M., Capdevila, A., 1999. Cerebral lateralization of language in normal left-handed people studied by functional MRI. Neurology 52, 1038–1038. doi:10.1212/WNL.52.5.1038
Purcell, S., Neale, B., Todd-Brown, K., Thomas, L., Ferreira, M.A.R., Bender, D., Maller, J., Sklar, P., de Bakker, P.I.W., Daly, M.J., Sham, P.C., 2007. PLINK: A Tool Set for Whole-Genome Association and Population-Based Linkage Analyses. Am. J. Hum. Genet. 81, 559–575. doi:10.1086/519795
Rakic, P., 2007. The radial edifice of cortical architecture: From neuronal silhouettes to genetic engineering. Brain Res. Rev. 55, 204–219. doi:10.1016/j.brainresrev.2007.02.010
Rakic, P., 1995. Radial versus tangential migration of neuronal clones in the developing cerebral cortex. Proc. Natl. Acad. Sci. U. S. A. 92, 11323–11327. doi:10.1073/pnas.92.25.11323
Rakic, P., 1988. Specification of cerebral cortical areas. Science (80-.). 241, 170–176. doi:10.1126/science.3291116
Rash, B.G., Rakic, P., 2014. Genetic Resolutions of Brain Convolutions. Science (80-.). 343, 744–745. doi:10.1126/science.1250246
Rash, B.G., Tomasi, S., Lim, H.D., Suh, C.Y., Vaccarino, F.M., 2013. Cortical Gyrification Induced by Fibroblast Growth Factor 2 in the Mouse Brain. J. Neurosci. 33, 10802–10814. doi:10.1523/JNEUROSCI.3621-12.2013
Raz, N., Lindenberger, U., Rodrigue, K.M., Kennedy, K.M., Head, D., Williamson, A., Dahle, C., Gerstorf, D., Acker, J.D., 2005. Regional brain changes in aging healthy adults: General trends, individual differences and modifiers. Cereb. Cortex 15, 1676–1689. doi:10.1093/cercor/bhi044
Raz, N., Rodrigue, K.M., 2006. Differential aging of the brain: Patterns, cognitive correlates and modifiers. Neurosci. Biobehav. Rev. 30, 730–748. doi:10.1016/j.neubiorev.2006.07.001
Redcay, E., Velnoskey, K.R., Rowe, M.L., 2016. Perceived communicative intent in gesture and language modulates the superior temporal sulcus. Hum. Brain Mapp. 37, 3444–3461. doi:10.1002/hbm.23251
Régis, J., Mangin, J.-F., Ochiai, T., Frouin, V., Riviére, D., Cachia, A., Tamura, M., Samson, Y., 2005. "Sulcal root" generic model: a hypothesis to overcome the variability of the human cortex folding patterns. Neurol. Med. Chir. (Tokyo). 45, 1–17. doi:10.2176/nmc.45.1
Reillo, I., De Juan Romero, C., García-Cabezas, M.Á., Borrell, V., 2011. A Role for intermediate radial glia in the tangential expansion of the mammalian cerebral cortex. Cereb. Cortex 21, 1674–1694. doi:10.1093/cercor/bhq238
Rettmann, M.E., Han, X., Xu, C., Prince, J.L., 2002. Automated Sulcal Segmentation Using Watersheds on the Cortical Surface. Neuroimage 15, 329–344. doi:10.1006/nimg.2001.0975
Ribas, G.C., 2010. The cerebral sulci and gyri. Neurosurg. Focus 28, E2. doi:10.3171/2009.11.FOCUS09245
Richman, D., Stewart, R., Hutchinson, J., Caviness, V.J., 1975. Mechanical model of brain convolutional development. Science (80-.). 189, 18–21. doi:10.1126/science.1135626

Rickard, T.., Romero, S.., Basso, G., Wharton, C., Flitman, S., Grafman, J., 2000. The calculating brain: an fMRI study. Neuropsychologia 38, 325–335. doi:10.1016/S0028-3932(99)00068-8
Rimfeld, K., Kovas, Y., Dale, P.S., Plomin, R., 2015. Pleiotropy across academic subjects at the end of compulsory education. Sci. Rep. 5, 11713. doi:10.1038/srep11713
Ringo, J.L., Doty, R.W., Demeter, S., Simard, P.Y., 1994. Time Is of the Essence: A Conjecture that Hemispheric Specialization Arises from Interhemispheric Conduction Delay. Cereb. Cortex 4, 331–343. doi:https://doi.org/10.1093/cercor/4.4.331
Rivière, D., Geffroy, D., Denghien, I., Souedet, N., Cointepas, Y., 2009. BrainVISA: an extensible software environment for sharing multimodal neuroimaging data and processing tools. Neuroimage 47, S163. doi:10.1016/S1053-8119(09)71720-3
Robinson, E.C., Jbabdi, S., Glasser, M.F., Andersson, J., Burgess, G.C., Harms, M.P., Smith, S.M., Van Essen, D.C., Jenkinson, M., 2014. MSM: A new flexible framework for multimodal surface matching. Neuroimage 100, 414–426. doi:10.1016/j.neuroimage.2014.05.069
Rogers, J., Kochunov, P., Zilles, K., Shelledy, W., Lancaster, J., Thompson, P., Duggirala, R., Blangero, J., Fox, P.T., Glahn, D.C., 2010. On the genetic architecture of cortical folding and brain volume in primates. Neuroimage 53, 1103–1108. doi:10.1016/j.neuroimage.2010.02.020
Ronan, L., Fletcher, P.C., 2014. From genes to folds: a review of cortical gyrification theory. Brain Struct. Funct. 220, 2475–2483. doi:10.1007/s00429-014-0961-z
Ronan, L., Voets, N., Rua, C., Alexander-Bloch, A., Hough, M., Mackay, C., Crow, T.J., James, A., Giedd, J.N., Fletcher, P.C., 2014. Differential tangential expansion as a mechanism for cortical gyrification. Cereb. Cortex 24, 2219–2228. doi:10.1093/cercor/bht082
Sarnat, H.B., Netsky, M.G., 1981. Evolution of the Nervous System. Oxford University Press, New York.
Schachter, S.C., Ransil, B.J., Geschwind, N., 1987. Associations of handedness with hair color and learning disabilities. Neuropsychologia 25, 269–276. doi:10.1016/0028-3932(87)90137-0
Schweizer, R., Helms, G., Frahm, J., 2014. Revisiting a historic human brain with magnetic resonance imaging - the first description of a divided central sulcus. Front. Neuroanat. 8, 35. doi:10.3389/fnana.2014.00035
Selzam, S., Krapohl, E., Von Stumm, S., O'Reilly, P.F., Rimfeld, K., Kovas, Y., Dale, P.S., Lee, J.J., Plomin, R., 2017. Predicting educational achievement from DNA. Mol. Psychiatry 22, 267–272. doi:10.1038/mp.2016.107
Shakeshaft, N.G., Trzaskowski, M., McMillan, A., Rimfeld, K., Krapohl, E., Haworth, C.M. a, Dale, P.S., Plomin, R., 2013. Strong Genetic Influence on a UK Nationwide Test of Educational Achievement at the End of Compulsory Education at Age 16. PLoS One 8, e80341. doi:10.1371/journal.pone.0080341
Shattuck, D.W., Joshi, A. a., Pantazis, D., Kan, E., Dutton, R. a., Sowell, E.R., Thompson, P.M., Toga, A.W., Leahy, R.M., 2009. Semi-automated method for delineation of landmarks on models of the cerebral cortex. J. Neurosci. Methods 178, 385–392. doi:10.1016/j.jneumeth.2008.12.025
Shen, X., Liu, T., Tao, D., Fan, Y., Zhang, J., Li, S., Jiang, J., Zhu, W., Wang, Y., Wang, Y., Brodaty, H., Sachdev, P., Wen, W., 2018. Variation in longitudinal trajectories of cortical sulci in normal elderly. Neuroimage 166, 1–9. doi:10.1016/j.neuroimage.2017.10.010
Shinmyo, Y., Terashita, Y., Dinh Duong, T.A., Horiike, T., Kawasumi, M., Hosomichi, K., Tajima, A., Kawasaki, H., 2017. Folding of the Cerebral Cortex Requires Cdk5 in Upper-Layer Neurons in Gyrencephalic Mammals. Cell Rep. 20, 2131–2143. doi:10.1016/j.celrep.2017.08.024
Simmonds, D.J., Pekar, J.J., Mostofsky, S.H., 2008. Meta-analysis of Go/No-go tasks demonstrating that fMRI activation associated with response inhibition is task-dependent. Neuropsychologia 46, 224–232. doi:10.1016/j.neuropsychologia.2007.07.015
Skeide, M.A., Brauer, J., Friederici, A.D., 2016. Brain Functional and Structural Predictors of Language Performance. Cereb. Cortex 26, 2127–2139. doi:10.1093/cercor/bhv042
Skeide, M.A., Friederici, A.D., 2016. The ontogeny of the cortical language network. Nat. Rev. Neurosci. 17, 323–332. doi:10.1038/nrn.2016.23
Skeide, M.A., Kirsten, H., Kraft, I., Schaadt, G., M??ller, B., Neef, N., Brauer, J., Wilcke, A., Emmrich, F., Boltze, J., Friederici, A.D., 2015. Genetic dyslexia risk variant is related to neural connectivity patterns underlying phonological awareness in children. Neuroimage 118, 414–421. doi:10.1016/j.neuroimage.2015.06.024

Sniekers, S., Stringer, S., Watanabe, K., Jansen, P.R., Coleman, J.R.I., Krapohl, E., Taskesen, E., Hammerschlag, A.R., Okbay, A., Zabaneh, D., Amin, N., Breen, G., Cesarini, D., Chabris, C.F., Iacono, W.G., Ikram, M.A., Johannesson, M., Koellinger, P., Lee, J.J., Magnusson, P.K.E., McGue, M., Miller, M.B., Ollier, W.E.R., Payton, A., Pendleton, N., Plomin, R., Rietveld, C.A., Tiemeier, H., van Duijn, C.M., Posthuma, D., 2017. Genome-wide association meta-analysis of 78,308 individuals identifies new loci and genes influencing human intelligence. Nat. Genet. 49, 1107–1112. doi:10.1038/ng.3869

Specht, K., Wigglesworth, P., 2018. The functional and structural asymmetries of the superior temporal sulcus. Scand. J. Psychol. 59, 74–82. doi:10.1111/sjop.12410

Springer, J.A., Binder, J.R., Hammeke, T.A., Swanson, S.J., Frost, J.A., Bellgowan, P.S.F., Brewer, C.C., Perry, H.M., Morris, G.L., Mueller, W.M., 1999. Language dominance in neurologically normal and epilepsy subjects. A functional MRI study. Brain 122, 2033–2045. doi:10.1093/brain/122.11.2033

Stahl, R., Walcher, T., De Juan Romero, C., Pilz, G.A., Cappello, S., Irmler, M., Sanz-Aquela, J.M., Beckers, J., Blum, R., Borrell, V., Götz, M., 2013. Trnp1 regulates expansion and folding of the mammalian cerebral cortex by control of radial glial fate. Cell 153, 535–549. doi:10.1016/j.cell.2013.03.027

Stein, J.L., Medland, S.E., Vasquez, A.A., Hibar, D.P., Senstad, R.E., Winkler, A.M., Toro, R., Appel, K., Bartecek, R., Bergmann, Ø., Bernard, M., Brown, A. a, Cannon, D.M., Chakravarty, M.M., Christoforou, A., Domin, M., Grimm, O., Hollinshead, M., Holmes, A.J., Homuth, G., Hottenga, J.-J., Langan, C., Lopez, L.M., Hansell, N.K., Hwang, K.S., Kim, S., Laje, G., Lee, P.H., Liu, X., Loth, E., Lourdusamy, A., Mattingsdal, M., Mohnke, S., Maniega, S.M., Nho, K., Nugent, A.C., O'Brien, C., Papmeyer, M., Pütz, B., Ramasamy, A., Rasmussen, J., Rijpkema, M., Risacher, S.L., Roddey, J.C., Rose, E.J., Ryten, M., Shen, L., Sprooten, E., Strengman, E., Teumer, A., Trabzuni, D., Turner, J., van Eijk, K., van Erp, T.G.M., van Tol, M.-J., Wittfeld, K., Wolf, C., Woudstra, S., Aleman, A., Alhusaini, S., Almasy, L., Binder, E.B., Brohawn, D.G., Cantor, R.M., Carless, M. a, Corvin, A., Czisch, M., Curran, J.E., Davies, G., de Almeida, M. a a, Delanty, N., Depondt, C., Duggirala, R., Dyer, T.D., Erk, S., Fagerness, J., Fox, P.T., Freimer, N.B., Gill, M., Göring, H.H.H., Hagler, D.J., Hoehn, D., Holsboer, F., Hoogman, M., Hosten, N., Jahanshad, N., Johnson, M.P., Kasperaviciute, D., Kent, J.W., Kochunov, P., Lancaster, J.L., Lawrie, S.M., Liewald, D.C., Mandl, R., Matarin, M., Mattheisen, M., Meisenzahl, E., Melle, I., Moses, E.K., Mühleisen, T.W., Nauck, M., Nöthen, M.M., Olvera, R.L., Pandolfo, M., Pike, G.B., Puls, R., Reinvang, I., Rentería, M.E., Rietschel, M., Roffman, J.L., Royle, N. a, Rujescu, D., Savitz, J., Schnack, H.G., Schnell, K., Seiferth, N., Smith, C., Steen, V.M., Valdés Hernández, M.C., Van den Heuvel, M., van der Wee, N.J., Van Haren, N.E.M., Veltman, J.A., Völzke, H., Walker, R., Westlye, L.T., Whelan, C.D., Agartz, I., Boomsma, D.I., Cavalleri, G.L., Dale, A.M., Djurovic, S., Drevets, W.C., Hagoort, P., Hall, J., Heinz, A., Jack, C.R., Foroud, T.M., Le Hellard, S., Macciardi, F., Montgomery, G.W., Poline, J.B., Porteous, D.J., Sisodiya, S.M., Starr, J.M., Sussmann, J., Toga, A.W., Veltman, D.J., Walter, H., Weiner, M.W., Bis, J.C., Ikram, M.A., Smith, A. V, Gudnason, V., Tzourio, C., Vernooij, M.W., Launer, L.J., DeCarli, C., Seshadri, S., Andreassen, O. a, Apostolova, L.G., Bastin, M.E., Blangero, J., Brunner, H.G., Buckner, R.L., Cichon, S., Coppola, G., de Zubicaray, G.I., Deary, I.J., Donohoe, G., de Geus, E.J.C., Espeseth, T., Fernández, G., Glahn, D.C., Grabe, H.J., Hardy, J., Hulshoff Pol, H.E., Jenkinson, M., Kahn, R.S., McDonald, C., McIntosh, A.M., McMahon, F.J., McMahon, K.L., Meyer-Lindenberg, A., Morris, D.W., Müller-Myhsok, B., Nichols, T.E., Ophoff, R. a, Paus, T., Pausova, Z., Penninx, B.W., Potkin, S.G., Sämann, P.G., Saykin, A.J., Schumann, G., Smoller, J.W., Wardlaw, J.M., Weale, M.E., Martin, N.G., Franke, B., Wright, M.J., Thompson, P.M., 2012. Identification of common variants associated with human hippocampal and intracranial volumes. Nat. Genet. 44, 552–561. doi:10.1038/ng.2250

Sun, T., Walsh, C. a, 2006. Molecular approaches to brain asymmetry and handedness. Nat. Rev. Neurosci. 7, 655–662. doi:10.1038/nrn1930

Sun, Z.Y., Pinel, P., Rivière, D., Moreno, A., Dehaene, S., Mangin, J.-F., 2016. Linking morphological and functional variability in hand movement and silent reading. Brain Struct. Funct. 221, 3361–3371. doi:10.1007/s00429-015-1106-8

Symonds, L.L., Archibald, S.L., Grant, I., Zisook, S., Jernigan, T.L., 1999. Does an Increase in Sulcal

or Ventricular Fluid Predict Where Brain Tissue Is Lost? J. Neuroimaging 9, 201–209. doi:10.1111/jon199994201
Tallinen, T., Chung, J.Y., Biggins, J.S., Mahadevan, L., 2014. Gyrification from constrained cortical expansion. Proc. Natl. Acad. Sci. 111, 12667–12672. doi:10.1073/pnas.1406015111
Tallinen, T., Chung, J.Y., Rousseau, F., Girard, N., Lefèvre, J., Mahadevan, L., 2016. On the growth and form of cortical convolutions. Nat. Phys. 12, 588–593. doi:10.1038/nphys3632
Taylor, K.R., Holzer, A.K., Bazan, J.F., Walsh, C.A., Gleeson, J.G., 2000. Patient mutations in doublecortin define a repeated tubulin-binding domain. J. Biol. Chem. 275, 34442–34450. doi:10.1074/jbc.M007078200
Thompson, P.M., Gledd, J.N., Woods, R.P., MacDonald, D., Evans, A.C., Toga, A.W., 2000. Growth patterns in the developing brain detected by using continuum mechanical tensor maps. Nature 404, 190–193. doi:10.1038/35004593
Thompson, P.M., Stein, J.L., Medland, S.E., Hibar, D.P., Vasquez, A.A., Renteria, M.E., Toro, R., Jahanshad, N., Schumann, G., Franke, B., Wright, M.J., Martin, N.G., Agartz, I., Alda, M., Alhusaini, S., Almasy, L., Almeida, J., Alpert, K., Andreasen, N.C., Andreassen, O.A., Apostolova, L.G., Appel, K., Armstrong, N.J., Aribisala, B., Bastin, M.E., Bauer, M., Bearden, C.E., Bergmann, Ø., Binder, E.B., Blangero, J., Bockholt, H.J., Bøen, E., Bois, C., Boomsma, D.I., Booth, T., Bowman, I.J., Bralten, J., Brouwer, R.M., Brunner, H.G., Brohawn, D.G., Buckner, R.L., Buitelaar, J., Bulayeva, K., Bustillo, J.R., Calhoun, V.D., Cannon, D.M., Cantor, R.M., Carless, M.A., Caseras, X., Cavalleri, G.L., Chakravarty, M.M., Chang, K.D., Ching, C.R.K., Christoforou, A., Cichon, S., Clark, V.P., Conrod, P., Coppola, G., Crespo-Facorro, B., Curran, J.E., Czisch, M., Deary, I.J., de Geus, E.J.C., den Braber, A., Delvecchio, G., Depondt, C., de Haan, L., de Zubicaray, G.I., Dima, D., Dimitrova, R., Djurovic, S., Dong, H., Donohoe, G., Duggirala, R., Dyer, T.D., Ehrlich, S., Ekman, C.J., Elvsåshagen, T., Emsell, L., Erk, S., Espeseth, T., Fagerness, J., Fears, S., Fedko, I., Fernández, G., Fisher, S.E., Foroud, T., Fox, P.T., Francks, C., Frangou, S., Frey, E.M., Frodl, T., Frouin, V., Garavan, H., Giddaluru, S., Glahn, D.C., Godlewska, B., Goldstein, R.Z., Gollub, R.L., Grabe, H.J., Grimm, O., Gruber, O., Guadalupe, T., Gur, R.E., Gur, R.C., Göring, H.H.H., Hagenaars, S., Hajek, T., Hall, G.B., Hall, J., Hardy, J., Hartman, C.A., Hass, J., Hatton, S.N., Haukvik, U.K., Hegenscheid, K., Heinz, A., Hickie, I.B., Ho, B.C., Hoehn, D., Hoekstra, P.J., Hollinshead, M., Holmes, A.J., Homuth, G., Hoogman, M., Hong, L.E., Hosten, N., Hottenga, J.J., Hulshoff Pol, H.E., Hwang, K.S., Jack, C.R., Jenkinson, M., Johnston, C., Jönsson, E.G., Kahn, R.S., Kasperaviciute, D., Kelly, S., Kim, S., Kochunov, P., Koenders, L., Krämer, B., Kwok, J.B.J., Lagopoulos, J., Laje, G., Landen, M., Landman, B.A., Lauriello, J., Lawrie, S.M., Lee, P.H., Le Hellard, S., Lemaître, H., Leonardo, C.D., Li, C. shan, Liberg, B., Liewald, D.C., Liu, X., Lopez, L.M., Loth, E., Lourdusamy, A., Luciano, M., Macciardi, F., Machielsen, M.W.J., MacQueen, G.M., Malt, U.F., Mandl, R., Manoach, D.S., Martinot, J.L., Matarin, M., Mather, K.A., Mattheisen, M., Mattingsdal, M., Meyer-Lindenberg, A., McDonald, C., McIntosh, A.M., McMahon, F.J., McMahon, K.L., Meisenzahl, E., Melle, I., Milaneschi, Y., Mohnke, S., Montgomery, G.W., Morris, D.W., Moses, E.K., Mueller, B.A., Muñoz Maniega, S., Mühleisen, T.W., Müller-Myhsok, B., Mwangi, B., Nauck, M., Nho, K., Nichols, T.E., Nilsson, L.G., Nugent, A.C., Nyberg, L., Olvera, R.L., Oosterlaan, J., Ophoff, R.A., Pandolfo, M., Papalampropoulou-Tsiridou, M., Papmeyer, M., Paus, T., Pausova, Z., Pearlson, G.D., Penninx, B.W., Peterson, C.P., Pfennig, A., Phillips, M., Pike, G.B., Poline, J.B., Potkin, S.G., Pütz, B., Ramasamy, A., Rasmussen, J., Rietschel, M., Rijpkema, M., Risacher, S.L., Roffman, J.L., Roiz-Santiañez, R., Romanczuk-Seiferth, N., Rose, E.J., Royle, N.A., Rujescu, D., Ryten, M., Sachdev, P.S., Salami, A., Satterthwaite, T.D., Savitz, J., Saykin, A.J., Scanlon, C., Schmaal, L., Schnack, H.G., Schork, A.J., Schulz, S.C., Schür, R., Seidman, L., Shen, L., Shoemaker, J.M., Simmons, A., Sisodiya, S.M., Smith, C., Smoller, J.W., Soares, J.C., Sponheim, S.R., Sprooten, E., Starr, J.M., Steen, V.M., Strakowski, S., Strike, L., Sussmann, J., Sämann, P.G., Teumer, A., Toga, A.W., Tordesillas-Gutierrez, D., Trabzuni, D., Trost, S., Turner, J., Van den Heuvel, M., van der Wee, N.J., van Eijk, K., van Erp, T.G.M., van Haren, N.E.M., van 't Ent, D., van Tol, M.J., Valdés Hernández, M.C., Veltman, D.J., Versace, A., Völzke, H., Walker, R., Walter, H., Wang, L., Wardlaw, J.M., Weale, M.E., Weiner, M.W., Wen, W., Westlye, L.T., Whalley, H.C., Whelan, C.D., White, T., Winkler, A.M., Wittfeld, K., Woldehawariat, G., Wolf, C., Zilles, D., Zwiers, M.P., Thalamuthu, A., Schofield, P.R., Freimer,

N.B., Lawrence, N.S., Drevets, W., 2014. The ENIGMA Consortium: Large-scale collaborative analyses of neuroimaging and genetic data. Brain Imaging Behav. 8, 153–182. doi:10.1007/s11682-013-9269-5
Toga, A.W., Thompson, P.M., 2003. Mapping brain asymmetry. Nat. Rev. Neurosci. 4, 37–48. doi:10.1038/nrn1009
Torii, M., Hashimoto-Torii, K., Levitt, P., Rakic, P., 2009. Integration of neuronal clones in the radial cortical columns by EphA and ephrin-A signalling. Nature 461, 524–528. doi:10.1038/nature08362
Toro, R., Burnod, Y., 2005. A morphogenetic model for the development of cortical convolutions. Cereb. Cortex 15, 1900–1913. doi:10.1093/cercor/bhi068
Toro, R., Perron, M., Pike, B., Richer, L., Veillette, S., Pausova, Z., Paus, T., 2008. Brain size and folding of the human cerebral cortex. Cereb. Cortex 18, 2352–2357. doi:10.1093/cercor/bhm261
Toro, R., Poline, J.-B., Huguet, G., Loth, E., Frouin, V., Banaschewski, T., Barker, G.J., Bokde, A., B?chel, C., Carvalho, F.M., Conrod, P., Fauth-B?hler, M., Flor, H., Gallinat, J., Garavan, H., Gowland, P., Heinz, A., Ittermann, B., Lawrence, C., Lema?tre, H., Mann, K., Nees, F., Paus, T., Pausova, Z., Rietschel, M., Robbins, T., Smolka, M.N., Str?hle, A., Schumann, G., Bourgeron, T., 2015. Genomic architecture of human neuroanatomical diversity. Mol. Psychiatry 20, 1011–1016. doi:10.1038/mp.2014.99
Trampush, J.W., Yang, M.L.Z., Yu, J., Knowles, E., Davies, G., Liewald, D.C., Starr, J.M., Djurovic, S., Melle, I., Sundet, K., Christoforou, A., Reinvang, I., DeRosse, P., Lundervold, A.J., Steen, V.M., Espeseth, T., Räikkönen, K., Widen, E., Palotie, A., Eriksson, J.G., Giegling, I., Konte, B., Roussos, P., Giakoumaki, S., Burdick, K.E., Payton, A., Ollier, W., Horan, M., Chiba-Falek, O., Attix, D.K., Need, A.C., Cirulli, E.T., Voineskos, A.N., Stefanis, N.C., Avramopoulos, D., Hatzimanolis, A., Arking, D.E., Smyrnis, N., Bilder, R.M., Freimer, N.A., Cannon, T.D., London, E., Poldrack, R.A., Sabb, F.W., Congdon, E., Conley, E.D., Scult, M.A., Dickinson, D., Straub, R.E., Donohoe, G., Morris, D., Corvin, A., Gill, M., Hariri, A.R., Weinberger, D.R., Pendleton, N., Bitsios, P., Rujescu, D., Lahti, J., Le Hellard, S., Keller, M.C., Andreassen, O.A., Deary, I.J., Glahn, D.C., Malhotra, A.K., Lencz, T., 2017. GWAS meta-analysis reveals novel loci and genetic correlates for general cognitive function: a report from the COGENT consortium. Mol. Psychiatry 22, 336–345. doi:10.1038/mp.2016.244
Turken, A.U., Dronkers, N.F., 2011. The Neural Architecture of the Language Comprehension Network: Converging Evidence from Lesion and Connectivity Analyses. Front. Syst. Neurosci. 5, 1–20. doi:10.3389/fnsys.2011.00001
van der Lely, H.K.J., Pinker, S., 2014. The biological basis of language: Insight from developmental grammatical impairments. Trends Cogn. Sci. 18, 586–595. doi:10.1016/j.tics.2014.07.001
Van Essen, D.C., 2005. A Population-Average, Landmark- and Surface-based (PALS) atlas of human cerebral cortex. Neuroimage 28, 635–662. doi:10.1016/j.neuroimage.2005.06.058
Van Essen, D.C., 1997. A tension-based theory of morphogenesis and compact wiring in the central nervous system. Nature 385, 313–8. doi:10.1038/385313a0
Van Essen, D.C., Ugurbil, K., Auerbach, E., Barch, D., Behrens, T.E.J., Bucholz, R., Chang, A., Chen, L., Corbetta, M., Curtiss, S.W., Della Penna, S., Feinberg, D., Glasser, M.F., Harel, N., Heath, A.C., Larson-Prior, L., Marcus, D., Michalareas, G., Moeller, S., Oostenveld, R., Petersen, S.E., Prior, F., Schlaggar, B.L., Smith, S.M., Snyder, A.Z., Xu, J., Yacoub, E., 2012. The Human Connectome Project: A data acquisition perspective. Neuroimage 62, 2222–2231. doi:10.1016/j.neuroimage.2012.02.018
van Ettinger-Veenstra, H.M., Ragnehed, M., Hällgren, M., Karlsson, T., Landtblom, A.M., Lundberg, P., Engström, M., 2010. Right-hemispheric brain activation correlates to language performance. Neuroimage 49, 3481–3488. doi:10.1016/j.neuroimage.2009.10.041
Vargha-Khadem, F., Watkins, K., Alcock, K., Fletcher, P., Passingham, R., 1995. Praxic and nonverbal cognitive deficits in a large family with a genetically transmitted speech and language disorder. Proc. Natl. Acad. Sci. U. S. A. 92, 930–3. doi:http://www.pnas.org/content/92/3/930
Vernes, S.C., Fisher, S.E., 2013. Genetic Pathways Implicated in Speech and Language, in: Helekar, S.A. (Ed.), Animal Models of Speech and Language Disorders. Springer New York, New York, NY, pp. 13–40.
Visscher, P.M., Hemani, G., Vinkhuyzen, A. a E., Chen, G.-B., Lee, S.H., Wray, N.R., Goddard,

M.E., Yang, J., 2014. Statistical power to detect genetic (co) variance of complex traits using SNP data in unrelated samples. PLoS Genet. 10, e1004269. doi:10.1371/journal.pgen.1004269
Visscher, P.M., Wray, N.R., Zhang, Q., Sklar, P., McCarthy, M.I., Brown, M.A., Yang, J., 2017. 10 Years of GWAS Discovery: Biology, Function, and Translation. Am. J. Hum. Genet. 101, 5–22. doi:10.1016/j.ajhg.2017.06.005
Vogel, S.E., Goffin, C., Ansari, D., 2015. Developmental specialization of the left parietal cortex for the semantic representation of Arabic numerals: An fMR-adaptation study. Dev. Cogn. Neurosci. 12, 61–73. doi:10.1016/j.dcn.2014.12.001
Vounou, M., Nichols, T.E., Montana, G., 2010. Discovering genetic associations with high-dimensional neuroimaging phenotypes: A sparse reduced-rank regression approach. Neuroimage 53, 1147–1159. doi:10.1016/j.neuroimage.2010.07.002
Wang, L., Hou, S., Han, Y.G., 2016. Hedgehog signaling promotes basal progenitor expansion and the growth and folding of the neocortex. Nat. Neurosci. 19, 888–896. doi:10.1038/nn.4307
Wang, W., Liu, D., Xiao, Q., Cai, J., Feng, N., Xu, S., Wang, L., Yin, D., Wang, X., 2018. Lig4-4 selectively inhibits TREK-1 and plays potent neuroprotective roles in vitro and in rat MCAO model. Neurosci. Lett. 671, 93–98. doi:10.1016/j.neulet.2018.02.015
Watanabe, K., Taskesen, E., Van Bochoven, A., Posthuma, D., 2017. Functional mapping and annotation of genetic associations with FUMA. Nat. Commun. 8, 1–10. doi:10.1038/s41467-017-01261-5
Welker, W., 1990. Why Does Cerebral Cortex Fissure and Fold? pp. 3–136. doi:10.1007/978-1-4615-3824-0_1
Winkler, A.M., Kochunov, P., Blangero, J., Almasy, L., Zilles, K., Fox, P.T., Duggirala, R., Glahn, D.C., 2010. Cortical thickness or grey matter volume? The importance of selecting the phenotype for imaging genetics studies. Neuroimage 53, 1135–1146. doi:10.1016/j.neuroimage.2009.12.028
Woolrich, M.W., Ripley, B.D., Brady, M., Smith, S.M., 2001. Temporal Autocorrelation in Univariate Linear Modeling of FMRI Data. Neuroimage 14, 1370–1386. doi:10.1006/nimg.2001.0931
Wu, M.C., Lee, S., Cai, T., Li, Y., Boehnke, M., Lin, X., 2011. Rare-variant association testing for sequencing data with the sequence kernel association test. Am. J. Hum. Genet. 89, 82–93. doi:10.1016/j.ajhg.2011.05.029
Xu, G., Knutsen, A.K., Dikranian, K., Kroenke, C.D., Bayly, P. V., Taber, L.A., 2010. Axons Pull on the Brain, But Tension Does Not Drive Cortical Folding. J. Biomech. Eng. 132, 071013. doi:10.1115/1.4001683
Yang, J., Benyamin, B., McEvoy, B.P., Gordon, S., Henders, A.K., Nyholt, D.R., Madden, P. a, Heath, A.C., Martin, N.G., Montgomery, G.W., Goddard, M.E., Visscher, P.M., 2010. Common SNPs explain a large proportion of the heritability for human height. Nat. Genet. 42, 565–569. doi:10.1038/ng.608
Yang, J., Lee, S.H., Goddard, M.E., Visscher, P.M., 2011. GCTA: A Tool for Genome-wide Complex Trait Analysis. Am. J. Hum. Genet. 88, 76–82. doi:10.1016/j.ajhg.2010.11.011
Yeni-Komshian, G.H., Benson, D.A., 1976. Anatomical study of cerebral asymmetry in the temporal lobe of humans, chimpanzees, and rhesus monkeys. Science (80-.). 192, 387–9. doi:10.1126/science.816005
Yun, H.J., Im, K., Yang, J.J., Yoon, U., Lee, J.M., 2013. Automated Sulcal Depth Measurement on Cortical Surface Reflecting Geometrical Properties of Sulci. PLoS One 8, 22–25. doi:10.1371/journal.pone.0055977
Zatorre, R.J., Belin, P., 2001. Spectral and temporal processing in human auditory cortex. Cereb. Cortex 11, 946–53. doi:10.1093/cercor/12.2.140
Zhang, T., Chen, H., Guo, L., Li, K., Li, L., Zhang, S., Shen, D., Hu, X., Liu, T., 2014. Characterization of U-shape streamline fibers: Methods and applications. Med. Image Anal. 18, 795–807. doi:10.1016/j.media.2014.04.005
Zlatkina, V., Petrides, M., 2014. Morphological patterns of the intraparietal sulcus and the anterior intermediate parietal sulcus of Jensen in the human brain. Proc. R. Soc. B Biol. Sci. 281, 20141493–20141493. doi:10.1098/rspb.2014.1493
Zlatkina, V., Petrides, M., 2010. Morphological patterns of the postcentral sulcus in the human brain. J. Comp. Neurol. 518, 3701–3724. doi:10.1002/cne.22418